

# Measurement of the $\pi^+ \rightarrow e^+ \nu_e$ Branching Ratio

**DISSERTATION**

Presented in Partial Fulfillment of the Requirements  
for the Degree of Doctor of Science

Department of Physics. Graduate School of Science.  
Osaka University.

**Shintaro Ito**

February 29, 2016

## Abstract

The study of rare decays is an important avenue to search for new physics beyond the Standard Model (SM). The ratio of the charged pion branching ratios,  $R^\pi = \Gamma[\pi^+ \rightarrow e^+ \nu_e(\gamma)]/\Gamma[\pi^+ \rightarrow \mu^+ \nu_\mu(\gamma)]$ , is one of the most precisely calculated processes involving quarks in the SM. Precise measurement of  $R^\pi$  provides the most stringent test of the hypothesis on electron-muon universality in weak interactions.

The PIENU experiment at TRIUMF aims to measure  $R^\pi$  with an improved precision by a factor of 5 over the previous experiment, to  $< 0.1\%$ .

This thesis presents the second result of  $R^\pi$  analysis using data taken in the run period of 2010 and 2011. The result for 2010 data set was completed,  $R_{\text{exp}}^\pi = [1.2344 \pm 0.0023(\text{stat}) \pm 0.0019(\text{syst})] \times 10^{-4}$ . The systematic uncertainties for 2011 data set were also analyzed, and the combined result of the uncertainties of  $R^\pi$  were estimated to be  $\Delta R_{\text{exp}}^\pi = [\pm 0.0014(\text{stat}) \pm 0.0013(\text{syst})] \times 10^{-4}$ , which corresponds to the precision level of 0.15%, an improvement by a factor of 3.

## Preface

The PIENU collaboration has about 30 people from 11 different institutions. I participated in the experiment starting in April 2011, before the beam time of that year.

The main data acquisition equipment consisted of 500 MHz Flash-ADC waveform digitizers, which recorded signals from all plastic scintillators and some crystals (§3.4.1). I was responsible for the waveform digitizer system including hardware, software, and data taking. In the course of the experiment, I augmented the digitizer system to perform more accurate waveform analysis for the CsI crystals. Accordingly, I updated all the software for on-line monitor program, data taking, and analysis. In addition, I participated in the operation and maintenance of all the detectors during the beam time.

I performed not only normal pion data taking, but also special runs for systematic studies such as the measurement of the NaI(Tl) and CsI crystals responses for low energy  $\pi^+ \rightarrow e^+ \nu_e$  tail using mono-energetic beam positrons (§5.2), and energy dependence of telescope counter response using beam muons stopped in the center of target (§4.6.2). The special positron data set was mainly analyzed by Tristan Sullivan, and I analyzed the muon data. The details of the detector and equipment were published in Ref. [1].

For the past three years, I have been working on the data analysis taken in 2010 and 2011. I analyzed all systematic uncertainties of  $R^\pi$ . I estimated the shapes and amplitudes of all background components existing in the time spectra, and optimized the fitting functions (Chapter 4).

After the extraction of ratio of the pion branching ratios before corrections, I estimated all the systematic corrections. The largest correction was the low energy  $\pi^+ \rightarrow e^+ \nu_e$  tail due to shower leakage from the calorimeter (Chapter 5). Since energy dependent effects altered the relative acceptance of the  $\pi^+ \rightarrow e^+ \nu_e$  and  $\pi^+ \rightarrow \mu^+ \rightarrow e^+$  decays, I performed Monte Carlo (MC) simulations for the acceptance correction (Chapter 6).

Additionally, I was in charge of the analysis codes and optimization of MC software for the data set in 2010 and 2011.

This is the second PhD thesis describing about  $R^\pi$  analysis. The first physics data taken in 2009 were mainly analyzed by Kaoru Yamada [2] to search for the massive neutrinos in  $\pi^+ \rightarrow e^+ \nu_e$  decay, and the initial  $R^\pi$  analysis was performed by Chloé Malbrunot [3]. After their work, we refined and completed the initial data set (taken in 2010) analysis, and published in Ref. [4]. The remaining data are currently being analyzed and I summarized the data taken in 2011.

## Acknowledgments

First of all, I would like to express my gratitude to my supervisor, Professor Yoshitaka Kuno. He accepted me into the Kuno-group in Osaka University and introduced me for the research of the high energy physics.

I would like to express my great appreciation to Associate Professor Masaharu Aoki. He supported many things, data taking and analysis, presentations in the conferences, and writing my thesis.

I want to thank all the PIENU collaborators, especially Professor Douglas Bryman and Doctor Toshio Numao, who are the spokesmen of the PIENU experiment. They accepted my participation into the PIENU experiment and supported all of my work in Canada. I am grateful to the PIENU posdocs: Doctor Luca Doria, Doctor Aleksey Sher and Doctor Dmitry Vavilov for the help of the data taking and analysis, and their advices. I want to acknowledge the insightful explanations and discussions with Doctor Richard Mischke. I really appreciate Doctor Youichi Igarashi, who supported my work in Canada and advised me about my analysis. I appreciate PhD students: Mr. Tristan Sullivan and Mr. Saul Cuen-Rochin, and Master student: Ms. Dorothea vom Bruch, who devoted time to discuss with me. I also thank to Doctor Chloé Malbrunot and Mr. Min-Min Ding. When I first came to Canada, they told me how to take the shift in the PIENU experiment and supported my life in Canada.

I am also grateful to all the members in the Kuno-group in Osaka University. In particular to Assistant Professor Akira Sato, Doctor Hideyuki Sakamoto, Professor Yoshio Koide, Professor Takahisa Itahashi, Doctor Hisataka Yoshida, and Professor Yoshitaka Kawashima, who spent time to discuss and advised me about my research. I also wish to express my gratitude to the secretaries of Kuno-group: Ms. Miki Ebisuya, Ms. Junko Komai, Ms. Hisae Takubo, Ms. Mitsuki Torikoshi, and Ms. Jun Imoto. I spent great research life in Osaka and Canada by their support.

Finally, I would like to express the special thanks to my parents. They allowed me to spend an wonderful student life with their continuous support.

# Contents

<b>1</b>	<b>Introduction</b>	<b>16</b>
1.1	The Standard Model of Particle Physics . . . . .	16
1.2	The Pion . . . . .	17
1.2.1	History of the Pion . . . . .	17
1.2.2	Review of Pion and Muon Decay Modes . . . . .	18
1.2.3	Review of $\pi^+ \rightarrow e^+ \nu_e$ Measurement . . . . .	18
1.2.4	Theory of $\pi^+ \rightarrow e^+ \nu_e$ Decay . . . . .	20
	Pion Decay Rate . . . . .	20
	Radiative Corrections . . . . .	22
1.3	Motivation of the $\pi^+ \rightarrow e^+ \nu_e$ Measurement . . . . .	23
1.3.1	Lepton Universality . . . . .	23
1.3.2	New Pseudoscalar Interaction . . . . .	24
	Charged Higgs Boson . . . . .	27
	R-Parity Violation SUSY . . . . .	27
	Leptoquark . . . . .	28
1.3.3	Massive Neutrino in the $\pi^+ \rightarrow e^+ \nu_e$ Measurement . . . . .	30
1.4	Outline of This Thesis . . . . .	31
<b>2</b>	<b>The PIENU Experiment</b>	<b>32</b>
2.1	Overview of the PIENU Experiment . . . . .	32
2.2	Previous Experiment at TRIUMF . . . . .	35
2.2.1	Raw Ratio Extraction . . . . .	36
2.2.2	Tail Correction . . . . .	37
2.3	Improvement in the PIENU Experiment . . . . .	39
2.4	History of the PIENU Experiment . . . . .	39
<b>3</b>	<b>Description of the PIENU Experiment</b>	<b>41</b>
3.1	The M13 Beam Line . . . . .	41
3.2	The PIENU Detector . . . . .	42
3.2.1	Overview . . . . .	42
3.2.2	Plastic Scintillators . . . . .	44
3.2.3	Wire Chambers . . . . .	44
	Beam Wire Chambers (WC1 and WC2) . . . . .	49

## CONTENTS

---

	Decay Positron Wire Chamber (WC3) . . . . .	49
3.2.4	Silicon Strip Detector . . . . .	51
3.2.5	NaI Calorimeter . . . . .	52
3.2.6	CsI Calorimeter . . . . .	52
3.2.7	Performance . . . . .	54
	Energy Resolution of the Calorimeters . . . . .	54
	Tracking Performance . . . . .	59
3.3	Trigger Logic for Data Taking . . . . .	59
3.4	The Data Acquisition System . . . . .	63
3.4.1	COPPER 500 MHz Flash-ADC System . . . . .	63
	COPPER . . . . .	63
	FINESSE . . . . .	64
	Clock Distributor . . . . .	65
	GPIO . . . . .	65
	Signal Synchronization . . . . .	66
3.4.2	Other Hardwares . . . . .	68
	VF48 . . . . .	68
	VT48 . . . . .	68
	TIGC . . . . .	68
3.4.3	Software of Data Acquisition System . . . . .	69
<b>4</b>	<b>Raw Ratio Extraction</b> . . . . .	<b>72</b>
4.1	Overview . . . . .	72
4.2	Waveform Calibration . . . . .	72
4.2.1	Pedestal Calibration . . . . .	72
4.2.2	Variable Extraction . . . . .	73
	COPPER . . . . .	73
	VF48 . . . . .	74
	VT48 . . . . .	74
4.2.3	Gain Correction . . . . .	74
	Scintillators . . . . .	74
	Silicon Strip Detector . . . . .	74
	CsI . . . . .	74
4.2.4	Energy Calibration . . . . .	75
	Scintillators and Silicon Strip Detectors . . . . .	75
	CsI Calibration . . . . .	75
4.3	Event Mask for Blind Analysis . . . . .	77
4.4	Event Selection . . . . .	79
4.4.1	Beam Pion Selection . . . . .	80
4.4.2	Decay Positron Selection . . . . .	81
4.4.3	Background Rejection . . . . .	81
	Pileup Cut . . . . .	81
	Charge Ratio Cut . . . . .	83
	Pre Pileup Cut . . . . .	84

CONTENTS

---

	Timing Consistency . . . . .	84
	B1-B2 Consistency Cut . . . . .	86
4.4.4	Acceptance Cut . . . . .	86
4.4.5	Summary of the Selection Cuts . . . . .	86
4.5	Time Spectrum Analysis . . . . .	87
4.5.1	Low-Energy Time Spectrum . . . . .	91
4.5.2	High-Energy Time Spectrum . . . . .	91
	$\pi^+ \rightarrow \mu^+ \nu_\mu \gamma$ Decays . . . . .	91
	Pileup in the Calorimeters . . . . .	92
	Pileup in T1 . . . . .	94
4.5.3	The Fitting Function . . . . .	95
4.5.4	Stability of the Fit . . . . .	101
4.5.5	Systematic Errors of the Time Fit . . . . .	101
4.6	Systematic Corrections to Raw Ratio . . . . .	103
4.6.1	$\mu$ DIF Correction . . . . .	103
4.6.2	Energy Dependence on $t_0$ . . . . .	105
4.7	Summary of Raw Ratio Extraction . . . . .	108
<b>5</b>	<b>Systematic Correction</b>	
	<b>–Low-Energy <math>\pi^+ \rightarrow e^+ \nu_e</math> Tail–</b>	<b>111</b>
5.1	Lower Limit . . . . .	112
5.1.1	$\pi^+ \rightarrow \mu^+ \rightarrow e^+$ Suppression Cuts . . . . .	112
5.1.2	Concept of Lower Limit Estimate . . . . .	116
5.1.3	Modification of $\mu$ DIF Contribution on Lower Limit . . . . .	118
5.1.4	Introduction of $\pi^+ \rightarrow e^+ \nu_e(\gamma)$ Events without Hadronic Reactions . . . . .	120
5.1.5	Lower Limit Estimate . . . . .	123
5.1.6	Systematic Uncertainty . . . . .	123
	Uncertainty of $\mu$ DIF Contribution . . . . .	123
	Shape of the $\pi^+ \rightarrow e^+ \nu_e(\gamma)$ MC Energy Spectrum . . . . .	124
	Shape of the $\mu$ DIF MC Energy Spectrum . . . . .	124
	Contribution of $E_{\text{tot}}$ Cut to $\pi^+ \rightarrow \mu^+ \rightarrow e^+$ Energy Spec- trum . . . . .	124
	Summary of Systematic Study . . . . .	127
5.1.7	Bhabha Correction . . . . .	127
5.1.8	Summary of the Lower Limit . . . . .	129
5.2	Upper Limit . . . . .	130
5.2.1	Measurement . . . . .	130
5.2.2	Analysis of the Upper Limit . . . . .	130
5.2.3	Result of the Upper Limit Estimate . . . . .	132
5.3	Combination of Two Limits . . . . .	132

## CONTENTS

---

<b>6</b>	<b>Systematic Correction</b>	<b>136</b>
	–Acceptance Correction–	
6.1	Monte Carlo Calculation . . . . .	136
6.2	The Pion Stopping Position . . . . .	137
6.3	Detector Geometry . . . . .	137
6.4	Trigger Threshold . . . . .	140
6.5	Summary of Acceptance Correction . . . . .	140
<b>7</b>	<b>Result</b>	<b>142</b>
7.1	Measured Ratio of the Branching Ratios . . . . .	142
7.2	Systematic Checks . . . . .	142
<b>8</b>	<b>Discussion</b>	<b>145</b>
8.1	Limits on Theoretical Models . . . . .	145
8.1.1	Limit on Lepton Universality . . . . .	145
8.1.2	Sensitivity to Pseudoscalar Interaction . . . . .	146
8.1.3	Limits on Massive Neutrino . . . . .	146
	Brief Introduction of the Theory . . . . .	146
	Limit from $R^\pi$ Measurement . . . . .	147
8.2	Foreseen Improvements . . . . .	147
8.2.1	Lepton Universality Test . . . . .	147
	Statistical Uncertainty . . . . .	147
	Systematic Uncertainty . . . . .	148
8.2.2	Sensitivity to Pseudoscalar Interaction . . . . .	149
8.2.3	Massive Neutrino Analysis . . . . .	149
<b>9</b>	<b>Conclusion</b>	<b>150</b>

# List of Figures

1.1	The Feynman diagram for the $\pi^+ \rightarrow l^+ \nu_l$ decay where $l = e, \mu$ .	19
1.2	History of measured ratio $R_{\text{exp}}^\pi$ . The red points are used for the current PDG average. The dashed green line indicates the theoretical predicted value. The top point shows the expected uncertainty by the PIENU experiment.	20
1.3	Schematic illustration of the helicity suppressed $\pi^+ \rightarrow e^+ \nu_e$ decay. Thin arrows indicate particle momenta, while thick arrows represent their spins.	22
1.4	Feynman diagrams of radiative $\pi^+ \rightarrow e^+ \nu_e$ decay process. (a) Inner Bremsstrahlung photons. (b) Virtual emission and re-absorption of photons.	23
1.5	Experimental bounds on $\Delta_{\mu\tau}$ and $\Delta_{e\tau}$ [36] as of 2008. (a) W decay. (b) $\tau$ decay. (c) $\pi$ and K decay. (d) All decays combination. The shaded areas represent the 68% (dark gray) and 90% (light gray) Confidence Levels (C.L.).	25
1.6	Tree level RPV contributions to $R^\pi$ [42].	28
1.7	Constraints on RPV parameters with 95% C.L. [42]. Blue curve corresponds to the value by the previous experiments, green curve indicates projected limit of proton weak charge experiment, and dashed red curve shows the constraint with precision $\Delta R_{\text{RPV}}^\pi = 0.1\%$	29
1.8	The Feynman diagram for the contribution of pseudoscalar leptoquark to $\pi^+ \rightarrow e^+ \nu_e$ .	30
2.1	Schematic of the PIENU experimental technique [56].	33
2.2	Simulated energy deposit in the target. Two $\pi^+ \rightarrow e^+ \nu_e$ (blue) and $\pi^+ \rightarrow \mu^+ \rightarrow e^+$ (red) peaks are seen due to the extra muon energy.	34
2.3	(a): Simulated energy spectra of decay positrons in the calorimeter [56]. (b): Simulated decay positron time spectra [56]. In both plots, the peak heights are normalized to 1.	34
2.4	Experimental setup of the previous experiment at TRIUMF [23].	35

LIST OF FIGURES

---

2.5	Energy spectrum of decay positron measured by the NaI calorimeter [23]. Horizontal axis is pulse height of decay positron. . .	37
2.6	Time spectra of decay positrons [22]. The energy threshold in Figure 2.5 was at 3400 channel. . . . .	38
2.7	Total energy deposit in the target with wide-gate and early part of the pion pulse with narrow-gate [23]. The region surrounded by two vertical lines and two slanting lines indicates selected $\pi^+ \rightarrow e^+ \nu_e$ events. . . . .	38
2.8	$\pi^+ \rightarrow \mu^+ \rightarrow e^+$ suppressed energy spectrum measured by the NaI calorimeter [23]. Most of low-energy background was due to $\pi$ DIF events. . . . .	39
3.1	The illustration of M13 beam channel [58]. Downstream parts of <i>F3</i> were extended line for the requirement of the PIENU experiment. . . . .	42
3.2	Pion, muon, and positron distributions at <i>F3</i> (histograms) [58]. Horizontal axis is position for X-axis, and vertical axis is amplitude. The heavy black lines indicate fitted Gaussian function for pions and positrons. . . . .	43
3.3	Picture of the extended area. . . . .	43
3.4	Schematic of the whole PIENU detector [1]. For the visualization, the thickness of each silicon strip detector in the zoom-in region is illustrated with larger size than an actual size. . . . .	45
3.5	Picture of PIENU-I. . . . .	46
3.6	Picture of PIENU-II. . . . .	46
3.7	The whole PIENU detector located in detector enclosure. PIENU-II was on a cart, and moved to PIENU-I during normal runs. . . . .	47
3.8	Schematic view of the B1,B2,B3, and T1 scintillator readout [1]. . . . .	47
3.9	Illustration of T2 scintillator readout. 33 parallel grooves ( $1.1 \times 1.1 \text{ mm}^2$ ) were milled on the surface of the scintillator [1].	49
3.10	Picture of WC1 and WC2 attached on the beam pipe. . . . .	50
3.11	Picture of WC3 placed on the flange of the NaI(Tl) enclosure. . . . .	50
3.12	Assembly of S1 and S2. . . . .	51
3.13	Schematic drawing of the silicon strip detector read out [1]. . . . .	52
3.14	Picture of the NaI crystal from its backside [3]. . . . .	53
3.15	Picture of whole calorimeter consisted by NaI and 97 CsI crystals [3]. . . . .	54
3.16	Picture of one CsI crystal [3]. . . . .	55
3.17	Schematic drawing of the detector setup for special positron runs. . . . .	56

LIST OF FIGURES

---

3.18 Response of the NaI crystal at 70 MeV positron beam. The additional structures below the full energy peak were due to photo-nuclear effects [62]. . . . . 57

3.19 Beam positron energy in the NaI calorimeter. Filled circles with error bars indicate data, and simulated spectra with and without hadronic reactions are respectively shown by red and blue histograms [62]. . . . . 57

3.20  $\pi^+ \rightarrow e^+ \nu_e$  energy spectra with  $\pi^+ \rightarrow \mu^+ \rightarrow e^+$  suppression cuts [1]. The unfilled histogram represents the energy spectrum with the radial acceptance cuts of 60 mm and the shaded histogram is with tighter 40 mm acceptance cut. . . . . 58

3.21 Tail measurement for the NaI and the NaI plus CsI rings [1]. The vertical axis indicates the low-energy tail fraction, which represents the integral of events below 50 MeV divided by the integral of full energy spectrum. . . . . 58

3.22 Schematic of pion decay at rest ( $\pi$ DAR, upper trajectory) and  $\pi$ DIF (lower trajectory) events. . . . . 59

3.23 Simulated kink angle distributions for different decay modes [1].  $\pi$ DAR and  $\mu$ DAR respectively stand for pion and muon decay at rest in the target. Dashed red line indicates the  $\pi$ DIF occurred after B2 counter and muon decays at rest in B3, and dotted blue line represents pion decays between WC2 and S1. . . . . 60

3.24 Kink angle distributions for  $\pi^+ \rightarrow e^+ \nu_e$  ( $T_{\text{NaI}} > 55$  MeV) and  $\pi^+ \rightarrow \mu^+ \rightarrow e^+$  ( $T_{\text{NaI}} < 30$  MeV) data events [1].  $\pi$ DAR events were suppressed using the energy deposit information in B3 (see §5.1.1 for detail). . . . . 60

3.25 Schematic of the trigger diagram for the three “physics triggers”. . . . . 62

3.26 Picture of main COPPER board mounted with four FINESSE modules. . . . . 64

3.27 Typical waveform digitized by COPPER. Blue plots indicate sampling points and red curve shows the fitting template. . . 65

3.28 Diagram of COPPER system [65]. CD in the box on FINESSE represents “Clock Divide”. The 250 MHz clock, gate, and reset signals for Clock Distributor were provided by GPIO. 66

3.29 Example of diagram for the gate timing mismatch [65]. WCLK was driven with 125 MHz, thus 8 ns shifted wave form would be observed. . . . . 67

3.30 Time difference of the peaks evaluated by wave form fit between COPPER1-FINESSE1-Channel2 and COPPER2-FINESSE1-Channel2. Those channels respectively recorded the signals of T1’s PMT1 and PMT2. . . . . 67

LIST OF FIGURES

---

3.31	Web interface of MIDAS data acquisition system. All the VME modules were integrated and easily controlled via this interface. . . . .	70
3.32	Example of the control for modules. The delay timings of gate and reset signals in Clock Distributor could be adjusted in this page. The delay timings of gate and reset signals were respectively set to 800 ps and 280 ps. . . . .	70
3.33	Example of the on-line histograms. In order to check the gate timing mismatch, new histograms were added into the software in 2012. Those histograms show the case of gate timing mismatch run. The time difference of the peak between each channel was histogramed (e.g. B1_1-B1_2 represents the time difference between PMT1 and PMT2 of B1). Tg_1 to Tg_4 stand for the PMT1 to 4 of B3. . . . .	71
4.1	Schematic of the variables extraction from waveforms of COPPER. This is the example of $\pi^+ \rightarrow \mu^+ \rightarrow e^+$ decay with one background signal in Pre-region in B3. . . . .	73
4.2	A typical waveform of the NaI with the pileup hit. The first smaller pulse was decay positron from pion decay, and the second larger pulse was due to the background. . . . .	76
4.3	Decay positron energy spectrum. Dashed red histogram represents pulse height based evaluation and black histogram indicates $Q_{\text{ww}}$ based evaluation. . . . .	76
4.4	$\pi^+ \rightarrow e^+ \nu_e$ energy spectra in the NaI. Dashed red histogram is data with $\pi^+ \rightarrow \mu^+ \rightarrow e^+$ suppression cuts and black histogram is MC simulated events. Data is in good agreement with MC spectrum. . . . .	77
4.5	Comparison of the cosmic signal in each CsI crystal of the inner upstream part between data (black) and MC (red). Horizontal axes are ADC counts. . . . .	78
4.6	History of neutron lifetime measurement experiments [16]. Dashed red line indicates the current average. The points shown by filled red circle are used for the average. . . . .	79
4.7	Blinding technique for the PIENU experiment [3]. A smooth inefficiency function removed events based on energy deposited in the target. Case a) lowered $R_{\text{raw}}^\pi$ from the actual value while case b) raised. . . . .	80
4.8	Energy deposit in B1 (left) and B2 (right, after the beam pion selection in B1). The regions between two vertical red lines in left and right were accepted as good pion events. . . . .	80
4.9	Contour plot of the beam profile of WC1 (left) and WC2 (right, after WC1 cut). The red boxes indicate the event selected regions. . . . .	81

LIST OF FIGURES

---

4.10	Energy in the NaI versus minimum energy loss in the downstream counters. Heavy red line indicates the cut position. . .	82
4.11	Time spectra below 52 MeV region with the pion and decay positron selection cuts (black), plus pileup cut (red), and plus pre pileup cut (blue). . . . .	82
4.12	The number of hits in B1 (left), B2(center), and T1(right). The legends indicate the PMT number. . . . .	83
4.13	The ratio of charge $Q/Q_w$ for PMT1 in B1. The events between the dashed red lines were accepted as good pion events. . . . .	84
4.14	The time of the first pulse in B1-PMT1. The events between two dashed lines were accepted as good events. . . . .	85
4.15	The time difference between T2 and T1 (VT48 signals). The events between two dashed lines were accepted as good events. . . . .	85
4.16	Time difference between B3 and B1 vs $Q_{ww}$ in B3. The events surrounded by the red lines were removed. . . . .	86
4.17	Reconstructed radial acceptance distribution at WC3. The events with radius less than 60 mm (red line) were selected. The spikes of this distribution are due to the resolution of WC3 wire pitch. . . . .	87
4.18	Combined energy spectrum of the NaI plus CsI detectors. The vertical red line indicates the $E_{cut}=52$ MeV. . . . .	88
4.19	Time spectra in the low- (a) and high- (b) energy regions on 2010 data set. Horizontal axes show decay times extracted from the time difference between T1 and B1. The solid red lines in the low- and high-energy regions represent $\pi^+ \rightarrow \mu^+ \rightarrow e^+$ decays and the solid blue lines in high-energy region shows $\pi^+ \rightarrow e^+ \nu_e$ decays. Other lines indicate background components and the solid green lines in both regions are the sums of the background components (see text for details). . . . .	89
4.20	Time spectra in the low- (a) and high- (b) energy regions on 2011 data set. . . . .	90
4.21	Simulated $\pi^+ \rightarrow \mu^+ \nu_\mu \gamma$ time distributions above $E_{cut} = 52$ MeV. Black histogram indicates the 2010 shape and red histogram shows the 2011 shape. Since the method of energy calibration for the NaI was modified on 2011 data set, the contribution of $\pi^+ \rightarrow \mu^+ \nu_\mu \gamma$ was reduced. . . . .	93
4.22	Simulated time distributions of pileup events above $E_{cut} = 52$ MeV. Black histogram indicates the 2010 shape and red histogram shows the 2011 data. The contribution of the pileup events for 2011 data set is less than that of 2010 data set because the different variable was used for the NaI in each data set. . . . .	93

LIST OF FIGURES

---

4.23	Pileup events with fitting functions. The artificial $\Delta T$ was 100 ns and the lower edge of Pre-region was at -5500ns. . . .	96
4.24	The result of the number of pileup events at each $\Delta T$ with a relaxation of pre pileup cut. Black points show the number of pileup events (case A + B) obtained by fit as shown in Figure 4.23. Those points were fitted to the quadratic function (red curves). Bottom right shows the number of pileup events estimated by extrapolation (absolute values of the intercepts $c$ ) versus the edge of Pre-region. . . . .	97
4.25	Number of pileup events versus old-muons. Those plots were fitted to the linear function, which was used for the fixed parameter of the fitting function for raw ratio extraction. . .	98
4.26	The extra hits time distributions in PMT2. Left: The main pulse and the extra hits shown by log scale in vertical axis. Right: Zoom-in of the extra hits time distribution fitted to a step function (black curve). . . . .	98
4.27	Residuals for 2010 data set. Top two residuals are high-energy time spectrum, while bottom two panels indicate the residuals in low-energy time spectrum. Left two panels show $t < 0$ region while residuals in $t > 0$ regions are shown in two right panels. Bin size for top left was 10 ns while another regions were 2 ns bin. . . . .	99
4.28	Residuals for 2011 data set. The place of each region is same as in Figure 4.27 . . . . .	100
4.29	Stability plots of the pre pileup cut for the fit using all components (black) and the fit without the functions of $\mathcal{G}$ and $\mathcal{F}_2$ . The values of $R_{\text{raw}}^\pi$ and the statistical errors were normalized to the value at -7750 ns. . . . .	102
4.30	Simulated decay time of $\mu\text{DIF}$ events after pion decay at rest in the target. . . . .	105
4.31	The energy spectra of $\pi^+ \rightarrow \mu^+ \rightarrow e^+$ events measured by the NaI and CsI. Red: Simulated $\mu\text{DIF}$ events. Black: $\mu\text{DAR}$ events (standard $\pi^+ \rightarrow \mu^+ \rightarrow e^+$ events) (2011 analysis). . . .	106
4.32	Left: Comparison for Michel spectrum between data (black) and MC (dashed red) measured by the NaI and CsI. Center: Discrepancy between data and MC. Vertical axis indicate the fraction of the amplitude of MC to the amplitude of data at each bin. Right: Before (black) and after (dashed red) modification of $\mu\text{DIF}$ energy spectrum in the NaI and CsI. . .	107
4.33	Zoom-in at $t = 0$ with the energy range of 0–5 MeV. Black histogram is the decay positron time spectrum, which was fitted to the step function (red). . . . .	108

LIST OF FIGURES

---

4.34	$E_{\text{tot}}$ distribution. The larger peak came from the beam muons plus decay positrons, and smaller peak was due to the beam positron. The events below 12.5 MeV (red line) were removed.	109
4.35	Energy dependence on $t_0$ .	109
5.1	Sum of the energy deposit in B1, B2, S1, S2, and B3. Vertical lines indicate $\pi^+ \rightarrow \mu^+ \rightarrow e^+$ suppression cut. The events indicated by red arrow were accepted.	113
5.2	Kink angle distributions for $\pi^+ \rightarrow e^+ \nu_e$ and $\pi^+ \rightarrow \mu^+ \rightarrow e^+$ events after time and energy loss cuts. Vertical red line indicates the $\pi^+ \rightarrow \mu^+ \rightarrow e^+$ suppression cut at 12 degrees. The events below 12 degrees were accepted.	113
5.3	Energy deposited in S3_X versus S3_Y. Two dashed red boxes are muon leakage from $\pi$ DIF that traversed B3. The events outside red curve were removed. S3_X was placed before S3_Y, so the events in the lower box shows that muon stopped in S3_X, and the events in the upper box shows that muon traversed S3_X and stopped in S3_Y.	114
5.4	2-pulse and 3-pulse fit for $\pi^+ \rightarrow \mu^+ \rightarrow e^+$ event in B3 [3].	115
5.5	$\Delta\chi^2$ versus energy loss information. $\pi^+ \rightarrow e^+ \nu_e$ events are mostly inside red lines. The events outside the red lines were removed.	115
5.6	Energy spectrum of the NaI plus CsI after each suppression cut. The black histogram is after only time cut and the pink histogram is after all suppression cuts. The legend box shows the low-energy fraction, which represents the integral of events below $E_{\text{cut}}$ (=52 MeV) divided by the integral of the full energy spectrum.	117
5.7	Simulated $E_{\text{tot}}$ distributions for the $\pi^+ \rightarrow e^+ \nu_e$ (black), $\pi$ DAR- $\mu$ DAR (dashed red), $\pi$ DIF- $\mu$ DAR (dashed green), and $\mu$ DIF (dashed blue) events. The energy resolution of each counter and Barks effect were included in the simulation. Two vertical heavy red lines indicate cut region for $\pi^+ \rightarrow \mu^+ \rightarrow e^+$ suppression.	117
5.8	(a) $\pi^+ \rightarrow \mu^+ \rightarrow e^+$ suppressed spectrum (same as that in Figure 5.6). (b) $\pi^+ \rightarrow \mu^+ \rightarrow e^+$ energy spectrum obtained by the late selection, which represents the time selection $t > 100$ ns after pion decay.	119
5.9	Energy (left) and time (right) spectra for the fit. The values shown in the legend in left indicate $\chi^2/n_d$ for the fit and the fractions of three components below 52 MeV.	120
5.10	The $\mu$ DAR (black) and $\mu$ DAR and $\mu$ DIF combined (dashed red) energy spectra.	121

LIST OF FIGURES

---

5.11	Dashed red: Simulated energy spectra of $\pi^+ \rightarrow e^+ \nu_e$ plus $\pi^+ \rightarrow e^+ \nu_e \gamma$ without hadronic reaction to exclude photo-nuclear effect. Black: Suppressed spectrum (data). The difference between 50 to 55 MeV was due to the photo-nuclear effect. . . . .	122
5.12	Comparison of $\pi^+ \rightarrow e^+ \nu_e$ (dashed red) and $\pi^+ \rightarrow e^+ \nu_e \gamma$ (black) events by MC. . . . .	123
5.13	Left: The result of the TF' study in the range of 1-52 MeV. Error bars indicate just statistical errors at each energy $x$ . Right: Zoom-in of the highest edge of the error bar at 30.50 MeV. . . . .	124
5.14	The simulated $\pi^+ \rightarrow e^+ \nu_e(\gamma)$ energy spectra with different upper bounds for the $E_{\text{tot}}$ cut. Tail fractions indicate the number of events below 52 MeV divided by the total number of events. . . . .	125
5.15	Left: Comparison of the $\pi^+ \rightarrow \mu^+ \rightarrow e^+$ energy spectra with the late decay selection ( $t > 100$ ns) only (red curve), and the late decay selection and the $E_{\text{tot}}$ cut (black with error bar). Black points were fitted to the red curve. Right: The ratio of the amplitude of the $\pi^+ \rightarrow \mu^+ \rightarrow e^+$ energy spectrum with the $E_{\text{tot}}$ cut and the late pion decay selection ( $t > 100$ ns) to the amplitude of the $\pi^+ \rightarrow \mu^+ \rightarrow e^+$ energy spectrum with the late pion decay selection. These points were fitted to the quadratic function. . . . .	126
5.16	The Michel spectra before (black) and after (red) modification by the quadratic function. . . . .	126
5.17	Simulated $\pi^+ \rightarrow e^+ \nu_e(\gamma)$ events with (yellow) or without (red) $E_{\text{tot}}$ cut. The low-energy $\pi^+ \rightarrow e^+ \nu_e(\gamma)$ events were removed by $E_{\text{tot}}$ cut. . . . .	128
5.18	Comparison of the energy spectra between data (black) and MC (red) at 47.7 degrees. . . . .	128
5.19	Comparison of the ADC counts in T2 between data (black) and MC (red) at 47.7 degrees. The T2 energy cut region was chosen to be less than 500 channels. . . . .	129
5.20	The result of the systematic study. Dashed horizontal red line indicates the central value of the tail fraction at 16.5 MeV (dashed vertical red line). The statistical errors were scaled at 16.5 MeV. . . . .	130
5.21	Comparison of the energy spectra between data (black) and MC (red) at each angle. The hadronic reaction was included in MC. . . . .	133
5.22	Comparison of the tail fraction between data (black) and MC (red) at each angle. Error bars are too small to be visible. . .	134
5.23	$E_e$ (black) and $E_{\text{NaICsI}}$ (dashed red) spectra at 0 degrees by MC. Dashed vertical black line indicates $E_{\text{cut}}$ at 52 MeV. . .	134

LIST OF FIGURES

---

5.24	$E_{\pi e \nu}$ spectrum for $\pi^+ \rightarrow e^+ \nu_e$ decay produced by MC. . . . .	135
5.25	Combination of the lower (red) and upper (blue) limits. The black histogram represents the combined region of the two values. . . . .	135
6.1	Reconstructed pion stopping position with data (black) and MC (dashed red) for 2011 data set. . . . .	138
6.2	Comparison of the reconstructed (black) and actual (red) pion stopping distributions by MC (2011 data set). . . . .	138
6.3	Result of the variation due to the different pion stopping position along the beam axis at each radius cut point (left) and zoom-in at 60 mm (right) (2011 data set). . . . .	139
6.4	Result of the variation due to the different width of stopping distribution at each radius cut point (left) and zoom-in at 60 mm (right) (2011 data set). . . . .	139
6.5	Result of the variation due to the different energy threshold of T1 and T2 at each radius cut point (left) and zoom-in at 60 mm (right) (2011 data set). . . . .	141
7.1	$E_{\text{cut}}$ dependence for 2011 data set before (black) and after (red) corrections. $R_{\text{exp}}^\pi$ were normalized to the value at 52 MeV. . . . .	143
7.2	Dependence of the radius cut at WC3 (§4.4.4) for 2011 data set before (black) correction and after tail plus $\mu\text{DIF}$ corrections (red) and all corrections (blue). In order to exclude the statistical correlation, 10 mm sliced cut was applied. For example, the cut value at 55 mm represents the radius cut with a range of 50 to 60 mm. The value of $R_{\text{exp}}^\pi$ at each radius cut were normalized to the value at 55 mm. . . . .	144
8.1	Upper limits to the mixing parameter $U_{ei}$ in the mass range of $< 55 \text{ MeV}/c^2$ . Compared to the previous work (black), the PIENU result in 2010 (red) improved by a factor of 1.5, and the combined PIENU result will improve by a factor of 2. . .	148

# List of Tables

1.1	Fermions in the three generations of matter. . . . .	16
1.2	The force-mediating-gauge and mass-generator bosons. . . . .	17
1.3	Measured pion decay modes [16]. . . . .	18
1.4	Measured muon decay modes [16]. . . . .	18
1.5	Current experimental results of the lepton universality tests. Numbers were taken from [33] except top four decay modes. . .	26
2.1	Summary of uncertainties in the previous experiment [23]. . .	36
2.2	History of the PIENU experiment. The numbers in parentheses indicate the numbers of $\pi^+ \rightarrow e^+ \nu_e$ events before off-line event selection. . . . .	40
3.1	Parameters for the PIENU detector [1]. . . . .	48
3.2	Trigger rates [1]. . . . .	63
4.1	Event selection cuts and their ratio of residual fraction. Each fraction of the cuts is differential to the previous cut. Total event-survival ratio represents the ratio of the number of events before and after applying all the event selection cuts. . .	88
4.2	Result of the fitting parameters for 2010 and 2011 data sets. $R_{\text{raw}}^\pi$ for 2011 data set is still blinded, so it is represented by asterisks. . . . .	101
4.3	Summary of the systematic errors for 2011 data set. . . . .	103
4.4	Summary of the uncertainties for the $R_{\text{raw}}^\pi$ , $\mu\text{DIF}$ correction, and $t_0$ energy dependence. The value of $R_{\text{raw}}^\pi$ on 2010 data set includes the $\mu\text{DIF}$ correction. Because the central value of $R_{\text{raw}}^\pi$ for 2011 data set is still blinded, it is represented by asterisks. The variation of $R_{\text{raw}}^\pi$ came from the error of $\mu\text{DIF}$ correction was estimated to be less than $10^{-8}$ . . . . .	110
5.1	Summary of the $\pi^+ \rightarrow \mu^+ \rightarrow e^+$ suppression cuts. . . . .	116
5.2	Summary of the special data sets and tail fractions at each angle. . . . .	131

## LIST OF TABLES

---

6.1	Uncertainties in the detector geometry measurement [3]. . . .	140
7.1	Summary of the ratio of the pion branching ratios before corrections $R_{\text{raw}}^\pi$ , the multiplicative corrections, and the result after applying the corrections with their uncertainties in 2010 [4] and 2011. $R_{\text{raw}}^\pi$ for 2011 data set is still blinded, so it is represented by asterisks. . . . .	143

# Chapter 1

## Introduction

### 1.1 The Standard Model of Particle Physics

The Standard Model (SM) of particle physics is a theory of fundamental particles and how they interact. The foundation of the current SM was solidified in the middle of 1970s by experimental discoveries of quarks. Since then, the existence of the top quark (1995) [6, 7], the tau neutrino (2000) [8], and more recently the Higgs boson (2013) [11, 12], were empirically confirmed, and had given further confidence to the SM. The theory is powerful since almost all of the SM predictions have been empirically verified.

Despite success of the SM, there are physical phenomena which the theory cannot explain (e.g. neutrino oscillations). The SM does not contain dark matter particles, and it does not describe the theory of gravitation. Theorists are now working hard for the development to extend Beyond the Standard Model (BSM) which explains disagreements between the theory and observations.

In the current SM, all matter is composed of fundamental spin-1/2 (fermion) particles categorized into leptons and quarks (Table 1.1). The interactions between each fermion are described by the exchange of “force mediator” particles with integer spin (boson). There are four interactions that occur in nature: strong, weak, electromagnetic, and gravitational<sup>1</sup> in-

Table 1.1: Fermions in the three generations of matter.

	Generations			Charge
	I	II	III	(Q/ e )
Leptons	e	$\mu$	$\tau$	-1
	$\nu_e$	$\nu_\mu$	$\nu_\tau$	0
Quarks	u	c	t	+2/3
	d	s	b	-1/3

<sup>1</sup>The gravitational interaction is not included in the SM.

## 1.2. THE PION

---

Table 1.2: The force-mediating-gauge and mass-generator bosons.

Force	Mediator
Strong	g (gluons)
Electromagnetic	$\gamma$ (photon)
Weak	$W^\pm, Z^0$ (weak bosons)
Gravitational	G (graviton)
Mass generator	H (Higgs boson)

teractions (Table 1.2). As explained above, the SM does not describe the gravity interaction, however it's negligible on the subatomic scale.

The Higgs particle is a mass-generating particle predicted by Robert Brout, François Englert, and Peter Higgs [9, 10]. It has no spin nor electric charge, and is classified as a boson. In July 2012, the two experimental groups at LHC in CERN (ATLAS and CMS) reported that they found a new particle with a mass of about  $125 \text{ GeV}/c^2$ , which was consistent with the Higgs boson [11, 12]. In March 2013, the existence of Higgs boson was tentatively confirmed [13].

## 1.2 The Pion

### 1.2.1 History of the Pion

In 1935, Hideki Yukawa predicted the existence of mesons as a carrier of the strong nuclear force [14]. He predicted the mass of the new particle to be about  $100 \text{ MeV}/c^2$  using the range of nuclear forces. In 1936, the muon was discovered first and initially thought that it was meson since it has a mass of  $105.7 \text{ MeV}/c^2$ . However, it was verified by later experiments that muon didn't appear in the strong nuclear interaction. In the current SM, the muon is classified as a lepton.

In 1947, the first true mesons, the charged pions were discovered by Cecil Powell and his collaborator using tracks left by cosmic rays in photographic nuclear emulsion plates [15]. For this discovery, H. Yukawa and C. Powell respectively won the 1949 and 1950 Nobel Prizes, respectively.

Since then, many experiments were done and we now know that the pion is a meson composed of two quarks in the first generation. The pion can be charged ( $\pi^\pm$ ) or neutral ( $\pi^0$ ). From this section, only the  $\pi^+$  will be discussed since it was used in our experiment. The  $\pi^-$  is absorbed by nuclei due to the opposite electric charge, therefore more difficult to deal with from the experimental point of view. On the other hand, such problems could be reduced for the  $\pi^+$ .

## 1.2. THE PION

---

Table 1.3: Measured pion decay modes [16].

	Decay mode	Fraction ( $\Gamma_i^\pi/\Gamma^\pi$ )
$\Gamma_1^\pi$	$\pi^+ \rightarrow \mu^+ \nu_\mu$	$0.9998770 \pm 0.00004$
$\Gamma_2^\pi$	$\pi^+ \rightarrow \mu^+ \nu_\mu \gamma$	$(2.00 \pm 0.25) \times 10^{-4}$ ( $E_\gamma > 1$ MeV)
$\Gamma_3^\pi$	$\pi^+ \rightarrow e^+ \nu_e$	$(1.230 \pm 0.004) \times 10^{-4}$
$\Gamma_4^\pi$	$\pi^+ \rightarrow e^+ \nu_e \gamma$	$(7.39 \pm 0.05) \times 10^{-7}$ ( $E_\gamma > 10$ MeV)
$\Gamma_5^\pi$	$\pi^+ \rightarrow \pi^0 e^+ \nu_e$	$(1.036 \pm 0.006) \times 10^{-8}$
$\Gamma_6^\pi$	$\pi^+ \rightarrow e^+ \nu_e e^+ e^-$	$(3.2 \pm 0.5) \times 10^{-9}$

Table 1.4: Measured muon decay modes [16].

	Decay mode	Fraction ( $\Gamma_i^\mu/\Gamma^\mu$ )
$\Gamma_1^\mu$	$\mu^+ \rightarrow e^+ \nu_e \bar{\nu}_\mu$	$\approx 100\%$
$\Gamma_2^\mu$	$\mu^+ \rightarrow e^+ \nu_e \bar{\nu}_\mu \gamma$	$(1.4 \pm 0.4)\%$ ( $E_\gamma > 10$ MeV)
$\Gamma_3^\mu$	$\mu^+ \rightarrow e^+ \nu_e \bar{\nu}_\mu e^+ e^-$	$(3.4 \pm 0.4) \times 10^{-5}$

### 1.2.2 Review of Pion and Muon Decay Modes

The  $\pi^+$  consists of one up ( $u$ ) and one anti-down ( $\bar{d}$ ) quark. The  $\pi^+$  has a mass of  $139.6 \text{ MeV}/c^2$  and a lifetime of  $26.033 \pm 0.005 \text{ ns}$  [16]. It can only decay into lighter leptons, a muon or an electron with a neutrino<sup>2</sup>. Table 1.3 shows several allowed decay modes of the pion. The interest in this thesis is the ratio of the branching ratios of decay mode  $\Gamma_3^\pi$  to decay mode  $\Gamma_1^\pi$ . Figure 1.1 shows the Feynman diagram for these decays. The decay mode with branching ratio smaller than  $10^{-7}$  is negligible at our precision level. Thus, the contributions of the last two decay modes listed in Table 1.3 are negligible.

The muon has a mass of  $105.7 \text{ MeV}/c^2$  and has a lifetime of  $2.1969811 \pm 0.0000022 \mu\text{s}$  [16]. The main three muon decay modes are listed in Table 1.4.

The calorimeter used in the experiment was sensitive to photons from radiative pion or muon decays. Therefore, those processes ( $\Gamma_2^\pi$  and  $\Gamma_4^\pi$ ) must be taken into account in the calculation of the ratio of the branching ratios.

### 1.2.3 Review of $\pi^+ \rightarrow e^+ \nu_e$ Measurement

In 1957, an experimental search for  $\pi^+ \rightarrow e^+ \nu_e$  decay mode at the Enrico Fermi Institute was carried out [17], but  $\pi^+ \rightarrow e^+ \nu_e$  decay was not observed and they set a limit on the branching ratio  $\Gamma_3^\pi$  at  $10^{-6}$ . The  $\pi^+ \rightarrow e^+ \nu_e$  decay mode was first discovered at CERN [18] in 1958. The first precise branching ratio measurement was done by Anderson *et al.* in 1960. They measured

---

<sup>2</sup>The  $\pi^\pm$  has slightly larger mass than  $\pi^0$ , thus charged pion decay to neutral one is allowed, but its branching ratio is small (see Table 1.3).

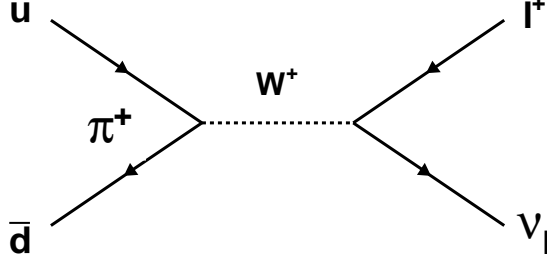


Figure 1.1: The Feynman diagram for the  $\pi^+ \rightarrow l^+ \nu_l$  decay where  $l = e, \mu$ .

the ratio of the branching ratios,  $R_{\text{exp}}^\pi = (1.21 \pm 0.07) \times 10^{-4}$  [19]. Four years later, DiCapua *et al.* improved the uncertainty,  $R_{\text{exp}}^\pi = (1.273 \pm 0.028) \times 10^{-4}$  [20].

A more precise measurement was carried out by Bryman *et al.* using large NaI(Tl) calorimeter at TRIUMF in 1983 [21]. Their result was  $R_{\text{exp}}^\pi = (1.218 \pm 0.014) \times 10^{-4}$ . Few years later, more refined measurements were performed at TRIUMF [22, 23] and PSI [24]. The collaborator at TRIUMF measured  $R^\pi$  using NaI(Tl) crystal while the PSI team used a  $4\pi$  BGO calorimeter surrounding the target. They obtained respectively

$$R_{\text{TRIUMF}}^\pi = [1.2265 \pm 0.0034(\text{stat}) \pm 0.0044(\text{syst})] \times 10^{-4}, \quad (1.1)$$

and

$$R_{\text{PSI}}^\pi = [1.2346 \pm 0.0035(\text{stat}) \pm 0.0036(\text{syst})] \times 10^{-4}. \quad (1.2)$$

Both experiments obtained comparable levels of statistical and systematic uncertainties. The details of this TRIUMF experiment will be discussed in §2.2 because the latest measurement at TRIUMF which I will describe in this thesis in greater details was based on it.

Figure 1.2 shows the summary of experimental results described above. Because the experimental technique was different with each experiment, the central value was statistically independent each other. The PDG average [16] is the average using Bryman's experiment, last TRIUMF and PSI values

$$R_{\text{AVG}}^\pi = (1.230 \pm 0.004) \times 10^{-4}. \quad (1.3)$$

In order to measure  $R^\pi$  with  $<0.1\%$  of precision, the PIENU experiment had been carried out at TRIUMF in Canada by 2012. The expected

## 1.2. THE PION

size of uncertainty is also shown in Figure 1.2. The details of the PIENU experiment will be described in Chapter 2.

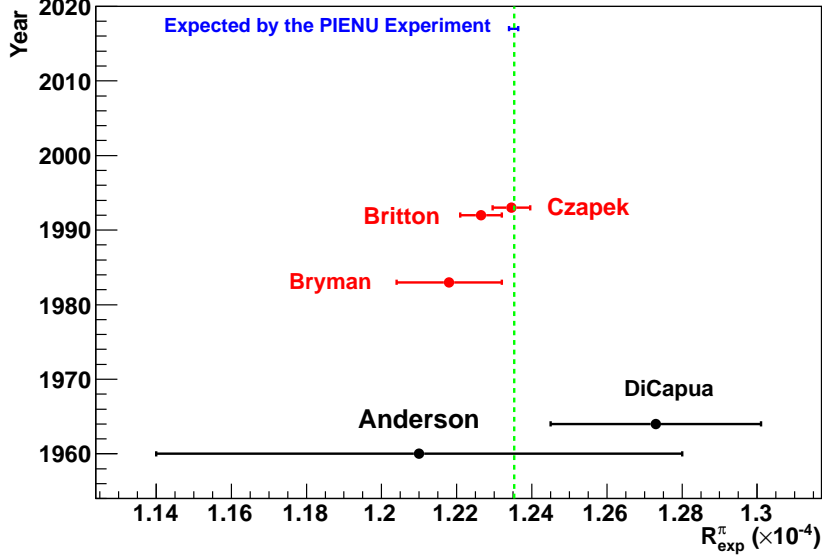


Figure 1.2: History of measured ratio  $R_{\text{exp}}^{\pi}$ . The red points are used for the current PDG average. The dashed green line indicates the theoretical predicted value. The top point shows the expected uncertainty by the PIENU experiment.

### 1.2.4 Theory of $\pi^{+} \rightarrow e^{+} \nu_e$ Decay

The ratio of the charged pion decay branching ratios including the radiative decays is

$$R^{\pi} = \frac{\Gamma[\pi^{+} \rightarrow e^{+} \nu_e(\gamma)]}{\Gamma[\pi^{+} \rightarrow \mu^{+} \nu_{\mu}(\gamma)]}. \quad (1.4)$$

This ratio has been precisely calculated within the framework of the SM. The detail of the theoretical description will be discussed in this section.

### Pion Decay Rate

The differential decay rate for the  $\pi^{+} \rightarrow l^{+} \nu_l$  decay can be given by:

$$d\Gamma = \frac{1}{2m_{\pi}} |\mathcal{M}|^2 \frac{1}{E_l E_{\nu}} \frac{d^3 p_l}{(2\pi)^3} \frac{d^3 p_{\nu}}{(2\pi)^3} (2\pi)^4 \delta(q - p_l - p_{\nu}), \quad (1.5)$$

where  $m_{\pi}$  is the pion mass,  $q$ ,  $p_l$ , and  $p_{\nu}$  are the four-momenta of the pion, lepton, and neutrino, respectively, and  $\mathcal{M}$  is the matrix element in the  $V - A$

## 1.2. THE PION

---

theory,

$$\mathcal{M} = \frac{iG_F}{\sqrt{2}} \langle 0 | V^\mu - A^\mu | \pi \rangle \bar{u}(p_l) \gamma_\mu (1 - \gamma_5) v(p_\nu), \quad (1.6)$$

where  $G_F = 1.16638 \times 10^{-11} \text{ MeV}^{-2}$  is the Fermi coupling constant [16]. The first bracket indicates the quark current between the pion state and the vacuum. It is not simple to calculate in general because the quarks inside the pions are not free particles. However, the pion is a pseudoscalar particle and available four-momentum is only  $q^\mu$ , the Eq. (1.6) can be rewritten as:

$$\mathcal{M} = -\frac{G_F}{\sqrt{2}} f_\pi q^\mu \bar{u}(p_l) \gamma_\mu (1 - \gamma_5) v(p_\nu), \quad (1.7)$$

where  $f_\pi$  is the pion decay constant. The squared matrix element can be given by summing over the final spin states:

$$|\mathcal{M}|^2 = 4G_F^2 f_\pi^2 m_l^2 (p_l p_\nu). \quad (1.8)$$

The expression for the decay rate can be given by integration over lepton momenta:

$$\Gamma = \frac{G_F^2 f_\pi^2 m_\pi m_l^2}{8\pi} \left(1 - \frac{m_l^2}{m_\pi^2}\right)^2. \quad (1.9)$$

The ratio of the branching ratios of the pion decay into positron and muon can be calculated using Eq. (1.9) as

$$R_0^\pi = \frac{\Gamma(\pi \rightarrow e \nu_e)}{\Gamma(\pi \rightarrow \mu \nu_\mu)} = \frac{g_e^2 m_e^2 (m_\pi^2 - m_e^2)^2}{g_\mu^2 m_\mu^2 (m_\pi^2 - m_\mu^2)^2}, \quad (1.10)$$

where  $g_e$  and  $g_\mu$  are respectively the coupling constants between the W boson and the positron or the muon. The relation between  $G_F$  and  $g_l$  ( $l = e, \mu$ ),  $\frac{G_F}{\sqrt{2}} = \frac{g_l^2}{8M_W^2}$  is used, where  $M_W$  is the mass of W boson. If the latest PDG values [16] are used for the masses, and the ratio of the coupling constants  $g_e^2/g_\mu^2$  is assumed to be canceled out ( $g_e^2 = g_\mu^2$ : “electron-muon universality”)

$$R_0^\pi = \frac{\Gamma(\pi \rightarrow e \nu_e)}{\Gamma(\pi \rightarrow \mu \nu_\mu)} = (1.28336 \pm 0.00002) \times 10^{-4}, \quad (1.11)$$

where the error is due to the uncertainties on the masses.

The ratio  $R_0^\pi$  is a small value because of larger muon mass in the term of  $m_e^2/m_\mu^2$  in Eq. (1.10). This result is the physical consequence of the  $(1 - \gamma_5)$  term known as the helicity projection operator for massless particles. This term selects left-handed massless particles and right-handed massless anti-particles. The neutrino must be left-handed, which means the direction of its momentum and spin are opposite. The positron and muon must be

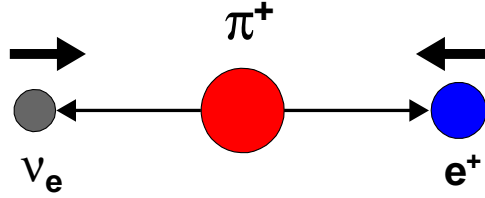


Figure 1.3: Schematic illustration of the helicity suppressed  $\pi^+ \rightarrow e^+ \nu_e$  decay. Thin arrows indicate particle momenta, while thick arrows represent their spins.

left-handed chirality because the pion has spin 0 and angular momentum must be conserved as illustrated in Figure 1.3 while their chirality should be right-handed handed due to  $(1 - \gamma_5)$  projection. Because the positron and muon are not massless particles, the leptonic decay of the pion is allowed, but muon has 200 times larger mass than positron. Therefore, the  $\pi^+ \rightarrow e^+ \nu_e$  decay mode is disfavored (“helicity suppression”).

### Radiative Corrections

The observed ratio of the pion branching ratios involves the effect of physical and virtual photons. The Feynman diagrams of the radiative corrections originating from the emission of real photons (Inner Bremsstrahlung) are shown in Figure 1.4(a), and the virtual emission and re-absorption of photons are shown in Figure 1.4(b). Berman [25] and Kinoshita [26] performed early calculation for the radiative corrections from Inner Bremsstrahlung and virtual photons assuming a point-like pion and electron-muon universality, and obtained

$$\begin{aligned} R^\pi &= R_0^\pi (1 + \delta)(1 + \epsilon) \\ &= 1.233 \times 10^{-4}, \end{aligned} \quad (1.12)$$

where  $\delta = -(3\alpha/\pi)\ln(m_\mu/m_e)$  and  $\epsilon = -0.92(\alpha/\pi)$ .

This result was first checked and confirmed by Goldman and Wilson [27], and Marciano and Sirlin subsequently [28]. They showed that the only uncalculable first-order approximation was a pure structure-dependent Inner Bremsstrahlung term parameterized using vector and axial-vector coupling constants [29]. This resulted in a very small structure-dependence contribution for the ratio of the pion branching ratios. The most recent theoretical estimation of the ratio of the pion branching ratios with radiative correction [30, 31] assuming electron-muon universality gives

$$R_{\text{SM}}^\pi = (1.2352 \pm 0.0002) \times 10^{-4}, \quad (1.13)$$

### 1.3. MOTIVATION OF THE $\pi^+ \rightarrow E^+ \nu_E$ MEASUREMENT

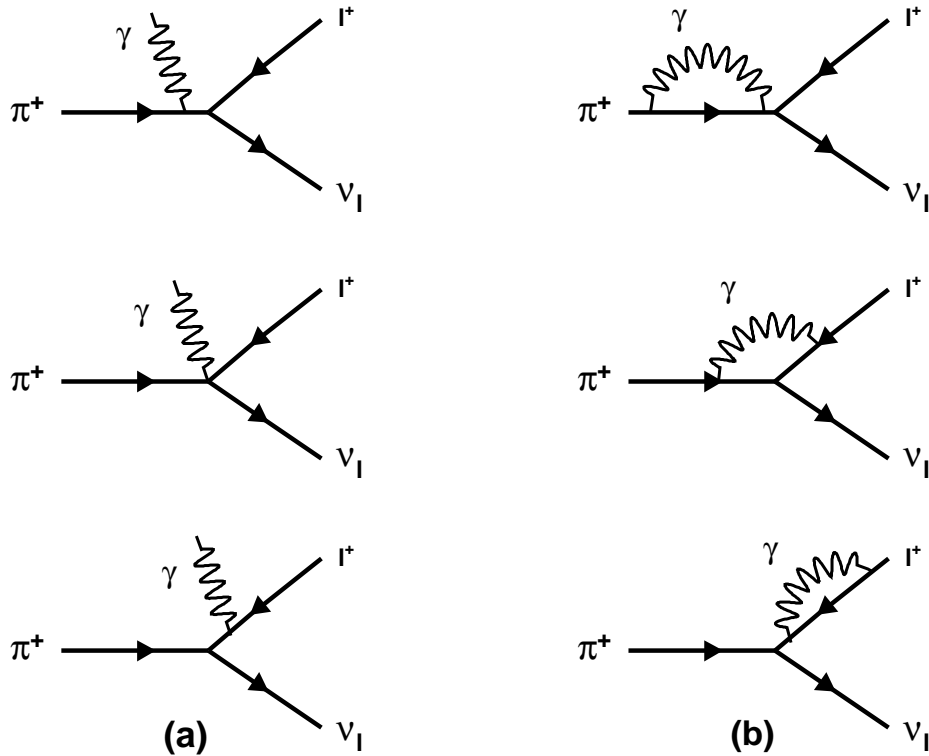


Figure 1.4: Feynman diagrams of radiative  $\pi^+ \rightarrow e^+ \nu_e$  decay process. (a) Inner Bremsstrahlung photons. (b) Virtual emission and re-absorption of photons.

where the uncertainty arises from uncalculated structure-dependent loop effects.

## 1.3 Motivation of the $\pi^+ \rightarrow e^+ \nu_e$ Measurement

Comparing Eq. (1.13) and Eqs. (1.1, 1.2), the previous experimental values were consistent with the SM but had a 20 times larger uncertainty than theory. This section presents several reasons motivating the precise  $R^\pi$  measurement.

### 1.3.1 Lepton Universality

In the SM, the lepton coupling constants,  $g_l$  ( $l = e, \mu, \tau$ ), between the weak boson and the leptons (e.g. in  $\pi^+ \rightarrow l^+ \nu_l$  decay, Figure 1.1) are assumed to be equal. This hypothesis, called “lepton universality”, is generally accepted in the SM. However, new physics could violate the lepton universality. It can

### 1.3. MOTIVATION OF THE $\pi^+ \rightarrow E^+ \nu_E$ MEASUREMENT

---

be revealed through an ‘‘apparent’’ deviation by describing  $R^\pi$  as:

$$R_{\text{exp}}^\pi = \frac{g_e^2}{g_\mu^2} R_{\text{SM}}^\pi. \quad (1.14)$$

The details of new physics will be discussed from the next section.

The universality has been tested in many decay modes so far. Table 1.5 shows the current experimental values for the universality test using  $\pi$ ,  $\tau$ ,  $B$ ,  $K$ , and  $W$ . A recent measurement of  $B^+ \rightarrow K^+ l^+ l^-$  ( $l = e$  or  $\mu$ ) by LHCb group implied a possible violation of electron-muon universality in second-order weak interactions [32]. The uncertainty of  $g_\mu/g_e$  by the pion is the most precise measurement since the pion is the lightest meson and less decay modes than other particles. The deviations of  $W$  decay modes for  $g_\tau/g_\mu$  and  $g_\tau/g_e$  tests are respectively  $3\sigma$  and  $2.6\sigma$ , but the precision level on each test is one-order larger than other decay modes.

Loinaz *et al.* [36] have parameterized the couplings  $g_l$  in order to quantify the current bounds as:

$$g_l \rightarrow g \left(1 - \frac{\varepsilon_l}{2}\right). \quad (1.15)$$

The linear combinations of the  $\varepsilon_l$  constrained by  $W$ ,  $\tau$ ,  $\pi$ , and  $K$  decay measurements are given by:

$$\frac{g_\mu}{g_e} = 1 + \frac{\varepsilon_e - \varepsilon_\mu}{2}, \quad \frac{g_\tau}{g_\mu} = 1 + \frac{\varepsilon_\mu - \varepsilon_\tau}{2}, \quad \text{and} \quad \frac{g_\tau}{g_e} = 1 + \frac{\varepsilon_e - \varepsilon_\tau}{2}. \quad (1.16)$$

Experimental bounds can be evaluated by  $\Delta_{e\mu} \equiv \varepsilon_e - \varepsilon_\mu$ ,  $\Delta_{\mu\tau} \equiv \varepsilon_\mu - \varepsilon_\tau$ , and  $\Delta_{e\tau} \equiv \varepsilon_e - \varepsilon_\tau$ . The choice of two of the three are respectively independent, and W.Loinaz *et al.* selected the latter two parameters. The experimental bounds of each decay mode are shown in Figure 1.5. Improved measurement of  $R^\pi$  will reduce the allowed  $\frac{g_\mu}{g_e}$  region in Figure 1.5 (c) and (d).

#### 1.3.2 New Pseudoscalar Interaction

The precise measurement of  $R^\pi$  would be sensitive to new pseudoscalar interactions. We here consider an effective Lagrangian and matrix element in the presence of pseudoscalar interactions. Equation (1.6) could be replaced with a scalar(S), pseudo-scalar (P), vector (V), or axial-vector (A) in general. However, because the pion is a pseudoscalar, only P or A is available for the replacement. The pseudoscalar current term could be written as [40]:

$$\langle 0 | \bar{u} \gamma_5 d | \pi \rangle = i f_{\pi P} = i \frac{f_\pi m_\pi^2}{m_u + m_d}. \quad (1.17)$$

A pseudoscalar contribution can be expressed as:

$$\mathcal{L}_P = -i \frac{\rho}{\Lambda^2} \left[ \bar{l} \left( \frac{1 - \gamma_5}{2} \right) \nu_l \right] [\bar{u} \gamma_5 d], \quad (1.18)$$

### 1.3. MOTIVATION OF THE $\pi^+ \rightarrow E^+ \nu_E$ MEASUREMENT

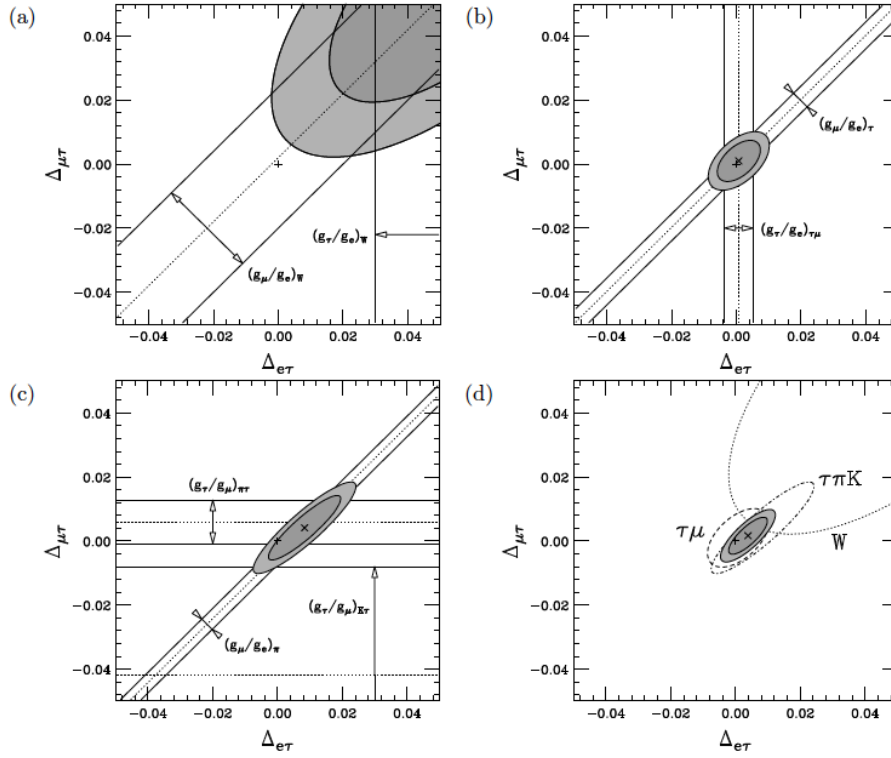


Figure 1.5: Experimental bounds on  $\Delta_{\mu\tau}$  and  $\Delta_{e\tau}$  [36] as of 2008. (a) W decay. (b)  $\tau$  decay. (c)  $\pi$  and K decay. (d) All decays combination. The shaded areas represent the 68% (dark gray) and 90% (light gray) Confidence Levels (C.L.).

### 1.3. MOTIVATION OF THE $\pi^+ \rightarrow E^+ \nu_E$ MEASUREMENT

Table 1.5: Current experimental results of the lepton universality tests. Numbers were taken from [33] except top four decay modes.

Decay mode	$g_\mu/g_e$
$B_{\pi \rightarrow \mu}/B_{\pi \rightarrow e}$	$1.0004 \pm 0.0012$ [4]
$B_{\tau \rightarrow \mu}/B_{\tau \rightarrow e}$	$1.0018 \pm 0.0014$ [34]
$B_{B \rightarrow K \mu \mu}/B_{B \rightarrow K e e}$	$1.159 \pm 0.069$ [32]
$B_{K \rightarrow \mu}/B_{K \rightarrow e}$	$0.996 \pm 0.005$ [35]
$B_{K \rightarrow \pi \mu}/B_{K \rightarrow \pi e}$	$1.002 \pm 0.002$
$B_{W \rightarrow \mu}/B_{W \rightarrow e}$	$0.997 \pm 0.010$
$g_\tau/g_\mu$	
$B_{\tau \rightarrow e \tau \mu}/\tau_\tau$	$1.0006 \pm 0.0022$
$\Gamma_{\tau \rightarrow \pi}/\Gamma_{\pi \rightarrow \mu}$	$0.996 \pm 0.005$
$\Gamma_{\tau \rightarrow K}/\Gamma_{K \rightarrow \mu}$	$0.979 \pm 0.017$
$B_{W \rightarrow \tau}/B_{W \rightarrow \mu}$	$1.039 \pm 0.013$
$g_\tau/g_e$	
$B_{\tau \rightarrow \mu \tau \mu}/\tau_\tau$	$1.0005 \pm 0.0023$
$B_{W \rightarrow \tau}/B_{W \rightarrow e}$	$1.036 \pm 0.014$

where  $\rho$  is the pseudoscalar coupling constant and  $\Lambda$  is the mass scale of pseudoscalar. The matrix element of pseudoscalar can be written using Eq. (1.17) as:

$$\begin{aligned}
 \mathcal{M}_P &= \rho \frac{f_{\pi P}}{\sqrt{2}\Lambda^2} [\bar{l}(1 - \gamma_5)\nu_l] \\
 &= \rho \frac{f_\pi m_\pi^2}{\sqrt{2}\Lambda^2(m_u + m_d)} [\bar{l}(1 - \gamma_5)\nu_l].
 \end{aligned} \tag{1.19}$$

Ignoring small contributions of the presence of pseudoscalar to  $\pi^+ \rightarrow \mu^+ \rightarrow e^+$ , and assuming that coupling constant of pseudoscalar interaction is similar to the coupling constant of weak interaction, we could obtain the deviation between the new physics and the SM prediction as [40]:

$$1 - \frac{R_{\text{exp}}^\pi}{R_{\text{SM}}^\pi} \approx \frac{\sqrt{2}\pi}{G_F} \frac{1}{\Lambda^2} \frac{m_\pi^2}{m_e(m_d + m_\mu)} \approx \left( \frac{1 \text{ TeV}}{\Lambda} \right)^2 \times 10^3. \tag{1.20}$$

In general, the contribution from a new rare process depends on  $1/\Lambda^4$ . However, because of the contributions from  $V - A$  current and the pseudoscalar current can interfere for this case, the deviation depends on  $1/\Lambda^2$ . Therefore, the precise  $R_{\text{exp}}^\pi$  is very sensitive to the mass scale of pseudoscalar interaction. Assuming a precision of 0.1%, it allows potential access up to the pseudoscalar mass scale  $\Lambda$  of 1000 TeV, which is well beyond the reach of colliders. Of course, the actual particle mass could be smaller than  $\Lambda$  and the scale directly depends on the couplings. We will consider several mediators of pseudoscalar interactions [39] in the following sub-sections.

### 1.3. MOTIVATION OF THE $\pi^+ \rightarrow E^+ \nu_E$ MEASUREMENT

---

#### Charged Higgs Boson

Let us consider a charged Higgs boson with coupling  $\frac{g}{2\sqrt{2}}\lambda_{ud}$  to the pseudoscalar current  $\bar{u}\gamma_5 d$  and  $\frac{g}{2\sqrt{2}}\lambda_{l\nu}$  to leptonic current  $\bar{l}(1-\gamma_5)\nu_l$ .  $R^\pi$  for this new physics (NP) scenario can be written as:

$$R_{\text{NP}}^\pi = R_{\text{SM}}^\pi \left[ 1 - \frac{2m_\pi^2}{m_e(m_u + m_d)} \frac{m_W^2}{m_{H^\pm}^2} \lambda_{ud} \left( \lambda_{e\nu} - \frac{m_e}{m_\mu} \lambda_{\mu\nu} \right) \right]. \quad (1.21)$$

A  $\pm 0.1\%$  measurement of  $R^\pi$  probes [30]

$$m_{H^\pm} \approx 200 \text{ TeV} \times \lambda_{ud}^{1/2} \left( \lambda_{e\nu} - \frac{m_e}{m_\mu} \lambda_{\mu\nu} \right)^{1/2}. \quad (1.22)$$

If  $\lambda_{e\nu}/\lambda_{\mu\nu} = m_e/m_\mu$ ,  $R^\pi$  is not sensitive to  $m_{H^\pm}$ . Indeed, this scenario is a simple extended definition of electron-muon universality. However, in more general multi-Higgs models, such a relationship is not required. If we assume couplings at the loop level ( $\lambda_{e\nu} \approx \lambda_{ud} \approx \lambda_{\mu\nu} \approx \alpha/\pi$ ),  $m_{H^\pm} \approx 400$  GeV would be probed by a measurement of the  $R^\pi$  with 0.1% level [30].

#### R-Parity Violation SUSY

R-parity is a concept in particle physics that requires conservation of baryon number and lepton number, which can be written as [41]:

$$P_R = (-1)^{3B+L+2s}, \quad (1.23)$$

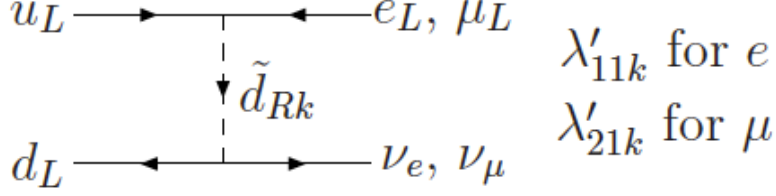
where  $s$  is spin,  $B$  is baryon number, and  $L$  is lepton number. All particles in the SM have R-parity of +1. However, in the Minimal Super-symmetric Standard Model (MSSM), baryon number and lepton number are no longer conserved and super-symmetric (SUSY) particles have R-parity of  $-1$  [41].

In the presence of R-Parity Violation (RPV) interactions, tree level exchanges of sfermions shown in Figure 1.6 lead to violations of lepton universality with violation of lepton number ( $\Delta L = 1$ ) and no helicity suppression in the  $R^\pi$ . The magnitude of these tree level contributions is determined by both the sfermion mass and the parameters  $\lambda'_{11k}$  and  $\lambda'_{21k}$ , which are the coefficients in RPV interactions [42]:

$$\mathcal{L}_{\text{RPV}, \Delta L=1} = \lambda'_{ijk} L_i Q_j \tilde{d}_k^\dagger + \dots \quad (1.24)$$

The coupling constant  $\lambda'_{ijk}$  can be normalized as: [43, 44]

$$\Delta'_{ijk}(f) = \frac{|\lambda'_{ijk}|^2}{4\sqrt{2}G_F m_f^2}, \quad (1.25)$$


 Figure 1.6: Tree level RPV contributions to  $R^\pi$  [42].

where  $G_F$  is the Fermi constant and  $m_{\tilde{f}}$  is the mass of the exchanged sfermion. Contributions to  $R^\pi$  from RPV interactions can be written using Eq. (1.25):

$$\frac{\Delta R_{\text{RPV}}^\pi}{R_{\text{SM}}^\pi} = 2\Delta'_{11k} - 2\Delta'_{21k}. \quad (1.26)$$

The quantities  $\Delta'_{ijk}$  are constrained by precision measurements. The present 95% C.L. constraints on the quantities  $\Delta'_{11k}$  and  $\Delta'_{21k}$  are shown in Figure 1.7. The blue curve shows the constraint by the previous experiments, the green curve indicates the possible implication of the proton weak charge experiment at Jefferson Lab [45]<sup>3</sup>, and the dashed red line shows the constraint with  $\Delta R_{\text{RPV}}^\pi = 0.1\%$ . We can see the current limit on those parameters, especially  $\Delta'_{21k}$ , are not strong and can be substantially improved by a precise  $R^\pi$  measurement.

The presence of RPV interactions would have significant effects on both neutrino physics and cosmology. For example, those interactions would induce a Majorana neutrino mass [47], and allow the lightest super-partner to decay to the SM particles too rapidly to make it a viable dark matter candidate.

### Leptoquark

Leptoquarks are hypothetical particles carrying both baryon and lepton numbers. Leptoquarks mediate transitions between quarks and leptons.  $R^\pi$  could be affected by pseudoscalar leptoquarks. Figure 1.8 shows a Feynman diagram which could contribute to  $\pi^+ \rightarrow e^+ \nu_e$  in these models. The parameter  $y$  in Figure 1.8 is the effective Yukawa couplings [48, 49], which is of order  $m_f/(250 \text{ GeV})$  where  $m_f$  is some average fermion mass ( $\approx 1 \text{ GeV}$ ) [39]. Figure 1.8 leads to a four-fermion interaction of the type:

$$\frac{y^2}{M_p^2} \bar{\nu}_e (1 + \gamma_5) u \bar{d} (1 + \gamma_5) e, \quad (1.27)$$

---

<sup>3</sup>They published an initial result in 2013 [46].

### 1.3. MOTIVATION OF THE $\pi^+ \rightarrow E^+ \nu_E$ MEASUREMENT

---

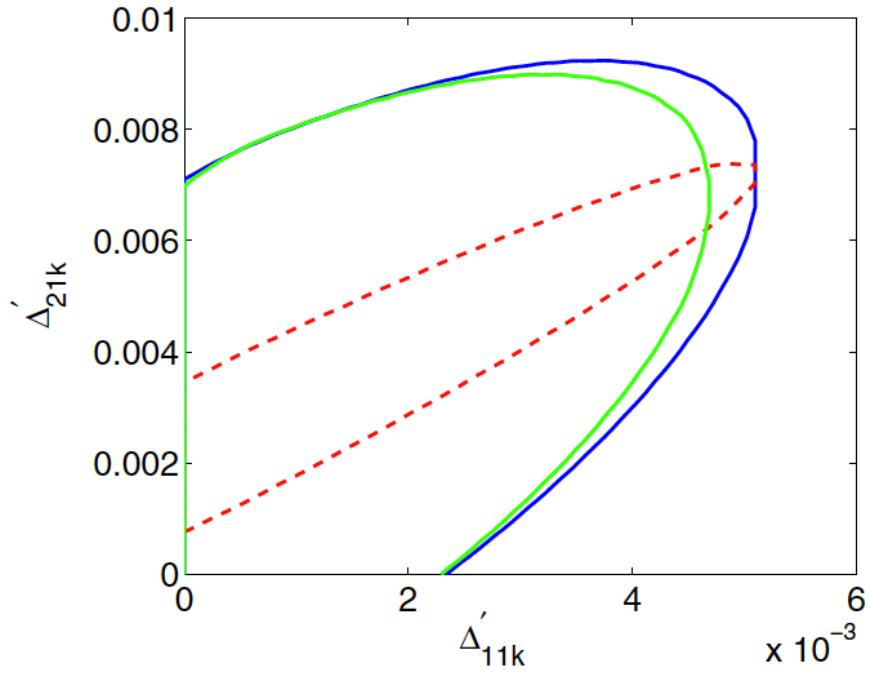


Figure 1.7: Constraints on RPV parameters with 95% C.L. [42]. Blue curve corresponds to the value by the previous experiments, green curve indicates projected limit of proton weak charge experiment, and dashed red curve shows the constraint with precision  $\Delta R_{\text{RPV}}^\pi = 0.1\%$

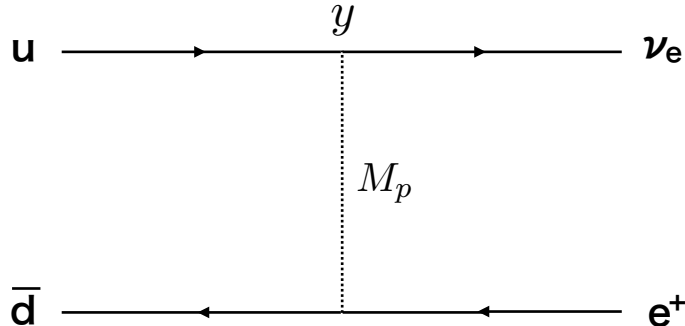


Figure 1.8: The Feynman diagram for the contribution of pseudoscalar leptoquark to  $\pi^+ \rightarrow e^+ \nu_e$ .

where  $M_p$  is the mass of the pseudoscalar leptoquark. Shanker [39] calculated the lower bound of  $M_p > 1$  TeV, which is larger than the expected mass of the leptoquark in the theory [48]. However, the theoretical estimates are affected by some uncertainties due to the absence of a realistic model.

### 1.3.3 Massive Neutrino in the $\pi^+ \rightarrow e^+ \nu_e$ Measurement

In the SM, neutrinos are the only particles that only interact through weak interaction. They are also only massless fermions in the SM. It means that they exist in a single helicity state ( $\nu_L$  and  $\bar{\nu}_R$ ). However, neutrinos were observed to oscillate between different generations [50, 51, 52], which implies the existence of at least two finite neutrino masses.

The  $\pi^+ \rightarrow e^+ \nu_e$  measurement can be sensitive to the existence of massive neutrinos through the  $R^\pi$  measurement. A massive neutrino would affect  $R^\pi$  and an apparent violation of equality of weak interaction couplings could be observed due to a change in the phase space. Consequently, it would cause the relaxation of helicity suppression. A direct additional peak search in the  $\pi^+ \rightarrow e^+ \nu_e$  energy spectrum is also sensitive to the existence of massive neutrino. We now note here that  $\pi^+ \rightarrow e^+ \nu_e$  decay is sensitive to mass range  $0 - 130$  MeV/ $c^2$ .

An analysis of the previous measurement was performed by Britton *et al.* [23, 53], and an initial analysis of the extra bump search in the PIENU experiment has been completed [54]. Those analyses will briefly be discussed in Chapter 8.

## 1.4 Outline of This Thesis

The ratio of the pion branching ratios  $R^\pi$  measurement is a very sensitive test of the SM, so many experiments for precise  $R^\pi$  measurement have been carried out as it was already described (§1.2.3). The previous experimental value is 20 times less precise than the theoretical value. Therefore, a measurement with comparable accuracy to the SM prediction may reveal non-standard physics. Non-standard physics could include new interactions or hypothetical particles. Alternatively if the SM value is confirmed, tighter constraints on new physics can be proved.

Two experiments, the PEN experiment at PSI [55], and the PIENU experiment at TRIUMF, have been working for the last few years on measuring  $R^\pi$  with the final goal of improving the measurement by a factor of five or more, to  $< 0.1\%$ . This thesis will describe the work done over the past 5 years on the detector and analysis for the PIENU experiment and will present the preliminary results obtained with a partial set of the available data. Chapter 2 will explain the PIENU experiment and its measurement method. The experimental detector will be described in Chapter 3, and the analysis will be presented in the following chapters.

## Chapter 2

# The PIENU Experiment

As described in Chapter 1, the ratio of the charged pion decay branching ratios  $R^\pi$  is one of the most precisely calculated values in the SM. Some new physics is predicted at the same level as the accuracy of the theoretical uncertainty. However, the previous experimental result is 20 times worse than the SM prediction. In order to improve the precision level on the measured  $R^\pi$  with  $< 0.1\%$ , the PIENU experiment was carried out. In this chapter, overview and measurement methods of the PIENU experiment are described.

### 2.1 Overview of the PIENU Experiment

The PIENU experiment was carried out at TRIUMF (Canada’s National Laboratory for Nuclear and Particle Physics), which is located in the University of British Columbia in Vancouver, Canada. The goal of the PIENU experiment is to measure  $R^\pi$  with a precision of  $< 0.1\%$ . In order to achieve this accuracy, we collected  $6 \times 10^6$  clean  $\pi^+ \rightarrow e^+ \nu_e$  events corresponding to more than 30 times higher statistics than the previous TRIUMF experiment [22, 23].

The decays  $\pi^+ \rightarrow e^+ \nu_e$ , and  $\pi^+ \rightarrow \mu^+ \nu_\mu$  followed by  $\mu^+ \rightarrow e^+ \nu_e \bar{\nu}_\mu$  (which will be referred as  $\pi^+ \rightarrow \mu^+ \rightarrow e^+$  in this thesis) decays have different energy characteristics that can be precisely measured and used to extract  $R^\pi$ . Figure 2.1 shows a schematic of pion decays and the measurement method. Positive pions stop in a plastic scintillator target and decay to muons or positrons. The muon in  $\pi^+ \rightarrow \mu^+ \rightarrow e^+$  has kinetic energy  $T_\mu = 4.1$  MeV (Figure 2.2) and range in plastic scintillators of about 1mm; the total energy of decay positrons have a continuous distribution from 0.5 to 52.8 MeV (this distribution is generally called “Michel” spectrum). The decay  $\pi^+ \rightarrow e^+ \nu_e$  produces a mono-energetic positron at 69.8 MeV. In the PIENU experiment,  $R^\pi$  is obtained from the ratio of the positron yields from  $\pi^+ \rightarrow e^+ \nu_e$  decays and  $\pi^+ \rightarrow \mu^+ \rightarrow e^+$  decays by taking advantage of these differences.

## 2.1. OVERVIEW OF THE PIENU EXPERIMENT

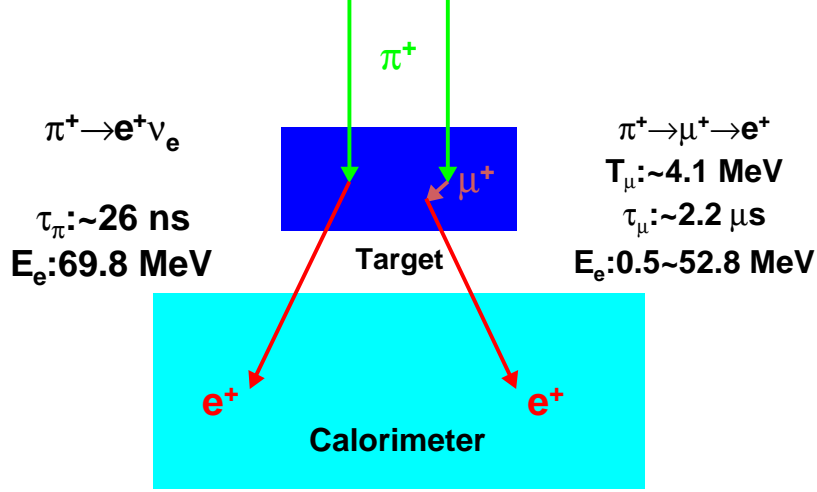


Figure 2.1: Schematic of the PIENU experimental technique [56].

Figure 2.3(a) shows energy spectra of decay positrons in the calorimeter produced by Monte Carlo (MC) simulation<sup>1</sup>. Two energy regions, above and below the dashed black line in Figure 2.3(a) are used to distinguish two pion decay modes. Figure 2.3(b) shows the time spectra in the high- and low-energy regions. Assuming the ideal condition where no background contamination exists at all, the time spectra for high- and low-energy regions are distributed as

$$\pi^+ \rightarrow e^+ \nu_e : \varepsilon_{\pi \rightarrow e \nu}(t) = \frac{\exp(-\frac{t}{\tau_\pi})}{\tau_\pi}, \quad (2.1)$$

$$\pi^+ \rightarrow \mu^+ \rightarrow e^+ : \varepsilon_{\pi \rightarrow \mu \rightarrow e}(t) = \frac{\exp(-\frac{t}{\tau_\mu}) - \exp(-\frac{t}{\tau_\pi})}{\tau_\mu - \tau_\pi}, \quad (2.2)$$

where  $\tau_\pi$ ,  $\tau_\mu$  are the lifetimes of pion (26.033 ns) and muon (2196.981 ns), respectively. The time spectra in the two energy regions are fitted to Eqs. (2.1) and (2.2) simultaneously in order to extract “raw” ratio  $R_{\text{raw}}^\pi$ , to which corrections are applied.

The most important corrections dominating the systematic uncertainties include the  $\pi^+ \rightarrow e^+ \nu_e$  low-energy distribution due to the shower leakage from the calorimeter. Additionally, the difference of positron acceptance between  $\pi^+ \rightarrow e^+ \nu_e$  and  $\pi^+ \rightarrow \mu^+ \rightarrow e^+$  events also requires a significant correction. They will be discussed in Chapters 4, 5, and 6.

<sup>1</sup>Unless otherwise specified, Geant4 package [57] was used for MC study.

## 2.1. OVERVIEW OF THE PIENU EXPERIMENT

---

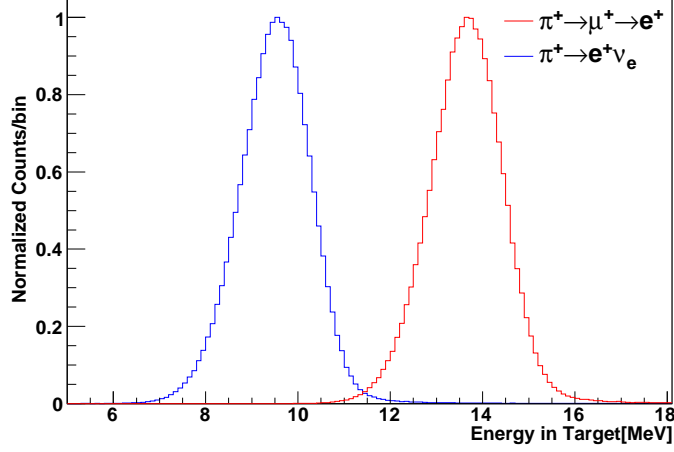


Figure 2.2: Simulated energy deposit in the target. Two  $\pi^+ \rightarrow e^+ \nu_e$  (blue) and  $\pi^+ \rightarrow \mu^+ \rightarrow e^+$  (red) peaks are seen due to the extra muon energy.

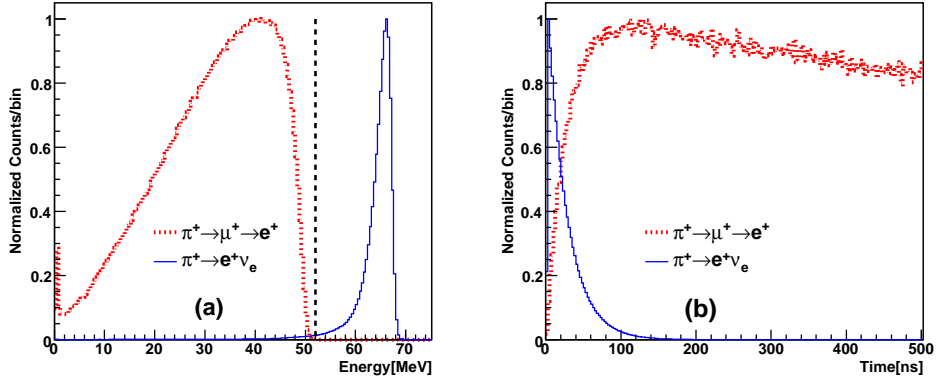


Figure 2.3: (a): Simulated energy spectra of decay positrons in the calorimeter [56]. (b): Simulated decay positron time spectra [56]. In both plots, the peak heights are normalized to 1.

## 2.2. PREVIOUS EXPERIMENT AT TRIUMF

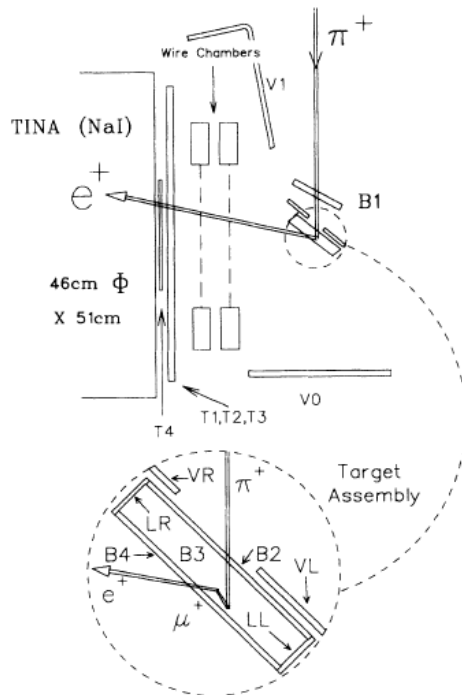


Figure 2.4: Experimental setup of the previous experiment at TRIUMF [23].

## 2.2 Previous Experiment at TRIUMF

In late 1980's, the previous experiment was performed to measure the  $R^\pi$  precisely at TRIUMF [22, 23]. The design of the PIENU experiment was influenced by this experiment. Therefore, its outline and lessons from this experiment are discussed here. Figure 2.4 shows the schematic of experimental setup. The detectors consisted of a target scintillator and a NaI calorimeter with some additional scintillators and wire chambers. Beam pions were stopped in the target scintillator B3. The axis of the main detector, cylindrical NaI(Tl) crystal called “TINA”, was oriented  $90^\circ$  to the beam axis in order to avoid direct hitting of the beam particles. The solid angle of decay positron was only 2% of  $4\pi$  steradians.

The experiment took data for a month and collected about  $1.5 \times 10^5$   $\pi^+ \rightarrow e^+ \nu_e$  events. The result of  $R_{\text{exp}}^\pi$  with statistical and systematic uncertainties are summarized in Table 2.1. The dominant systematic uncertainties came from  $R_{\text{raw}}^\pi$  analysis and “tail correction” are discussed in the following sections.

## 2.2. PREVIOUS EXPERIMENT AT TRIUMF

Table 2.1: Summary of uncertainties in the previous experiment [23].

$R_{\text{raw}}^{\pi}$ ( $\times 10^{-4}$ )	$1.1994 \pm 0.0034(\text{stat}) \pm 0.0023(\text{syst})$
<b>Multiplicative corrections</b>	
Tail corrections	$1.0193 \pm 0.0025$
Acceptance corrections	$1.0027 \pm 0.0011$
Pion stop time $t_0$	$0.9998 \pm 0.0008$
Pion lifetime	$1.0000 \pm 0.0008$
Others	$1.0007 \pm 0.0007$
$R_{\text{exp}}^{\pi}$ ( $\times 10^{-4}$ )	$1.2265 \pm 0.0034(\text{stat}) \pm 0.0044(\text{syst})$

### 2.2.1 Raw Ratio Extraction

$R_{\text{raw}}^{\pi}$  was basically extracted by the same method as already explained in §2.1; simultaneous fitting of the measured positron time spectra. The measured decay positron energy spectrum is shown in Figure 2.5, and time spectra for the high-energy ( $\pi^+ \rightarrow e^+ \nu_e$ ) and the low-energy ( $\pi^+ \rightarrow \mu^+ \rightarrow e^+$ ) regions are shown in Figure 2.6. The energy threshold was set at 56.4 MeV (3400 channel in Figure 2.5). The actual fitting function for the time spectrum in the high-energy region  $F_{\pi e \nu}$  should include the backgrounds and can be written by using Eqs. (2.1) and (2.2) as

$$F_{\pi e \nu} = A[R_{\text{raw}}^{\pi} \varepsilon_{\pi \rightarrow e \nu}(t) + r \varepsilon_{\pi \rightarrow \mu \rightarrow e}(t)]\theta(t) + A_{\text{BG1}} \varepsilon_{\mu \rightarrow e \nu \bar{\nu}}(t) + C_{\text{BG1}}, \quad (2.3)$$

where  $t = t' - t_0$  for positron decay time  $t'$  and pion stop time  $t_0$ ,  $\theta(t) = 0$  for  $t < 0$  and  $\theta(t) = 1$  for  $t > 0$ , and  $\varepsilon_{\mu \rightarrow e \nu \bar{\nu}}(t)$  is muon background

$$\varepsilon_{\mu \rightarrow e \nu \bar{\nu}}(t) = \frac{\exp(-\frac{t}{\tau_{\mu}})}{\tau_{\mu}}. \quad (2.4)$$

This muon background will be called ‘‘old-muon’’ hereafter. The parameters  $A$ ,  $R_{\text{raw}}^{\pi}$ ,  $r$ ,  $A_{\text{BG1}}$  and  $C_{\text{BG1}}$  are, respectively, the number of  $\pi^+ \rightarrow \mu^+ \rightarrow e^+$  events, the ratio of the branching ratios before corrections, the fraction of the  $\pi^+ \rightarrow \mu^+ \rightarrow e^+$  events above the energy threshold (due to pileup or energy resolution of ‘‘TINA’’), the number of old-muon events, and constant background. The equation for the time spectrum in the low-energy region  $F_{\pi \mu e}$  is

$$F_{\pi \mu e} = A[(1 - r)\varepsilon_{\pi \rightarrow \mu \rightarrow e}(t)]\theta(t) + A_{\text{BG2}} \varepsilon_{\mu \rightarrow e \nu \bar{\nu}}(t) + C_{\text{BG2}}, \quad (2.5)$$

where  $A_{\text{BG2}}$  and  $C_{\text{BG2}}$  are the numbers of backgrounds from the old-muon and constant backgrounds, respectively. The fitting parameters  $A$ ,  $R_{\text{raw}}^{\pi}$ ,  $r$ ,  $t_0$ , and all background amplitudes were used as free parameters in the fit.

The simultaneous fit gave the ratio of the branching ratios before corrections  $R_{\text{raw}}^{\pi}$ :

$$R_{\text{raw}}^{\pi} = [1.1994 \pm 0.0034(\text{stat}) \pm 0.0023(\text{syst})] \times 10^{-4} \quad (2.6)$$

## 2.2. PREVIOUS EXPERIMENT AT TRIUMF

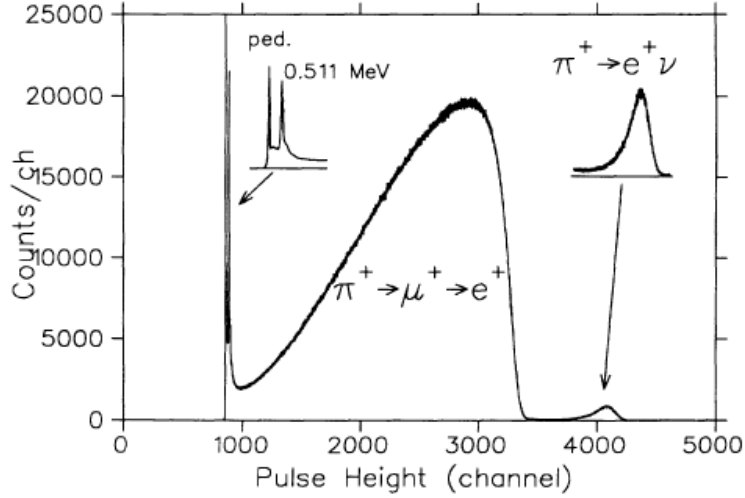


Figure 2.5: Energy spectrum of decay positron measured by the NaI calorimeter [23]. Horizontal axis is pulse height of decay positron.

with a  $\chi^2$  per degrees of freedom ( $\chi^2/n_d$ ) being 1.47. The systematic error of the fitting analysis was evaluated from the statistical error inflated with  $\sqrt{\chi^2/n_d} = \sqrt{1.47}$  as it is widely used by Particle Data Group [16]. We can see that a bad fitting accuracy and large statistical error were dominant sources on the  $R_{\text{raw}}^\pi$  analysis.

### 2.2.2 Tail Correction

The largest source of systematic uncertainty in the previous experiment arose from low-energy  $\pi^+ \rightarrow e^+ \nu_e$  tail events underneath the  $\pi^+ \rightarrow \mu^+ \rightarrow e^+$  distribution. In order to suppress the  $\pi^+ \rightarrow \mu^+ \rightarrow e^+$  events and estimate the amount of this tail, they used two kinds of ADC gates for the target counter, narrow-gate and wide-gate. The former was sensitive to the stopping pion mainly, while the latter covered decay muon's energy deposit in B3. The two-dimensional distribution of wide-gate versus narrow-gate is shown in Figure 2.7. The energy spectrum with the target's ADC gates cut is shown in Figure 2.8. One can clearly see a residual component below 3400 channel. These were mostly from pions decayed in flight ( $\pi$ DIF) before the target and deposited a smaller amount of energy in the target than the pions decayed at rest ( $\pi$ DAR). Thus, the sum of the energy deposited in the target mimics  $\pi^+ \rightarrow e^+ \nu_e$  events, and the cuts shown in Figure 2.7 did not work. The fraction of  $\pi^+ \rightarrow \mu^+ \rightarrow e^+$  suppressed spectrum below the energy threshold was about 20%. Additionally, this estimation was also limited by statistics.

## 2.2. PREVIOUS EXPERIMENT AT TRIUMF

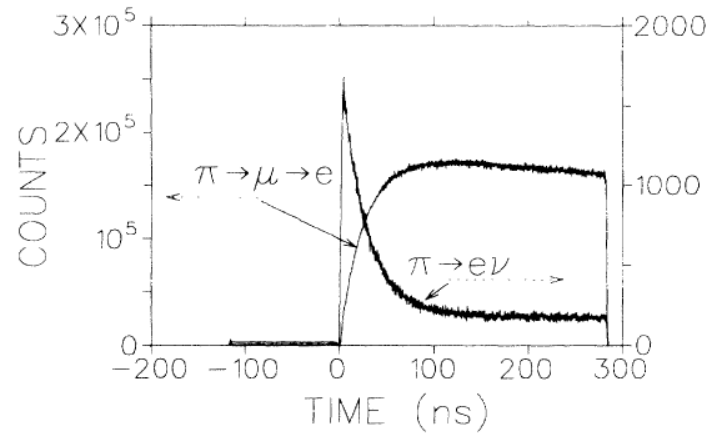


Figure 2.6: Time spectra of decay positrons [22]. The energy threshold in Figure 2.5 was at 3400 channel.

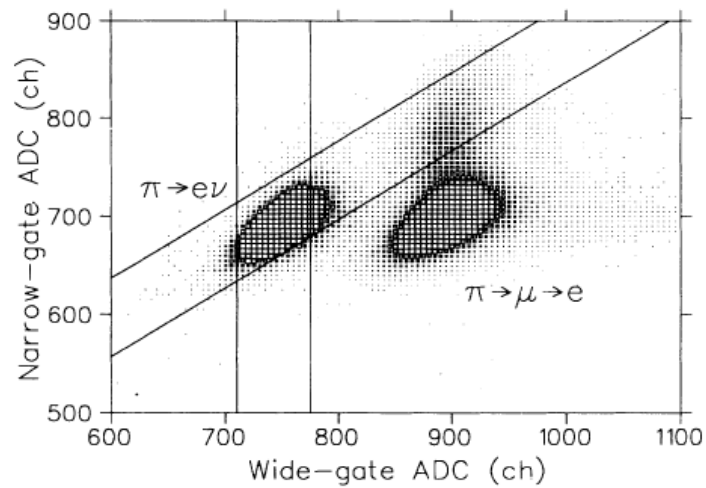


Figure 2.7: Total energy deposit in the target with wide-gate and early part of the pion pulse with narrow-gate [23]. The region surrounded by two vertical lines and two slanting lines indicates selected  $\pi^+ \rightarrow e^+ \nu_e$  events.

## 2.3. IMPROVEMENT IN THE PIENU EXPERIMENT

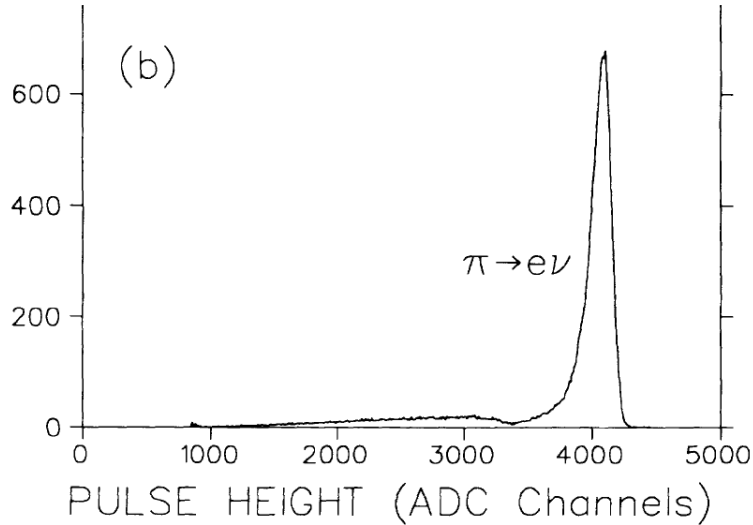


Figure 2.8:  $\pi^+ \rightarrow \mu^+ \rightarrow e^+$  suppressed energy spectrum measured by the NaI calorimeter [23]. Most of low-energy background was due to  $\pi$ DIF events.

### 2.3 Improvement in the PIENU Experiment

In order to measure  $R^\pi$  with  $< 0.1\%$  of precision, the experimental setup was improved with taking into account “weak points” described above. First of all, the most important improvement was to put the NaI crystal in the beam axis. This allowed a close geometry between the target and the NaI for a larger solid angle. Additionally, a smaller error on the acceptance correction could be expected because the acceptance correction depends on the size of solid angle. The beam positron contamination was largely reduced by upgrading the beam line [58].

Second, sets of tracking detectors had been added upstream of target in order to detect  $\pi$ DIF events. Third, a high energy resolution NaI(Tl) calorimeter with CsI rings was used to reduce the  $\pi^+ \rightarrow e^+ \nu_e$  low-energy tail. Fourth, fast digitizing electronics were introduced for accurate waveform analysis and decay mode identification. Finally, much longer data taking run was carried out to increase event statistics. The details of the improved PIENU detector will be described in Chapter 3.

### 2.4 History of the PIENU Experiment

A brief history of the PIENU experiment is summarized in Table 2.2. The data taking was completed in 2012, and we are currently in the analysis period. The initial result of the measured ratio  $R_{\text{exp}}^\pi$  for the Run-IV was published in August, 2015 [4]. This thesis focuses on the data analysis for the Run-IV and Run-V.

## 2.4. HISTORY OF THE PIENU EXPERIMENT

---

Table 2.2: History of the PIENU experiment. The numbers in parentheses indicate the numbers of  $\pi^+ \rightarrow e^+ \nu_e$  events before off-line event selection.

Year	Month	Events
2005	Dec.	Proposal was approved by TRIUMF
2006		Detector design and test
2007		Detector construction and beam tests in M9
2008	May	Beam test in M13
2008	Oct.	2008 Oct. M13 beam channel extension completed
2008	Oct.-Nov.	Test in M13 with most of the detectors
2009	May	PIENU detector completed
2009	May-Sep.	Run-I (1M)
2009	Oct.-Dec.	Run-II (0.5M)
2010	March	Temperature controlled enclosure completed
2010	Apr.-Sep.	Run-III (4M)
2010	Oct.-Dec.	Run-IV (2M)
2011	Aug.-Oct.	Special runs for systematic studies
2011	Sep.	First publication of massive neutrino search [54]
2011	Nov.-Dec.	Run-V (3.5M)
2012	Jul.-Dec.	Run-VI (12M)
2012	Dec.	Special runs for systematic studies
2013-2015		Analysis period
2015	Aug	First publication of the $R_{\text{exp}}^\pi$ [4]

## Chapter 3

# Description of the PIENU Experiment

### 3.1 The M13 Beam Line

The PIENU experiment was located at the TRIUMF M13 beam line [58]. The M13 beam line is illustrated in Figure 3.1. The TRIUMF cyclotron provided a 500 MeV proton beam with an intensity of about  $120 \mu\text{A}$  to a 12 mm thick beryllium pion production target (*BL1A-T1*)<sup>1</sup> every 43 ns with a 4 ns wide pulse. The secondary beam line took off from the primary proton beam line (*BL1A*) at an angle of  $135^\circ$  from the production target. The beam line consisted of three dipole magnets (*B1* ( $+60^\circ$ ), *B2* ( $-60^\circ$ ), *B3* ( $-70^\circ$ )), ten quadrupole magnets (*Q1* – *Q10*), and four foci (*F1* – *F4*). In order to increase the acceptance of decay positrons from pion decay events, the detector was located on the beam axis right downstream of the pion stopping target. The number of beam positrons came from production target had to be reduced to suppress the detector hit rate. To accomplish this, the M13 beam line was upgraded and extended from the downstream part of *F3* [58]. The PIENU detector was located at the end of *F4*.

A 1.45 mm thick Lucite absorber was placed near *F1*. The energy loss of pions and positrons in the absorber were different; thus a clear particle separation was performed at *F3* as shown in Figure 3.2. A 5 cm thick lead collimator was installed into *F3* at the position hit by positrons to suppress them.

After the collimator, the pions were bent by *B3* and refocused by *Q8* – *Q10* (Figure 3.3), and led into the PIENU detector. The total length of the extended parts between *F3* and *F4* was 4.5 m.

In the normal pion data taking, the beam momentum into detector area was  $P = 75 \pm 1 \text{ MeV}/c$ , the beam rate was 70 kHz, and the beam was

---

<sup>1</sup>In order to avoid confusion with the names for the detectors, italics are used for the beam line components.

### 3.2. THE PIENU DETECTOR

---

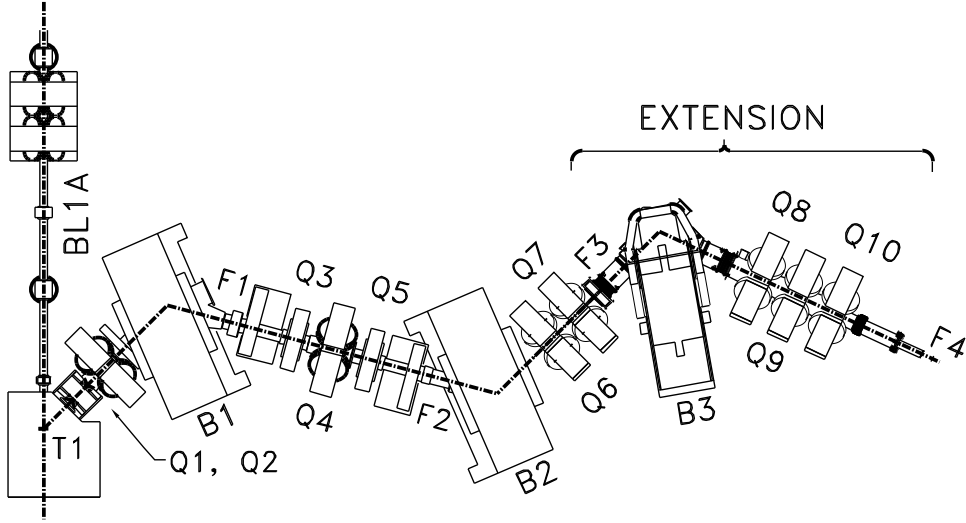


Figure 3.1: The illustration of M13 beam channel [58]. Downstream parts of  $F3$  were extended line for the requirement of the PIENU experiment.

composed of 84% pions, 14% muons, and 2% positrons.

## 3.2 The PIENU Detector

### 3.2.1 Overview

As explained in Chapter 2, the PIENU detector was based on an active pion stopping target and calorimeters to measure the decay positron. Figure 3.4 is the schematic of the whole PIENU detector. This detector was placed immediately downstream of the exit of the M13 beam line. The beam with a momentum of  $75 \text{ MeV}/c$  traversed the vacuum window of the beam duct, and passed through two multi-wire proportional chambers (WC1 and WC2), which provided the beam profile. After WC2, the beam momentum was degraded by two thin plastic scintillators B1 and B2 (beam counters), which were used for time and energy loss measurements in order to identify the beam pions. The beam counters were followed by two sets of Si strip trackers (S1 and S2) with strips oriented along the X and Y axes (Z axis indicates the beam axis, see Figure 3.4). The pions stopped and decayed at rest in the center of a plastic scintillator target (B3) which was placed downstream of S2.

In order to reconstruct the decay-positron tracks and define their acceptance, another pair of X-Y Si strip detector (S3) and three layers of circular multi-wire proportional chamber (WC3) were also employed. Two thin plastic scintillators (telescope counters T1 and T2) were used to measure the

### 3.2. THE PIENU DETECTOR

---

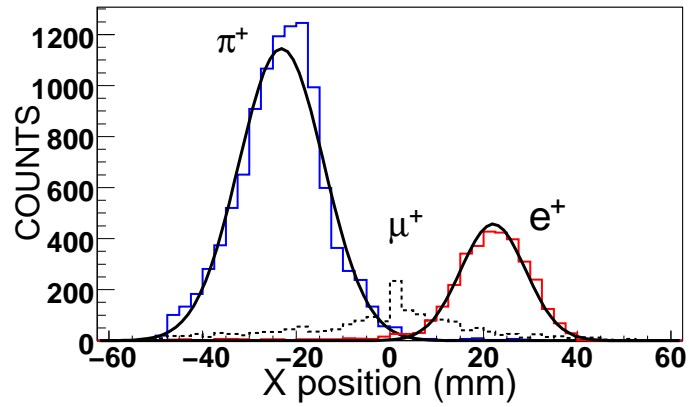


Figure 3.2: Pion, muon, and positron distributions at  $F3$  (histograms) [58]. Horizontal axis is position for X-axis, and vertical axis is amplitude. The heavy black lines indicate fitted Gaussian function for pions and positrons.

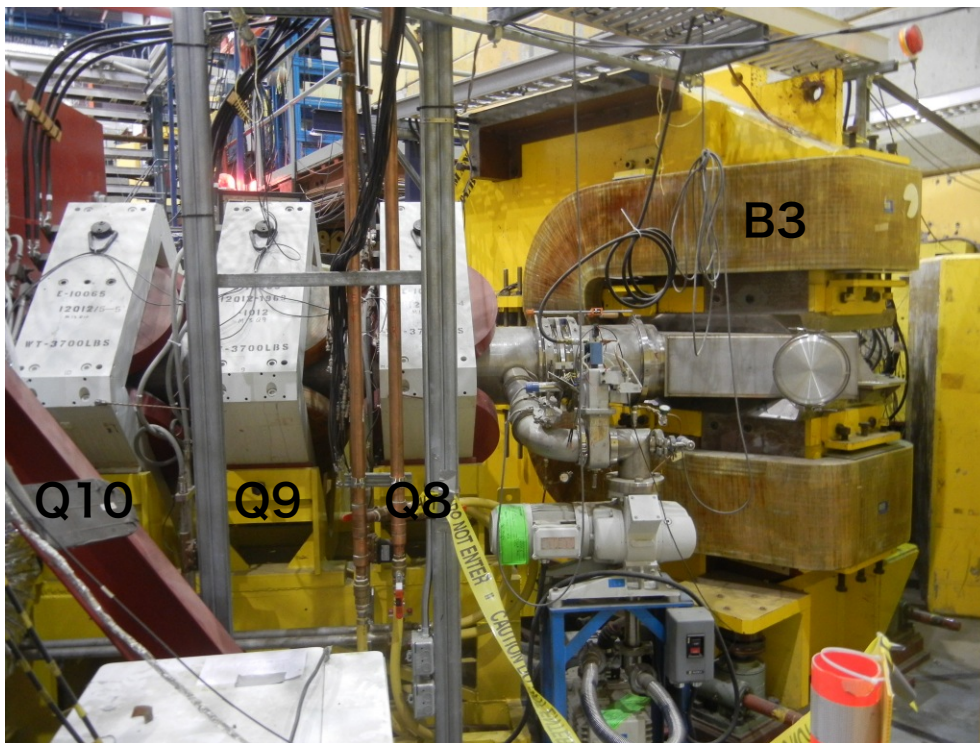


Figure 3.3: Picture of the extended area.

## 3.2. THE PIENU DETECTOR

---

decay time of positron and make an on-line trigger. Decay positrons entered a large single crystal NaI(Tl) calorimeter. Two layers of pure CsI pentagonal crystals (97 in total) surrounded the NaI(Tl) crystal for shower leakage detection. Three veto scintillators (V1, V2, and V3) were installed to cover inactive material. V1 covered the front frame of WC1, V2 covered the frame of WC3, and V3 covered the front flange of the NaI(Tl) crystal. The solid angle acceptance was 20%, which was about 10 times larger than in the previous TRIUMF experiment [22, 23]. Table 3.1 shows the detector parameters.

The PIENU detector was composed of two modules called PIENU-I and PIENU-II. PIENU-I consisted of the beam assembly (V1, WC1, WC2, B1, B2, S1, and S2), B3, S3, and T1 (Figure 3.5), and PIENU-II was formed from WC3, T2, V2, V3, NaI, and CsI crystals (Figure 3.6).

PIENU-I was attached to the end of the beam pipe and could be divided into three sub-assemblies (V1+WC1+WC2, B1+B2+S1+S2, and B3+S3+T1). PIENU-II was enclosed in a steel cylinder, and on a cart to move independently from PIENU-I. PIENU-II was moved as close as possible to PIENU-I by a cart during normal runs.

The PIENU detector was enclosed by a temperature-controlled enclosure shown in Figure 3.7 to reduce the effect from variation of temperature. The temperature was maintained at  $20 \pm 0.5$  °C during the data taking.

See Ref. [1] for more details of the PIENU detector.

### 3.2.2 Plastic Scintillators

The plastic scintillators were made of Bicron BC-408 (polyvinyltoluene) scintillator. B1<sup>2</sup> fully covered the aperture of WC1 and WC2. B2 was smaller than the target B3 in order to ensure that particles came into the center of B3. T1 defined positron timing. B3 and T1 were rotated with respect to B1 and B2 by an angle of 45° around the beam axis. T2 was the largest plastic scintillator to define on-line acceptance, which was placed directly in the front of the NaI(Tl) detector. Due to the limited space and circular shape, T2 and veto (V1–3) counters were read out by 1 mm diameter wavelength-shifting (WLS) fibers (Kuraray Y-11). Each scintillator except veto counters was read out by four PMTs. The schematic of this configuration is shown in Figure 3.8, and T2 and its WLS fibers are illustrated in Figure 3.9.

### 3.2.3 Wire Chambers

Each wire chamber (WC1–3) consisted of three wire planes rotated by an angle of 120° with respect to each other. All the chambers were filled

---

<sup>2</sup>To change the stopping position of the beam pion, additional Mylar foils (457  $\mu$ s of thickness) were attached to the face of B1 only during 2011.

### 3.2. THE PIENU DETECTOR

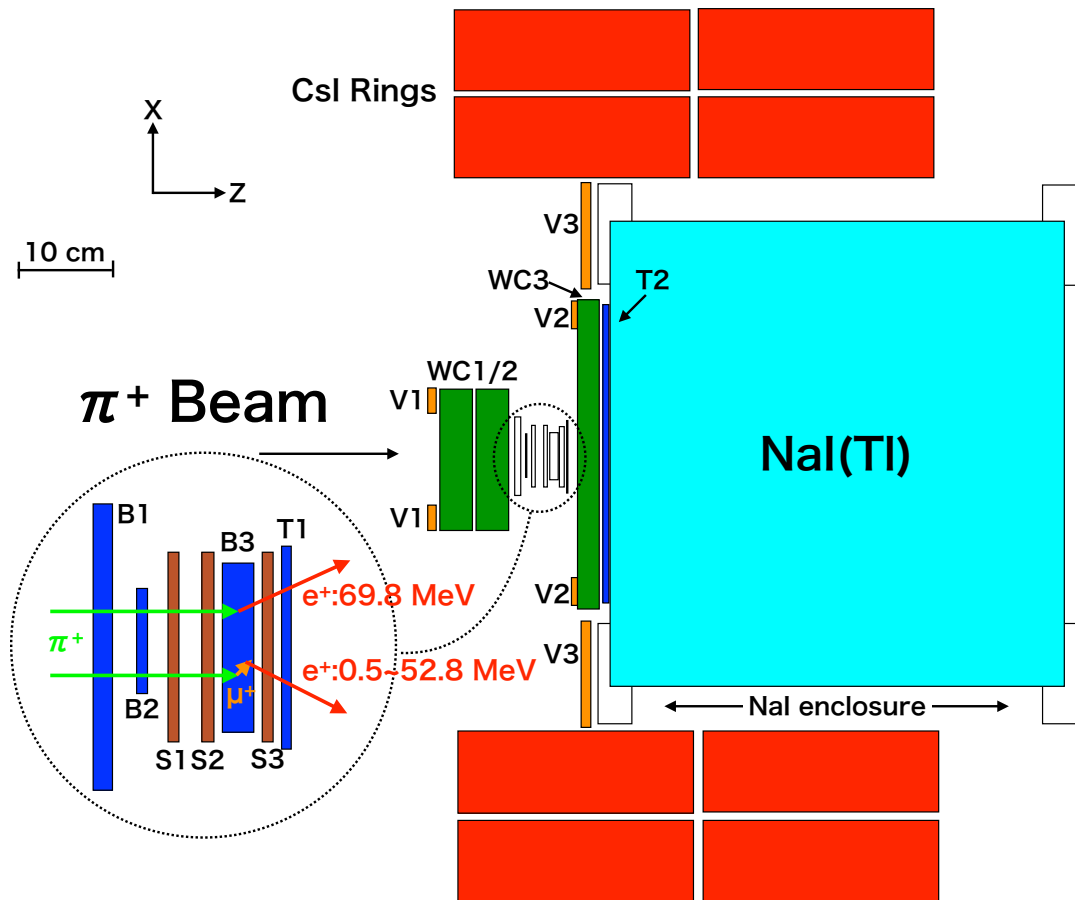


Figure 3.4: Schematic of the whole PIENU detector [1]. For the visualization, the thickness of each silicon strip detector in the zoom-in region is illustrated with larger size than an actual size.

### 3.2. THE PIENU DETECTOR

---

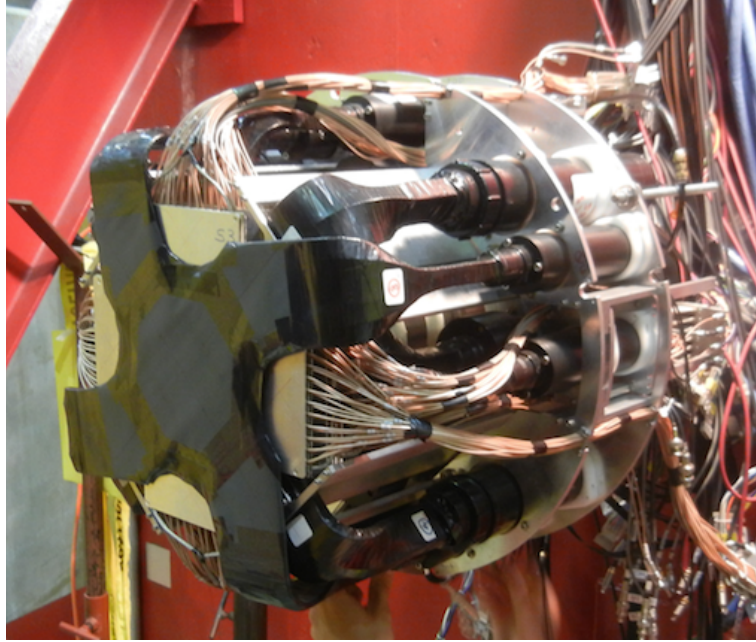


Figure 3.5: Picture of PIENU-I.

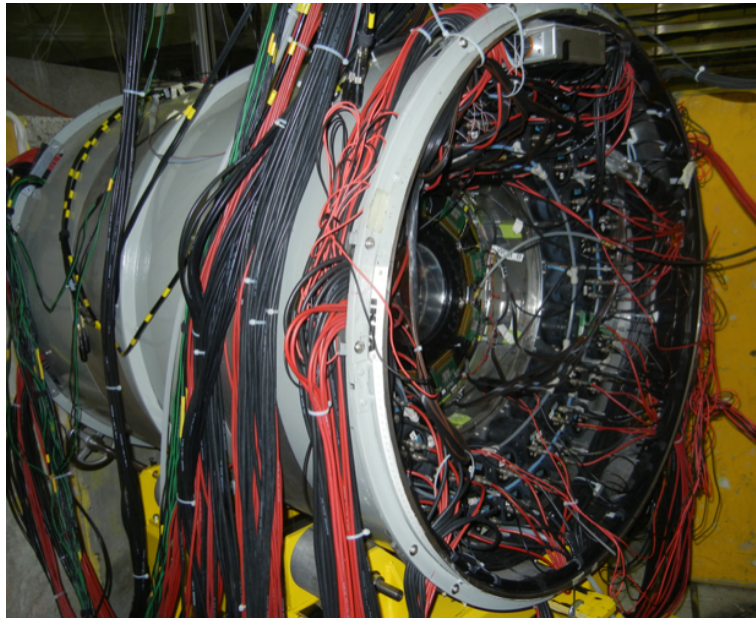


Figure 3.6: Picture of PIENU-II.

### 3.2. THE PIENU DETECTOR

---

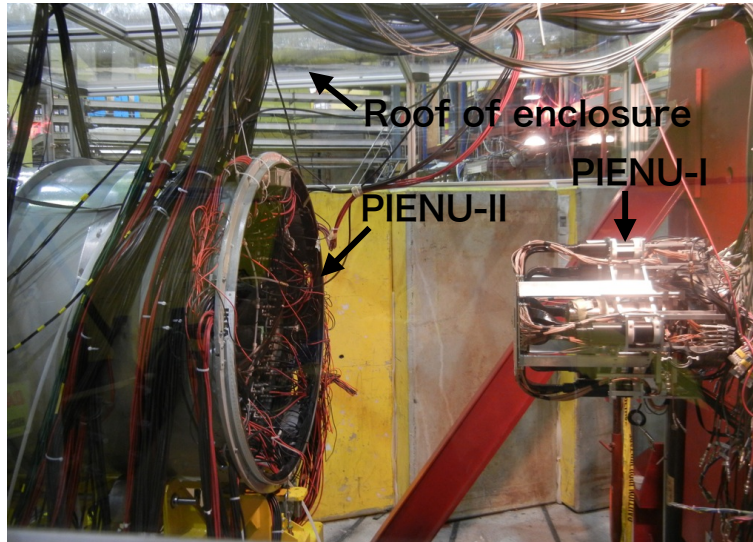


Figure 3.7: The whole PIENU detector located in detector enclosure. PIENU-II was on a cart, and moved to PIENU-I during normal runs.

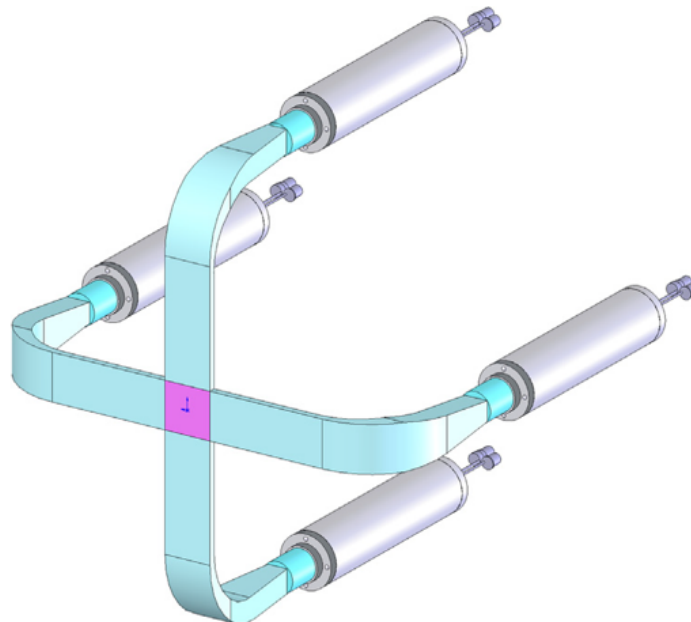


Figure 3.8: Schematic view of the B1,B2,B3, and T1 scintillator readout [1].

### 3.2. THE PIENU DETECTOR

Table 3.1: Parameters for the PIENU detector [1].

<b>Plastic Scintillator counters</b>					
Trigger Counters	B1	B2	B3	T1	T2
Size in X (Inner radius)	100 mm	45 mm	70 mm	80 mm	(0) mm
Size in Y (Outer radius)	100 mm	45 mm	70 mm	80 mm	(171.45) mm
Size in Z	6.604 mm	3.07 mm	8.05 mm	3.04 mm	6.6 mm
Z position	-39.03 mm	-30.02 mm	0 mm	19.92 mm	72.18 mm
Photomultiplier model/ manufacturer	H3178-51 Hamamatsu	83112-511 Burle	XP2262B Photonis	83112-511 Burle	H3165-10 Hamamatsu
Photocathode diameter	34 mm	22 mm	mm 44 mm	22 mm	10 mm
Veto Counters			V1	V2	V3
Inner radius			40 mm	107.95 mm	177.8 mm
Outer radius			52 mm	150.65 mm	241.3 mm
Size in Z			3.175 mm	6.35 mm	6.35 mm
Photomultiplier model/ Photomultiplier manufacturer			H3164-10 Hamamatsu	H3165-10 Hamamatsu	
Photomultiplier Photocathode diameter			8 mm	10 mm	
<b>Tracking Detectors</b>					
Multi Wire Proportional Chambers			WC1	WC2	WC3
Wire spacing			0.8 mm		2.4 mm
Number of Planes/wires/readout channels			3/120/40		3/96/48
Active area diameter			96.0 mm		230.4 mm
Cathode plane to Anode wire spacing			1.6 mm		2.0 mm
Anode wire diameter			15 $\mu$ m		
Wire orientation			0°, +120°, -120°		
Silicon Strip Detector Pair (X and Y oriented strips)					S1/S2/S3
Active area					61 $\times$ 61 mm <sup>2</sup>
Silicon strip pitch					80 $\mu$ m
Effective pitch after binding 4 strips					320 $\mu$ m
Number of planes/readout channels per plane					2/48
Thickness (size in Z)					0.285 mm
Separation between X and Y strip detectors					12 mm
<b>Electromagnetic Calorimeter</b>					
Crystal			NaI(T $\ell$ )	CsI	
Number used			1	97	
Energy Resolution (FWHM) at 70 MeV			2.2%	~10%	
Thickness (size in Z)			480 mm	250 mm	
Outer Radius			240 mm	-	
Approximate width $\times$ height for pentagon shaped CsI crystals			-	90 $\times$ 80 mm <sup>2</sup>	
Number of PMTs per crystal			19	1	
Hamamatsu PMT model (central PMT for NaI(T $\ell$ ) was R1911-07)			R1911	R5543	
Photomultiplier Photocathde diameter			76.2 mm		

### 3.2. THE PIENU DETECTOR

---

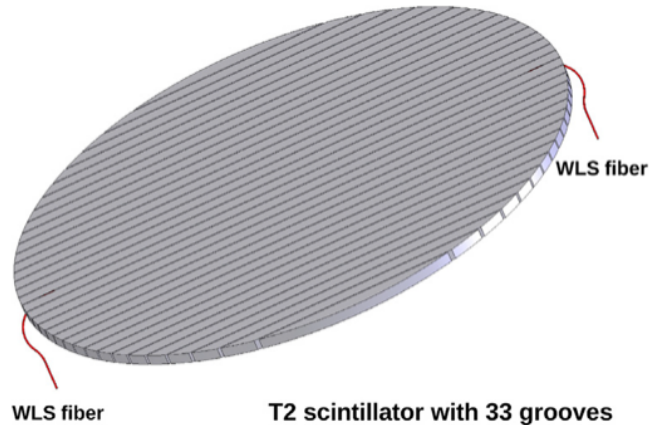


Figure 3.9: Illustration of T2 scintillator readout. 33 parallel grooves ( $1.1 \times 1.1 \text{ mm}^2$ ) were milled on the surface of the scintillator [1].

with the mixed gas of 80% tetrafluoromethane ( $\text{CF}_4$ ) and 20% isobutane ( $\text{C}_4\text{H}_{10}$ ) at atmospheric pressure. Signals from neighboring sense wires were grouped and fed to preamplifiers, discriminators, and time-to-digital converters (VT48, see in §3.4.2) to record the time of hits. The efficiency of every plane was measured to be  $> 99\%$  with beam positrons.

#### **Beam Wire Chambers (WC1 and WC2)**

WC1 and WC2 were used for tracking beam particles in order to extract position and angle information. They were the first detectors seen by the beam and mounted on the beam pipe (Figure 3.10). Each plane had 120 sense wires (0.8 mm in pitch) grouped by three to reduce the number of read-out channels. Thus the number of read-out channels was 40 in a plane and the effective wire read-out pitch was 2.4 mm. The active diameters of WC1 and WC2 were 9.6 cm.

#### **Decay Positron Wire Chamber (WC3)**

WC3 was used to define the acceptance for decay positrons at the entrance of NaI(Tl) (Figure 3.11). It was mounted on the flange of the NaI(Tl) crystal enclosure. Each plane had 96 sense wires with a pitch of 2.4 mm. The wires were grouped in pairs to reduce the number of read-out channels. Thus an effective read out spacing was 4.8 mm. The active diameter of WC3 was 23 cm.

### 3.2. THE PIENU DETECTOR

---

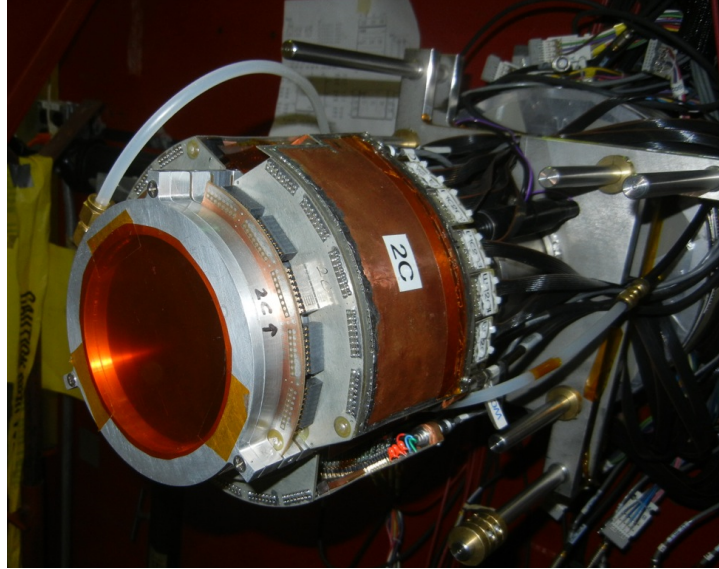


Figure 3.10: Picture of WC1 and WC2 attached on the beam pipe.

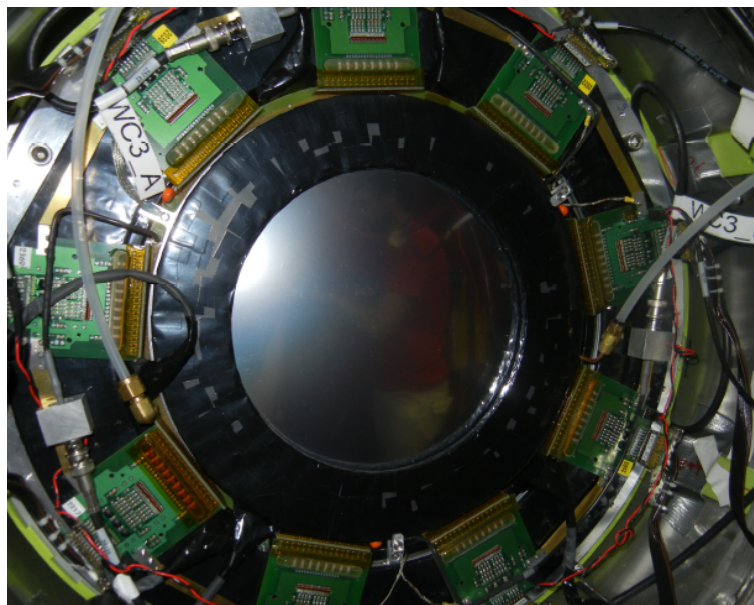


Figure 3.11: Picture of WC3 placed on the flange of the NaI(Tl) enclosure.

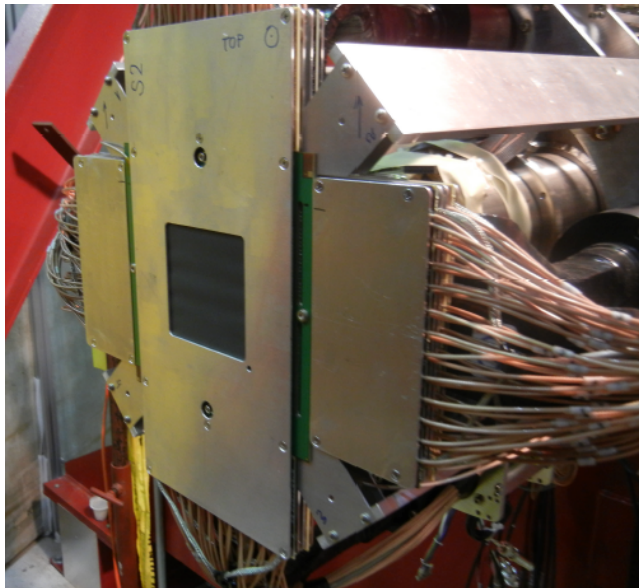


Figure 3.12: Assembly of S1 and S2.

### 3.2.4 Silicon Strip Detector

There were three sets of silicon strip detectors (S1–3). Each set had two planes of Si strip sensors to measure X and Y coordinates. S1-S2 and S3 were respectively placed immediately upstream and downstream of B3. They provided position and angle information of incoming pions to and outgoing positrons from B3. Each sensor had an active volume of  $61 \text{ mm} \times 61 \text{ mm} \times 285 \mu\text{m}$ . Figure 3.12 shows the assembly of S1 and S2.

Each Si sensor was a single sided AC-coupled micro-strip device. Each strip had a pitch of  $80 \mu\text{m}$ . Since the required resolution for the PIENU experiment was of the order of  $300 \mu\text{m}$ , four strips were connected to one read-out line together. The read-out lines were interconnected with capacitors and only every fourth line was read out by an amplifier. Figure 3.13 shows schematic of the silicon strip read-out. Each plane had 48 channels (288 in total of read-out). The signals were recorded by 60 MHz FADCs (VF48, see in §3.4.2). The position resolution provided by each plane was  $95 \mu\text{m}$  (r.m.s) if at least two read-out channels had a signal and  $370 \mu\text{m}$  (r.m.s) when only one read-out channel had a signal.

In order to reduce the data size, pulse-signal waveforms above the pre-defined thresholds were recorded. In S1 and S2, the thresholds were adjusted for pions. The thresholds of S3 were set lower than S1 and S2 to ensure that the efficiency for decay positrons in at least one plane was higher than 99%.

### 3.2. THE PIENU DETECTOR

---

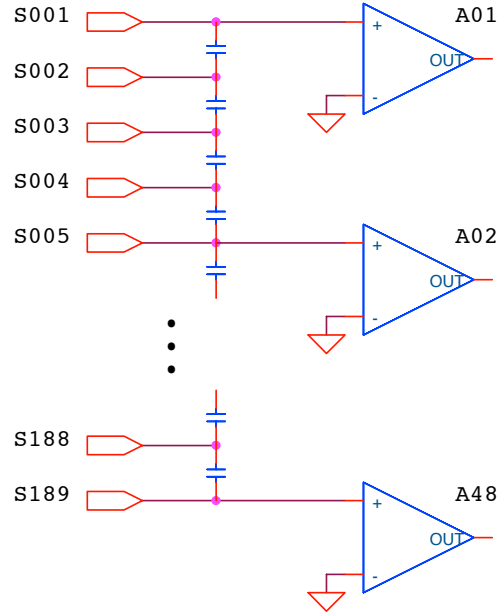


Figure 3.13: Schematic drawing of the silicon strip detector read out [1].

#### 3.2.5 NaI Calorimeter

The main calorimeter was a single crystal of Thallium-doped NaI (“NaI” will be used instead of “NaI(Tl)” from now on). We borrowed the crystal from LEGS group [59] in Brookhaven National Laboratory. The NaI was enclosed by a 3 mm thick aluminum enclosure while the front face was covered by 0.5 mm Aluminum foil to minimize the amount of material for the positron path. This enclosure had nineteen of 76.2 mm diameter circular quartz windows at the rear end to connect PMTs (Figure 3.14). Each of the quartz windows except for the central one was covered by 76.2 mm diameter Hamamatsu R1911 PMT, the central one was covered by R1911-07 PMT. All PMT were surrounded by  $\mu$ -metal shields to reduce the influence from the external magnetic field.

#### 3.2.6 CsI Calorimeter

A primary source of systematic error in the PIENU experiment was the uncertainty of low-energy tail of  $\pi^+ \rightarrow e^+ \nu_e$  events buried under the energy distribution of  $\pi^+ \rightarrow \mu^+ \rightarrow e^+$  events. In order to reduce the  $\pi^+ \rightarrow e^+ \nu_e$  low-energy tail, CsI crystals were installed to detect shower leakage from the NaI crystal.

Ninety seven of pure CsI crystals were placed around the NaI calorimeter

### 3.2. THE PIENU DETECTOR

---



Figure 3.14: Picture of the NaI crystal from its backside [3].

enclosure to form two layers of rings in order to detect shower leakage from the NaI (Figure 3.15). Each crystal in the CsI rings was pentagonal shape with a length of 25 cm (13.5 radiation lengths), a width of 9 cm and a height of 8 cm (4.5 radiation lengths). Figure 3.16 shows a typical CsI crystal. The crystals were divided into two upstream and two downstream layers, making a total of four rings. Each layer of the crystals was supported by a 2 mm thick stainless steel cylinders with 2 mm thick fins separating and supporting every 3–5 crystals from its neighbors (six fins in a layer).

The interior of CsI rings was filled with dry Nitrogen gas to keep the humidity level low enough. Each crystal was read out by a fine mesh 76.2 mm diameter Hamamatsu R5543 PMT. Those crystals and phototubes were on loan from BNL, which had been once used in the E949 experiment [60].

A  $\text{YAlO}_3:\text{Ce}^{245}\text{Am}$  source [61] was attached to front face of each crystal to monitor its light output and the gain of the PMT. This source emits about 8 MeV light pulses with a rate of about 50 Hz. A quartz fiber from a Xe lamp flasher was connected to each crystal. The flash light from the Xe lamp was triggered at 2 Hz during whole data taking period. This Xe lamp monitoring system traced only the changes in the gain of CsI PMT. A comparison between the YAlO and Xe-lamp monitoring gave access to the crystal's light collection stability. The instability of the light yield from the Xe lamp was measured to be less than 1%. Seven reference PMTs of the same type as the one used for the crystals were enclosed in an incubator with a constant temperature of 24.0 °C. The Xe lamp was also enclosed in

## 3.2. THE PIENU DETECTOR

---



Figure 3.15: Picture of whole calorimeter consisted by NaI and 97 CsI crystals [3].

an incubator at the same temperature. To reduce the influences of pick-up electric noise from the light flasher, the Xe lamp was placed at a long distance from the detector area.

### 3.2.7 Performance

#### Energy Resolution of the Calorimeters

Energy resolution and response of the NaI calorimeter was studied using mono-energetic 70 MeV positron beam. In order to minimize the amount of material for positron path, PIENU-II and only the first sub-assembly (V1+WC1+WC2) of PIENU-I were used for the measurement (Figure 3.17).

The energy spectrum of the NaI to the positron beam at the center of the crystal is shown in Figure 3.18. The highest energy peak at 68 MeV corresponds to the full energy deposit of the beam positrons. The energy resolution of the peak was 2.2% (FWHM). As shown in §3.1, beam momentum bite was known to be 0.5%, which was much smaller than the observed width of the peak. It is worth noting that there are sizable bumps below the main peak in Figure 3.18. These three bumps were due to photo-nuclear absorption in the NaI calorimeter [62]. In this process, one or more photons of the shower are absorbed by iodine and neutrons are emitted after the

### 3.2. THE PIENU DETECTOR

---

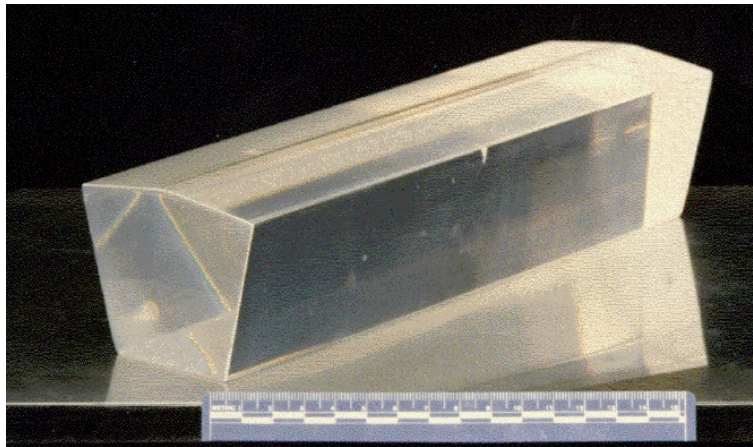


Figure 3.16: Picture of one CsI crystal [3].

absorption. Because the neutron binding energy is approximately 8 MeV, this process results in the deficit of the energy deposit to NaI by 8 MeV for every escaped neutron. In order to check the correctness of this hypothesis, a MC simulation with this process implemented was performed. Figure 3.19 shows the result of MC with and without photo-nuclear hadronic reaction contributions. The MC simulation showed the additional bumps were due to photo-nuclear effect, and the positions of the additional bumps were consistent with the observed data. Thus, MC studies supported the correctness of our understanding to the nature of these bumps.

Photo-nuclear effect was also present when measuring the  $\pi^+ \rightarrow e^+ \nu_e$  decay positrons. Figure 3.20 shows the observed  $\pi^+ \rightarrow e^+ \nu_e$  energy spectrum with special event selections to reduce the contamination of  $\pi^+ \rightarrow \mu^+ \rightarrow e^+$  decays, where the details of the event selection will be described in §5.1.1. The small bump at 56 MeV was due to one neutron escape.

The study of the calorimeter response with the positron beam was repeated for the rotated-axis detector configurations in order to see the transversal shower leakage effect. The crystal was rotated to 10 different angles up to  $47.7^\circ$ . The amount of the shower leakage was evaluated with the ratio between the number of events below 50 MeV normalized to the total number of events. This ratio will be called “tail fraction” hereafter. The result for the measurement is shown in Figure 3.21. When only the energy in the NaI crystal was used, tail fraction reached 12% at the highest angle, while if CsI energy was added, the tail fraction never exceed 2% for the whole angular range.

### 3.2. THE PIENU DETECTOR

---

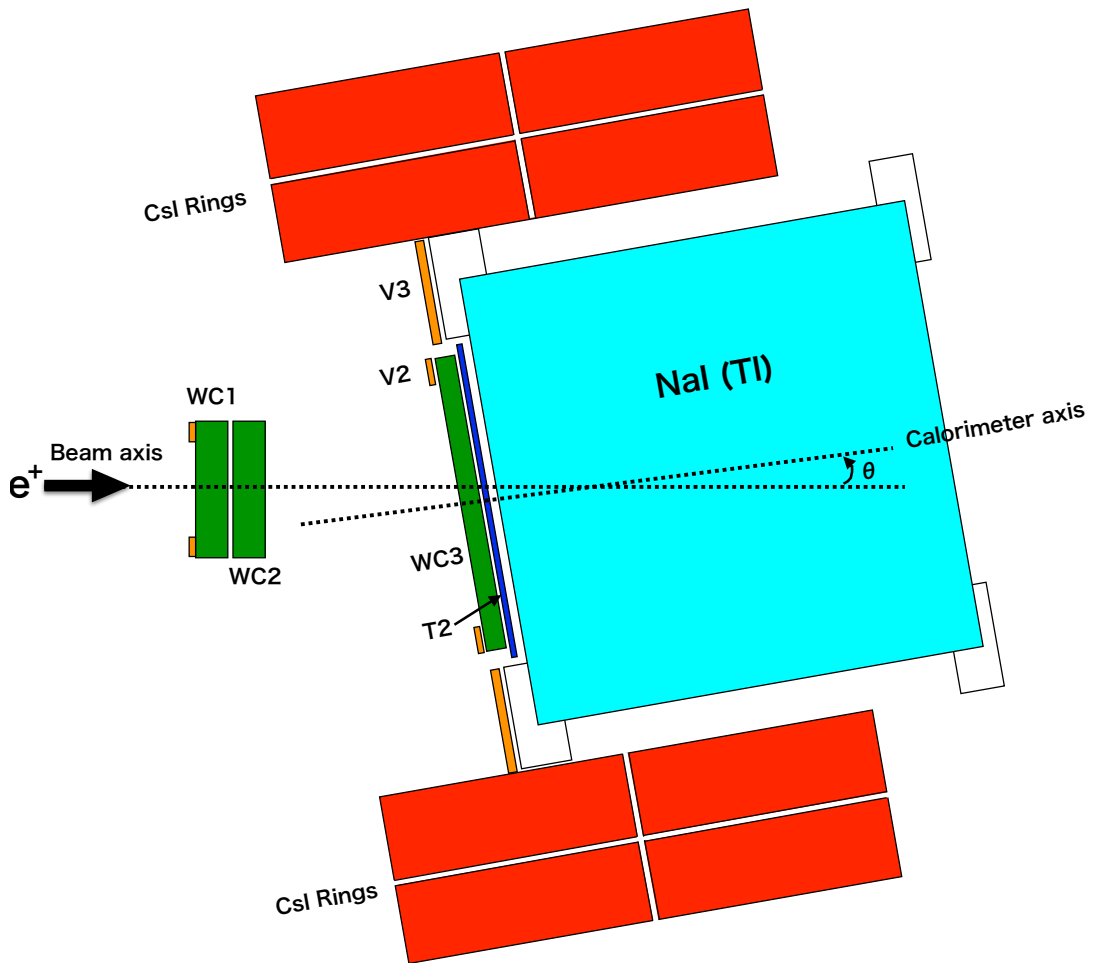


Figure 3.17: Schematic drawing of the detector setup for special positron runs.

### 3.2. THE PIENU DETECTOR

---

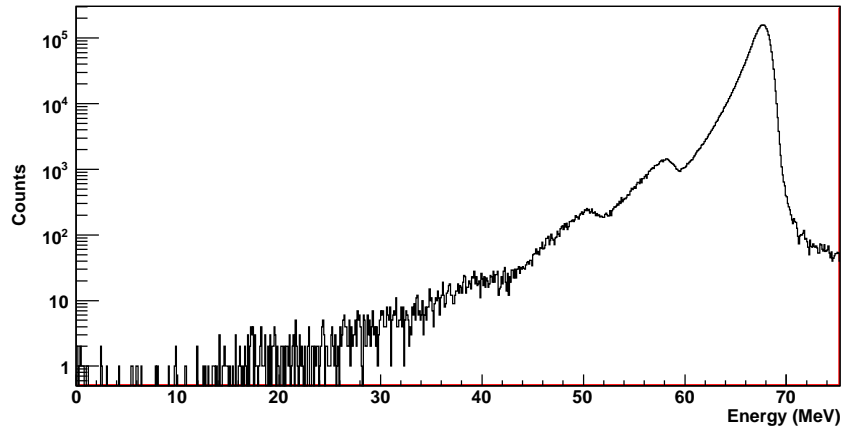


Figure 3.18: Response of the NaI crystal at 70 MeV positron beam. The additional structures below the full energy peak were due to photo-nuclear effects [62].

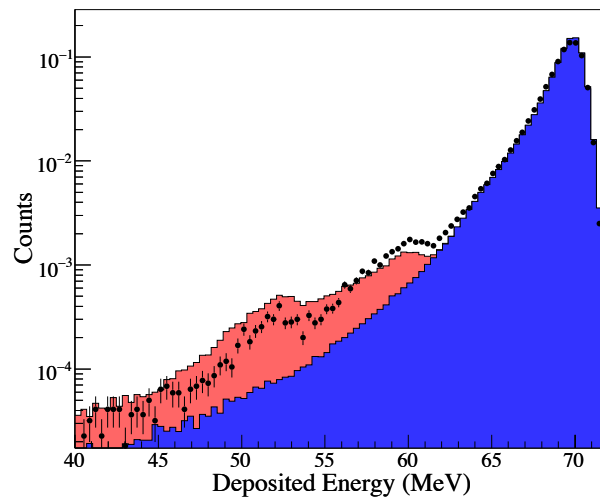


Figure 3.19: Beam positron energy in the NaI calorimeter. Filled circles with error bars indicate data, and simulated spectra with and without hadronic reactions are respectively shown by red and blue histograms [62].

### 3.2. THE PIENU DETECTOR

---

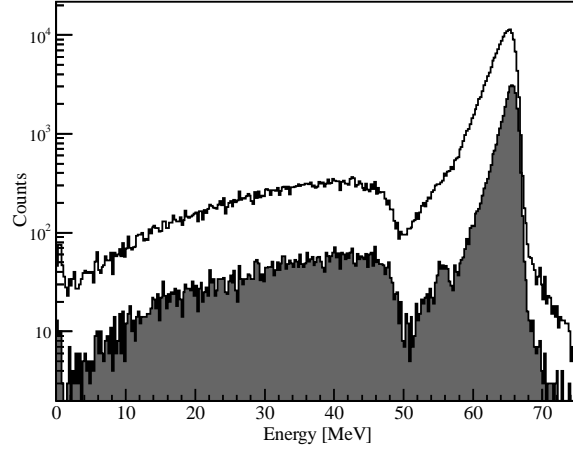


Figure 3.20:  $\pi^+ \rightarrow e^+ \nu_e$  energy spectra with  $\pi^+ \rightarrow \mu^+ \rightarrow e^+$  suppression cuts [1]. The unfilled histogram represents the energy spectrum with the radial acceptance cuts of 60 mm and the shaded histogram is with tighter 40 mm acceptance cut.

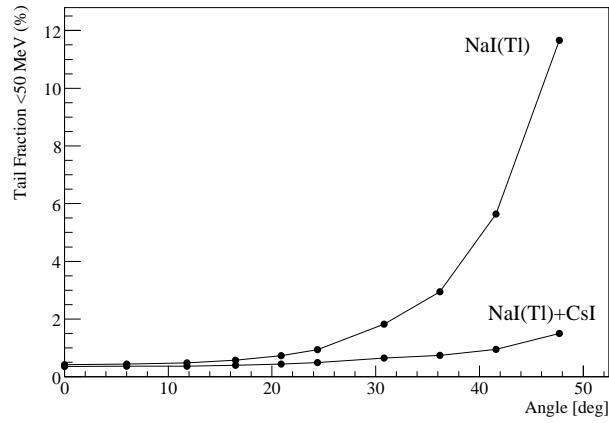


Figure 3.21: Tail measurement for the NaI and the NaI plus CsI rings [1]. The vertical axis indicates the low-energy tail fraction, which represents the integral of events below 50 MeV divided by the integral of full energy spectrum.

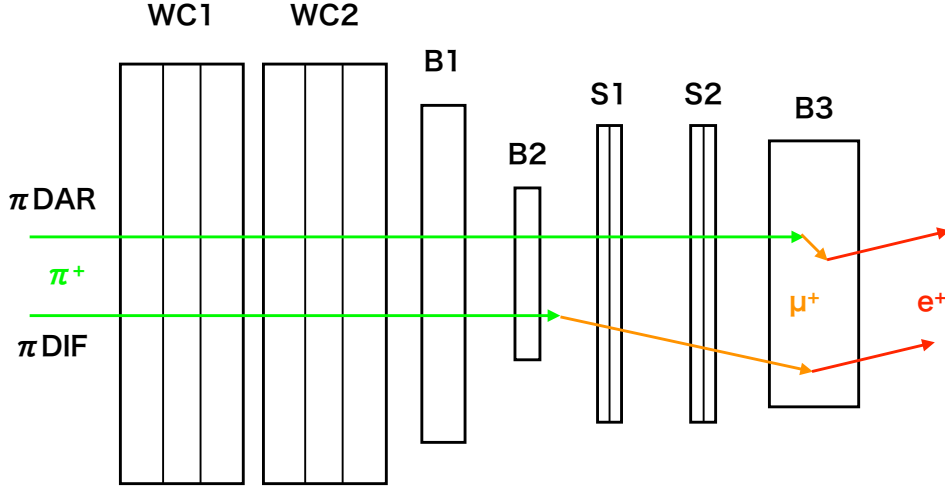


Figure 3.22: Schematic of pion decay at rest ( $\pi$ DAR, upper trajectory) and  $\pi$ DIF (lower trajectory) events.

### Tracking Performance

As already described in §2.2.2,  $\pi$ DIF events were the dominant background in the previous experiment. The tracking detectors were designed to minimize these  $\pi$ DIF events. About 3.6% of the pions decayed in flight upstream or inside the target. These  $\pi$ DIF events have lower energy deposit in the target than  $\pi^+ \rightarrow \mu^+ \rightarrow e^+$  decays and therefore mimic the energy deposit of  $\pi^+ \rightarrow e^+ \nu_e$  decays. About half of those  $\pi$ DIF events happen upstream of the target, between WC2 and S1, and can be identified by the tracking detectors as illustrated in Figure 3.22. The angular distributions (kink angle) between the track detected by WC1 and WC2 and track detected by S1 and S2 with different decay types are shown in Figure 3.23 for MC and in Figure 3.24 for data with  $\pi^+ \rightarrow \mu^+ \rightarrow e^+$  suppression cuts (see §5.1.1).  $\pi$ DIF events between WC2 and S1 can be rejected by their larger angle.

## 3.3 Trigger Logic for Data Taking

Figure 3.25 shows the schematic of the PIENU trigger diagram. Pions and a small number of muons and positrons were selected using energy deposit in B1. Beam muons were used for the calibration of B3 and T1, and beam positrons were used for calibrating the NaI. In the trigger logic, a coincidence of B1, B2, and B3 defined the pion signal, and a coincidence of positron signals in T1 and T2 defined the decay positron signal. A coincidence of beam pion and decay positron signals within -300 ns to 540 ns was the basis

### 3.3. TRIGGER LOGIC FOR DATA TAKING

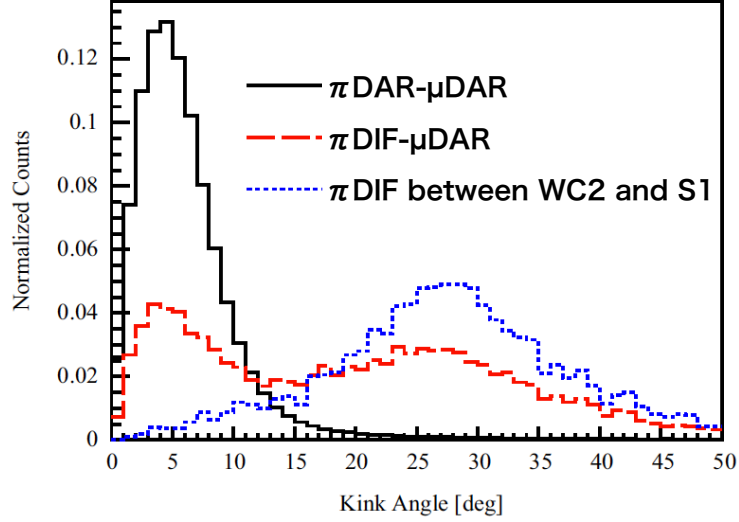


Figure 3.23: Simulated kink angle distributions for different decay modes [1].  $\pi$ DAR and  $\mu$ DAR respectively stand for pion and muon decay at rest in the target. Dashed red line indicates the  $\pi$ DIF occurred after B2 counter and muon decays at rest in B3, and dotted blue line represents pion decays between WC2 and S1.

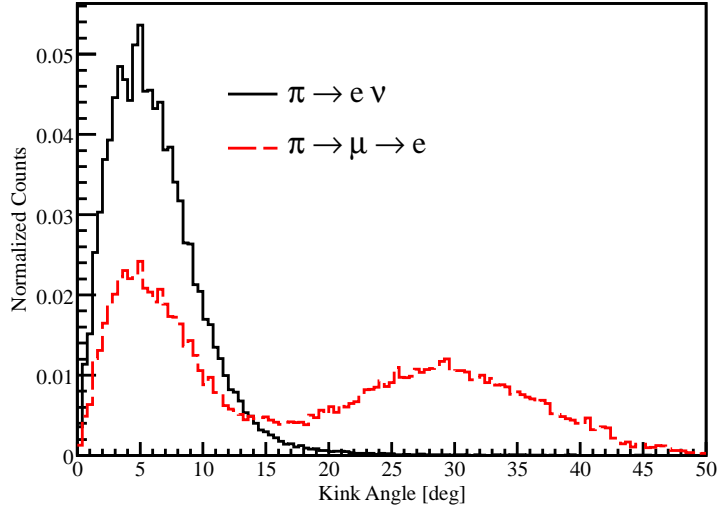


Figure 3.24: Kink angle distributions for  $\pi^+ \rightarrow e^+ \nu_e$  ( $T_{\text{NaI}} > 55$  MeV) and  $\pi^+ \rightarrow \mu^+ \rightarrow e^+$  ( $T_{\text{NaI}} < 30$  MeV) data events [1].  $\pi$ DAR events were suppressed using the energy deposit information in B3 (see §5.1.1 for detail).

### 3.3. TRIGGER LOGIC FOR DATA TAKING

---

of the main trigger.

Since the main trigger was dominated by  $\pi^+ \rightarrow \mu^+ \rightarrow e^+$  decays whose branching ratio is larger than  $\pi^+ \rightarrow e^+ \nu_e$  decays by four orders of magnitude, only 1/16 of main trigger were selected as the unbiased trigger (Prescale trigger) for the calibration purpose. The triggers that enhanced  $\pi^+ \rightarrow e^+ \nu_e$  events were constructed by an Early trigger and a TIGC trigger. The Early trigger selected the decay positron events in the early time window (6–46 ns) after pion decay. Due to the short pion lifetime, more than 70% of the  $\pi^+ \rightarrow e^+ \nu_e$  events fall within this time window. The TIGC trigger selected events with  $E_e > 46$  MeV in the calorimeter (NaI and CsI). The TIGC trigger was generated by a TIGC module (see §3.4.2). Almost all the  $\pi^+ \rightarrow e^+ \nu_e$  events with the exclusion of the tail events were selected by this trigger. Those three triggers made up the “physics triggers”.

The deadtime of the trigger logic was about 100  $\mu$ s. The busy signals from all the trigger and DAQ logic were used as a veto signal for the coincidence module of beam pion and decay positron signals before pre-scaling. If the veto signal was only used for the modules after pre-scaling, the following case might occur: when the deadtime was made by Prescale trigger (240 Hz), the following Early or TIGC trigger came in the deadtime was blocked. However, the following Prescale trigger did not come in this deadtime because Prescale trigger was triggered once in 16 times. Therefore, the different trigger inefficiency between each physics trigger might be produced. In this case, the probability of Early or TIGC trigger blocked was  $100 \mu\text{s} \times 240 \text{ Hz} = 2.4\%$ . In order to avoid such a possible bias, the veto signal was used for the coincidence module before the event was pre-scaled. By this veto signal, the bias between each physics trigger was not observed. It was confirmed by the energy spectrum in the calorimeters made by each physics trigger, and the shape of the energy spectrum was consistent with each other.

There were another triggers used for data quality checks and calibration. The Cosmic trigger provided cosmic-ray events, mostly high energy cosmic muons, were selected by the requirement of a high energy deposit in the CsI outer layer or the coincidence of inner and outer layers. These events were used for CsI calibration (see §4.2.4). As described in §3.2.6, the Xe lamp provided flashes to all the CsI crystals (Xe trigger) for monitoring. This lamp was triggered by a pulse generator twice in a second. Finally, the Beam positron trigger was used for the NaI and plastic scintillators calibration.

During a normal data taking run, all 6 triggers were used and several of them could be triggered at the same time. In order to distinguish the associated trigger types to a particular event, the trigger logic pulses were also recorded with multi-hit TDC (VT48). The rates of the triggers are listed in Table 3.2.

The trigger signal made by any of the six triggers was then latched by the

### 3.3. TRIGGER LOGIC FOR DATA TAKING

---

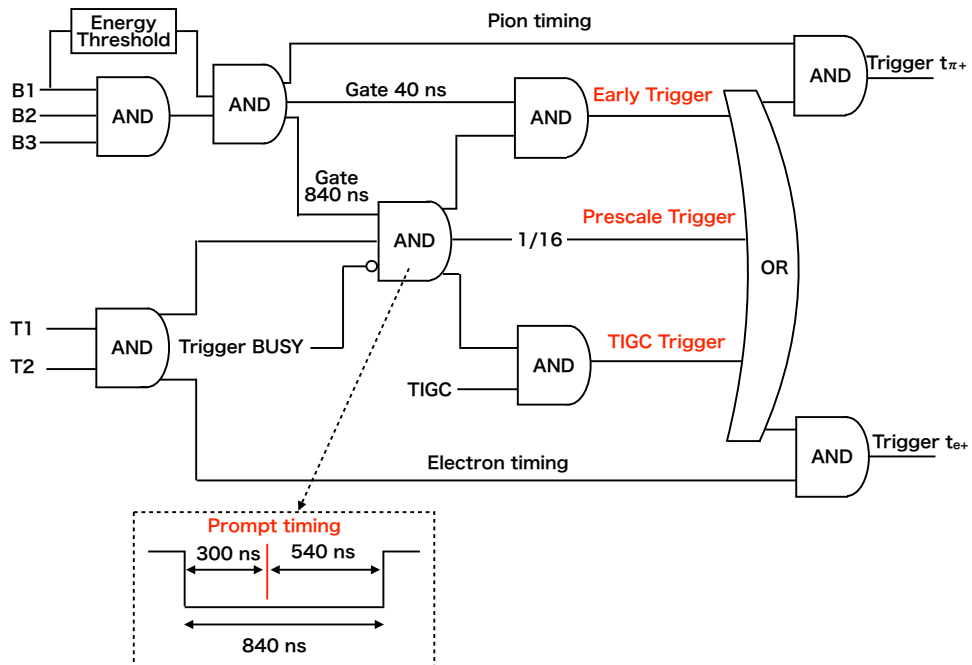


Figure 3.25: Schematic of the trigger diagram for the three “physics triggers”.

### 3.4. THE DATA ACQUISITION SYSTEM

---

Table 3.2: Trigger rates [1].

Trigger	Rate [Hz]
Pion stop in target	$5 \times 10^4$
Physics trigger	
Early trigger	160
TIGC trigger	170
Prescale trigger	240
Other Triggers	
Cosmic trigger	15
Beam positron trigger	5
Xe lamp trigger	2
Total triggers	600

pion ( $t_{\pi^+}$ ) and the positron ( $t_{e^+}$ ) timing. These latched signals triggered the data acquisition.  $t_{e^+}$  was used for the trigger of the VME modules (VF48 and VT48), while  $t_{\pi^+}$  triggered the COPPER data acquisition. Detail of those modules will be described in the next section.

## 3.4 The Data Acquisition System

### 3.4.1 COPPER 500 MHz Flash-ADC System

#### COPPER

PMTs of all plastic scintillators and some calorimeters were read out by a 500-MHz-sampling-frequency Flash-ADC (FADC) system based on COPPER (COMmon Pipelined Platform for Electronics Readout) platform [63, 64].

COPPER was developed by KEK for the Belle experiment. Main COPPER board was a 9U-size VME board. The major advantage of the COPPER system was its on-board data processing capability. The CPU (Linux) was on the board, and the data suppression was performed by a software.

One COPPER board had four frontend modules called “FINESSE”. FINESSE provided frontend digitization feature and the backend process for the digital data were handled on the COPPER main board. Many different variations of FINESSE were developed. For the PIENU experiment, a FINESSE board with two channel 500-MHz FADC was employed. Thus, each COPPER board could receive a total of 8 signals. The PIENU experiment was equipped with four COPPER boards to digitize the signals coming from the 23 PMTs of all plastic scintillators and a few other additional signals. An additional COPPER board was installed during the 2012 run to record

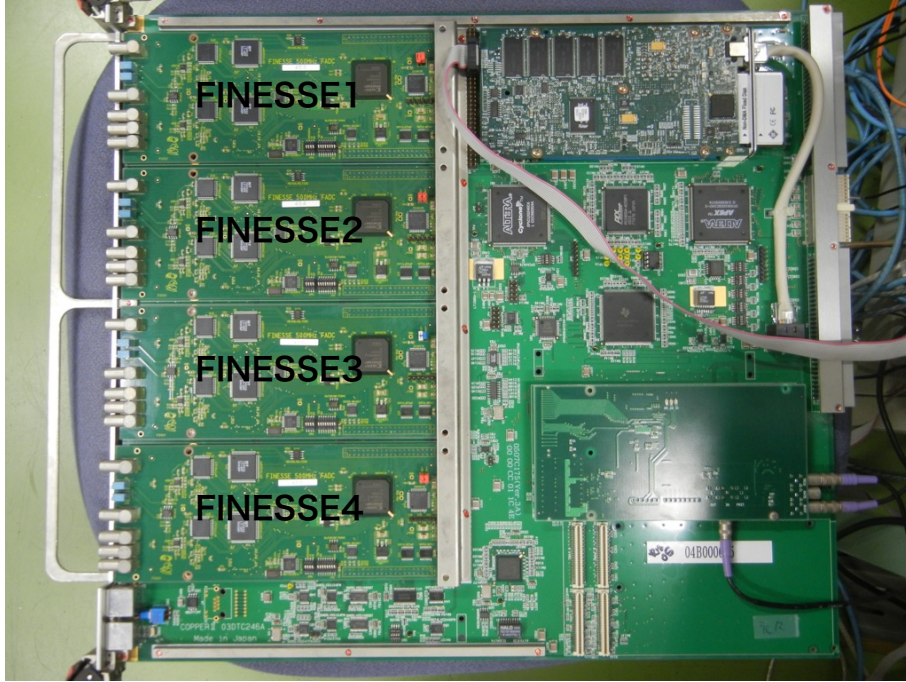


Figure 3.26: Picture of main COPPER board mounted with four FINESSE modules.

partial analog sums of the CsI crystal PMTs.

Figure 3.26 shows main COPPER board with FINESSE modules. The typical digitized waveform from a PMT is shown in Figure 3.27.

For the PIENU experiment, the dynamic range of FADC was set from  $-950$  mV to  $50$  mV, and the time window of the signals recorded by this system covered  $7.75$   $\mu$ s ( $-6.40$  to  $1.35$   $\mu$ s with respect to pion timing in B1 counter) to be able to detect pre- and post-pile up particles (see §4.2.2).

#### **FINESSE**

Based on the original 500 MHz FADC FINESSE developed in KEK, the firmware was heavily modified in Osaka University for the PIENU experiment [65]. Each FINESSE channel had two 250 MHz FADC devices. They were driven in alternating phases in order to achieve 500 MHz sampling. The gains of these two FADCs were monitored and adjusted run-by-run using beam particle signals. All ADCs and FIFOs were controlled by FPGA driven with 125 MHz.

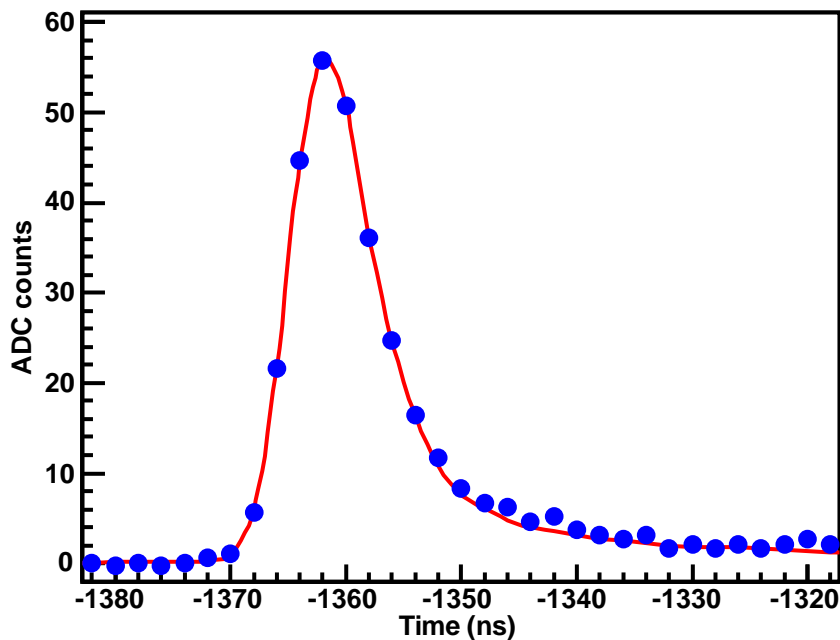


Figure 3.27: Typical waveform digitized by COPPER. Blue plots indicate sampling points and red curve shows the fitting template.

### Clock Distributor

If the 250 MHz clock going into each FINESSE channel were not synchronized, the pulse timing in each ADC was different and that might degrade the time resolution between different signals to the different FINESSE boards. Clock Distributor module was developed by the PIENU collaboration to synchronize different FINESSE cards. Clock Distributor provided synchronized 250 MHz sampling clocks, latched-gate signals, and latched-reset signals to all FINESSE cards. The form factor of Clock Distributor was 6U-size VME and the numbers of output channels were 13 for clock, latched-gate and latched-reset, respectively. Two Clock Distributor modules were used to drive a total of 16 (20 from 2012) FINESSE cards in the PIENU experiment.

### GPIO

A General Purpose Input Output (GPIO) module developed by KEK provided gate and reset signals into Clock Distributor module. Additionally, GPIO module received busy signal from COPPER boards and provided it to the trigger logic, and received trigger signal from the trigger logic to distribute it to the COPPER system. Namely, GPIO was used for the interface between the COPPER system and the main trigger logic.

### 3.4. THE DATA ACQUISITION SYSTEM

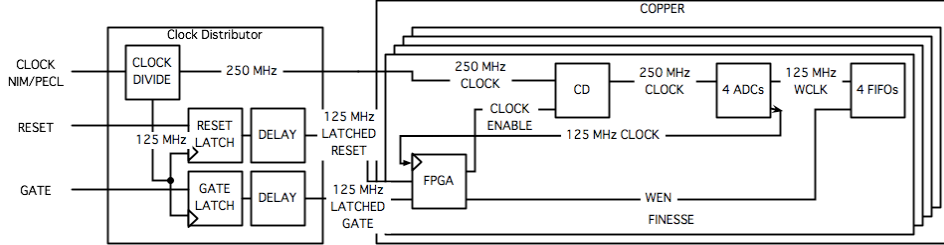


Figure 3.28: Diagram of COPPER system [65]. CD in the box on FINESSE represents “Clock Divide”. The 250 MHz clock, gate, and reset signals for Clock Distributor were provided by GPIO.

#### Signal Synchronization

Figure 3.28 shows the schematic diagram of the COPPER system. The 125 MHz internal clock of Clock Distributor was generated by dividing 250 MHz clock, which was used for the timing of latched signals. The timings of those signals could be adjusted by programmable delay circuits. When the gate signal was open, the write enable (WEN) signal was provided from FPGA and data were written into FIFOs. The 125 MHz internal clock of FINESSE was used for write clock (WCLK) timing, namely 4 sampling points were recorded. The data were sent to the host computer through Ethernet.

In principle, the different phases of gate signal between each ADC should not occur due to the synchronized signals from Clock Distributor. However, an actual gate signal was affected by jitter or electric noise. If the edge of the gate signal was set at the same timing with that of WCLK for FINESSE, it was possible to break the synchronization and 8 ns shift would be observed (“gate timing mismatch”, schematically drawn in Figure 3.29). The timing mismatch of the reset was also possible with the same reason.

At the end of 2011, the gate timing mismatch was observed. Figure 3.30 shows the distribution of the time difference between T1’s PMT1 and PMT2 in the problematic run. If the gate timing was properly adjusted, there was only one Gaussian distribution around 0 ns. However, 8 ns shift was observed due to the gate timing mismatch. The gate and reset timings were tuned using programmable delay circuits in Clock Distributor before the beam time in 2012. The timings of all FINESSE channels including the fifth COPPER were adjusted using test pulse provided by a function generator.

### 3.4. THE DATA ACQUISITION SYSTEM

---

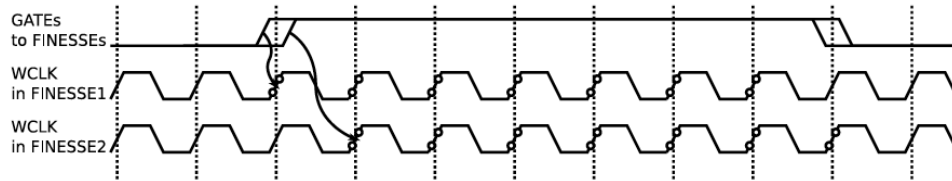


Figure 3.29: Example of diagram for the gate timing mismatch [65]. WCLK was driven with 125 MHz, thus 8 ns shifted wave form would be observed.

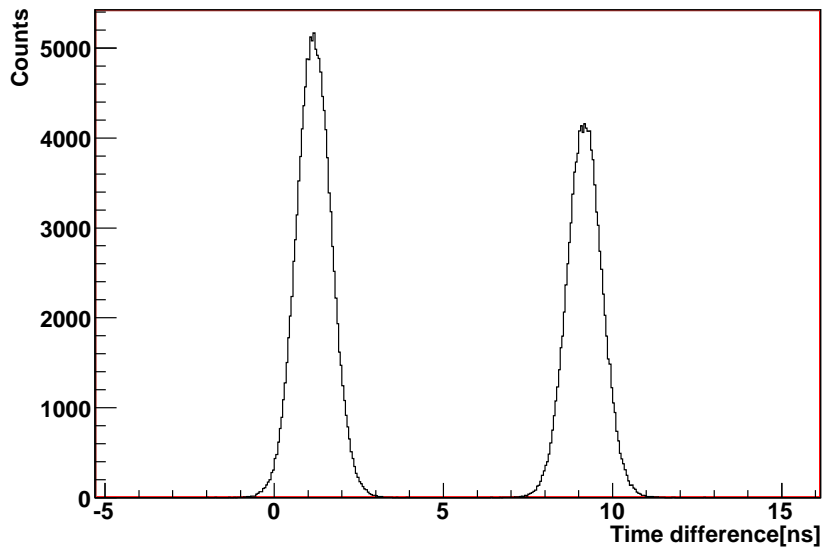


Figure 3.30: Time difference of the peaks evaluated by wave form fit between COPPER1-FINESSE1-Channel2 and COPPER2-FINESSE1-Channel2. Those channels respectively recorded the signals of T1's PMT1 and PMT2.

### 3.4. THE DATA ACQUISITION SYSTEM

---

#### 3.4.2 Other Hardwares

##### VF48

A VF48 was a 60 MHz FADC single-width VME 6-U module, which was designed at the University of Montreal in 2004[66]. It had a resolution of 10 bits and a dynamic range of  $\pm 250$  mV. All the NaI and the CsI PMT signals and silicon strip channels were read out by VF48 modules. This made a total of 404 channels (NaI:19, CsI:97, silicon strips: 288) read out by 10 VF48 modules. All VF48 modules were fed with the same 20 MHz clock provided by TIGC module (see §3.4.2). This clock was multiplied internally in the VF48 to reach 60 MHz sampling.

Because there were a large number of channels, data suppression technique, with which the waveform was not recorded if the signal pulse was lower than a given threshold, was implemented. For the CsI channels the data suppression threshold was set at 2 MeV, while it was 0.2 MeV for S1 and S2, and 0.1 MeV for S3. Further data suppression by reducing the data sampling frequency to 30 MHz was employed for the NaI signals because the waveform length in the NaI was long,  $\sim 1.3 \mu\text{s}$ .

The number of sample points by VF48 were 40 (666 ns) for the CsI, 40 (1333 ns) for the NaI, and 70 (1162 ns) for S1, S2, and S3.

##### VT48

Logic signals from three wire chambers (WC1–3), counter PMT, and major trigger logic were recorded by multi-hit TDC modules called VT48. This module was a single width VME 6-U module, and designed at TRIUMF in 2006 for the KOPIO experiment[67]. The AMT-2[68] developed for ATLAS was used as a TDC chip on the VT48. This device had a 25-MHz on board clock which was multiplied internally to achieve 0.625 ns resolution. All VT48 modules, however, were fed with an external 25-MHz clock to ensure the synchronization of all modules.

One board could read out 48 channels for up to 20  $\mu\text{s}$ . In order to minimize the dead-time, only two channels were read out for 20  $\mu\text{s}$  to detect long lifetime backgrounds while all other channels were read out 4.0  $\mu\text{s}$  before and after the decay positron signal timing. A total of 11 VT48 modules were used in the PIENU experiment.

##### TIGC

A TIGC (Tigress Collector) was a VME-based module developed by the University of Montreal and TRIUMF for the TIGRESS experiment at TRIUMF [69]. This module could read in the digitized output data from the VF48 and performed data process for trigger decision in fast speed. The highest values of samples of the waveforms in every 250 ns of all NaI and

### 3.4. THE DATA ACQUISITION SYSTEM

---

CsI channels were sent to the TIGC module. If the highest values passed given threshold, TIGC provided a signal called “TIGC” used for the TIGC trigger (Figure 3.25). This threshold was set to be about 4 MeV lower than the Michel edge.

The TIGC module also provided the clock to all the VF48 to synchronize each other.

#### 3.4.3 Software of Data Acquisition System

The PIENU data acquisition system consisted of three VME crates. Two VME crates were used for the VF48 and VT48 modules while the third was mostly used for slow control modules and COPPER boards with a processor on each board. The slow control modules recorded a number of quantities such as high voltage of PMTs, pressure of WC gas, hardware threshold (e.g. threshold of TIGC module), and so on in order to monitor the data taking conditions.

A data collection software was developed by using the MIDAS data acquisition system [70]. MIDAS was designed to integrate multiple data sources from multiple computers through TCP/IP network. This base design ensures the scalability of the MIDAS DAQ system. It can be used for a small test system with one computer and for a large production system with many computers. The PIENU DAQ system made use of this advantage of MIDAS to seamlessly integrate all the VME modules.

The MIDAS server computer could be controlled via a web interface (Figure 3.31 and 3.32). All the information and errors from the DAQ modules were issued on the web page. Programs to make on-line histograms for the data quality check were also controlled by the MIDAS during data taking (Figure 3.33).

### 3.4. THE DATA ACQUISITION SYSTEM

MIDAS experiment "pienu"		Fri Dec 14 14:19:11 2012 Refr:60			
<input type="button" value="Stop"/> <input type="button" value="Pause"/> <input type="button" value="ODB"/> <input type="button" value="CNAF"/> <input type="button" value="Messages"/> <input type="button" value="ELog"/> <input type="button" value="Alarms"/> <input type="button" value="Programs"/> <input type="button" value="History"/> <input type="button" value="Config"/> <input type="button" value="Help"/>					
monitor					
VME0_settings VME1_settings B1_Setpt B2_Setpt B3_Setpt Shifts Cameras Histos Operators Runlog HV_PIENU HVBERTan					
Run #82584		Running	Alarms: On	Restart: Yes	Data dir: /home/pienu/online/data
Start: Fri Dec 14 14:03:40 2012			Running time: 0h15m31s		
Equipment	FE Node	Events	Event rate[/s]	Data rate[MB/s]	Analyzed
Vme0	feVme0@lxpienu01.triumf.ca	86890	105.8	0.467	N/A
Vme1	feVme1@lxpienu02.triumf.ca	87085	107.3	0.576	N/A
Copper1	feCopper01@copper1	86908	107.7	0.071	N/A
Copper2	feCopper02@copper2	86849	107.7	0.038	N/A
Copper3	feCopper03@copper3	87085	108.3	0.055	N/A
Copper4	feCopper04@copper4	87018	103.5	0.025	N/A
Copper5	feCopper05@copper5	86864	107.7	3.202	N/A
EB	Ebuilder@pienu01.triumf.ca	87018	88.4	3.675	N/A
PostAmp	PostAmp@pienu01.triumf.ca	0	0.0	0.000	N/A
u_Beam	fe3hp@pienu01.triumf.ca	0	0.0	0.000	N/A
NMR	femmr@pienu01.triumf.ca	0	0.0	0.000	N/A
Epics	feepics@pienu01.triumf.ca	0	0.0	0.000	N/A
M13DVM	fem13dvm@pienu01.triumf.ca	0	0.0	0.000	N/A
GASDVM	fegasdvm@pienu01.triumf.ca	0	0.0	0.000	N/A
ScalerN	feScalerN@lxpienu03.triumf.ca	0	0.0	0.000	N/A
LRS1440	FeLrs1440@pienu03.triumf.ca	0	0.0	0.000	N/A
RunLog	feRunLog@pienu01.triumf.ca	0	0.0	0.000	N/A
QOD	feqod@pienu02.triumf.ca	0	0.0	0.000	N/A
Temperature	FeTemperature@pienu01.triumf.ca	90	0.0	0.000	N/A
scbertan	scbertan@lxpienu03.triumf.ca	0	0.0	0.000	N/A
Channel	Events	MB written	Compression	GB total	
run82584.mid.gz	86976	1170.957	67.7%	116315.892	
Lazy Label	Progress	File Name	# Files	Total	
Dcache	0 %	run82581.mid.gz	20206	0.0 %	

Figure 3.31: Web interface of MIDAS data acquisition system. All the VME modules were integrated and easily controlled via this interface.

MIDAS experiment "Pienu"		Thu Jul 19 11:35:59 2012	
<input type="button" value="Find"/> <input type="button" value="Create"/> <input type="button" value="Delete"/> <input type="button" value="Alarms"/> <input type="button" value="Programs"/> <input type="button" value="Status"/> <input type="button" value="Help"/>			
Create Elog from this page			
/ Equipment / ScalerN / Settings / KEKVME / ClockDistributor /			
Key	Value		
GateDelay_CD1	800 (0x320)		
ResetDelay_CD1	280 (0x118)		

Figure 3.32: Example of the control for modules. The delay timings of gate and reset signals in Clock Distributor could be adjusted in this page. The delay timings of gate and reset signals were respectively set to 800 ps and 280 ps.

### 3.4. THE DATA ACQUISITION SYSTEM

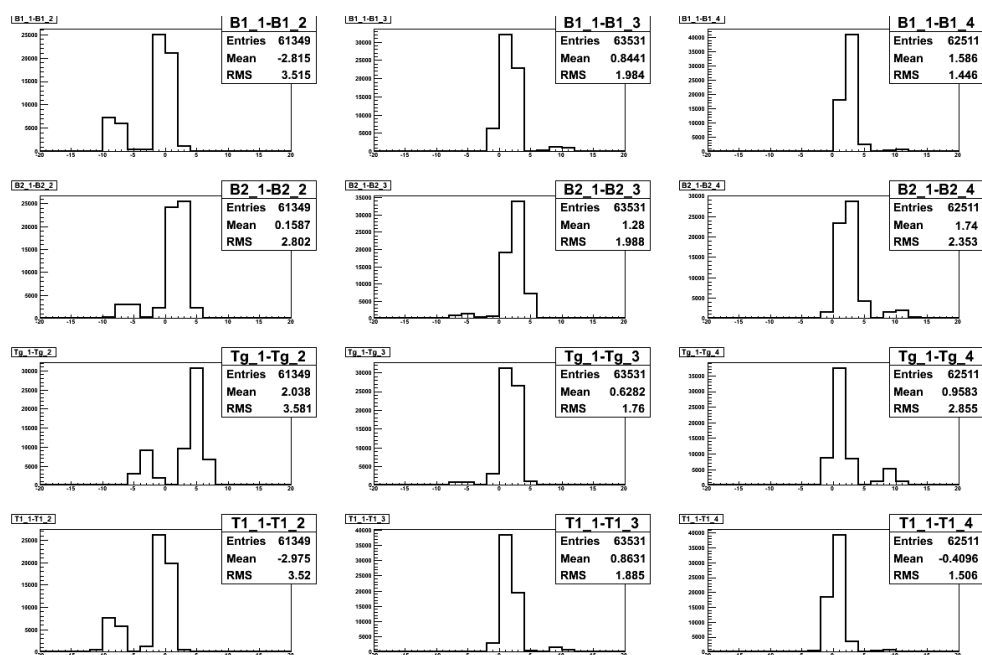


Figure 3.33: Example of the on-line histograms. In order to check the gate timing mismatch, new histograms were added into the software in 2012. Those histograms show the case of gate timing mismatch run. The time difference of the peak between each channel was histogrammed (e.g. B1.1-B1.2 represents the time difference between PMT1 and PMT2 of B1). Tg.1 to Tg.4 stand for the PMT1 to 4 of B3.

## Chapter 4

# Raw Ratio Extraction

### 4.1 Overview

The PIENU experiment collected about  $6 \times 10^6$   $\pi^+ \rightarrow e^+ \nu_e$  events during run periods from 2009 to 2012 corresponding to more than 30 times higher statistics than in the previous TRIUMF experiment[22, 23]. The data discussed here were taken in November in 2010 and from November to December in 2011, which correspond to about 25% statistics of the full data set. The number of runs in 2010 is 1904 while there are 3692 runs in 2011 data set. At present, the analysis of 2010 data set has been completed [4] and 2011 data set is still blinded.

In this section, the method for the extraction of the ratio of the pion branching ratios before corrections (raw ratio;  $R_{\text{raw}}^\pi$ ) is described. Before the analysis,  $R_{\text{raw}}^\pi$  was shifted (“blinded”) by a hidden random value within 0.5% in order to reduce possible bias. The variable extraction from waveforms, calibration, and event selection with the blind technique are discussed in each following section.

### 4.2 Waveform Calibration

#### 4.2.1 Pedestal Calibration

In the waveform analysis, the baseline offset might be able to be evaluated event by event if necessary. This method is robust if the baseline offset may different event by event. However, it requires extremely smart algorithm to remove the bias coming from the random signal pulse that may change the level of baseline. In order to prevent such situation, the baseline offset was evaluated by taking its mean value for one run. There was no structure in the baseline and its stability in a run was within 0.5 ADC count (r.m.s), thus this method worked very well. The pedestal of each ADC channel in COPPER and VF48 was calculated based on the mean value of the first

## 4.2. WAVEFORM CALIBRATION

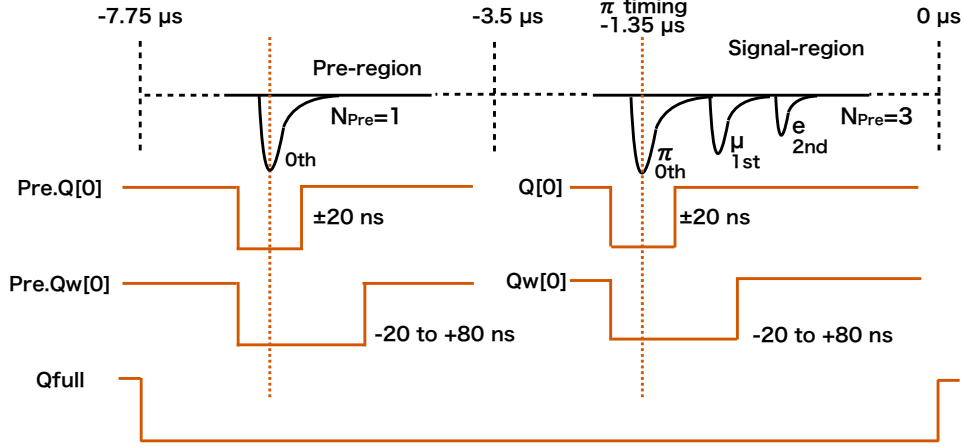


Figure 4.1: Schematic of the variables extraction from waveforms of COPPER. This is the example of  $\pi^+ \rightarrow \mu^+ \rightarrow e^+$  decay with one background signal in Pre-region in B3.

three samples of waveforms for every run.

### 4.2.2 Variable Extraction

#### COPPER

After pedestal calibration, the information of each signal pulse was extracted from the waveform. Figure 4.1 shows the schematic of waveforms and definitions of variables for COPPER. The time region  $-6.40$  to  $-2.15 \mu\text{s}$  with respect to pion timing  $t_{\pi^+}$  was defined as the “Pre-region”, and “Signal-region” was defined after Pre-region. The number of hits in each region ( $N_{\text{Pre}}$ ,  $N_{\text{Sig}}$ ) was identified by a hit finding algorithm based on the highest point before a drop. The time of the peak point ( $t$ ), the pulse height of the peak point (PH), and the charge deposit ( $Q$ ) were recorded as array variables. For example, if three hits ( $N_{\text{Sig}} = 3$ ) were found in the Signal-region, the time, pulse height, and charge deposit were respectively stored as  $t[3] = \{t_{0\text{th}}, t_{1\text{st}}, t_{2\text{nd}}\}$ ,  $\text{PH}[3] = \{\text{PH}_{0\text{th}}, \text{PH}_{1\text{st}}, \text{PH}_{2\text{nd}}\}$ , and  $Q[3] = \{Q_{0\text{th}}, Q_{1\text{st}}, Q_{2\text{nd}}\}$ . There were three types of the charge deposit variables,  $Q$ ,  $Q_w$ , and  $Q_{\text{full}}$ , respectively represented the integrated charge between  $-20$  and  $+20$  ns,  $-20$  and  $+80$  ns from the highest point, and full range in COPPER.  $Q_{\text{full}}$  was recorded as single variable since this was the integration of the full range.

## 4.2. WAVEFORM CALIBRATION

---

### VF48

Mostly the same algorithm as COPPER was used for the waveforms of VF48. The number of hits ( $N$ ), the pulse height (PH), the time ( $t$ ) of pulse peak and integrated charge variables were defined like COPPER, but the integration ranges were different ( $Q$ : -5 to +5 samples,  $Q_w$ : -10 to +10 samples, and  $Q_{ww}$ : -10 to +25 samples around the position of the highest ADC value in the peak respectively).

### VT48

The VT48 recorded times of the hits in a time window from -3.6 to 4.4  $\mu$ s with respect to the pion timing  $t_{\pi^+}$  in B1. The hits in the Wire Chambers were converted to the hit position information. Based on the hit position at Wire Chambers and the Silicon Detectors (§4.2.2), incoming beam pion and outgoing decay positron tracks were reconstructed by fitting straight lines to hit positions. In case of multiple hits in the same detector plane, track candidates were constructed with all possible combinations of hits. For each reconstructed track,  $\chi^2$ , degrees of freedom, direction and position information were extracted.

### 4.2.3 Gain Correction

#### Scintillators

For all PMTs except the ones for CsI rings, gain calibration was based on the charge deposit by beam particles. The beam positron was used for the NaI, beam pion was used for B1 and B2, and beam muon was used for B3 and T1. All peaks of those beam particles were monitored every run to compare with a reference run. Due to the sizable position dependence of the signal height for T2, the calibration of T2's PMTs were performed using decay positrons from the  $\pi^+ \rightarrow \mu^+ \rightarrow e^+$  decay.

#### Silicon Strip Detector

A calibration pulser was connected to the amplifier of all silicon channels. In every run, the charge by pulser in each silicon detector was checked and compared to the reference run.

#### CsI

As described in §3.2.6, each CsI PMT was connected to the Xe lamp through the quartz fiber. The pulse height of the Xe lamp signals in each PMT was compared run by run to a reference run in order to correct for the PMTs gain fluctuation.

#### 4.2.4 Energy Calibration

##### Scintillators and Silicon Strip Detectors

The energy calibration was based on the amount of energy deposit by a minimum ionizing particle (beam positron) traversing a scintillator or a silicon sensor. The energy loss of beam positron was calculated by a MC simulation with a Geant4 package.

The energies in plastic scintillators were calibrated so that the mean value of  $Q$  from COPPER became to the same as the value calculated by the MC. The energies in S1–3 and CsI were calculated by using the variable  $Q$  from VF48.

The energy in the NaI was calibrated by using  $Q_{\text{ww}}$  from VF48 for 2010 data set. As for the data set of 2011 and after that, the energy deposit from the NaI was evaluated by the pulse height instead of  $Q_{\text{ww}}$  in order to reduce the pileup effect. Figure 4.2 shows the typical waveform with pileup hit event in the NaI. If the energy calibration was based on the integration of the waveform, the ADC counts of second pulse was also counted in the integration. On the other hand, only the first pulse in Figure 4.2 was took into account for the energy calculation if the pulse height based evaluation was taken. Figure 4.3 shows the decay positron energy spectrum with  $Q_{\text{ww}}$  and the pulse height based evaluation for the NaI. The pileup events above 70 MeV were reduced by 35%. Figure 4.4 shows the comparison of energy spectrum in the NaI between data and MC. The precision of the calibration for the  $\pi^+ \rightarrow e^+ \nu_e$  peak was less than 0.1 MeV.

##### CsI Calibration

The energy from each CsI crystal was calibrated using cosmic rays. The observed peak of energy deposit by the cosmic ray was compared to the predicted value by the MC simulation using CRY package [71]. The CRY package specializes in the generation of the cosmic-ray particle. Figure 4.5 shows the comparison of energy between data and simulation for the inner upstream part. The charge deposit in each CsI crystal was converted to the energy deposit by using a multiplicative factor  $f$

$$f = \frac{\Delta E_{\text{MC}}^{\text{Cosmic}}}{\Delta Q_{\text{Data}}^{\text{Cosmic}}} \frac{Q_{\text{Data}}[\text{Xe}_{\text{ref}}]}{Q_{\text{Data}}[\text{Xe}]}, \quad (4.1)$$

where  $\Delta E_{\text{MC}}^{\text{Cosmic}}$  is the peak position of the energy deposit obtained by MC,  $\Delta Q_{\text{Data}}^{\text{Cosmic}}$  is the charge deposit from the Cosmic trigger,  $Q_{\text{Data}}[\text{Xe}_{\text{ref}}]$  is the reference charge of Xe lamp trigger event, and  $Q_{\text{Data}}[\text{Xe}]$  is the charge of Xe lamp trigger event for each run.

The precision of the energy calibration in the calorimeters (NaI plus CsI) was better than 0.1 MeV.

## 4.2. WAVEFORM CALIBRATION

---

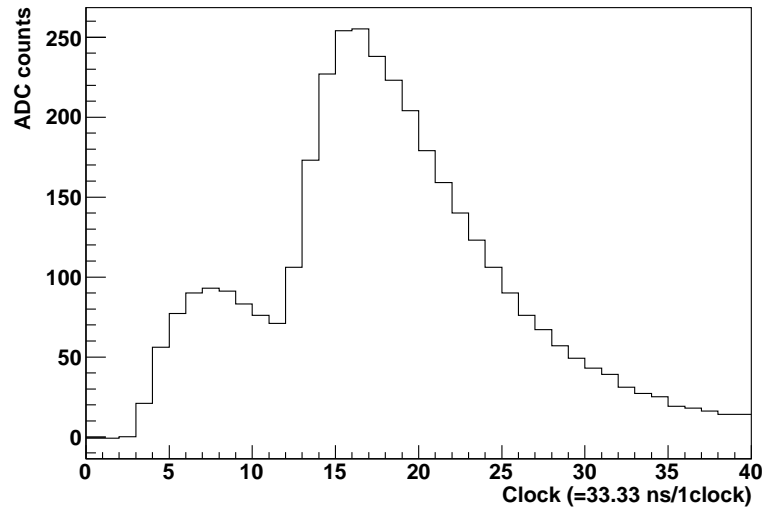


Figure 4.2: A typical waveform of the NaI with the pileup hit. The first smaller pulse was decay positron from pion decay, and the second larger pulse was due to the background.

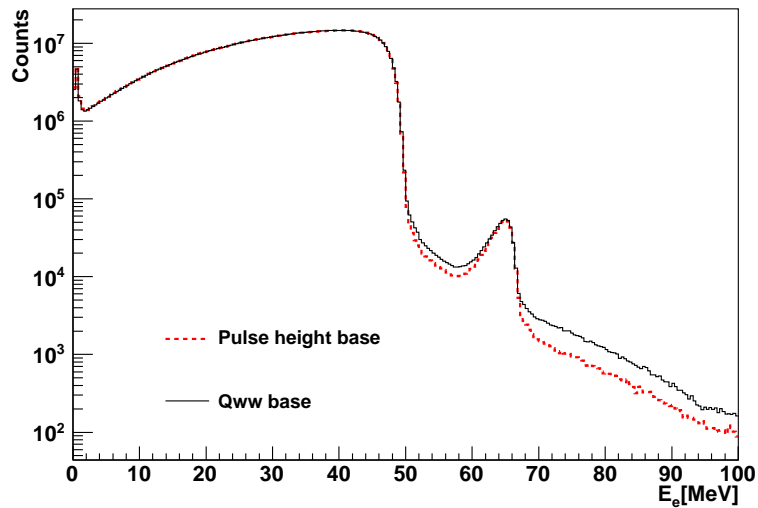


Figure 4.3: Decay positron energy spectrum. Dashed red histogram represents pulse height based evaluation and black histogram indicates  $Q_{ww}$  based evaluation.

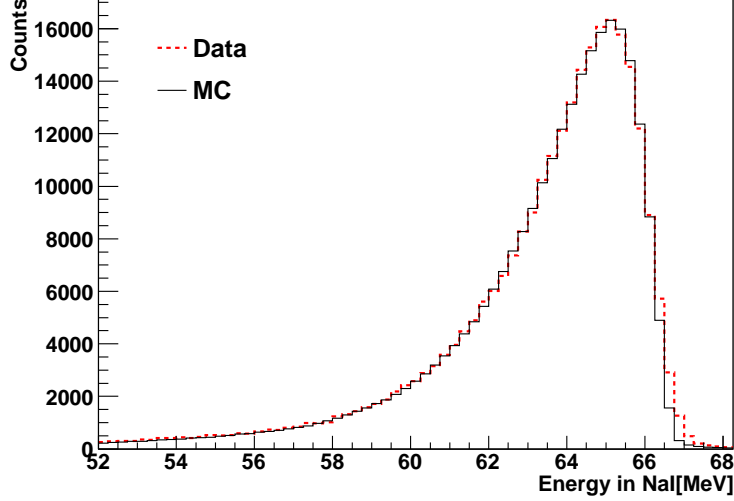


Figure 4.4:  $\pi^+ \rightarrow e^+ \nu_e$  energy spectra in the NaI. Dashed red histogram is data with  $\pi^+ \rightarrow \mu^+ \rightarrow e^+$  suppression cuts and black histogram is MC simulated events. Data is in good agreement with MC spectrum.

### 4.3 Event Mask for Blind Analysis

A blind analysis is widely known as an important method to reduce possible biases in analysis. Especially, the impact of human conscious or unconscious bias cannot be neglected in high precision experiments. A famous example that shows a need for blind analysis is the history of neutron lifetime measurements as shown in Figure 4.6. The remarkably good agreement of the central value for subsequent experimental results (around 1990) might indicate the presence of a bias.

The way of blind analysis greatly depends on the experiment. Additionally, the blinding procedure shouldn't artificially hide or create new systematic effects.

In the PIENU experiment, the energy information in the target was used to blind the value of  $R_{\text{raw}}^\pi$ . Figure 4.7 shows the schematic of the blind method in the PIENU experiment. A smooth stepping function with hidden efficiency was used to remove  $\pi^+ \rightarrow e^+ \nu_e$  and  $\pi^+ \rightarrow \mu^+ \rightarrow e^+$  events. Since  $\pi^+ \rightarrow e^+ \nu_e$  and  $\pi^+ \rightarrow \mu^+ \rightarrow e^+$  events were randomly rejected with different efficiencies,  $R_{\text{raw}}^\pi$  was changed without distortion on the time spectrum and energy spectrum. This inefficiency factor was produced by a uniform random number within the size of 0.5% for the 2011 data set. The position of the edge of the stepping function was aligned at the position of “valley” between  $\pi^+ \rightarrow e^+ \nu_e$  and  $\pi^+ \rightarrow \mu^+ \nu_\mu$  peaks so that the edge should be hidden under the statistical fluctuation of the low statistics region. This blind method

### 4.3. EVENT MASK FOR BLIND ANALYSIS

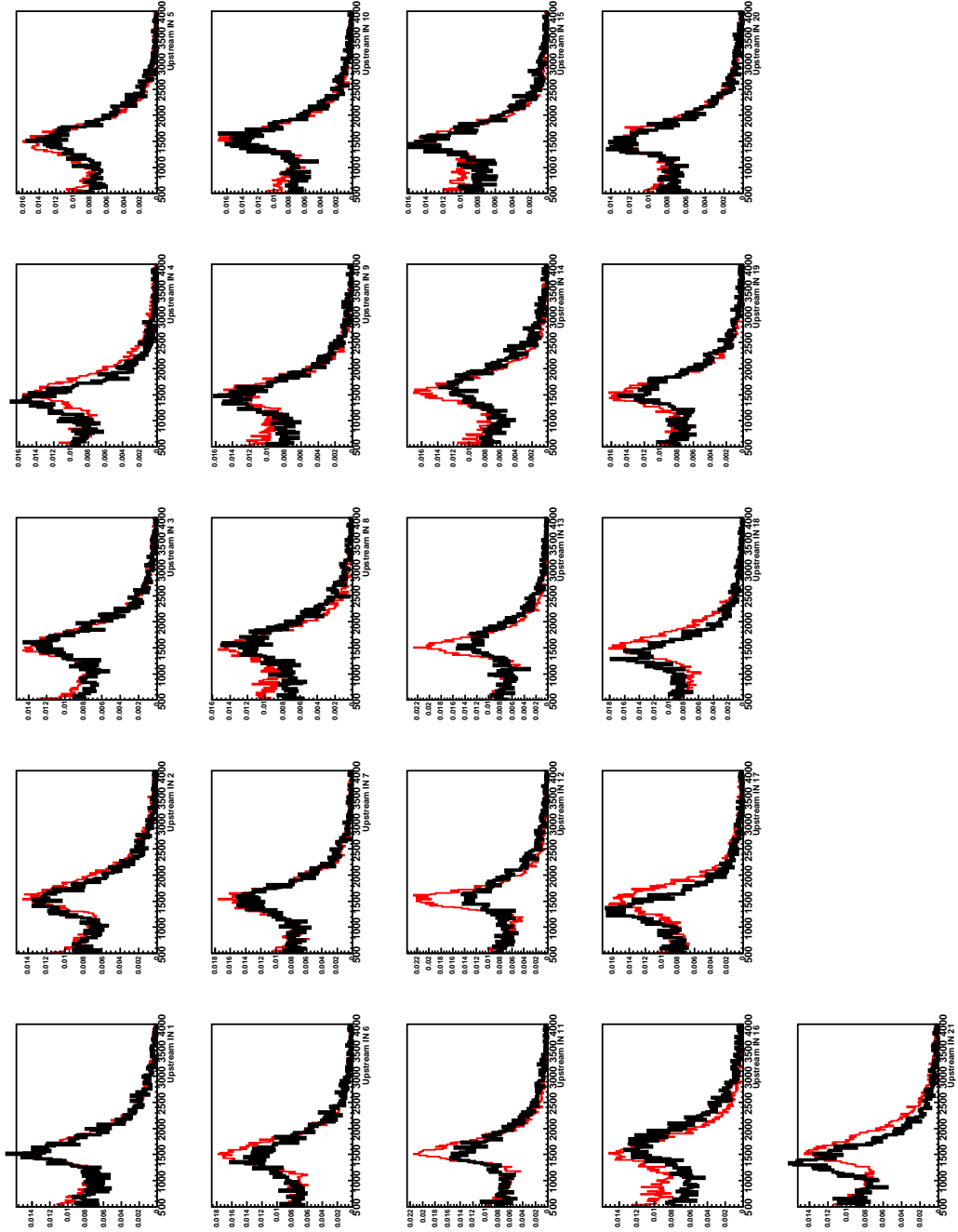


Figure 4.5: Comparison of the cosmic signal in each CsI crystal of the inner upstream part between data (black) and MC (red). Horizontal axes are ADC counts.

#### 4.4. EVENT SELECTION

---

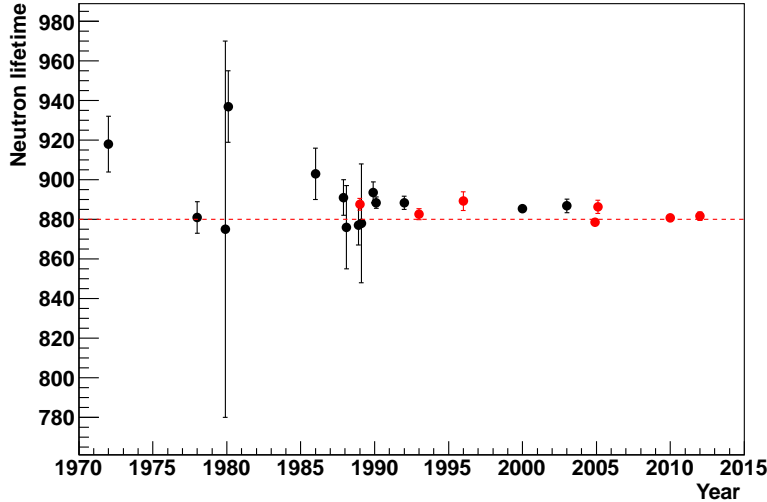


Figure 4.6: History of neutron lifetime measurement experiments [16]. Dashed red line indicates the current average. The points shown by filled red circle are used for the average.

was applied to pion data set before event selection and “unblind analysis” should not be done until all systematics are entirely evaluated. The blind analysis was also performed for 2010 data set with the same method. The event selection cuts for the time spectrum analysis are described in the next sections.

#### 4.4 Event Selection

The important thing for event selection is that the possible bias on  $R_{\text{raw}}^{\pi}$  should be avoid. Therefore, the energy or pulse fit information from positron-detection counters (B3, S3, T1, T2, NaI and CsI) was not used for event selection with a few exceptions. The exceptions were a proton cut (§4.4.2) and B1-B2 consistency cut (§4.4.3); the effects of these cut conditions were small to be neglected.

For the event selection, beam pion and decay positron selection cuts were applied. Since the beam rate was about 75 kHz, many beam pileup events occurred. Thus, the single hit in the counters were also required. The timings in the counters were also checked for the consistency of the trigger timing. Additionally, information of the downstream trackers were used to reconstruct the trajectory of decay positrons.

Unless otherwise specified, time, charge, and number of hits derived from waveforms of COPPER were used for event selection cuts, and figures were

#### 4.4. EVENT SELECTION

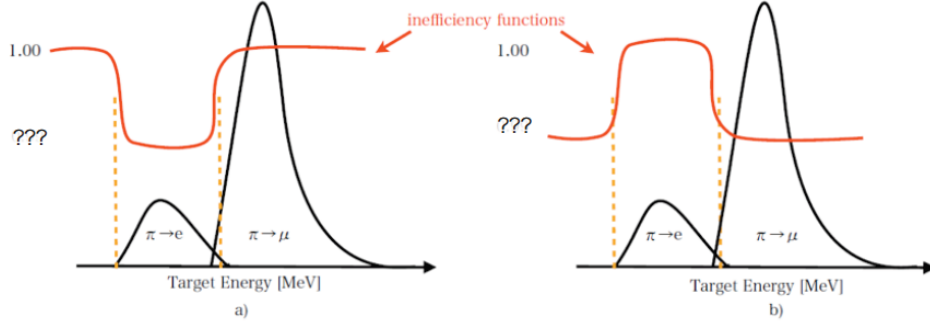


Figure 4.7: Blinding technique for the PIENU experiment [3]. A smooth inefficiency function removed events based on energy deposited in the target. Case a) lowered  $R_{\text{raw}}^\pi$  from the actual value while case b) raised.

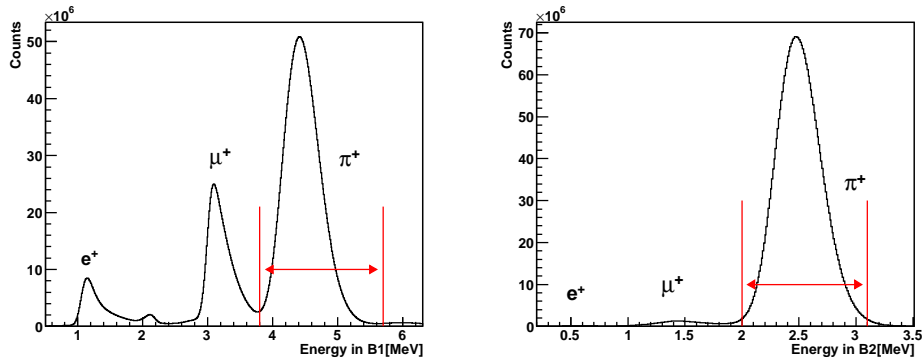


Figure 4.8: Energy deposit in B1 (left) and B2 (right, after the beam pion selection in B1). The regions between two vertical red lines in left and right were accepted as good pion events.

produced from 2011 data set.

##### 4.4.1 Beam Pion Selection

The beam pions were selected by their energy loss in B1 and B2. Figure 4.8 shows energy deposit in B1 and B2, and event selection regions. Additionally, the firing of “physics trigger” (TIGC, Early or Prescale) without calibration trigger (cosmic, beam positrons, Xe lamp) was required.

The beam profile in WC1 and WC2 was used to remove particles with unusual trajectories. Figure 4.9 shows beam profile of WC1 and WC2 with event selection conditions.

#### 4.4. EVENT SELECTION

---

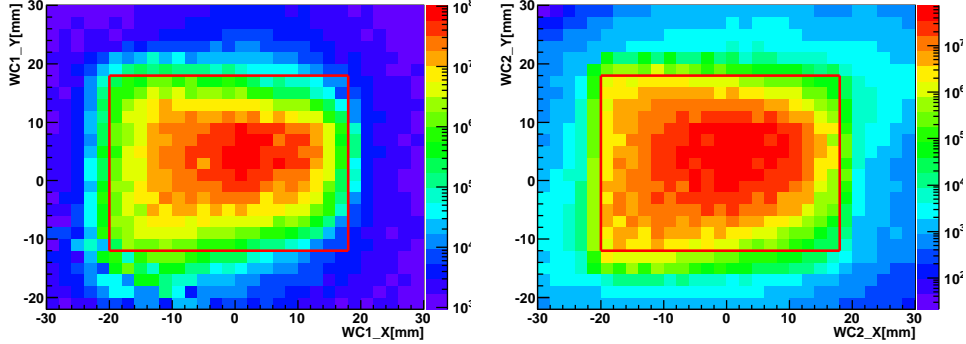


Figure 4.9: Contour plot of the beam profile of WC1 (left) and WC2 (right, after WC1 cut). The red boxes indicate the event selected regions.

#### 4.4.2 Decay Positron Selection

In order to reject prompt events (mostly muons from  $\pi$ DIF events which stopped in T1, and remaining beam muons or beam positrons survived the pion selection cuts), events which had T1 pulse in coincidence with the pion timing were removed. This cut was applied with VT48 signals.

Protons extending to  $\sim 100$  MeV were produced by beam pions via ( $\pi^+$ ,  $p^+$ ) reactions in B3. Since protons deposit a large amount of energy in the downstream counters, they were easily identified from the minimum-ionizing positrons. Figure 4.10 shows the correlation between the minimum  $dE/dx$  in the downstream counters (S3, T1, T2) and energy deposit in the NaI. Because decay positrons could undergo Bhabha scattering in the counters to produce rather higher energy deposit, the minimum  $dE/dx$  in three counters was used for the proton rejection. The potential bias produced by this cut was  $< 1 \times 10^{-8}$  in  $R_{\text{raw}}^\pi$ , which was small enough to be neglected.

The time spectrum of decay positrons below 52 MeV with pion and decay positron selection cuts described above is shown by a black histogram in Figure 4.11. The drop at  $t = 0$  is due to the prompt event cut by VT48. The decay time was extracted from the time difference between T1 and B1. The spikes with 43 ns cycle in the spectrum are due to the pileup of the beam pions and beam positrons. Those events were removed as will be described in the next section.

#### 4.4.3 Background Rejection

##### Pileup Cut

Figure 4.12 shows the number of hits in B1, B2, and T1 in the Signal-region (Figure 4.1). In order to reject pileup events, those counters should be required to have a single hit. However, sometimes those signals had a

#### 4.4. EVENT SELECTION

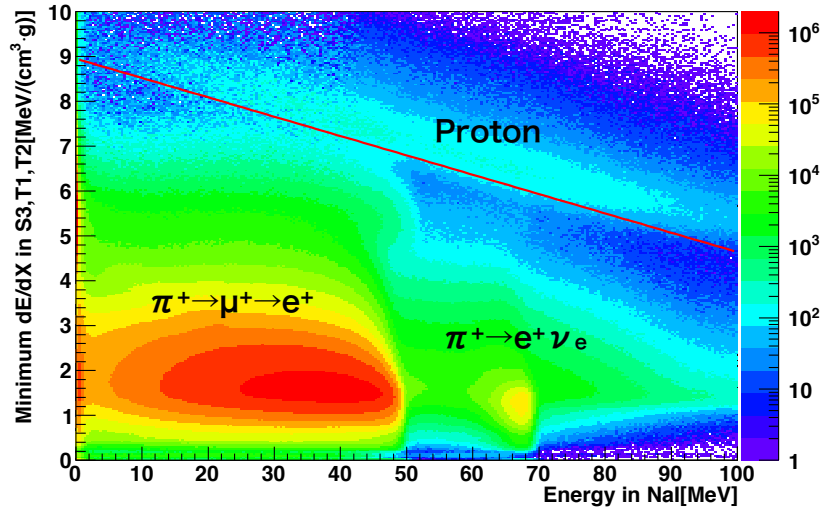


Figure 4.10: Energy in the NaI versus minimum energy loss in the downstream counters. Heavy red line indicates the cut position.

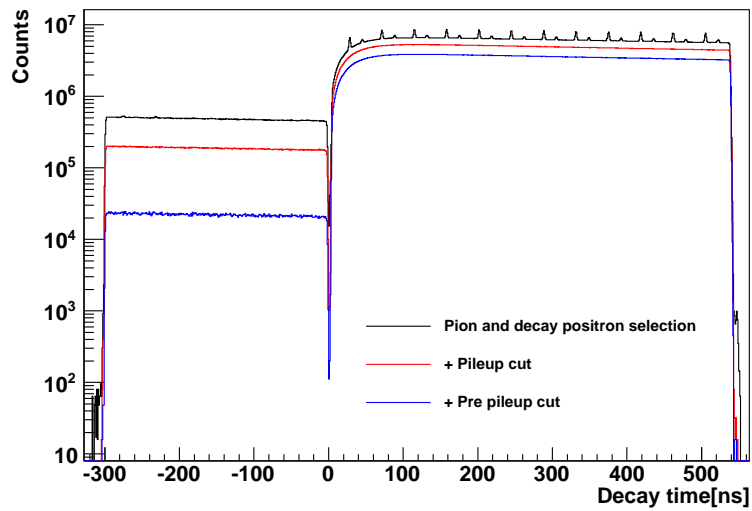


Figure 4.11: Time spectra below 52 MeV region with the pion and decay positron selection cuts (black), plus pileup cut (red), and plus pre pileup cut (blue).

#### 4.4. EVENT SELECTION

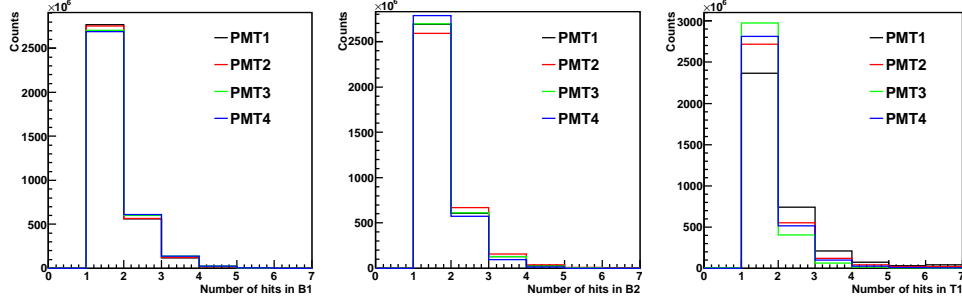


Figure 4.12: The number of hits in B1 (left), B2(center), and T1(right). The legends indicate the PMT number.

second pulse due to electrical noise or reflection. In order to avoid those fake pileup, each counter was required that at least one PMT had only a single hit in the Signal-region not to be rejected. Using pulse shape information for T1 produced the positron-energy dependence on the event selection and thus affected  $R_{\text{raw}}^{\pi}$ , so only the number of hits information was used for the pileup cut.

T2 counter should also be required to have the same type of a pileup cut, but signals from its PMTs had large position dependent due to its read-out design (Figure 3.9). Requiring a single hit for each PMT may introduce unwanted position dependence inefficiency. Thus, the analog sum information of T2's 4 PMTs was used for pileup cut. The events with an extra hit after more than 100 ns from the first pulse in the Signal-region were rejected. More than 100 ns of time difference was required to reduce the accidental rejection coming from electric noises in the analog sum signal. The summary of the cuts discussed here is shown below ( $N_{\text{Sig}}^{\text{Name}}$ : the number of hits in each counter, e.g. B1\_1 represents PMT1 in B1,  $N_{\text{Sig}}^{\text{T2sum}}$ : the number of hits in the analog sum of PMT1,2,3 and 4).

$$\begin{aligned}
 \text{B1} & : \{(N_{\text{Sig}}^{\text{B1-1}} == 1) \cup (N_{\text{Sig}}^{\text{B1-2}} == 1) \cup (N_{\text{Sig}}^{\text{B1-3}} == 1) \cup (N_{\text{Sig}}^{\text{B1-4}} == 1)\} \\
 \text{B2} & : \{(N_{\text{Sig}}^{\text{B2-1}} == 1) \cup (N_{\text{Sig}}^{\text{B2-2}} == 1) \cup (N_{\text{Sig}}^{\text{B2-3}} == 1) \cup (N_{\text{Sig}}^{\text{B2-4}} == 1)\} \\
 \text{T1} & : \{(N_{\text{Sig}}^{\text{T1-1}} == 1) \cup (N_{\text{Sig}}^{\text{T1-2}} == 1) \cup (N_{\text{Sig}}^{\text{T1-3}} == 1) \cup (N_{\text{Sig}}^{\text{T1-4}} == 1)\} \\
 \text{T2} & : N_{\text{Sig}}^{\text{T2sum}} == 1 \text{ (with 100 ns artificial multi pulse separation)}.
 \end{aligned}$$

In order to avoid a potential bias, the energy information of T1 and T2 was not used for the pileup cut.

#### Charge Ratio Cut

When the pileup occurred very close to the first pulse, those events were not rejected by the pileup cut described above. This type of pileup events

#### 4.4. EVENT SELECTION

---

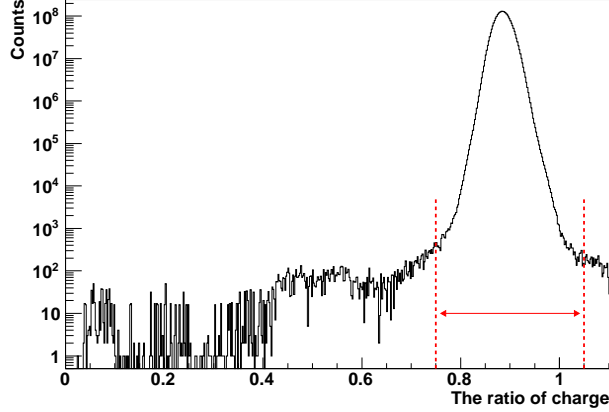


Figure 4.13: The ratio of charge  $Q/Q_w$  for PMT1 in B1. The events between the dashed red lines were accepted as good pion events.

could be eliminated using the charge ratio  $Q/Q_w$ . Figure 4.13 shows  $Q/Q_w$  distributions of PMT1 in B1. No-pileup condition was defined as the event with  $0.75 < Q/Q_w < 1.05$ , and was required for all hits in the Signal-Region of all PMTs of B1 and B2. The time spectrum after the number of hits and the ratio of charge cuts below 52 MeV is shown by a red histogram in Figure 4.11.

#### Pre Pileup Cut

In order to reject stopped-muon background from the beam or decay of beam pion (“old-muon”), all plastic scintillators were required that there was no hit in Pre-region. The time spectrum below 52 MeV after pre pileup cuts is shown by a blue histogram in Figure 4.11. Compared to the red histogram in Figure 4.11, the events in  $t < 0$  region (old-muons) were reduced to  $\sim 14\%$ .

#### Timing Consistency

The pulse timing in B1 should be consistent with trigger timing. Figure 4.14 shows the time of first pulse in B1-PMT1.

Additionally, the time difference between T1 and T2 was also checked in order to avoid accidental pileup events which decay positron fired T1 and missed T2 but background particle (e.g. decay positron from old-muon) hits T2 without firing T1 (or the inverse case). Figure 4.15 shows the time difference between T1 and T2 recorded by VT48.

#### 4.4. EVENT SELECTION

---

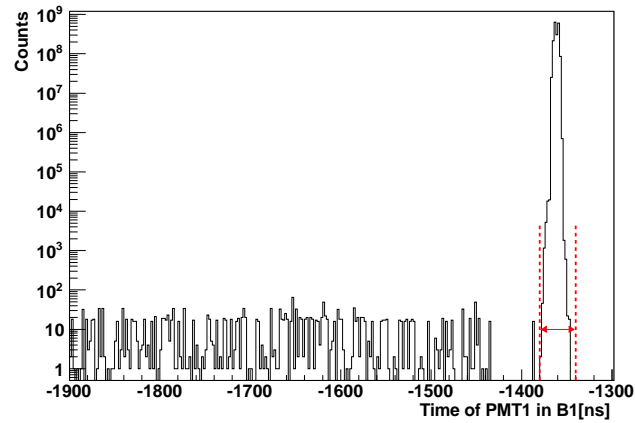


Figure 4.14: The time of the first pulse in B1-PMT1. The events between two dashed lines were accepted as good events.

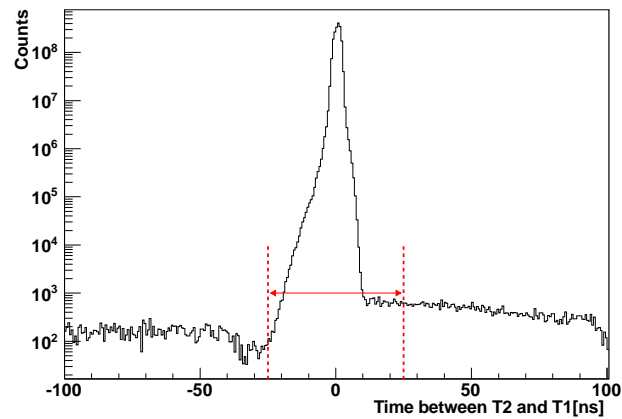


Figure 4.15: The time difference between T2 and T1 (VT48 signals). The events between two dashed lines were accepted as good events.

#### 4.4. EVENT SELECTION

---

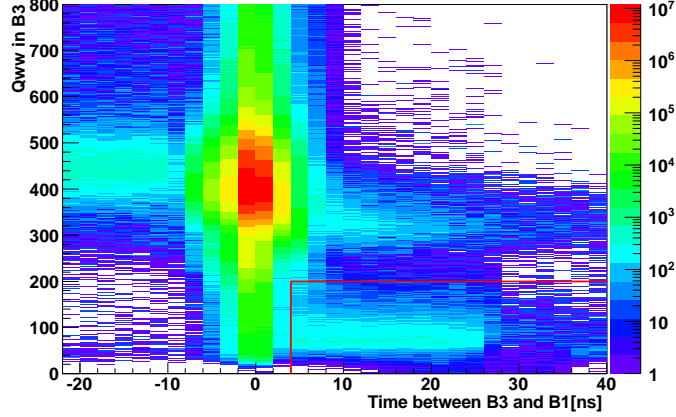


Figure 4.16: Time difference between B3 and B1 vs  $Q_{\text{ww}}$  in B3. The events surrounded by the red lines were removed.

#### B1-B2 Consistency Cut

Sometimes beam pion stopped in B2 due to range straggling, low momentum beam pion, or  $\pi$ DIF events. If those events occur within the coincidence window of B1, B2, and B3, this fake trigger was accepted. However, they can be removed since the energy deposit in B3 by decay positron was smaller than that of  $\pi$ DAR event. Figure 4.16 shows the correlation plot for  $Q_{\text{ww}}$  variable in B3 and time difference between B3 and B1.

The energy cut in B3 largely depended on  $R_{\text{raw}}^{\pi}$ , so the minimum energy cut in B3 was used for the event selection cut.

#### 4.4.4 Acceptance Cut

A radial acceptance cut in WC3 using tracks reconstructed with S3 and WC3 was used to ensure that the decay positrons hit all the downstream counters and to reduce shower leakage from the NaI. A tight radial acceptance cut leads less low-energy  $\pi^+ \rightarrow e^+ \nu_e$  events but large loss of statistics. Considering those arguments, the radial cut was set to be 60 mm for 2010 and 2011 data sets. The radial distribution at WC3 is shown in Figure 4.17.

In case of multiple tracks, the track with the smallest radial value was used to define the acceptance.

#### 4.4.5 Summary of the Selection Cuts

About 75% of the events were removed by the event selection cuts discussed above. The major cuts were the pion selection cuts, the pileup cuts, and the pre pileup cuts. The combination of those three cuts rejected about 50% of all the events. The acceptance cut after all other cuts removed about 30%

## 4.5. TIME SPECTRUM ANALYSIS

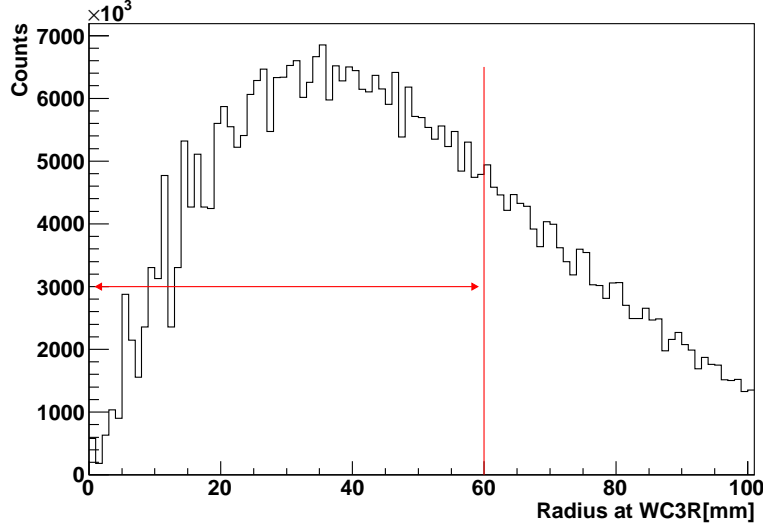


Figure 4.17: Reconstructed radial acceptance distribution at WC3. The events with radius less than 60 mm (red line) were selected. The spikes of this distribution are due to the resolution of WC3 wire pitch.

of the remaining events. Table 4.1 is a summary of the event selection cuts with the ratio of event reduction.

## 4.5 Time Spectrum Analysis

Figure 4.18 is the total energy spectrum of the NaI and CsI for physics trigger data after all event selection cuts were applied. It shows the  $\pi^+ \rightarrow e^+ \nu_e$  peak at 65.5 MeV and the continuous spectrum of  $\pi^+ \rightarrow \mu^+ \rightarrow e^+$  decays below 52 MeV. The raw ratio of  $\pi^+ \rightarrow e^+ \nu_e(\gamma)$  to  $\pi^+ \rightarrow \mu^+ \nu_\mu(\gamma)$  was extracted by performing a simultaneous fit of the time spectra to  $\pi^+ \rightarrow e^+ \nu_e$  energy region and  $\pi^+ \rightarrow \mu^+ \rightarrow e^+$  energy region using an energy threshold ( $E_{\text{cut}}$ ) at 52 MeV. The events below  $E_{\text{cut}}$  were triggered by Prescale trigger and Early trigger, and the events above  $E_{\text{cut}}$  were triggered by TIGC trigger. In the region below  $E_{\text{cut}}$ , the events with the decay time of  $6 < t < 46$  ns were triggered by Early trigger, and the events outside of this region were triggered by Prescale trigger. When the time and energy spectra were produced, the events produced by using Prescale trigger were scaled by a factor of 16.

Figure 4.19 and 4.20 respectively show the fitted time spectra for 2010 and 2011 data sets. Decay time was obtained based on the timings of fitted pulses in B1 and T1.

## 4.5. TIME SPECTRUM ANALYSIS

---

Table 4.1: Event selection cuts and their ratio of residual fraction. Each fraction of the cuts is differential to the previous cut. Total event-survival ratio represents the ratio of the number of events before and after applying all the event selection cuts.

Selection cut	Ratio before and after event selection cut(%)
Pion selection	77.51
Decay positron selection	96.28
Pileup cut	76.40
Charge ratio	99.99
Pre pileup cut	73.15
Timing consistency	99.74
Decay at B2	99.72
Acceptance cut	69.32
Total event-survival	25.86

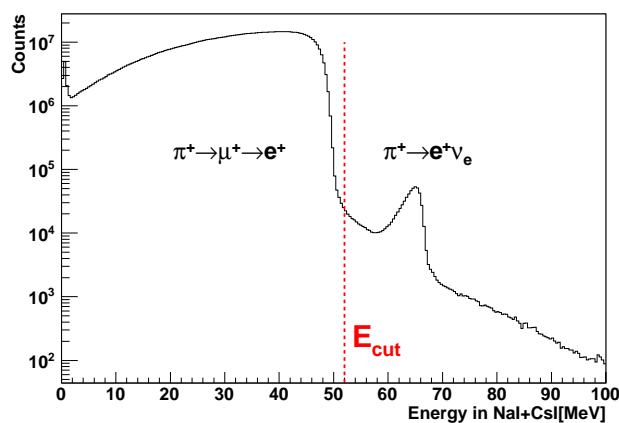


Figure 4.18: Combined energy spectrum of the NaI plus CsI detectors. The vertical red line indicates the  $E_{\text{cut}}=52$  MeV.

#### 4.5. TIME SPECTRUM ANALYSIS

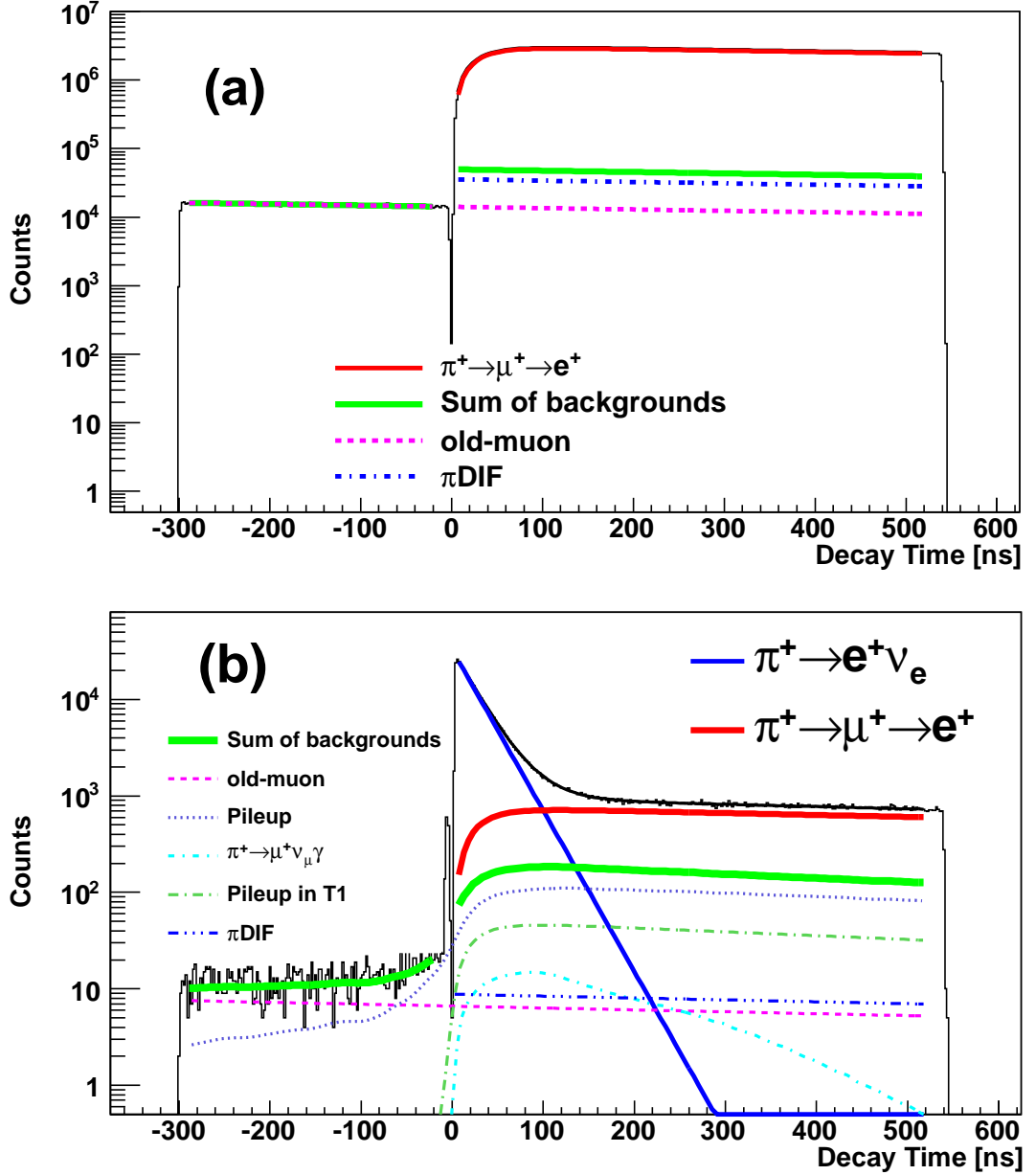


Figure 4.19: Time spectra in the low- (a) and high- (b) energy regions on 2010 data set. Horizontal axes show decay times extracted from the time difference between T1 and B1. The solid red lines in the low- and high-energy regions represent  $\pi^+ \rightarrow \mu^+ \rightarrow e^+$  decays and the solid blue lines in high-energy region shows  $\pi^+ \rightarrow e^+ \nu_e$  decays. Other lines indicate background components and the solid green lines in both regions are the sums of the background components (see text for details).

#### 4.5. TIME SPECTRUM ANALYSIS

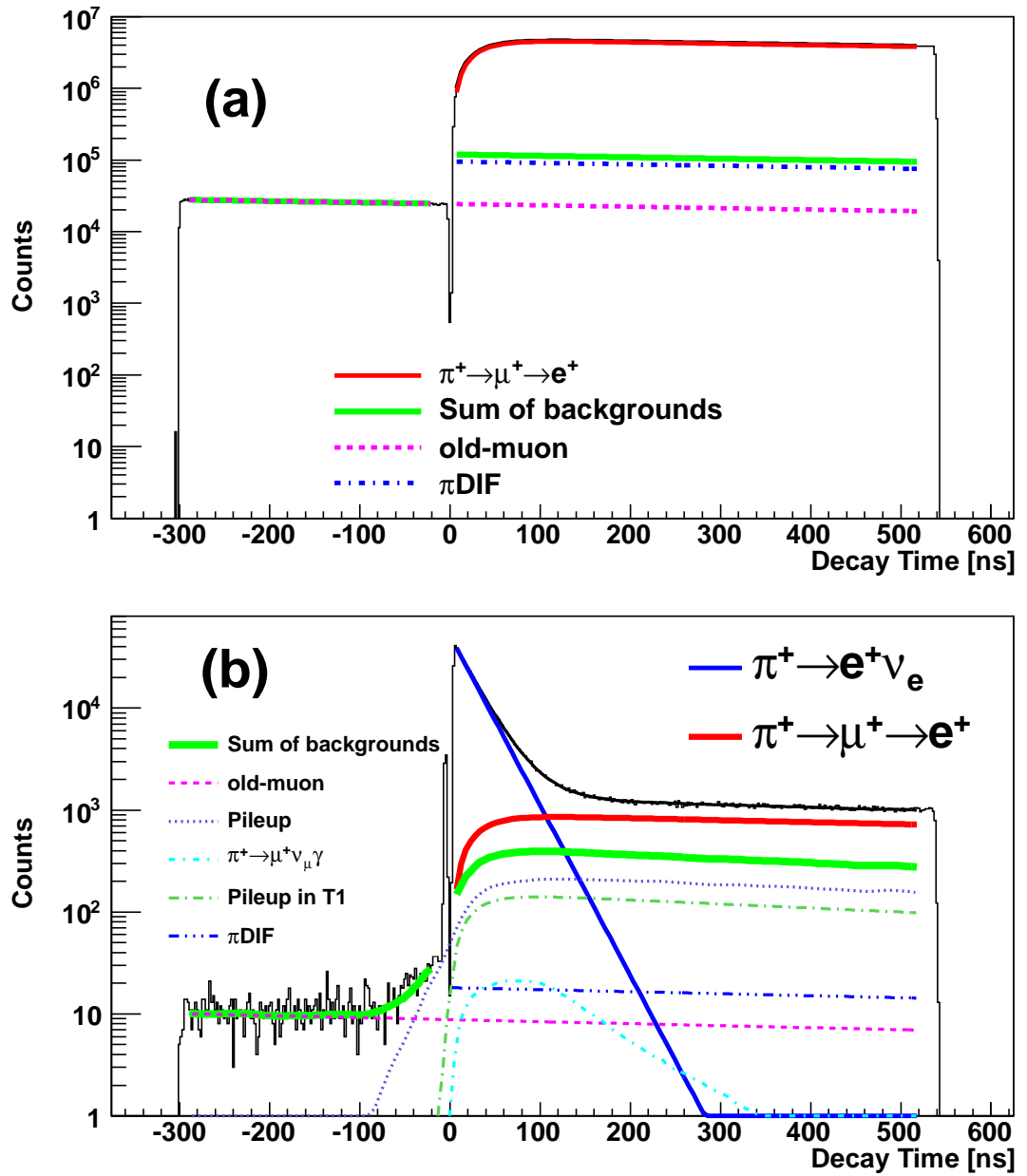


Figure 4.20: Time spectra in the low- (a) and high- (b) energy regions on 2011 data set.

## 4.5. TIME SPECTRUM ANALYSIS

---

### 4.5.1 Low-Energy Time Spectrum

The events in the low-energy region ( $E_{\text{cut}} \leq 52$  MeV) were triggered by the Prescale trigger and Early trigger. The events triggered by Early trigger were not only  $\pi^+ \rightarrow e^+ \nu_e$  events, but also the  $\pi^+ \rightarrow \mu^+ \rightarrow e^+$  events. Because the efficiency of Early trigger was mostly 100%,  $\pi^+ \rightarrow \mu^+ \rightarrow e^+$  events decayed in 6 to 46 ns were triggered by Early trigger and the boundary between Early trigger and Prescale trigger was not distorted. Compared to the time spectrum using only Prescale trigger, the combination of these trigger reduced the statistical uncertainty on  $R_{\text{raw}}^\pi$  about 10%. The variation of  $R_{\text{raw}}^\pi$  between time spectrum with only Prescale trigger and the combined triggers was  $< 1 \times 10^{-8}$ .

In the low-energy time spectrum, the components included were  $\pi^+ \rightarrow \mu^+ \rightarrow e^+$  decays (Eq. (2.2)) and muon decays arising from  $\pi$ DIF (about 2% of  $\pi^+ \rightarrow \mu^+ \rightarrow e^+$ ) and old-muon in B3 (Eq. (2.4)). The  $\pi^+ \rightarrow \mu^+ \rightarrow e^+$  and  $\pi$ DIF distributions begin at time  $t = 0$ . The solid red lines, dashed dark blue lines, and dashed pink lines in Figure 4.19 (a) and 4.20 (a) indicate  $\pi^+ \rightarrow \mu^+ \rightarrow e^+$ ,  $\pi$ DIF, and old-muon decays, respectively. The time spectrum components coming from multiple muon decays and low-energy tail of  $\pi^+ \rightarrow e^+ \nu_e$  decays were estimated to contribute to be less than  $10^{-8}$  to  $R_{\text{raw}}^\pi$ , thus were neglected in the time fit analysis.

### 4.5.2 High-Energy Time Spectrum

The events in the high-energy region ( $E_{\text{cut}} > 52$  MeV) were produced by using TIGC trigger. The main component in the high-energy time spectrum was due to the  $\pi^+ \rightarrow e^+ \nu_e$  decays (Eq. (2.1)), which were represented by blue lines in Figure 4.19 (b) and 4.20 (b). The major backgrounds were muon decays ( $\pi^+ \rightarrow \mu^+ \rightarrow e^+$ ,  $\pi$ DIF, and old-muons) which were promoted to the high-energy time spectrum by the energy resolutions of the NaI and CsI crystals, radiative muon decays in which the  $\gamma$ -ray increases the apparent positron energy, and pileup events in the calorimeter with a flat time distribution (e.g. due to neutrons coming from the production target). The  $\pi^+ \rightarrow \mu^+ \rightarrow e^+$ ,  $\pi$ DIF, and old-muon decays in the high-energy region are shown as the solid red lines, the dashed dark blue lines, and the dashed pink lines in Figure 4.19 (b) and 4.20 (b). The shapes of the time distribution of these components are the same as ones in the low-energy region. The time spectra from  $\pi^+ \rightarrow \mu^+ \nu_\mu \gamma$ , calorimeter pileup and T1 pileup existed only in the high-energy region. Details of these components will be described below.

#### $\pi^+ \rightarrow \mu^+ \nu_\mu \gamma$ Decays

$\pi^+ \rightarrow \mu^+ \nu_\mu \gamma$  component was produced by the decay branching ratio  $2 \times 10^{-4}$  (Table 1.3) followed by  $\mu^+ \rightarrow e^+ \nu_e \bar{\nu}_\mu$  decays. This distribution ( $\mathcal{G}$ ) is shown

## 4.5. TIME SPECTRUM ANALYSIS

---

as the long dashed and short dashed light blue curves in Figure 4.19 (b) and 4.19 (b). The timing of the  $\gamma$  is the same as the timing of the pion decay, while the timing of the decay positron is the same as the timing of the muon decay from  $\pi^+ \rightarrow \mu^+ \nu_\mu$ . The recorded region of the waveforms for the NaI and CsI crystals were determined by decay positron timing in T1 and T2 because VF48 modules were triggered by the timing in T1 and T2. Thus, if the  $\gamma$ -ray from this decay hits the calorimeter, it looks like a “pre pileup” event. This contribution was estimated by MC simulation using a waveform template for the NaI and CsI detectors. Figure 4.21 shows the result of the simulation. When the decay timing of the pion was very close to the decay timing of the muon, the two pulses by  $\gamma$  and decay positron were piled up in the calorimeters. If the decay timing of the muon was far from the decay timing of the pion, the two pulses by  $\gamma$  and decay positron were separate each other. Therefore, as the decay timing of the muon delayed compared to the decay timing of the pion, the contribution from  $\gamma$  was gradually getting small.

MC study showed that the fraction of the  $\pi^+ \rightarrow \mu^+ \nu_\mu \gamma$  events with  $E_{\text{cut}} > 52$  MeV in all  $\pi^+ \rightarrow \mu^+ \rightarrow e^+$  decays were respectively  $48.8 \times 10^{-8}$  for 2010 data set, and  $32.3 \times 10^{-8}$  for 2011 data set. These fractions were used as fixed parameters in the fitting function. The uncertainty of the fractions mainly came from the energy calibration in the NaI and CsI, and the error of the branching ratio of  $\pi^+ \rightarrow \mu^+ \nu_\mu \gamma$ . The uncertainty of the fractions were conservatively estimated by changing the amplitude by  $\pm 20\%$ . The variation of  $R_{\text{raw}}^\pi$  for 2011 data set was  $2.9 \times 10^{-8}$ . This was not negligible size, so it was included in the systematic uncertainty of the time fit. Detail of the systematic uncertainty of the time fit will be discussed in the following section.

### Pileup in the Calorimeters

The distributions shown by the dashed violet line in the high-energy region in Figure 4.19 (b) and 4.20 (b) which increase as approaching  $t = 0$  in the  $t < 0$  region and decrease in the  $t > 0$  region are the pileup component of  $\pi^+ \rightarrow \mu^+ \rightarrow e^+$  plus old-muon decays. When one decay positron made a T1-T2 trigger and the other decay positron did not hit T1 nor T2, the pileup cut (§4.4.3) did not work, and this pileup event was accepted. The shape of time spectrum for this background was obtained by MC simulation using the pulse shapes of the NaI and CsI detectors with the same pileup cut and trigger requirement as the data. Figure 4.22 shows such obtained time spectra. The amplitude of this component was a free parameter in the fitting function, represented by  $\mathcal{F}_1$ .

#### 4.5. TIME SPECTRUM ANALYSIS

---

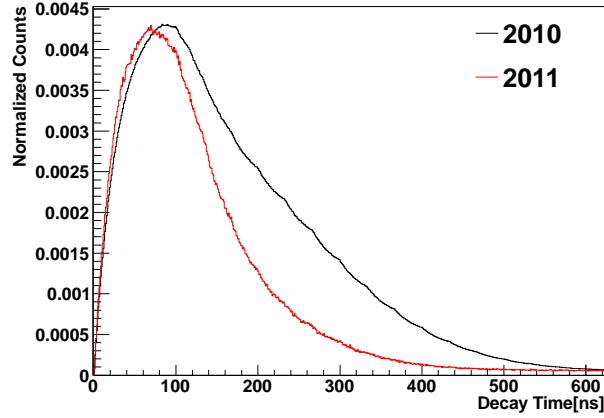


Figure 4.21: Simulated  $\pi^+ \rightarrow \mu^+ \nu_\mu \gamma$  time distributions above  $E_{\text{cut}} = 52$  MeV. Black histogram indicates the 2010 shape and red histogram shows the 2011 shape. Since the method of energy calibration for the NaI was modified on 2011 data set, the contribution of  $\pi^+ \rightarrow \mu^+ \nu_\mu \gamma$  was reduced.

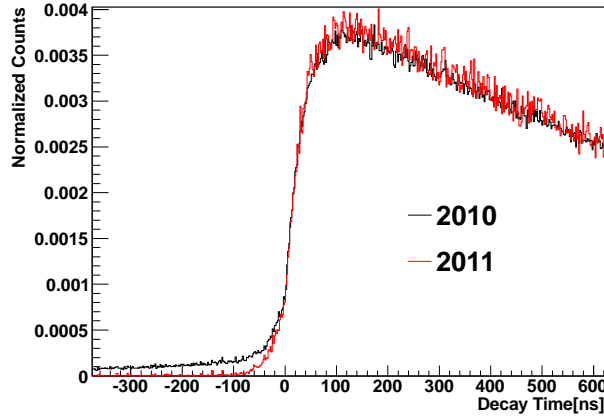


Figure 4.22: Simulated time distributions of pileup events above  $E_{\text{cut}} = 52$  MeV. Black histogram indicates the 2010 shape and red histogram shows the 2011 data. The contribution of the pileup events for 2011 data set is less than that of 2010 data set because the different variable was used for the NaI in each data set.

### Pileup in T1

The pileup cut in T1 was based on the number-of-hits information (§4.4.3). If extra hits were observed in T1, the events were rejected. However, if two hits occurring within the double pulse resolution time of T1 ( $\Delta T \sim 15$  ns), this event was accepted. The shape of time spectrum for these pileup events was the same as that for the pileup in the calorimeters described above but with shorter effective time constant  $\Delta T$ .

Those pileup events can be categorized into two cases; the first case was that the electron timing was made by decay positron from old-muon decay (case A), and the second case was that decay positron from  $\pi^+ \rightarrow \mu^+ \rightarrow e^+$  event first issued T1 and T2 (case B). The function of case A can be written using  $\Delta T$  as

$$\mathcal{F}_{2A}(t) = \begin{cases} 0 & t < -\Delta T \\ \frac{\exp(-\frac{t}{\tau_\mu})}{\tau_\mu} \int_0^{t+\Delta T} \frac{\exp(-\frac{y}{\tau_\mu}) - \exp(-\frac{y}{\tau_\pi})}{\tau_\mu - \tau_\pi} dy & -\Delta T < t < 0 \\ \frac{\exp(-\frac{t}{\tau_\mu})}{\tau_\mu} \int_t^{t+\Delta T} \frac{\exp(-\frac{y}{\tau_\mu}) - \exp(-\frac{y}{\tau_\pi})}{\tau_\mu - \tau_\pi} dy & t > 0 \end{cases} \quad (4.2)$$

and case B can be represented as

$$\mathcal{F}_{2B}(t) = \begin{cases} 0 & t < 0 \\ \frac{\exp(-\frac{t}{\tau_\mu}) - \exp(-\frac{t}{\tau_\pi})}{\tau_\mu - \tau_\pi} \int_t^{t+\Delta T} \frac{\exp(-\frac{y}{\tau_\mu})}{\tau_\mu} dy & t > 0 \end{cases} \quad (4.3)$$

The effect of pileup coming within the double pulse resolution time in T1 was estimated by artificially increasing the double pulse resolution time up to 100 ns. Figure 4.23 shows the time spectrum of the pileup events for the case of 100 ns double pulse resolution, and the time distribution of the pileup events was fitted to the Eqs. 4.2, 4.3, and 2.4. The amplitudes of Eqs. 4.2 and 4.3 should be the same magnitude, therefore a common amplitude for the fitting parameter was used for the fit.

The amplitude of the case A and B can be normalized to the amplitude of old-muons. To estimate the relation between the number of old-muons and the number of the pileup events in T1, the pre pileup cut was relaxed. As shown in Figure 4.1, the lower edge of Pre-region was defined at -7750 ns. In order to relax the pre pileup cut, this edge was gradually moved up to -3500 ns. Figure 4.24 shows the result of the number of pileup events (case A + B) at each  $\Delta T$  with a relaxed pre pileup edge. The plots shown in Figure 4.24 were fitted to the quadratic functions. In theoretical estimation, the relation between the number of pileup events and  $\Delta T$  was linear. However, because of the same reason as  $\pi^+ \rightarrow \mu^+ \nu_\mu \gamma$  decay, as the timing of the second decay positron delayed compared to the timing of the first decay positron, the contribution from the second decay positron was gradually getting smaller. Therefore, the actual relation between between the number

## 4.5. TIME SPECTRUM ANALYSIS

---

of pileup events and  $\Delta T$  was quadratic. The extrapolation to the given  $\Delta T$  provides the estimation of the numbers of the pileup events (absolute values of the intercepts in Figure 4.24) for that  $\Delta T$ . As shown in Figure 4.25, the numbers of pileup events are scaled to the numbers of the old-muon events.

Those components were represented as  $\mathcal{F}_2 (= \mathcal{F}_{2A} + \mathcal{F}_{2B})$  in the fitting function for the high-energy time spectrum. The weight of  $\mathcal{F}_{2A}$  is the same weight with  $\mathcal{F}_{2B}$ . The amplitude of  $\mathcal{F}_2$  was scaled to the number of old-muons ( $b$ ) with the parameters obtained by the fit shown in Figure 4.25;  $1.428 \times 10^{-3} \cdot b + 4493$ , and included into the fitting function for the high-energy time spectrum. The effect of the uncertainties for the parameters was  $\Delta R_{\text{raw}}^\pi = 1.9 \times 10^{-8}$  for 2011 data, which was included in the systematic uncertainty of the time fit, see §4.5.5 for detail.

The same procedure was performed on 2010 data set [4], and the amplitude of the pileup scaled to the old-muons ( $b$ ) was  $8.722 \times 10^{-4} \cdot b + 181$ .

An actual  $\Delta T$  was estimated by using the observed deficit after the main hit in the time distribution of T1. Figure 4.26 shows the time distribution of T1 hits seen by PMT2. The position of the edge of the second hit distribution was obtained by fitting the edge to a step function with Gaussian resolution represented,

$$\frac{1}{2} \left\{ 1 + \operatorname{erf} \left( \frac{t - \Delta T}{\sqrt{2}\sigma} \right) \right\}, \quad (4.4)$$

where  $\operatorname{erf}(t)$  is

$$\operatorname{erf}(t) = \frac{2}{\sqrt{\pi}} \int_0^t e^{-x^2} dx. \quad (4.5)$$

The result of the fit showed that the average of four PMTs is  $\Delta T = 15.8$  ns. The effect of uncertainty with  $\Delta T$  was conservatively estimated by changing the value by  $\pm 1.2$  ns. The variation of  $R_{\text{raw}}^\pi$  was about  $0.1 \times 10^{-8}$ , which was negligible.

### 4.5.3 The Fitting Function

The fitting functions to the time spectra including all the components described above in the low- ( $\phi_{\text{low}}(t)$ ) and high- ( $\phi_{\text{high}}(t)$ ) energy regions are:

$$\begin{aligned} \phi_{\text{low}}(t) = & \mathcal{H}(t) \left[ a(1-r)\varepsilon_{\pi \rightarrow \mu \rightarrow e}(t) + b\varepsilon(t)_{\mu \rightarrow e\nu_e\bar{\nu}_\mu} \right] \\ & + c\varepsilon(t)_{\mu \rightarrow e\nu_e\bar{\nu}_\mu} \end{aligned} \quad (4.6)$$

$$\begin{aligned} \phi_{\text{high}}(t) = & \mathcal{H}(t) \left[ a \left\{ (R_{\text{raw}}^\pi + C_{\mu\text{DIF}})\varepsilon(t)_{\pi \rightarrow e\nu} + d\mathcal{G}(t) + r\varepsilon_{\pi \rightarrow \mu \rightarrow e}(t) \right\} \right. \\ & \left. + b'\varepsilon(t)_{\mu \rightarrow e\nu_e\bar{\nu}_\mu} \right] + c'\varepsilon(t)_{\mu \rightarrow e\nu_e\bar{\nu}_\mu} + e\mathcal{F}_1 + f\mathcal{F}_2 \end{aligned} \quad (4.7)$$

#### 4.5. TIME SPECTRUM ANALYSIS

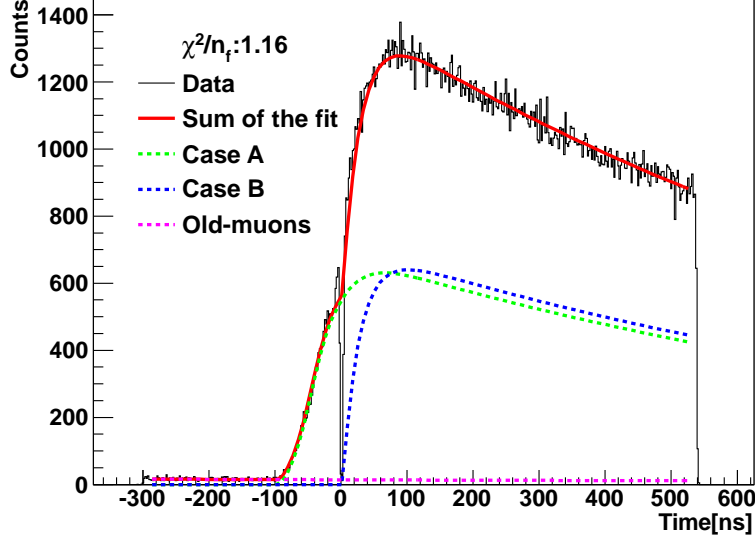


Figure 4.23: Pileup events with fitting functions. The artificial  $\Delta T$  was 100 ns and the lower edge of Pre-region was at -5500ns.

where  $\mathcal{H}(t)$  is the Heaviside step function ( $\mathcal{H}(t > 0) = 1$ ,  $\mathcal{H}(t < 0) = 0$ ), and  $\varepsilon(t)_{\pi \rightarrow e\nu}$ ,  $\varepsilon_{\pi \rightarrow \mu \rightarrow e}(t)$ , and  $\varepsilon(t)_{\mu \rightarrow e\nu e\bar{\nu}_\mu}$  are the same functions as in Eq. (2.1), (2.2), and (2.4), and  $t = t' - t_0$  where  $t'$  is the measured time and  $t_0$  is the pion stop time which was determined by prompt events and was fixed in the fit. In Eqs. (4.6) and (4.7), the parameter  $a$  represents the number of  $\pi^+ \rightarrow \mu^+ \rightarrow e^+$  decays, and  $ar$  indicates the number of  $\pi^+ \rightarrow \mu^+ \rightarrow e^+$  decays in the high-energy region. The other parameters  $b$ ,  $b'$ ,  $c$ ,  $c'$ ,  $d$ ,  $e$ , and  $f$  are the amplitudes of each function. The free parameters were  $R$ ,  $a$ ,  $r$ ,  $b$ ,  $c$ ,  $c'$  and  $e$ . The parameters  $d$ ,  $f$ , and  $C_{\mu\text{DIF}}$  were fixed to the estimated values as described in the previous sections. However, the correlation between  $\pi\text{DIF}$  decays and old-muon decays or  $\mathcal{F}_1$  was significant. Therefore, the parameter  $b'$  was scaled to the amplitude of  $\pi\text{DIF}$  in the low-energy region; namely,  $b' = rb$ . The parameter  $C_{\mu\text{DIF}}$  was the corrected amplitude for  $\mu\text{DIF}$  events in the target, which will be discussed in §4.6.1. The fitting range was from -290 to 520 ns omitting the prompt region of -20 to 5 ns. The bin size for the low-energy spectrum and high-energy  $t > 0$  was 2 ns, while the bin size for the high-energy  $t < 0$  was chosen 10 ns due to the small statistics.

The residuals plot of all regions are shown in Figure 4.27 and 4.28. They show there was no structure on the time spectrum fit.  $\chi^2/n_d = 1.02$  ( $n_d = 673$ ) for 2010 and 1.22 for 2011 data sets. It is worth noting that the goodness of the fit was improved over the previous TRIUMF experiment ( $\chi^2/n_d = 1.47$ ). The parameters are shown in Table 4.2. Because the way of the energy cal-

#### 4.5. TIME SPECTRUM ANALYSIS

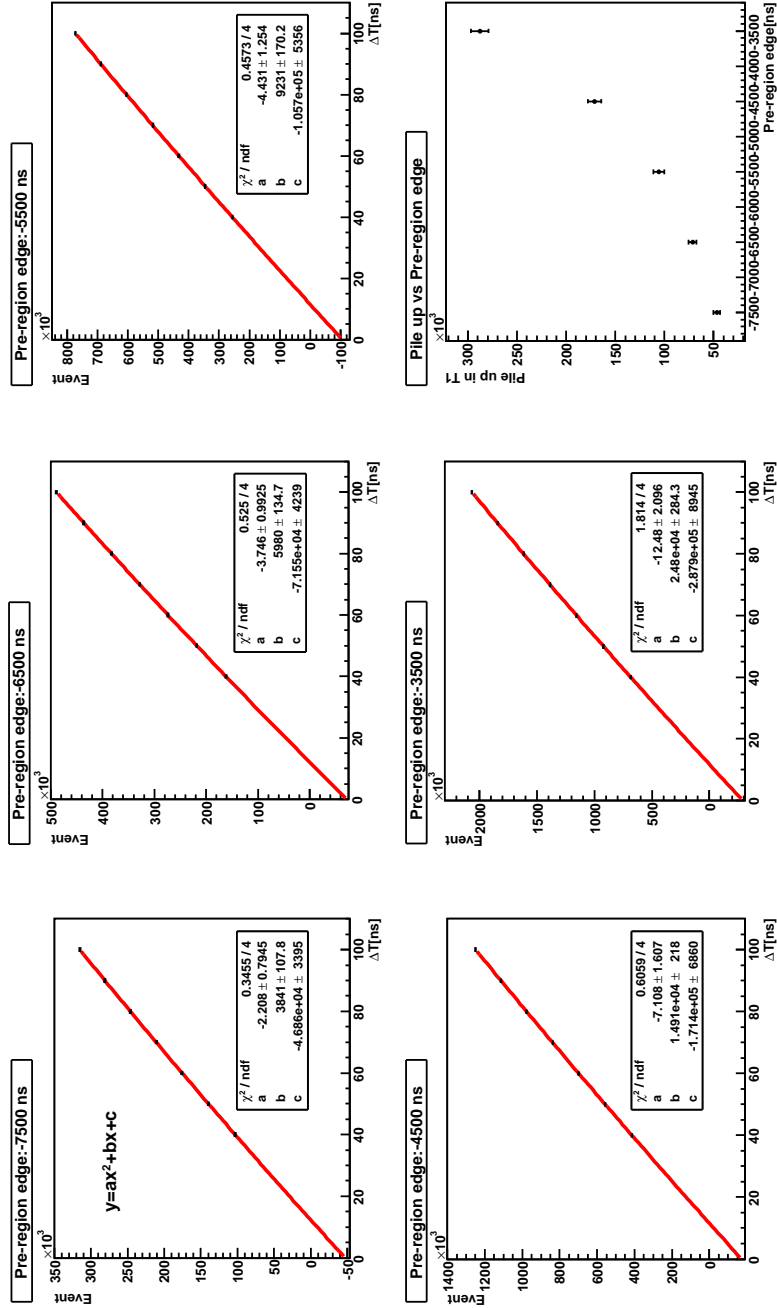


Figure 4.24: The result of the number of pileup events at each  $\Delta T$  with a relaxation of pre pileup cut. Black points show the number of pileup events (case A + B) obtained by fit as shown in Figure 4.23. Those points were fitted to the quadratic function (red curves). Bottom right shows the number of pileup events estimated by extrapolation (absolute values of the intercepts  $c$ ) versus the edge of Pre-region.

#### 4.5. TIME SPECTRUM ANALYSIS

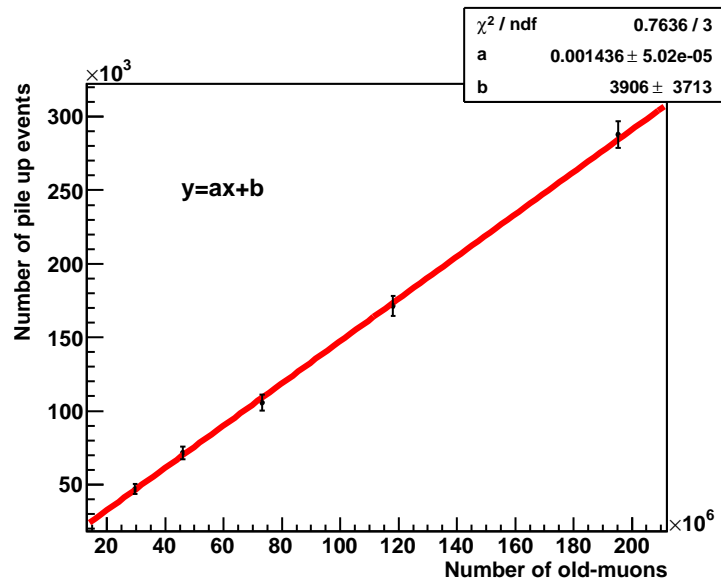


Figure 4.25: Number of pileup events versus old-muons. Those plots were fitted to the linear function, which was used for the fixed parameter of the fitting function for raw ratio extraction.

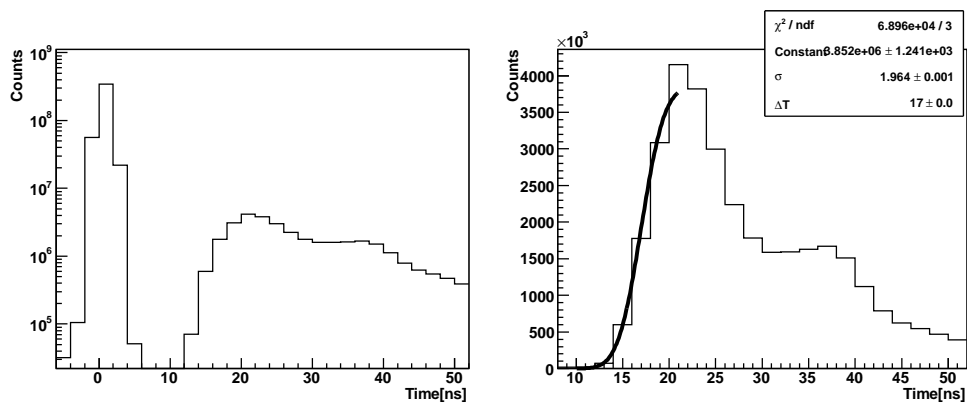


Figure 4.26: The extra hits time distributions in PMT2. Left: The main pulse and the extra hits shown by log scale in vertical axis. Right: Zoom-in of the extra hits time distribution fitted to a step function (black curve).

## 4.5. TIME SPECTRUM ANALYSIS

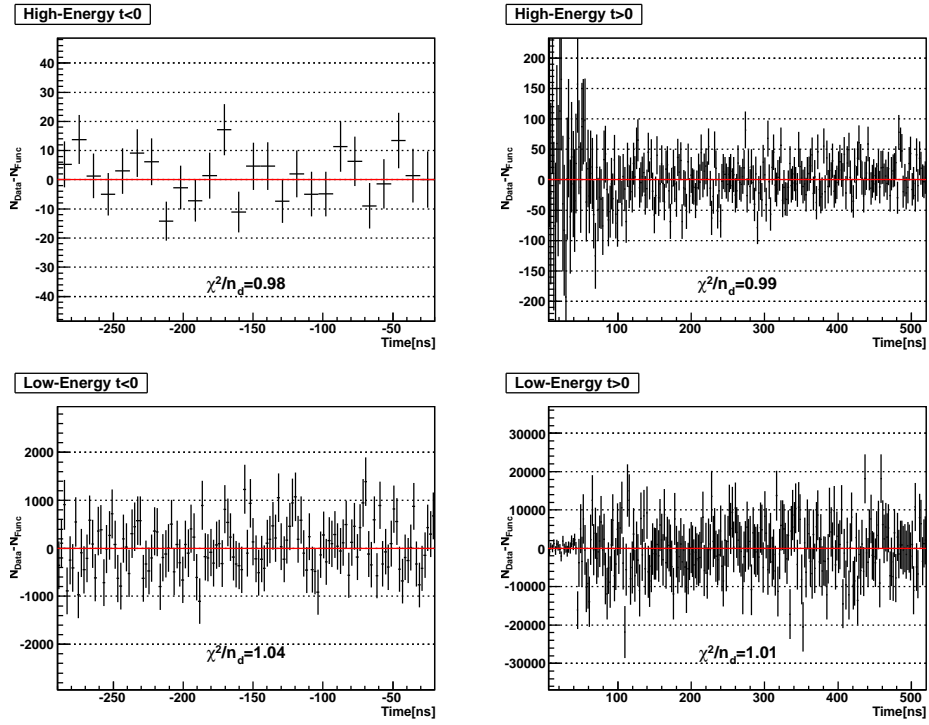


Figure 4.27: Residuals for 2010 data set. Top two residuals are high-energy time spectrum, while bottom two panels indicate the residuals in low-energy time spectrum. Left two panels show  $t < 0$  region while residuals in  $t > 0$  regions are shown in two right panels. Bin size for top left was 10 ns while other regions were 2 ns bin.

## 4.5. TIME SPECTRUM ANALYSIS

---

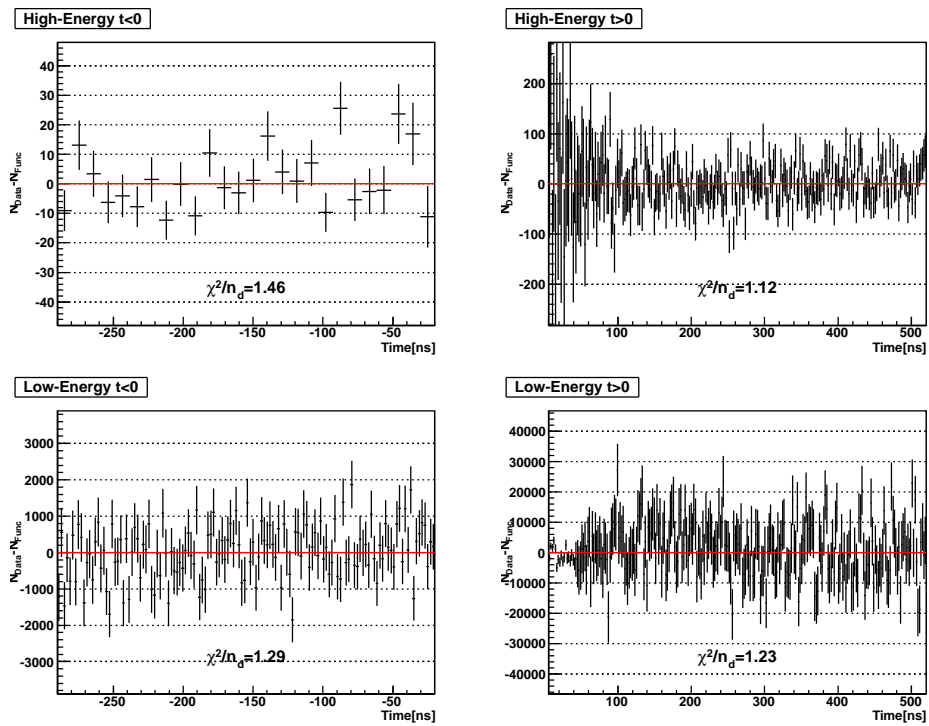


Figure 4.28: Residuals for 2011 data set. The place of each region is same as in Figure 4.27

#### 4.5. TIME SPECTRUM ANALYSIS

Table 4.2: Result of the fitting parameters for 2010 and 2011 data sets.  $R_{\text{raw}}^\pi$  for 2011 data set is still blinded, so it is represented by asterisks.

Parameter	Value (2010)	Value (2011)
$a$	$(3.2903 \pm 0.0010) \times 10^9$	$(5.1902 \pm 0.0011) \times 10^9$
$r$	$(2.458 \pm 0.047) \times 10^{-4}$	$(1.912 \pm 0.039) \times 10^{-4}$
$t_0$	1.68 ns	2.24 ns
$b$	$(3.821 \pm 0.067) \times 10^7$	$(1.055 \pm 0.069) \times 10^8$
$R_{\text{raw}}^\pi$	$(1.1971 \pm 0.0022) \times 10^{-4}$	$(1.*** \pm 0.0017) \times 10^{-4}$
$c$	$(1.533 \pm 0.004) \times 10^7$	$(2.670 \pm 0.006) \times 10^7$
$c'$	$(7.18 \pm 0.65) \times 10^3$	$(8.66 \pm 0.29) \times 10^3$
$d$	$48.8 \times 10^{-8}$	$32.3 \times 10^{-8}$
$e$	$(2.930 \pm 0.390) \times 10^4$	$(5.513 \pm 0.497) \times 10^4$
$f$	$8.722 \times 10^{-4} \cdot b + 181$	$1.428 \times 10^{-3} \cdot b + 4493$
$C_{\mu\text{DIF}}$	$20.71 \times 10^{-8}$	$18.99 \times 10^{-8}$

ibration in the NaI was modified, the contamination of  $\pi^+ \rightarrow \mu^+ \rightarrow e^+$  events in the high-energy region (parameter  $r$ ) was reduced.

#### 4.5.4 Stability of the Fit

The stability of  $R_{\text{raw}}^\pi$  is important to confirm the validity of the time-spectrum shapes or estimated amplitudes included as background components. Figure 4.29 shows the stability of the fit result against the variation of the lower edge of Pre-region. The stability of the fit without  $\mathcal{G}$  and  $\mathcal{F}_2$  is also shown with red symbols in order to demonstrate the effect of these components. When the all backgrounds were included,  $R_{\text{raw}}^\pi$  did not depend on the pre pileup cut. This confirms the correctness and validity of the components discussed in above sections.

#### 4.5.5 Systematic Errors of the Time Fit

The systematic uncertainty of the time fit was evaluated by changing the fitting range, bin size, lifetime of pion ( $\tau_\pi$ ) and muon ( $\tau_\mu$ ), additional background component, and fixed parameters of  $\mathcal{G}$  and  $\mathcal{F}_2$ .

The standard fitting range was from -290 ns to -20 ns for  $t < 0$  region, and from 5 ns to 520 ns for  $t > 0$  region. The systematic uncertainty came from the different fitting range was estimated by changing these values.

The standard bin size was 2 ns for low-energy and high-energy  $t > 0$  region, and was 10 ns for high-energy  $t < 0$  region. The effect of the different bin size was also checked.

The  $\tau_\pi$  and  $\tau_\mu$  were fixed to the PDG values [16] in the fit. The effect of the uncertainty from the lifetimes were conservatively evaluated by fixing

#### 4.5. TIME SPECTRUM ANALYSIS

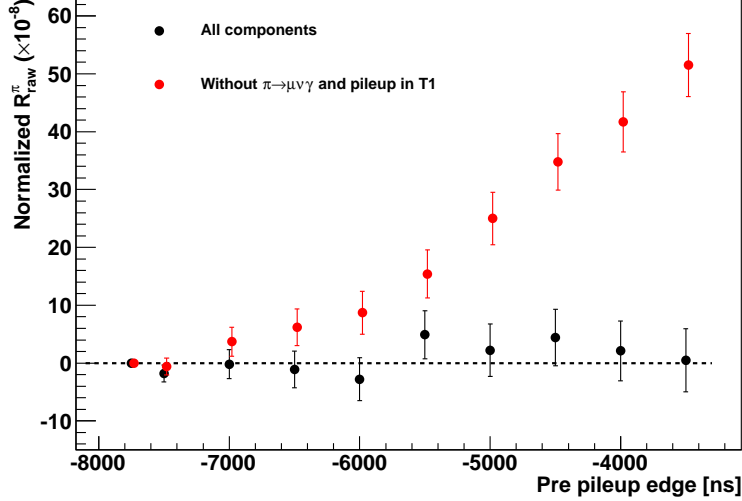


Figure 4.29: Stability plots of the pre pileup cut for the fit using all components (black) and the fit without the functions of  $\mathcal{G}$  and  $\mathcal{F}_2$ . The values of  $R_{\text{raw}}^\pi$  and the statistical errors were normalized to the value at -7750 ns.

the lifetime to the central value plus or minus 2 standard deviations of the lifetimes.

In order to check the possibility of yet unknown pileup events, the time distribution with the lifetime of  $\tau_\mu/2$  was added in the fit for the high-energy region with a free parameter. Additionally, the flat component was also included in the low- and high-energy regions.

The variations of  $R_{\text{raw}}^\pi$  came from the uncertainty of the parameters for  $\mathcal{G}$  and  $\mathcal{F}_2$  were already discussed in §4.5.2.

Table 4.3 shows the summary of the systematic errors. The variations of  $R_{\text{raw}}^\pi$  were observed by changing the fitting range, but those variations were within the statistical errors due to the shorter fitting range. Thus, there was no visible systematic effect from the different choices of the fitting range. The effect of the different choices of the bin size was estimated to be  $< 1 \times 10^{-8}$ . It was confirmed that the choice of the bin size was not significant systematic source.

The variations by the uncertainty of the muon lifetime was small to be negligible because the muon lifetime was precisely measured by another experiments<sup>1</sup>. While the effect of the uncertainty of the pion lifetime was  $1.1 \times 10^{-7}$  by changing the fixed value with 2 standard deviations.

The effect of the  $\tau_\mu/2$  component was estimated to be  $< 0.1 \times 10^{-8}$ . While the variation of  $R_{\text{raw}}^\pi$  by the flat component was  $5.0 \times 10^{-8}$ . This was

<sup>1</sup>The most precise muon lifetime is given by the result of MuLan group [72].

## 4.6. SYSTEMATIC CORRECTIONS TO RAW RATIO

Table 4.3: Summary of the systematic errors for 2011 data set.

Test	Variation of $R_{\text{raw}}^\pi$ (Unit: $\times 10^{-8}$ )
<b>Fitting range</b>	(Statistical fluctuations)
$t < 420$	2.4
$15 < t$	10.1
$t < -30$	0.4
$-250 < t$	0.2
<b>Bin size</b>	
Bin=1 ns	0.4
Bin=4 ns	0.2
Bin=2 ns for high-energy $t < 0$	0.5
<b>Lifetime</b> [16]	
$\tau_\mu = 2196.981 \pm 0.002$ ns	$< 0.1$
$\tau_\pi = 26.033 \pm 0.005$ ns	1.1
<b>Additional background</b>	
$\tau_\mu/2$ component	$< 0.1$
Flat component	5.0
<b>Fixed parameter</b>	(§4.5.2)
$d$ for $\mathcal{G}$	2.9
$f$ for $\mathcal{F}_2$	1.9

the largest effect because including the flat component largely correlated with old-muons or  $\pi$ DIF events.

The dominant sources came from the flat component, the lifetime of pion, and the uncertainties of fixed parameters. By taking the combination of these effects, the uncertainty of  $R_{\text{raw}}^\pi$  for 2011 data set  $\sigma_{\text{raw}}^{2011}$  is

$$\sigma_{\text{raw}}^{2011} = [\pm 0.0017(\text{stat}) \pm 0.0006(\text{syst})] \times 10^{-4}. \quad (4.8)$$

The uncertainties on  $R_{\text{raw}}^\pi$  for 2010 data set  $\sigma_{\text{raw}}^{2010}$  was estimated with the same procedure [4],

$$\sigma_{\text{raw}}^{2010} = [\pm 0.0022(\text{stat}) \pm 0.0006(\text{syst})] \times 10^{-4}. \quad (4.9)$$

The magnitude of the systematic uncertainty is the same with each other, and the statistical uncertainty on 2011 data set was improved due to the higher statistics.

## 4.6 Systematic Corrections to Raw Ratio

### 4.6.1 $\mu$ DIF Correction

As shown in Eq. 4.7, the contribution of  $\mu$ DIF was included in the fitting function. We here discuss how  $\mu$ DIF correction was estimated.

#### 4.6. SYSTEMATIC CORRECTIONS TO RAW RATIO

---

$\pi$ DAR followed by  $\mu$ DIF events in the target cannot be distinguished from  $\pi^+ \rightarrow e^+ \nu_e$  events due to the same time distributions. Figure 4.30 shows the muon decay time of  $\mu$ DIF events after pion decay at rest, obtained by MC. Due to Lorentz boost, the positron energy (Figure 4.31) was raised and  $\mu$ DIF events inflated the apparent number of  $\pi^+ \rightarrow e^+ \nu_e$  decays. The probability of muon going to  $\mu$ DIF can be approximated by

$$1 - \exp\left(-\frac{\tau_{\mu\text{DIF}}/\gamma}{\tau_{\mu}}\right) \sim 8 \times 10^{-6} \quad (4.10)$$

where  $\gamma = 1/\sqrt{1 - v^2/c^2} = 1.039$  for the muon kinetic energy of  $T_{\mu} = 4.1$  MeV,  $\tau_{\mu\text{DIF}}$  is the time that the muon travels before it stops (the maximum time:  $\tau_{\mu\text{DIF}} = 19$  ps as shown in Figure 4.30). This probability was evaluated using MC.

The contribution of  $\mu$ DIF events,  $C_{\mu\text{DIF}}$ , was estimated by MC. The fraction of positrons from  $\mu$ DIF above  $E_{\text{cut}} (= 52 \text{ MeV})$  to the number of all  $\mu$ DIF positrons was 2.374%. Therefore, the correction value  $C_{\mu\text{DIF}}$  was found to be

$$2.374 \times 10^{-2} \times 8 \times 10^{-6} = 18.99 \times 10^{-8}. \quad (4.11)$$

The correction value  $C_{\mu\text{DIF}}$  was included into Eq. (4.7) and scaled to the number of  $\pi^+ \rightarrow \mu^+ \rightarrow e^+$  decays (parameter  $a$ ).

The statistical uncertainty of the correction value was  $0.30 \times 10^{-8}$ . The systematic uncertainty of the correction value came from the energy calibration in the NaI and CsI at 52 MeV, and the discrepancy between data and MC. The energy calibration in the calorimeters was better than 0.1 MeV, and this translated into an error of  $0.58 \times 10^{-8}$ . The discrepancy between data and MC was evaluated from the difference in the energy-spectrum shape of the Michel decay at rest between data and MC. The Michel spectra of data and MC are shown in Figure 4.32 (left), and the difference between data and MC is shown in Figure 4.32 (center). The striking discrepancy was around 5 MeV with few % level. The energy spectrum of  $\mu$ DIF events was modified using this difference of Michel spectrum between data and MC (Figure 4.32 (right)). In order to avoid 511 keV peak and pileup events, the range of the modification was from 2 to 46 MeV. The difference of the correction value between the modified spectrum and the original spectrum was  $0.02 \times 10^{-8}$ .

The total uncertainty on  $C_{\mu\text{DIF}}$  is

$$\begin{aligned} \sigma_{\mu\text{DIF}} &= \sqrt{0.30^2 + 0.58^2 + 0.02^2} \times 10^{-8} \\ &= 0.64 \times 10^{-8} \end{aligned} \quad (4.12)$$

The variation of  $R_{\text{raw}}^{\pi}$  that came from the uncertainty of this correction was estimated to be less than  $10^{-8}$ .

$\mu$ DIF correction for 2010 data set was evaluated with the same procedure, but the beam momentum and the detector geometry were different

#### 4.6. SYSTEMATIC CORRECTIONS TO RAW RATIO

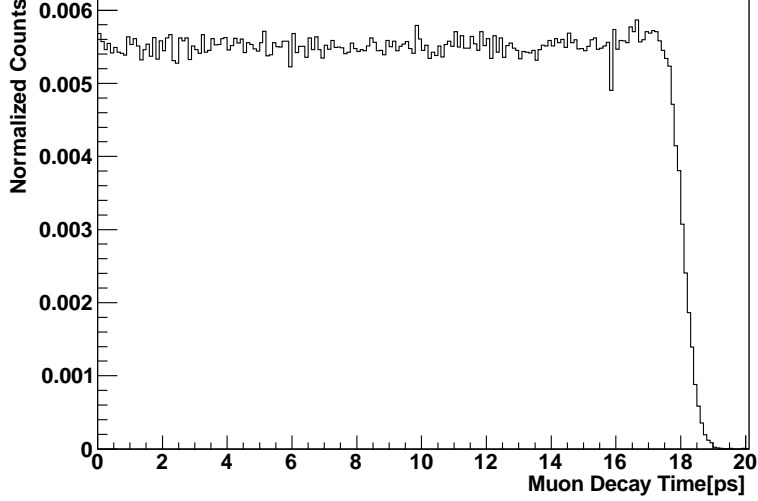


Figure 4.30: Simulated decay time of  $\mu$ DIF events after pion decay at rest in the target.

between 2010 and 2011, so the different MC was used for 2010 data set. The result of the  $\mu$ DIF correction for 2010 was  $C_{\mu\text{DIF}} = (20.71 \pm 0.66) \times 10^{-8}$  [4]. The variation of  $R_{\text{raw}}^{\pi}$  for 2010 data set that came from the uncertainty of this correction was also estimated to be less than  $10^{-8}$ .

#### 4.6.2 Energy Dependence on $t_0$

The timing of the decay positron was based on the signal from energy loss in T1. Because the energies of decay positrons were different between  $\pi^+ \rightarrow e^+ \nu_e$  and  $\pi^+ \rightarrow \mu^+ \rightarrow e^+$  decays. This difference might produce the difference in the T1 response time. The possible dependence between the pion stop time  $t_0$  and the decay positrons energy was studied using decay positrons from muons stopped at the center of B3.

First of all, the Michel energy spectrum obtained from muon data was sliced every 5 MeV up to 50 MeV. Second, the edge of the time distribution was fitted to a step function with a Gaussian resolution (Eq. 4.4) plus flat component. Third, the prompt timing  $t_0$  at each energy region was obtained. Black histogram in Figure 4.33 shows the zoom-in around  $t = 0$  for the decay positron time spectrum for  $0 \leq E_{\text{NaI+CsI}} < 5$  MeV. Red curve in Figure 4.33 shows the fitting function, which was the sum of a step function and flat component. The beam component for this data set was mostly muons plus small contamination of positrons. The beam positron contamination was removed by an energy cut in the sum of B1, B2, S1, S2, and B3 ( $= E_{\text{tot}}$ , in Figure 4.34). This procedure was repeated every 5 MeV up to 50 MeV.

#### 4.6. SYSTEMATIC CORRECTIONS TO RAW RATIO

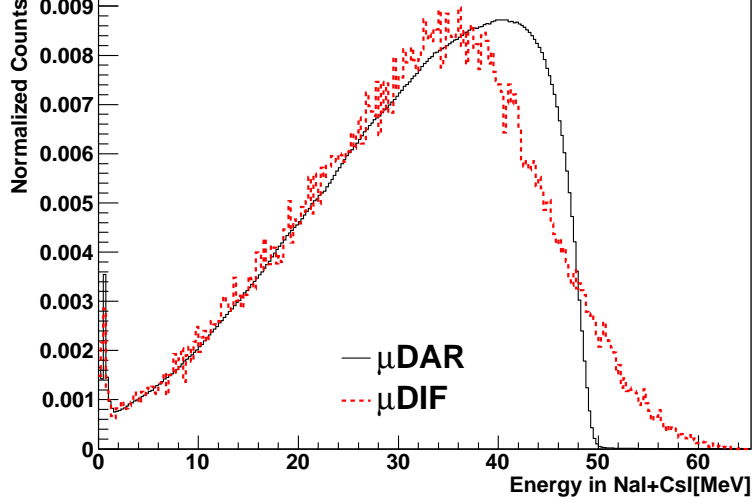


Figure 4.31: The energy spectra of  $\pi^+ \rightarrow \mu^+ \rightarrow e^+$  events measured by the NaI and CsI. Red: Simulated  $\mu$ DIF events. Black:  $\mu$ DAR events (standard  $\pi^+ \rightarrow \mu^+ \rightarrow e^+$  events) (2011 analysis).

Figure 4.35 shows the decay positrons energy dependence of  $t_0$  obtained by a step function fit. The red line shows the linear function. The  $t_0$  for  $\pi^+ \rightarrow e^+ \nu_e$  decays was evaluated from the result of a linear fit using the peak energy of  $\pi^+ \rightarrow e^+ \nu_e$  decays (65.5 MeV), and the  $t_0$  for  $\pi^+ \rightarrow \mu^+ \rightarrow e^+$  events were obtained by the weighted average of the plot shown in Figure 4.35. The systematic uncertainty was estimated by changing the bin size, the fitting range, and the energy loss cut in the counters. The difference of  $t_0$  between  $\pi^+ \rightarrow e^+ \nu_e$  and  $\pi^+ \rightarrow \mu^+ \rightarrow e^+$  events using 2011 data set was

$$\Delta t_0 = [0.017 \pm 0.009(\text{stat}) \pm 0.006(\text{syst})] \text{ ns (2011 data set)}. \quad (4.13)$$

The multiplicative correction value to  $R_{\text{raw}}^\pi$  came from  $\Delta t_0$  is

$$\begin{aligned} C_{t_0} &= \frac{\int_{-0.017 \pm 0.011}^{\infty} \exp(-t/\tau_\pi)}{\int_0^{\infty} \exp(-t/\tau_\pi)} \\ &= 1.0007 \pm 0.0004 \text{ (2011 data set)}. \end{aligned} \quad (4.14)$$

The analysis of 2010 data set was also performed using the same procedure, and the  $\Delta t_0$  and correction value  $C_{t_0}$  were estimated to be [4]

$$\Delta t_0 = [0.012 \pm 0.011(\text{stat}) \pm 0.08(\text{syst})] \text{ ns (2010 data set)} \quad (4.15)$$

$$C_{t_0} = 1.0004 \pm 0.0005 \text{ (2010 data set)}. \quad (4.16)$$

#### 4.6. SYSTEMATIC CORRECTIONS TO RAW RATIO

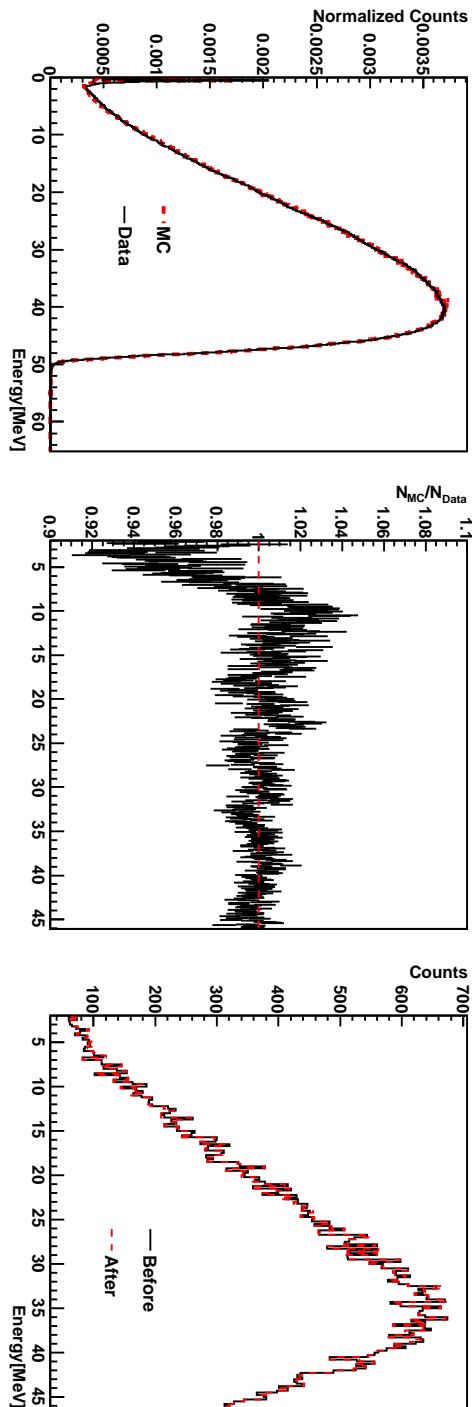


Figure 4.32: Left: Comparison for Michel spectrum between data (black) and MC (dashed red) measured by the NaI and CsI. Center: Discrepancy between data and MC. Vertical axis indicate the fraction of the amplitude of MC to the amplitude of data at each bin. Right: Before (black) and after (dashed red) modification of  $\mu DIF$  energy spectrum in the NaI and CsI.

## 4.7. SUMMARY OF RAW RATIO EXTRACTION

---

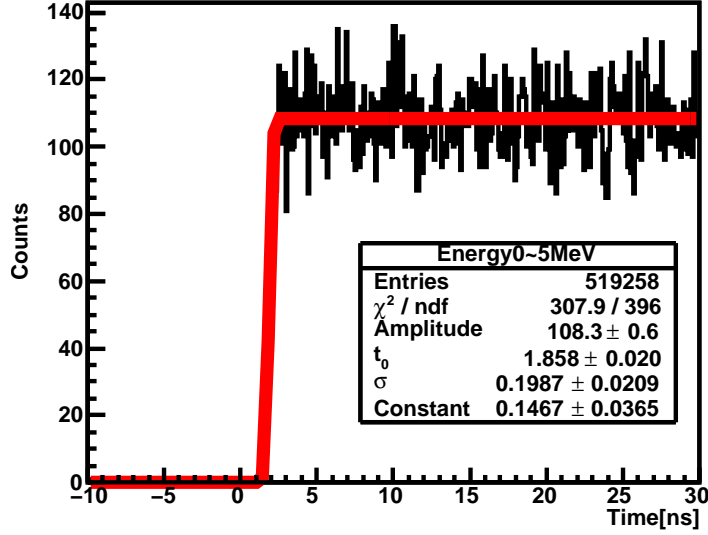


Figure 4.33: Zoom-in at  $t = 0$  with the energy range of 0–5 MeV. Black histogram is the decay positron time spectrum, which was fitted to the step function (red).

Those two values were combined with weighted average. The result of the combination is

$$C_{t_0} = 1.0006 \pm 0.0003. \quad (4.17)$$

The variation of  $R_{\text{raw}}^\pi$  coming from the error of this correction was estimated to be 0.0003.

## 4.7 Summary of Raw Ratio Extraction

Table 4.4 shows the summary of the time fit. Compared to the result of 2010 data set, the statistical uncertainty of  $R_{\text{raw}}^\pi$  for 2011 data set was improved by factor of 1.3. The systematic uncertainties of  $R_{\text{raw}}^\pi$  and  $\mu\text{DIF}$  were estimated to be at the same level as 2010 analysis. We took about twice higher statistics of muon data in 2011 than 2010. Therefore, compared to the result of 2010 data set, the precision of the  $t_0$  energy dependence was improved.

#### 4.7. SUMMARY OF RAW RATIO EXTRACTION

---

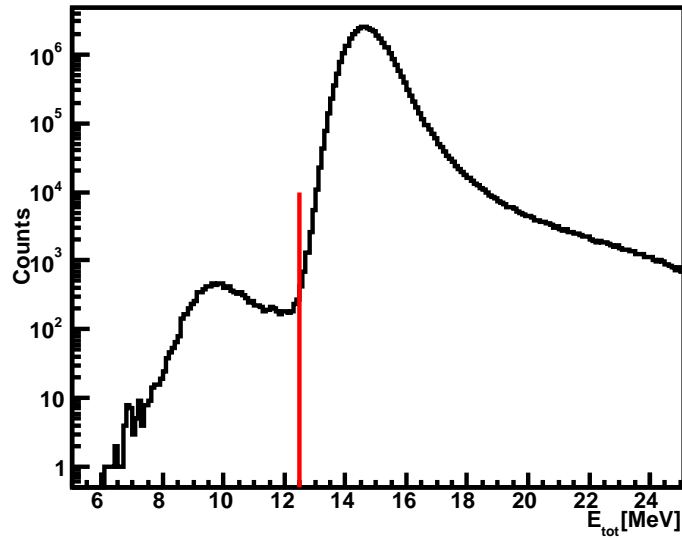


Figure 4.34:  $E_{\text{tot}}$  distribution. The larger peak came from the beam muons plus decay positrons, and smaller peak was due to the beam positron. The events below 12.5 MeV (red line) were removed.

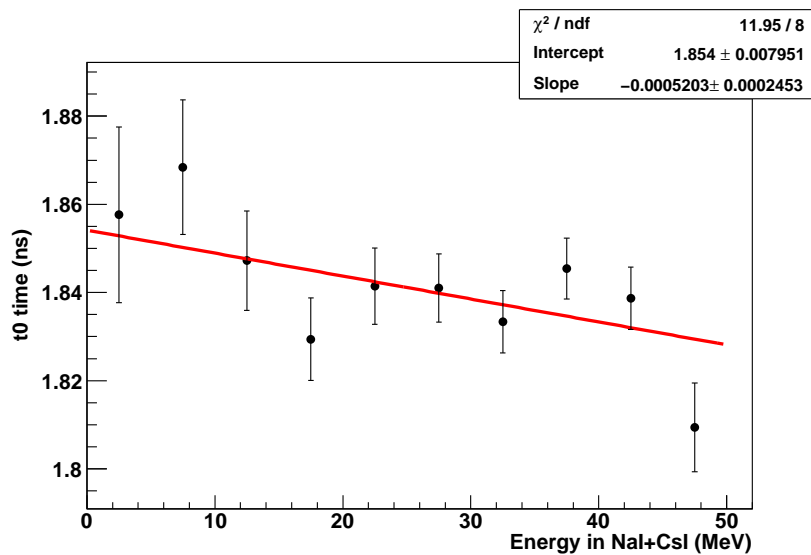


Figure 4.35: Energy dependence on  $t_0$ .

#### 4.7. SUMMARY OF RAW RATIO EXTRACTION

---

Table 4.4: Summary of the uncertainties for the  $R_{\text{raw}}^\pi$ ,  $\mu\text{DIF}$  correction, and  $t_0$  energy dependence. The value of  $R_{\text{raw}}^\pi$  on 2010 data set includes the  $\mu\text{DIF}$  correction. Because the central value of  $R_{\text{raw}}^\pi$  for 2011 data set is still blinded, it is represented by asterisks. The variation of  $R_{\text{raw}}^\pi$  came from the error of  $\mu\text{DIF}$  correction was estimated to be less than  $10^{-8}$ .

	2010			2011		
	Values	Uncertainties		Values	Uncertainties	
		Stat	Syst		Stat	Syst
$R_{\text{raw}}^\pi (\times 10^{-4})$	1.1972	0.0022	0.0006	1.****	0.0017	0.0006
$C_{\mu\text{DIF}} (\times 10^{-8})$	20.71		0.66	18.99		0.64
$t_0$ energy dependence	1.0004		0.0005	1.0006		0.0003

## Chapter 5

# Systematic Correction –Low-Energy $\pi^+ \rightarrow e^+ \nu_e$ Tail–

The largest correction to  $R_{\text{raw}}^\pi$  came from the low-energy  $\pi^+ \rightarrow e^+ \nu_e$  tail events below  $E_{\text{cut}}$ , which were buried under the  $\pi^+ \rightarrow \mu^+ \rightarrow e^+$  distribution. The low-energy  $\pi^+ \rightarrow e^+ \nu_e$  tail was mainly due to the shower leakage from the calorimeters. On the analysis of the tail correction, relying on MC simulation only was not satisfactory since hadronic reactions in the NaI were not completely reproduced by simulation (Figure 3.18). Therefore, an empirical determination of the tail was performed.

In the PIENU experiment, the amount of the low-energy tail was estimated using two ways. First, the dominant  $\pi^+ \rightarrow \mu^+ \rightarrow e^+$  events were suppressed in the energy spectrum, and the  $\pi^+ \rightarrow e^+ \nu_e$  low-energy tail was estimated by subtracting the remaining  $\pi^+ \rightarrow \mu^+ \rightarrow e^+$  events from the  $\pi^+ \rightarrow \mu^+ \rightarrow e^+$  suppressed spectrum. Second, a special measurement of the energy spectrum in the calorimeter using mono-energetic positron beam was performed in order to obtain the low-energy tail empirically (Figure 3.17).

It is possible that the first method results in an over-subtraction of  $\pi^+ \rightarrow \mu^+ \rightarrow e^+$  events from  $\pi^+ \rightarrow \mu^+ \rightarrow e^+$  suppressed spectrum due to the mechanism described in the coming section, giving smaller amount of the low-energy  $\pi^+ \rightarrow e^+ \nu_e$  tail. In the second method, it was possible that the low-energy beam positrons came into the NaI due to the scattering in the beam line. The low-energy beam positrons might enhance the low-energy tail, so the low-energy tail obtained by this measurement was possible to give a larger tail than the actual tail. Therefore, the first and second ways respectively gave access to the lower and upper limit of the  $\pi^+ \rightarrow e^+ \nu_e$  low-energy tail. The combination of the lower and upper limits was used for the correction value.

## 5.1 Lower Limit

### 5.1.1 $\pi^+ \rightarrow \mu^+ \rightarrow e^+$ Suppression Cuts

In order to determine the lower limit on the low-energy  $\pi^+ \rightarrow e^+ \nu_e$  tail, it was necessary to suppress the dominant  $\pi^+ \rightarrow \mu^+ \rightarrow e^+$  components. Before applying the  $\pi^+ \rightarrow \mu^+ \rightarrow e^+$  suppression cuts, all the event selection cuts described in §4.4 were used. In §4.4, the pulse shape cut in B3 was not used, and the minimum energy information was used in order to avoid the possible bias for  $R_{\text{raw}}^\pi$ . In this section, the information of B3 was used as the  $\pi^+ \rightarrow \mu^+ \rightarrow e^+$  suppression cuts just in order to estimate the correction value to  $R_{\text{raw}}^\pi$ .

The  $\pi^+ \rightarrow \mu^+ \rightarrow e^+$  suppression was performed using five suppression methods. First, by exploiting the short pion lifetime compared to the muon lifetime; the early time region 7–42 ns after the pion stop triggered by Early trigger enriched  $\pi^+ \rightarrow e^+ \nu_e$  decays relative to  $\pi^+ \rightarrow \mu^+ \rightarrow e^+$  events by a factor of 100. The second method used the energy loss information in the sum of B1, B2, S1, S2, and B3 ( $= E_{\text{tot}}$ ). As described in §2.1, the energy loss of the  $\pi^+ \rightarrow e^+ \nu_e$  decay in B3 was the sum of the kinetic energy of the stopping pion and a small contribution from the exiting decay positron. On the other hand,  $\pi^+ \rightarrow \mu^+ \rightarrow e^+$  decays had an additional 4.1 MeV energy deposit from the kinetic energy of the decay muon which stopped in B3 (Figure 2.1 and 2.2). Figure 5.1 shows the  $E_{\text{tot}}$  distribution after early time selection. There are two peaks in the spectrum of  $E_{\text{tot}}$ , the smaller peak came from  $\pi^+ \rightarrow e^+ \nu_e$  decays, and the larger peak was due to  $\pi^+ \rightarrow \mu^+ \rightarrow e^+$  events. The  $\pi^+ \rightarrow \mu^+ \rightarrow e^+$  suppression cut of  $E_{\text{tot}}$  was employed by removing events with  $E_{\text{tot}} < 15.5$  MeV or  $E_{\text{tot}} > 16.5$  MeV.

The third, the beam pion tracking before B3 was employed to remove  $\pi$ DIF contamination. As shown in Figure 3.22,  $\pi$ DIF events may result in a mismatch of the particle trajectory as determined by WC1 and WC2 compared to that obtained using S1 and S2. These events left energy in B3 similar to  $\pi^+ \rightarrow e^+ \nu_e$  events but had a larger mismatched (“kink”) angle than  $\pi$ DAR events. Figure 5.2 shows the result of the kink angle distributions. The  $\pi^+ \rightarrow \mu^+ \rightarrow e^+$  suppression cut was applied by rejecting the kink angle being larger than 12 degrees.

The fourth method used the energy loss in S3. About 30% of muons from  $\pi$ DIF events traversed B3 and deposited larger energy in S3 than the decay positron. Figure 5.3 shows the correlation plot of the energy deposit in the X and Y planes of S3. The  $\pi^+ \rightarrow \mu^+ \rightarrow e^+$  suppression cut based on the energy deposits  $E_{\text{S3X}}$  and  $E_{\text{S3Y}}$  is requiring

$$\sqrt{E_{\text{S3X}}^2 + E_{\text{S3Y}}^2} < 1.0 \text{ MeV}. \quad (5.1)$$

The fifth method was based on pulse shape fitting in B3. For every event, the waveform in B3 recorded by COPPER was consecutively fitted by

## 5.1. LOWER LIMIT

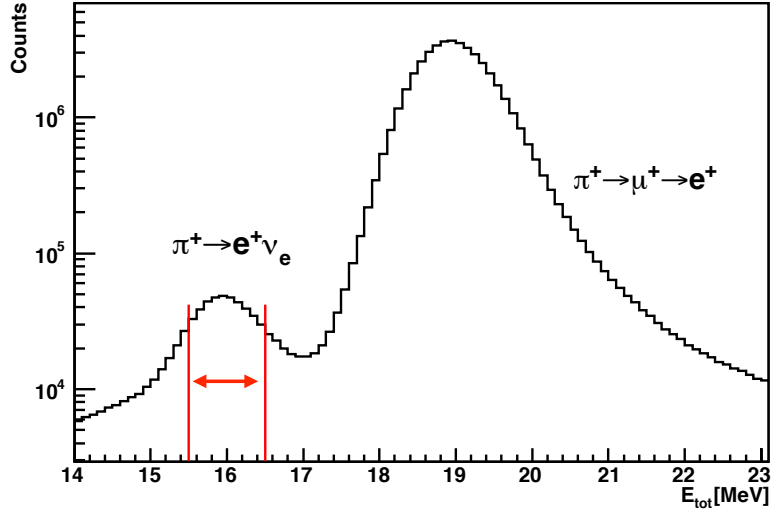


Figure 5.1: Sum of the energy deposit in B1, B2, S1, S2, and B3. Vertical lines indicate  $\pi^+ \rightarrow \mu^+ \rightarrow e^+$  suppression cut. The events indicated by red arrow were accepted.

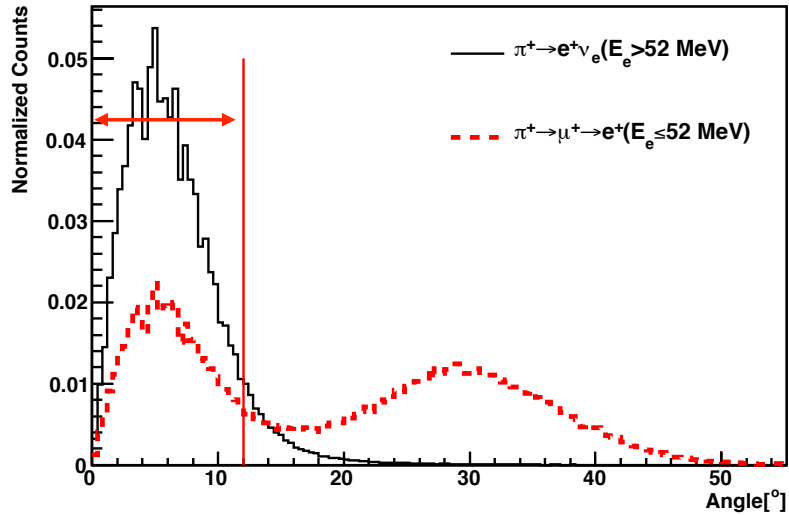


Figure 5.2: Kink angle distributions for  $\pi^+ \rightarrow e^+ \nu_e$  and  $\pi^+ \rightarrow \mu^+ \rightarrow e^+$  events after time and energy loss cuts. Vertical red line indicates the  $\pi^+ \rightarrow \mu^+ \rightarrow e^+$  suppression cut at 12 degrees. The events below 12 degrees were accepted.

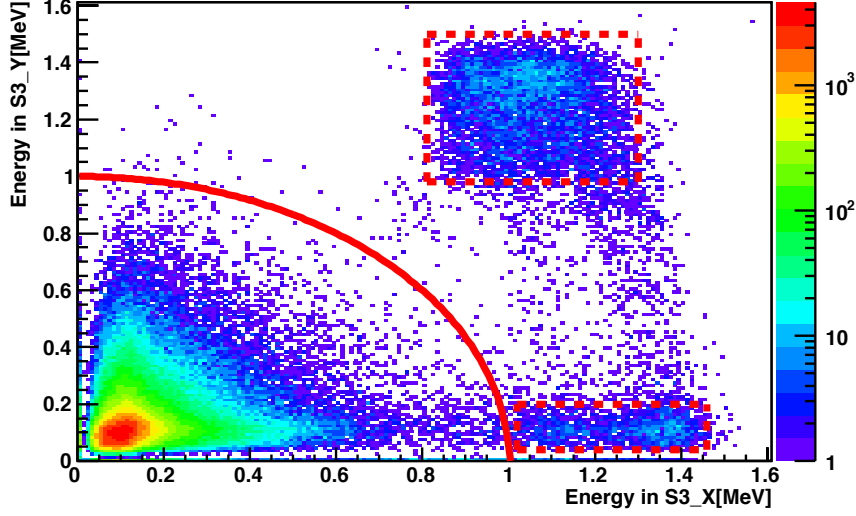


Figure 5.3: Energy deposited in S3\_X versus S3\_Y. Two dashed red boxes are muon leakage from  $\pi$ DIF that traversed B3. The events outside red curve were removed. S3\_X was placed before S3\_Y, so the events in the lower box shows that muon stopped in S3\_X, and the events in the upper box shows that muon traversed S3\_X and stopped in S3\_Y.

2-pulse (for  $\pi^+ \rightarrow e^+ \nu_e$  event) and 3-pulse (for  $\pi^+ \rightarrow \mu^+ \rightarrow e^+$  event) functions. In the case of the 2-pulse fit, the timings of the first and the second pulses were determined by the B1 and T1 timings respectively. For the 3-pulse fit, the result from the 2-pulse fit was first subtracted from the waveform. The highest peak after subtraction was associated with the muon, so the pulse height and time information were used for the initial fitting parameters in the 3-pulse fit. Figure 5.4 shows an example of the waveform with the 2-pulse and 3-pulse fit in B3. Removing 3-pulse like events by using this fit result could reduce the remaining  $\pi^+ \rightarrow \mu^+ \rightarrow e^+$  events. The  $\pi^+ \rightarrow \mu^+ \rightarrow e^+$  suppression cut with pulse fit is represented as

$$\Delta\chi^2 = \chi_{2\text{-pulse}}^2/n_{d;2\text{-pulse}} - \chi_{3\text{-pulse}}^2/n_{d;3\text{-pulse}} < 0, \quad (5.2)$$

where  $n_{d;2\text{-pulse}}$  and  $n_{d;3\text{-pulse}}$  are the degrees of freedom of the fit for 2-pulse hypothesis and 3-pulse hypothesis, respectively. Figure 5.5 shows correlation plots for  $\Delta\chi^2$  versus  $E_{\text{tot}}$ .

Table 5.1 shows the summary of all the  $\pi^+ \rightarrow \mu^+ \rightarrow e^+$  suppression cuts with low-energy fraction and efficiency at  $\pi^+ \rightarrow e^+ \nu_e$  peak. The low-energy fraction is defined as the ratio of the integral below  $E_{\text{cut}} (= 52 \text{ MeV})$  to the integral of the full energy spectrum. Efficiency at  $\pi^+ \rightarrow e^+ \nu_e$  peak is the fraction of the height at 65.5 MeV after and before each suppression cut with the order listed in Table 5.1. Figure 5.6 shows the energy spectrum

## 5.1. LOWER LIMIT

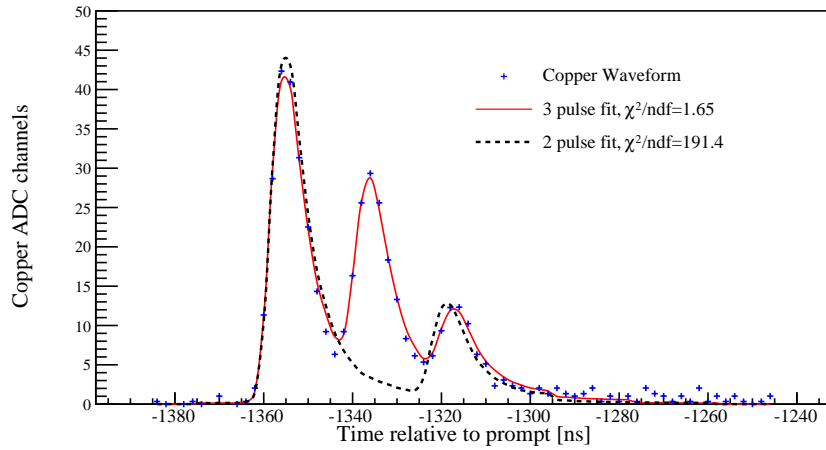


Figure 5.4: 2-pulse and 3-pulse fit for  $\pi^+ \rightarrow \mu^+ \rightarrow e^+$  event in B3 [3].

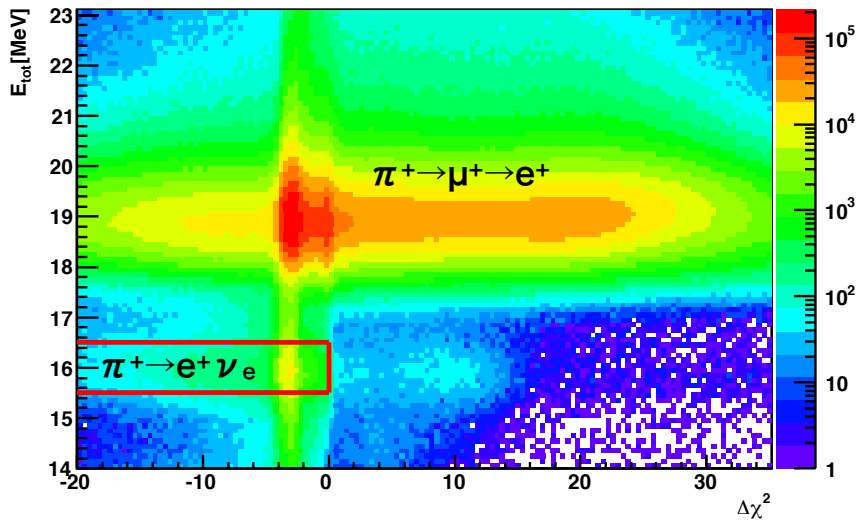


Figure 5.5:  $\Delta\chi^2$  versus energy loss information.  $\pi^+ \rightarrow e^+ \nu_e$  events are mostly inside red lines. The events outside the red lines were removed.

## 5.1. LOWER LIMIT

Table 5.1: Summary of the  $\pi^+ \rightarrow \mu^+ \rightarrow e^+$  suppression cuts.

Cut	Low-energy fraction (%)	Efficiency at $\pi^+ \rightarrow e^+ \nu_e$ peak (%)
Time	99.16	56.50
$E_{\text{tot}}$	29.47	77.12
Kink	15.42	92.44
S3	14.57	99.99
Pulse fit	14.41	96.95

of the calorimeters (NaI + CsI) with the  $\pi^+ \rightarrow \mu^+ \rightarrow e^+$  suppression cuts applied sequentially. Applying all the five suppression methods gave the total  $\pi^+ \rightarrow \mu^+ \rightarrow e^+$  suppression factor of  $10^5$ . Compared to the previous experiment at TRIUMF (§2.2.2), the low-energy fraction was reduced by factor of 1.3.

The most powerful cut to reduce  $\pi^+ \rightarrow \mu^+ \rightarrow e^+$  events was  $E_{\text{tot}}$  cut. Figure 5.7 shows MC-simulated  $E_{\text{tot}}$  spectra for  $\pi^+ \rightarrow e^+ \nu_e$ ,  $\pi$ DAR- $\mu$ DAR,  $\pi$ DIF- $\mu$ DAR, and  $\mu$ DIF events.  $\pi$ DAR- $\mu$ DAR events could be totally removed with  $E_{\text{tot}}$  cut. Any residual  $\pi$ DAR- $\mu$ DAR events were removed by the pulse-shape cut. Figure 5.7 also shows that a part of  $\pi$ DIF- $\mu$ DAR and  $\mu$ DIF events could not be removed with  $E_{\text{tot}}$  cut. The  $\pi^+ \rightarrow e^+ \nu_e$  events removed by  $E_{\text{tot}}$  cut were mostly due to Bhabha scattering in B3. In the previous experiment at TRIUMF, the thickness of the target was 13 mm [22], and the target was rotated by an angle of 45 degrees with the calorimeter axis (Figure 2.4). Therefore, the path length of the decay positrons in the previous experiment was larger than that in the PIENU experiment, and the contribution of Bhabha scattering events in the target in the PIENU experiment was smaller than that in the previous experiment. The correction of the removed  $\pi^+ \rightarrow e^+ \nu_e$  events by  $E_{\text{tot}}$  cut will be discussed in §5.1.7. The energy spectrum with all the  $\pi^+ \rightarrow \mu^+ \rightarrow e^+$  suppression cuts (pink histogram in Figure 5.6) will be called “ $\pi^+ \rightarrow \mu^+ \rightarrow e^+$  suppressed spectrum” hereafter.

### 5.1.2 Concept of Lower Limit Estimate

The low-energy  $\pi^+ \rightarrow e^+ \nu_e$  tail was obtained by subtracting the remaining  $\pi^+ \rightarrow \mu^+ \rightarrow e^+$  component from the  $\pi^+ \rightarrow \mu^+ \rightarrow e^+$  suppressed spectrum. The caveat was that it was not easy to estimate the amount of  $\pi^+ \rightarrow \mu^+ \rightarrow e^+$  component since the shape of the low-energy  $\pi^+ \rightarrow e^+ \nu_e$  tail is unknown. There was only one assumption that should be true: the shape of the  $\pi^+ \rightarrow e^+ \nu_e$  tail should monotonically decrease as the energy decreases. It was further assumed that the  $\pi^+ \rightarrow e^+ \nu_e$  tail did not exist below some arbitrary energy  $x$  (1-52 MeV), and thus all events below that energy  $x$  came only from  $\pi^+ \rightarrow \mu^+ \rightarrow e^+$  events. The amount of the  $\pi^+ \rightarrow e^+ \nu_e$  tail, LL, was found to

## 5.1. LOWER LIMIT

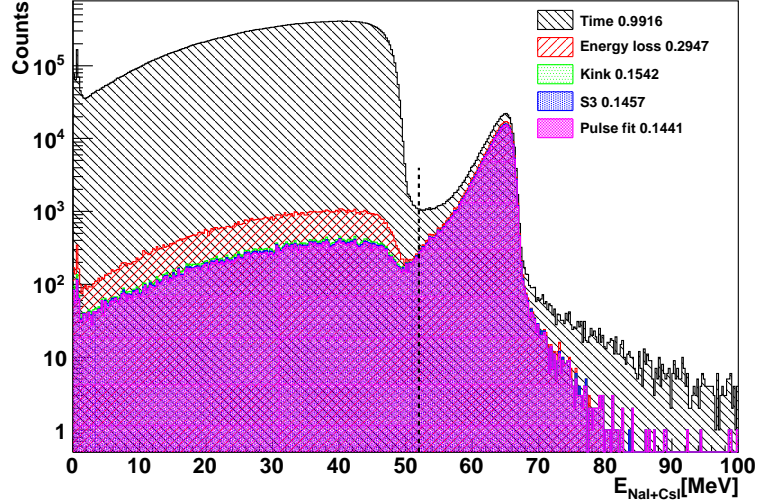


Figure 5.6: Energy spectrum of the NaI plus CsI after each suppression cut. The black histogram is after only time cut and the pink histogram is after all suppression cuts. The legend box shows the low-energy fraction, which represents the integral of events below  $E_{\text{cut}} (=52 \text{ MeV})$  divided by the integral of the full energy spectrum.

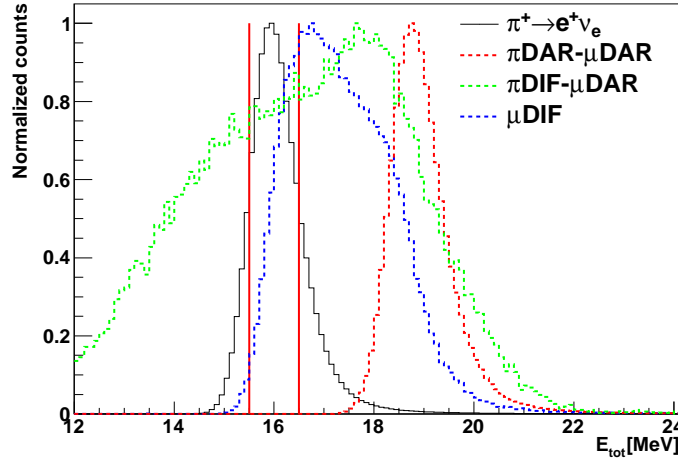


Figure 5.7: Simulated  $E_{\text{tot}}$  distributions for the  $\pi^+ \rightarrow e^+ \nu_e$  (black),  $\pi\text{DAR}-\mu\text{DAR}$  (dashed red),  $\pi\text{DIF}-\mu\text{DAR}$  (dashed green), and  $\mu\text{DIF}$  (dashed blue) events. The energy resolution of each counter and Barks effect were included in the simulation. Two vertical heavy red lines indicate cut region for  $\pi^+ \rightarrow \mu^+ \rightarrow e^+$  suppression.

## 5.1. LOWER LIMIT

---

be

$$\text{LL}(x) = A - \frac{a(x)}{b(x)}B, \quad (5.3)$$

where  $A$  is the number of events in the  $\pi^+ \rightarrow \mu^+ \rightarrow e^+$  suppressed spectrum (Figure 5.8 (a)) with energy from 1 to 52 MeV;  $a(x)$  is the number of events in the  $\pi^+ \rightarrow \mu^+ \rightarrow e^+$  suppressed spectrum with energy from 1 to  $x$ ;  $b(x)$  is the number of events in the  $\pi^+ \rightarrow \mu^+ \rightarrow e^+$  spectrum (Figure 5.8 (b)) with energy from 1 to energy  $x$ ;  $B$  is the number of events in the  $\pi^+ \rightarrow \mu^+ \rightarrow e^+$  spectrum with energy from 1 to 52 MeV. The reason for choosing the starting point of integration at 1 MeV instead of zero was to avoid the 511 keV peak. The fraction of the number of  $\pi^+ \rightarrow e^+ \nu_e$  events below 1 MeV to the number of all  $\pi^+ \rightarrow e^+ \nu_e$  events was less than 0.01%. Therefore, this did not affect the estimation of low-energy  $\pi^+ \rightarrow e^+ \nu_e$  tail. For small energy  $x$ , the assumption was relatively good since the fraction of  $\pi^+ \rightarrow e^+ \nu_e$  tail below  $x$  was small enough, but it was limited by the statistical error of  $a(x)$ . As the energy  $x$  was increased the assumption became worse, but the statistical significance was improved. If energy  $x$  was too high and the spectrum below  $x$  was contaminated with the tail of  $\pi^+ \rightarrow e^+ \nu_e$  events,  $\text{LL}(x)$  gave smaller value than true one. Therefore, this procedure only gives access lower limit for the low-energy  $\pi^+ \rightarrow e^+ \nu_e$  tail.

The tail fraction TF, which represents the number of the low-energy  $\pi^+ \rightarrow e^+ \nu_e$  tail divided by the number of all  $\pi^+ \rightarrow e^+ \nu_e$  events, can be written using the number of events above 52 MeV in the  $\pi^+ \rightarrow \mu^+ \rightarrow e^+$  suppressed spectrum (HE in Figure 5.8 (a)),

$$\text{TF} = \frac{\text{LL}(x)}{\text{LL}(x) + \text{HE}}. \quad (5.4)$$

In order to obtain the lower limit using this procedure, the shape of the  $\pi^+ \rightarrow \mu^+ \rightarrow e^+$  energy spectrum used to calculate parameters  $B$  and  $b(x)$  should be the same as that of the remaining  $\pi^+ \rightarrow \mu^+ \rightarrow e^+$  events in the  $\pi^+ \rightarrow \mu^+ \rightarrow e^+$  suppressed spectrum. Actually, the remaining  $\pi^+ \rightarrow \mu^+ \rightarrow e^+$  events were  $\pi\text{DIF}$ - $\mu\text{DAR}$  or  $\mu\text{DIF}$  events, and the energy distribution of  $\mu\text{DIF}$  events was considerably different with  $\mu\text{DAR}$  events (Figure 4.31). The modification of the  $\pi^+ \rightarrow \mu^+ \rightarrow e^+$  energy spectrum for the parameters  $B$  and  $b(x)$  due to the  $\mu\text{DIF}$  events will be discussed in the next section.

### 5.1.3 Modification of $\mu\text{DIF}$ Contribution on Lower Limit

As described in §4.6.1, the probability of  $\mu\text{DIF}$  is  $8 \times 10^{-6}$  of  $\pi\text{DAR}$ - $\mu\text{DAR}$  event. The MC simulation showed that 23.22% of  $\mu\text{DIF}$  remained after  $E_{\text{tot}}$  cut. Taking the theoretical branching ratio of  $\pi^+ \rightarrow e^+ \nu_e = 1.24 \times 10^{-4}$  and the efficiency of the  $E_{\text{tot}}$  cut for  $\pi^+ \rightarrow e^+ \nu_e$  0.771 (Table 5.1), the ratio of the

## 5.1. LOWER LIMIT

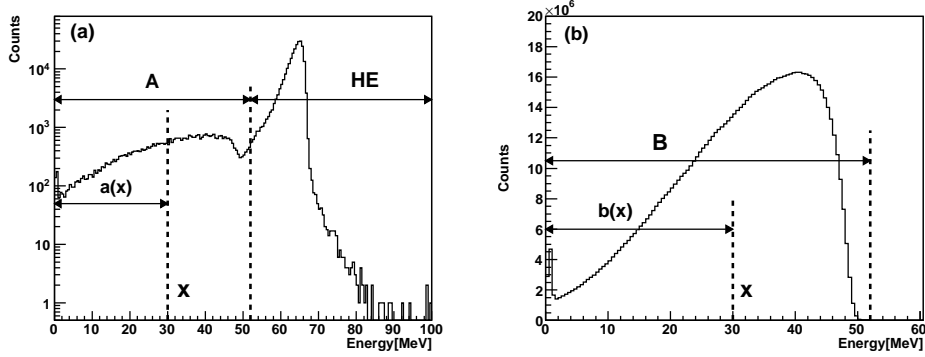


Figure 5.8: (a)  $\pi^+ \rightarrow \mu^+ \rightarrow e^+$  suppressed spectrum (same as that in Figure 5.6). (b)  $\pi^+ \rightarrow \mu^+ \rightarrow e^+$  energy spectrum obtained by the late selection, which represents the time selection  $t > 100$  ns after pion decay.

number of  $\mu$ DIF events to the number of  $\pi^+ \rightarrow e^+ \nu_e$  events is

$$\frac{N[\mu\text{DIF}]}{N[\pi^+ \rightarrow e^+ \nu_e]} = \frac{8 \times 10^{-6} \times 0.2322}{1.24 \times 10^{-4} \times 0.771} = 1.94 \times 10^{-2}. \quad (5.5)$$

The ratio of  $\mu$ DIF events below 52 MeV to the number of all events below 52 MeV could roughly be estimated using this value and the low-energy fraction after all  $\pi^+ \rightarrow \mu^+ \rightarrow e^+$  suppression cuts, 14.41% (Table 5.1),

$$\frac{1.94\%}{14.41\%} = 13.47\%. \quad (5.6)$$

This value could be also derived from the experimental data by simultaneous fit of energy and time spectra (Figure 5.9). The two components,  $\pi$ DIF- $\mu$ DAR and  $\mu$ DIF below 52 MeV, could be separated by using the difference in the shape of the positron time spectra. The former showed muon life time spectrum since pions did already decay to muons when they hit B3 while the latter showed pion life time spectrum since only muons that decayed to positrons without any delay survived the  $\pi^+ \rightarrow \mu^+ \rightarrow e^+$  suppression selection. The positron energy spectrum for  $\pi$ DIF- $\mu$ DAR was obtained from data by assuming that it was the same as that of the standard  $\pi$ DAR- $\mu$ DAR events. The positron energy spectrum for  $\mu$ DIF was estimated by MC. The tail component from  $\pi^+ \rightarrow e^+ \nu_e$  was also estimated by using the MC-produced energy spectrum. The fit range in the energy spectrum was from 1 to 55 MeV while the time spectrum was fitted from 12 to 42 ns. As shown in Figure 5.9, the combined  $\chi^2$  divided by the number of degrees of freedom was 1.84 and the fraction of those 3 components below 52 MeV were respectively estimated to be,  $\pi$ DIF- $\mu$ DAR=74.93 $\pm$ 1.42%,  $\mu$ DIF=13.40 $\pm$ 1.48%, and  $\pi^+ \rightarrow e^+ \nu_e$ =11.67 $\pm$ 0.16%. The fit result shows

## 5.1. LOWER LIMIT

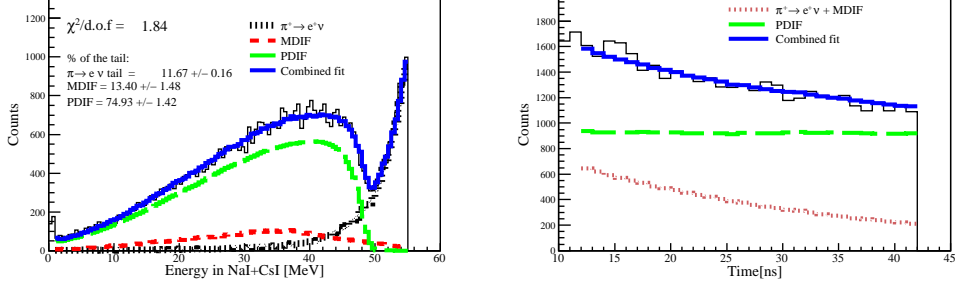


Figure 5.9: Energy (left) and time (right) spectra for the fit. The values shown in the legend in left indicate  $\chi^2/n_d$  for the fit and the fractions of three components below 52 MeV.

that the fraction of  $\mu\text{DIF}$  events below 52 MeV is 13.40%, which is consistent with the theoretically calculated value shown in Eq. (5.6).

The  $\pi^+ \rightarrow \mu^+ \rightarrow e^+$  energy spectrum used for the parameters  $B$  and  $b(x)$  was modified by combining  $\mu\text{DIF}$  and  $\pi\text{DIF}$  (late selected decays,  $t > 100$  ns) energy spectra with the ratio of  $\alpha = 13.40/74.93 = 0.1788 \pm 0.0274$ . The error on  $\alpha$  was estimated by the errors of parameters inflated by  $\sqrt{\chi^2/n_d}$ . Figure 5.10 shows the  $\pi^+ \rightarrow \mu^+ \rightarrow e^+$  energy spectra before and after the modification of  $\mu\text{DIF}$  events. The modified  $\pi^+ \rightarrow \mu^+ \rightarrow e^+$  energy spectrum represented by dashed red in Figure 5.10 was used for parameter  $B$  and  $b(x)$  in Eq (5.3).

### 5.1.4 Introduction of $\pi^+ \rightarrow e^+ \nu_e(\gamma)$ Events without Hadronic Reactions

The procedure of the lower limit estimation discussed in the previous sections was based on the assumption that there was no  $\pi^+ \rightarrow e^+ \nu_e$  tail below the energy  $x$ . In order to assure the assumption, a new parameter  $c(x)$  was introduced, which represents the integral of the  $\pi^+ \rightarrow e^+ \nu_e$  and  $\pi^+ \rightarrow e^+ \nu_e \gamma$  energy spectrum from 1 to  $x$  MeV without hadronic reactions produced by MC.

As shown in Figure 3.19, the photo-nuclear reaction was not completely reproduced by MC. If the hadronic reactions were excluded from the process in the simulation, we could obtain the  $\pi^+ \rightarrow e^+ \nu_e(\gamma)$  energy spectrum without additional bumps due to the photo-nuclear effect. Figure 5.11 shows the comparison of the  $\pi^+ \rightarrow \mu^+ \rightarrow e^+$  suppressed spectrum and the simulated  $\pi^+ \rightarrow e^+ \nu_e(\gamma)$  energy spectrum without hadronic reactions. If the simulated  $\pi^+ \rightarrow e^+ \nu_e(\gamma)$  energy spectrum without hadronic reactions was subtracted from the  $\pi^+ \rightarrow \mu^+ \rightarrow e^+$  suppressed spectrum, the remaining events were composed of  $\pi\text{DIF}-\mu\text{DAR}$  events,  $\mu\text{DIF}$  events, and residual  $\pi^+ \rightarrow e^+ \nu_e$  bumps due to the photo-nuclear effect.

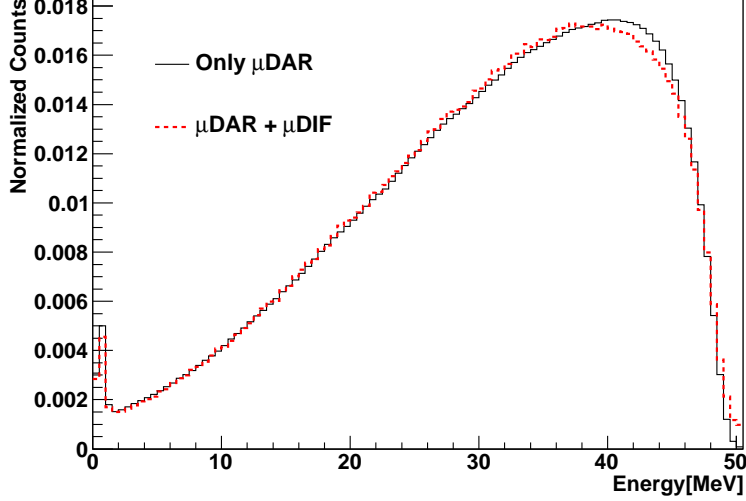


Figure 5.10: The  $\mu$ DAR (black) and  $\mu$ DAR and  $\mu$ DIF combined (dashed red) energy spectra.

MC studies showed that the pion radiative decay  $\pi^+ \rightarrow e^+ \nu_e \gamma$  spectrum had a larger tail than non-radiative decay because a  $\gamma$  sometimes did not hit the calorimeters. Figure 5.12 shows the energy spectra for only  $\pi^+ \rightarrow e^+ \nu_e \gamma$  and  $\pi^+ \rightarrow e^+ \nu_e$  events produced by MC. In order to take this into account,  $\pi^+ \rightarrow e^+ \nu_e \gamma$  events were also included in the simulation. The ratio of the branching ratio of radiative decay with a photon cut-off energy of 1 MeV to the branching ratio of radiative and non-radiative decay is

$$\frac{\Gamma(\pi^+ \rightarrow e^+ \nu_e \gamma)}{\Gamma[(\pi^+ \rightarrow e^+ \nu_e) + (\pi^+ \rightarrow e^+ \nu_e \gamma)]} = 0.1397. \quad (5.7)$$

The calculation was checked with different photon cut-off energies and angular restrictions against theoretical calculations [73, 74] and experiment [75].

Eq. (5.3) has been rewritten to include the new factor  $c(x)$  as

$$LL'(x) = A - \frac{a(x) - c(x)}{b(x)} B. \quad (5.8)$$

The simulated  $\pi^+ \rightarrow e^+ \nu_e$  plus  $\pi^+ \rightarrow e^+ \nu_e \gamma$  energy spectrum was normalized so that it had the same  $\pi^+ \rightarrow e^+ \nu_e$  peak at 65.5 MeV in the  $\pi^+ \rightarrow \mu^+ \rightarrow e^+$  suppressed spectrum. In order to ensure the consistency between data and MC, the same  $E_{\text{tot}}$  cut was applied to the simulated  $\pi^+ \rightarrow e^+ \nu_e(\gamma)$  energy spectrum without hadronic reactions. Therefore, the  $\pi^+ \rightarrow e^+ \nu_e(\gamma)$  events with Bhabha scattering in B3 were removed.

## 5.1. LOWER LIMIT

---

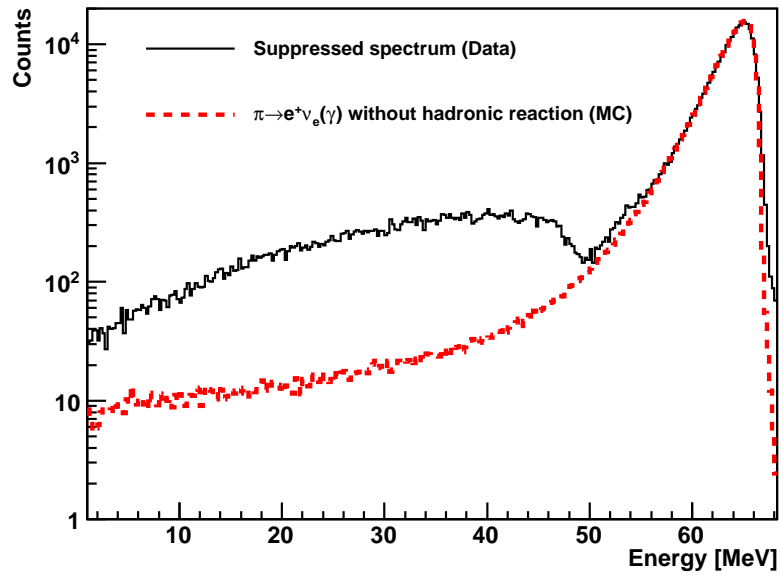


Figure 5.11: Dashed red: Simulated energy spectra of  $\pi^+ \rightarrow e^+ \nu_e$  plus  $\pi^+ \rightarrow e^+ \nu_e \gamma$  without hadronic reaction to exclude photo-nuclear effect. Black: Suppressed spectrum (data). The difference between 50 to 55 MeV was due to the photo-nuclear effect.

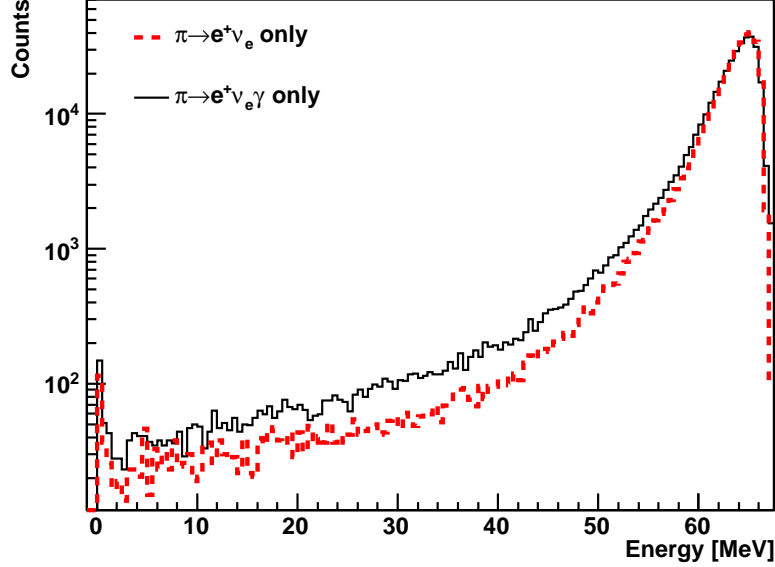


Figure 5.12: Comparison of  $\pi^+ \rightarrow e^+ \nu_e$  (dashed red) and  $\pi^+ \rightarrow e^+ \nu_e \gamma$  (black) events by MC.

### 5.1.5 Lower Limit Estimate

Using Eq. 5.8, the lower limit  $LL'(x)$  was calculated in the range of energy  $x$  from 1 to 52 MeV. Figure 5.13 shows the result of the tail fraction of the lower limit  $TF'$  calculation using  $LL'(x)$ . The  $TF'$  used for the correction was selected at the point of the highest lower edge of the statistical error, which was calculated as

$$TF' = \frac{LL'(30.50 \text{ MeV})}{LL'(30.50 \text{ MeV}) + HE} = [1.97 \pm 0.09(\text{stat})]\%. \quad (5.9)$$

### 5.1.6 Systematic Uncertainty

The systematic uncertainty of the lower limit was estimated by considering the following items <sup>1</sup>.

#### Uncertainty of $\mu$ DIF Contribution

The uncertainty of  $\mu$ DIF contribution to the  $\pi^+ \rightarrow \mu^+ \rightarrow e^+$  spectrum used for the parameters  $B$  and  $b(x)$  was directly obtained from the energy- and time-fit described in §5.1.3. The ratio of the  $\mu$ DIF events to  $\pi$ DIF- $\mu$ DAR events

<sup>1</sup>The numbers shown below represent absolute uncertainties, not relative errors since the  $TF'$  is expressed as a percentage.

## 5.1. LOWER LIMIT

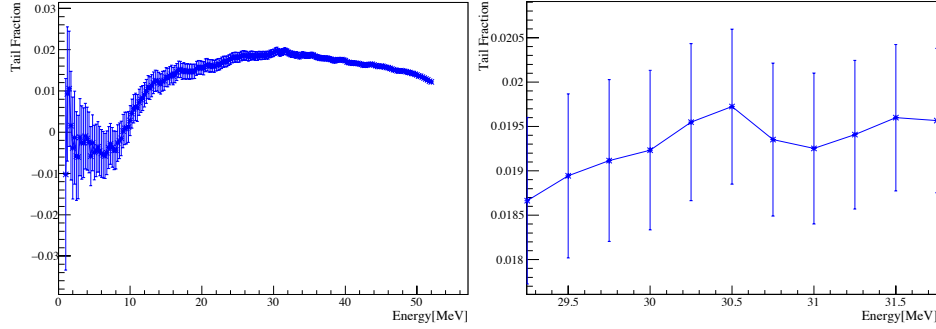


Figure 5.13: Left: The result of the  $TF'$  study in the range of 1-52 MeV. Error bars indicate just statistical errors at each energy  $x$ . Right: Zoom-in of the highest edge of the error bar at 30.50 MeV.

was  $\alpha = 0.1788 \pm 0.0274$ . The lower limit was re-calculated by changing the parameter  $\alpha$  with a one standard deviation. The variation of  $TF'$  that came from the error on  $\alpha$  was estimated to be  $\Delta TF' = 0.007\%$ .

### Shape of the $\pi^+ \rightarrow e^+ \nu_e(\gamma)$ MC Energy Spectrum

It was possible that the simulated  $\pi^+ \rightarrow e^+ \nu_e(\gamma)$  energy spectrum did not completely reproduce the real spectrum. The  $E_{tot}$  cut affected the shape of the  $\pi^+ \rightarrow e^+ \nu_e(\gamma)$  energy spectrum since Bhabha scattering events were removed. As the conservative estimate, the simulated  $\pi^+ \rightarrow e^+ \nu_e(\gamma)$  energy spectrum was artificially increased or decreased by changing the upper bound of  $E_{tot}$  cut by  $\pm 0.1$  MeV. Figure 5.14 shows the result of changing the upper bound for  $E_{tot}$  cut. The change of the tail fraction corresponding to the  $\pm 0.1$  MeV of  $E_{tot}$  was 0.08%. The variation of  $TF'$  was estimated to be  $\Delta TF' = 0.025\%$ .

### Shape of the $\mu$ DIF MC Energy Spectrum

Because of the same reason as described in the previous section, the upper bound of the  $E_{tot}$  cut for  $\mu$ DIF events was also changed by  $\pm 0.1$  MeV. The variation of  $TF'$  was estimated to be  $\Delta TF' = 0.007\%$ .

### Contribution of $E_{tot}$ Cut to $\pi^+ \rightarrow \mu^+ \rightarrow e^+$ Energy Spectrum

From §5.1.2 to here, the energy shape of  $\pi$ DIF- $\mu$ DAR events was assumed to be same as the  $\pi^+ \rightarrow \mu^+ \rightarrow e^+$  energy spectrum with late time selected decays. But MC studies showed that  $E_{tot}$  cut slightly affected the shape of the  $\pi^+ \rightarrow \mu^+ \rightarrow e^+$  energy spectrum. Because the position distribution of the muon that decayed in B3 for  $\pi$ DIF- $\mu$ DAR events was different than that

## 5.1. LOWER LIMIT

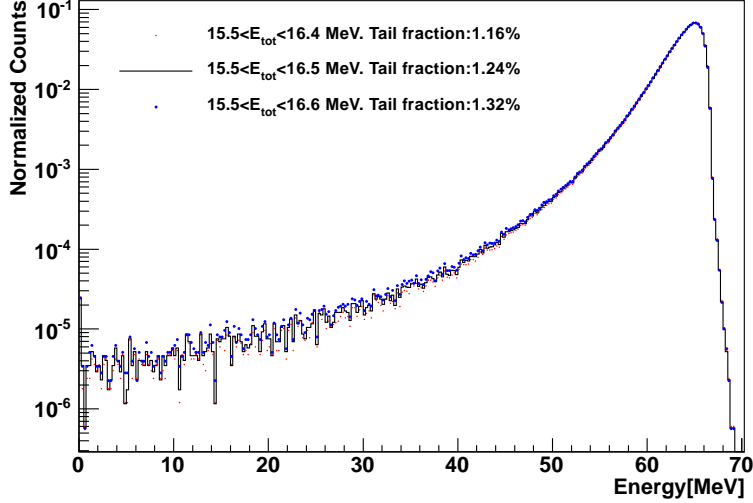


Figure 5.14: The simulated  $\pi^+ \rightarrow e^+ \nu_e (\gamma)$  energy spectra with different upper bounds for the  $E_{\text{tot}}$  cut. Tail fractions indicate the number of events below 52 MeV divided by the total number of events.

for  $\pi\text{DAR}-\mu\text{DAR}$  events, the path length of the decay positrons for  $\pi\text{DIF}-\mu\text{DAR}$  was also different than that of  $\pi\text{DAR}-\mu\text{DAR}$  events. Therefore, the  $\pi^+ \rightarrow \mu^+ \rightarrow e^+$  energy spectrum with the  $E_{\text{tot}}$  cut should be used for the lower limit estimate. However, the cut on  $E_{\text{tot}}$  removed many  $\pi^+ \rightarrow \mu^+ \rightarrow e^+$  events, so the  $\pi^+ \rightarrow \mu^+ \rightarrow e^+$  energy spectrum after applying the  $E_{\text{tot}}$  cut could not be used for the estimate due to large statistical uncertainty. In order to estimate the effect of the  $E_{\text{tot}}$  cut on the shape of  $\pi^+ \rightarrow \mu^+ \rightarrow e^+$  energy spectrum, the energy spectrum of  $\pi^+ \rightarrow \mu^+ \rightarrow e^+$  events with the  $E_{\text{tot}}$  cut and the late decay selection ( $t > 100$  ns) was fitted to the energy spectrum of  $\pi^+ \rightarrow \mu^+ \rightarrow e^+$  events with the late decay selection only. The result of the fit is shown in Figure (5.15) left. The ratio of the amplitude of the  $\pi^+ \rightarrow \mu^+ \rightarrow e^+$  energy spectrum with the late decay selection and the  $E_{\text{tot}}$  cut to the amplitude of the  $\pi^+ \rightarrow \mu^+ \rightarrow e^+$  energy spectrum with the late decay selection only was calculated in each bin, and the result is shown in Figure (5.15) right. The curve of the ratio was fitted to a quadratic function and it was used to modify the much-higher statistics energy spectrum. The tendency of the plots was also confirmed by MC. Figure 5.16 shows the  $\pi^+ \rightarrow \mu^+ \rightarrow e^+$  energy spectra before and after the modification by the quadratic function. The variation of  $\text{TF}'$  from this effect was estimated to be  $\Delta\text{TF}'=0.040\%$ .

## 5.1. LOWER LIMIT

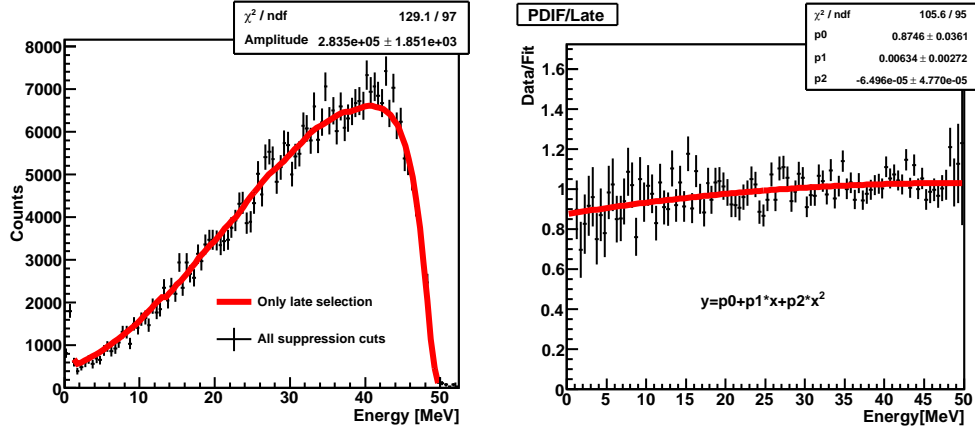


Figure 5.15: Left: Comparison of the  $\pi^+ \rightarrow \mu^+ \rightarrow e^+$  energy spectra with the late decay selection ( $t > 100$  ns) only (red curve), and the late decay selection and the  $E_{\text{tot}}$  cut (black with error bar). Black points were fitted to the red curve. Right: The ratio of the amplitude of the  $\pi^+ \rightarrow \mu^+ \rightarrow e^+$  energy spectrum with the  $E_{\text{tot}}$  cut and the late pion decay selection ( $t > 100$  ns) to the amplitude of the  $\pi^+ \rightarrow \mu^+ \rightarrow e^+$  energy spectrum with the late pion decay selection. These points were fitted to the quadratic function.

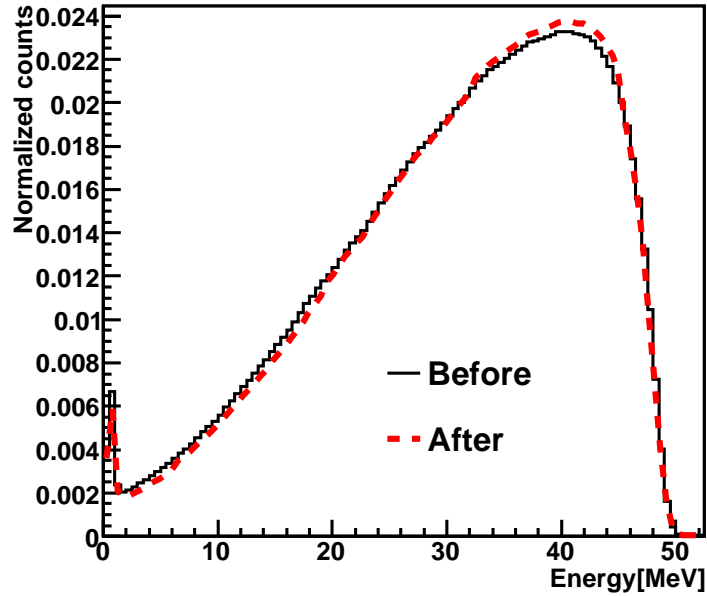


Figure 5.16: The Michel spectra before (black) and after (red) modification by the quadratic function.

### Summary of Systematic Study

The tail fraction of the lower limit with statistical and systematic uncertainties was

$$\text{TF}' = \frac{\text{LL}'(30.50 \text{ MeV})}{\text{LL}'(30.50 \text{ MeV}) + \text{HE}} = [1.97 \pm 0.09(\text{stat}) \pm 0.05(\text{syst})]\%. \quad (5.10)$$

#### 5.1.7 Bhabha Correction

In the previous sections, in order to suppress the dominant  $\pi^+ \rightarrow \mu^+ \rightarrow e^+$  events, the energy deposited in B3 ( $E_{\text{tot}}$ ) was used. However, a part of  $\pi^+ \rightarrow e^+ \nu_e$  events were also removed by the cut. One type of events that produced larger  $E_{\text{tot}}$  than the standard  $\pi^+ \rightarrow e^+ \nu_e$  events were those that underwent Bhabha scattering in B3. These events tended to deposit less energy in the calorimeters than standard  $\pi^+ \rightarrow e^+ \nu_e$  events due to the escape of scattered  $e^\pm$ . Figure 5.17 shows the effect of Bhabha scattering events by MC. Using MC, the amount of the removed  $\pi^+ \rightarrow e^+ \nu_e$  tail by  $E_{\text{tot}}$  cut was estimated to be 1.26% of total  $\pi^+ \rightarrow e^+ \nu_e$  events. The tail correction discussed above should be corrected with this value in order to obtain  $R^\pi$  free from the potential bias coming from  $E_{\text{tot}}$  cut.

The systematic uncertainty from this ‘‘Bhabha correction’’ came from the energy calibration in the calorimeters and discrepancy of Bhabha scattering events between data and MC. As it was already shown in §4.2.4, the energy calibration in the NaI and CsI was better than 0.1 MeV. This translated into the uncertainty on Bhabha correction of 0.005%. The  $E_{\text{tot}}$  was more precisely calibrated than the NaI and CsI. Therefore, the effect coming from the energy calibration of  $E_{\text{tot}}$  was negligible.

The discrepancy of Bhabha events between data and MC was estimated using a special data set with a positron beam for the upper limit study. The schematic of the detector setup is shown in Figure 3.17, which will be described in the next section. Figure 5.18 shows the energy spectra of data and MC at 47.7 degrees. In the normal pion runs, the decay positrons from  $\pi^+ \rightarrow e^+ \nu_e$  events traversed half of B3. In the positron beam measurement, the beam positrons with 70 MeV/ $c^2$  hit T2 and sometimes underwent Bhabha scattering. Thus, by comparing the removed events between data and MC with T2 energy cut (5.19), the discrepancy of Bhabha scattering between data and MC was estimated. The differences of the tail fractions below 52 MeV before and after T2 energy cut were 1.010% for data and 1.030% for MC. By this result, the discrepancy of Bhabha scattering events between data and MC was found to be 0.020%.

The additional correction value  $C_{\text{Bhabha}}$  for the lower limit with systematic uncertainty was estimated to be

$$C_{\text{Bhabha}} = (1.26 \pm 0.02) \times 10^{-2}. \quad (5.11)$$

## 5.1. LOWER LIMIT

---

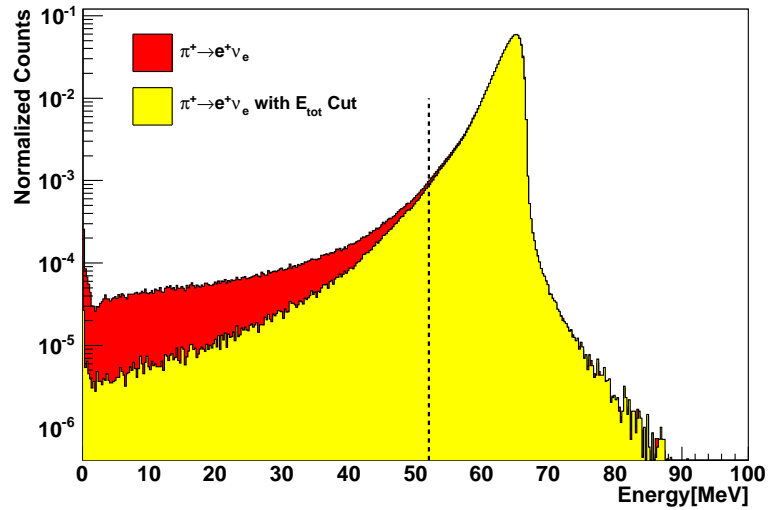


Figure 5.17: Simulated  $\pi^+ \rightarrow e^+ \nu_e (\gamma)$  events with (yellow) or without (red)  $E_{\text{tot}}$  cut. The low-energy  $\pi^+ \rightarrow e^+ \nu_e (\gamma)$  events were removed by  $E_{\text{tot}}$  cut.

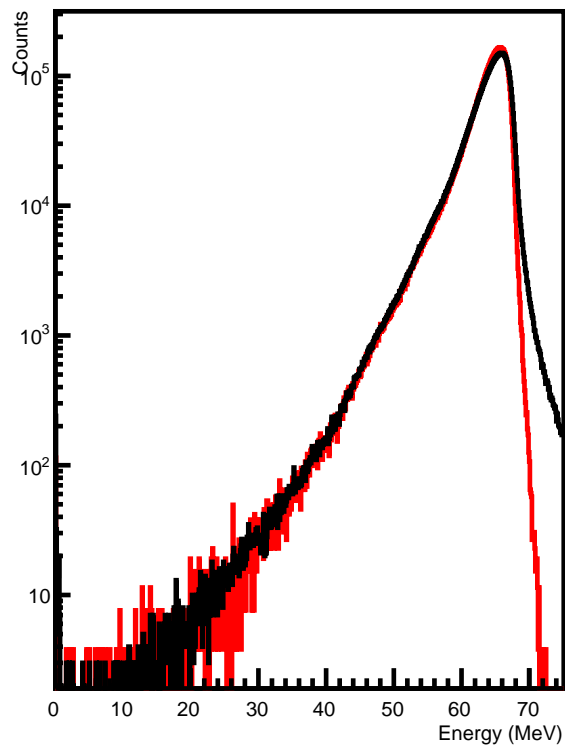


Figure 5.18: Comparison of the energy spectra between data (black) and MC (red) at 47.7 degrees.

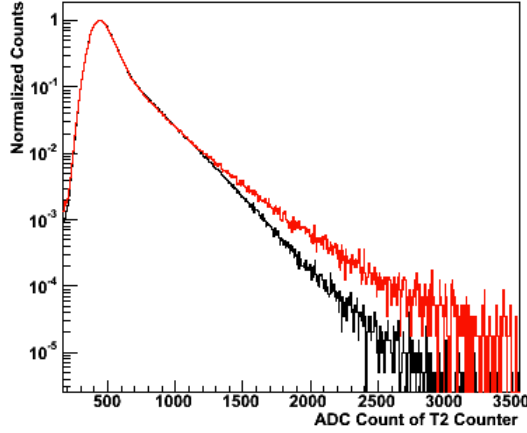


Figure 5.19: Comparison of the ADC counts in T2 between data (black) and MC (red) at 47.7 degrees. The T2 energy cut region was chosen to be less than 500 channels.

### 5.1.8 Summary of the Lower Limit

The lower limit of the tail fraction  $TF_{LL}$  with the statistical and total systematic uncertainties including Bhabha correction was estimated to be

$$TF_{LL} = TF' + C_{\text{Bhabha}} = [3.22 \pm 0.09(\text{stat}) \pm 0.05(\text{syst})]\%. \quad (5.12)$$

In order to check the unknown hidden systematic effect not discussed above, the procedure of the lower limit study was repeated using different upper bound of  $E_{\text{tot}}$  cut. The larger upper bound of  $E_{\text{tot}}$  cut increased  $\pi^+ \rightarrow e^+ \nu_e$  events but the contamination of the unsuppressed  $\pi\text{DIF}-\mu\text{DAR}$  and  $\mu\text{DIF}$  was also increased. The tighter  $E_{\text{tot}}$  cut reduced the  $\pi\text{DIF}-\mu\text{DAR}$  and  $\mu\text{DIF}$  events but  $\pi^+ \rightarrow e^+ \nu_e$  events were also removed. Figure 5.20 shows the result of the study. The upper bound of  $E_{\text{tot}}$  cut at 16.5 MeV gave the smallest statistical error on the tail fraction. Since each point in Figure 5.20 was statistically correlated, the statistical error at each point was obtained from the value at 16.5 MeV by equation of  $\sigma = \sqrt{\sigma_E^2 - \sigma_{16.5}^2}$ . The tail fractions above 16.5 MeV were consistent within the statistical fluctuations. Because many  $\pi^+ \rightarrow e^+ \nu_e$  events were removed below 16.4 MeV due to the tighter  $E_{\text{tot}}$  cut, the estimate of the lower limit was affected by poor statistics.

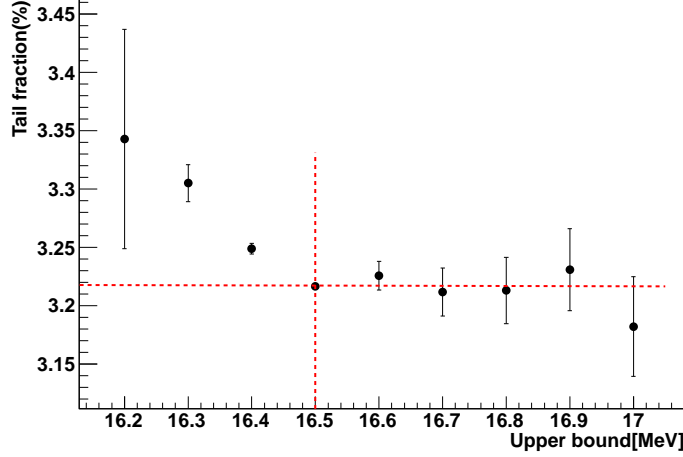


Figure 5.20: The result of the systematic study. Dashed horizontal red line indicates the central value of the tail fraction at 16.5 MeV (dashed vertical red line). The statistical errors were scaled at 16.5 MeV.

## 5.2 Upper Limit

### 5.2.1 Measurement

We performed special data taking using mono-energetic beam positrons in order to empirically estimate the  $\pi^+ \rightarrow e^+ \nu_e$  low-energy tail. The setup was simplified by removing B1, B2, B3, S1, S2 and S3 to reduce material in the path of the beam, leaving only WC1–3 and T2 (Figure 3.17). The crystal was rotated to obtain different angles of entry. Table 5.2 shows the summary of the special data sets. Tail fraction represents the integral of the energy spectrum below 52 MeV divided by the integral of the full energy spectrum. It was possible that there were also low-energy beam positrons due to scattering in the beam line. Thus, the low-energy tail obtained by these data set might be larger than an actual tail. Therefore, we could only obtain the upper limit of the low-energy tail by these measurements.

The analysis of these data sets has been completed [4]. At present, the upper limit of the  $\pi^+ \rightarrow e^+ \nu_e$  tail is the same value as in [4], but briefly discussed here.

### 5.2.2 Analysis of the Upper Limit

As it was already described in above sections, the present MC was not able to reproduce the photo-nuclear effect. Figure 5.21 shows the comparison of the energy spectra for data and MC with hadronic reactions, and the compared tail fraction between data and MC at each angle is shown in Figure 5.22. MC

## 5.2. UPPER LIMIT

Table 5.2: Summary of the special data sets and tail fractions at each angle.

Angle [°]	Number of events (Unit: $\times 10^6$ )	Tail fraction ( $E_{\text{cut}} = 52$ MeV) and statistical error (%)
0.0	6.225	$0.451 \pm 0.007$
6.0	11.136	$0.448 \pm 0.004$
11.8	6.438	$0.467 \pm 0.009$
16.5	6.965	$0.484 \pm 0.005$
20.9	6.164	$0.574 \pm 0.008$
24.4	6.128	$0.636 \pm 0.005$
30.8	5.866	$0.854 \pm 0.010$
36.2	5.893	$0.995 \pm 0.005$
41.6	6.451	$1.350 \pm 0.005$
47.7	9.079	$2.321 \pm 0.005$

simulations were performed with the same geometry and beam as the data. The difference between the tail fractions in the positron data and MC was primarily due to the photo-nuclear effect. The upper limit was estimated by using this difference to correct the tail fraction of  $\pi^+ \rightarrow e^+ \nu_e (\gamma)$  events obtained by MC.

In this procedure, the energy spectrum of beam positrons entering the NaI after traversing T2 ( $E_e$ ) and measured energy spectrum by the NaI and CsI crystals ( $E_{\text{NaICsI}}$ ) were obtained by MC. Figure 5.23 shows  $E_e$  and  $E_{\text{NaICsI}}$  spectra at 0 degrees produced by MC. The low-energy events for  $E_e$  spectrum were due to the Bhabha scattering in T2. Figure 5.24 shows the energy spectrum of the decay positrons from  $\pi^+ \rightarrow e^+ \nu_e$  events entering the NaI ( $E_{\pi e \nu}$ ) produced by MC. Since the decay positrons from  $\pi^+ \rightarrow e^+ \nu_e$  decays traveled through half of B3, S3, T1, and T2 before reaching the NaI,  $E_{\pi e \nu}$  energy distribution was different than the  $E_e$  spectrum.

The impact of energy loss in the extra material in the  $\pi^+ \rightarrow e^+ \nu_e$  case should be well-reproduced in MC, since the cross-sections of the processes are very well-known theoretically. However, the impact of the photo-nuclear effect for  $\pi^+ \rightarrow e^+ \nu_e$  events will be greater than for the positron data, since many positrons of  $\pi^+ \rightarrow e^+ \nu_e$  decays lost appreciable amounts of energy before reaching the calorimeter. This means that the event with the extra energy lost is more likely to cause the event to fall below  $E_{\text{cut}}$ .

Initially, the correction to the  $\pi^+ \rightarrow e^+ \nu_e$  tail was obtained simply from averaging the difference in the tail fractions between positron beam data and positron beam MC as a function of angle (Figure 5.22), and adding it to the tail obtained from the simulated  $\pi^+ \rightarrow e^+ \nu_e (\gamma)$  events. In order to take into account the effect just described, the  $E_{\pi e \nu}$  spectrum was sliced every 1 MeV from 52 MeV to 100 MeV, and estimated how many events fell below  $E_{\text{cut}}$ . These events were corrected by using the average difference between

### 5.3. COMBINATION OF TWO LIMITS

---

positron beam data and positron beam MC. The result of this procedure increased slightly than the initial analysis, as expected, but by less than one standard deviation, showing that this is not a sizeable effect.

#### 5.2.3 Result of the Upper Limit Estimate

The result of the upper limit for the tail fraction was

$$\text{TF}_{\text{UL}} = [3.19 \pm 0.03(\text{stat}) \pm 0.08(\text{syst})]\%. \quad (5.13)$$

Please note that it happens to be consistent with the lower limit (Eq. (5.12)).

The systematic error mainly came from the uncertainty of the beam momentum (0.04%), beam momentum spread (0.01%), energy calibration in the calorimeters (0.04%), the position of the calorimeters (0.02%), and angle ( $\theta$  in Figure 3.17) between crystal and beam axis (0.01%)<sup>2</sup>. The size of error in  $\text{TF}_{\text{UL}}$  related to beam momentum and momentum spread were respectively estimated by changing the beam momentum by  $\pm 1\%$  and momentum spread by  $\pm 10\%$  in MC. The energy calibration in the calorimeters was accurate within 0.1 MeV, so the  $E_{\text{cut}}$  was changed by  $\pm 0.1$  MeV and the effects of that were estimated. The uncertainty of the position of the calorimeters was less than 1 mm and the uncertainty of the angle between the NaI axis and the beam axis was less than 0.1 degrees; thus, the detectors were displaced in MC by these amounts.

### 5.3 Combination of Two Limits

In order to combine the two limits (Eqs. (5.12) and (5.13)), the errors were assumed to be Gaussian. The tail was allowed to take on any value higher than the lower limit, and any value lower than the upper limit. Thus, using error function including Gaussian resolution (Eq. (4.4)) and obtained the combined region from the lower and upper limits (Figure 5.25). The combined tail fraction TF was obtained to be

$$\text{TF} = (3.19 \pm 0.09)\%. \quad (5.14)$$

Please note that the tail fraction for 2010 data set was  $(3.07 \pm 0.12)\%$  [4]. The lower limit for 2010 data set was  $[2.95 \pm 0.08(\text{stat}) \pm 0.07(\text{syst})]\%$  [4]. The central value of the lower limit for 2011 data set became closer to the central value of the upper limit than that for 2010 data set. Therefore, the combined tail fraction for 2011 data set was improved.

---

<sup>2</sup>These numbers represent absolute uncertainties, not relative errors since the  $\text{TF}_{\text{UL}}$  is expressed as a percentage.

### 5.3. COMBINATION OF TWO LIMITS

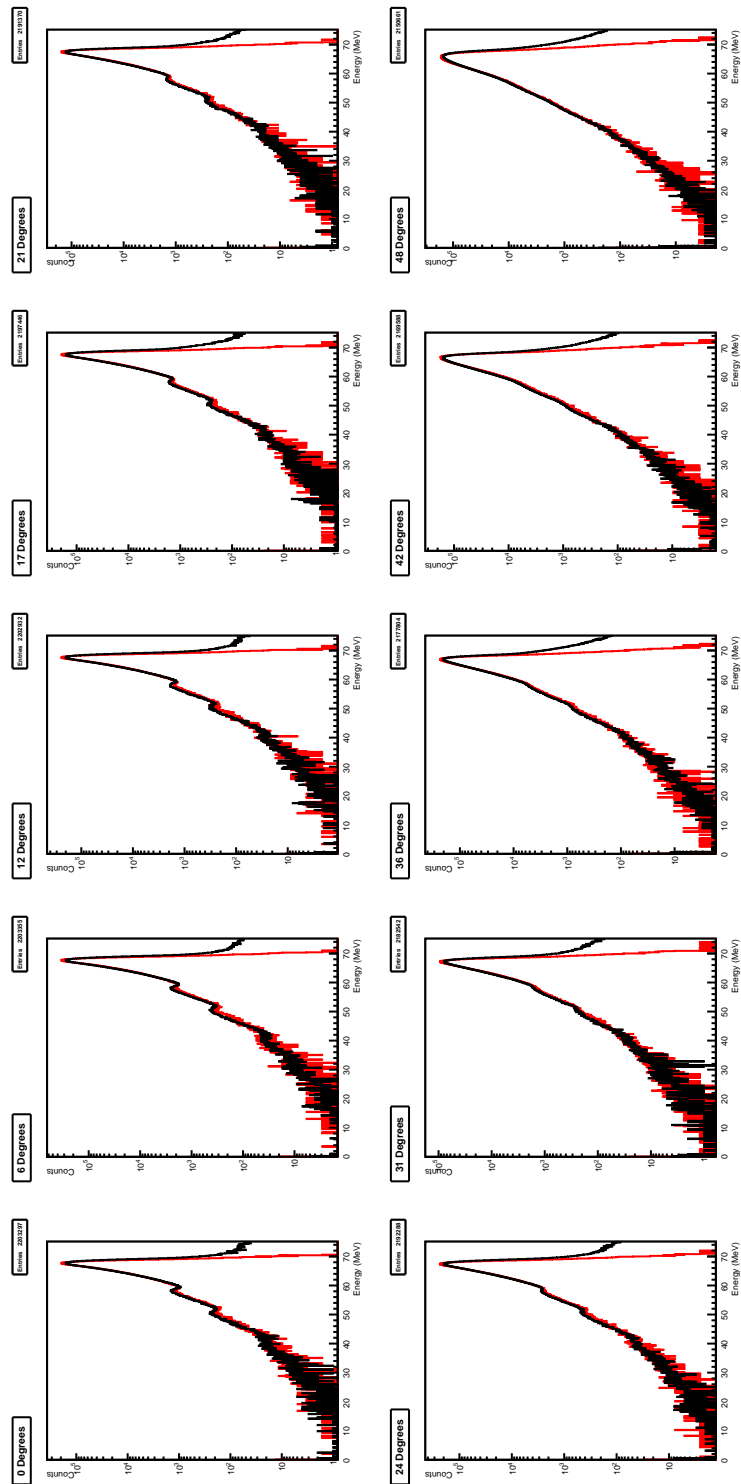


Figure 5.21: Comparison of the energy spectra between data (black) and MC (red) at each angle. The hadronic reaction was included in MC.

### 5.3. COMBINATION OF TWO LIMITS

---

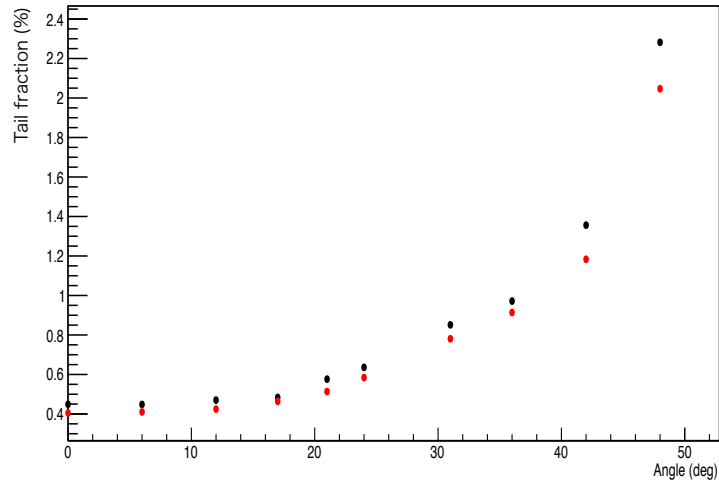


Figure 5.22: Comparison of the tail fraction between data (black) and MC (red) at each angle. Error bars are too small to be visible.

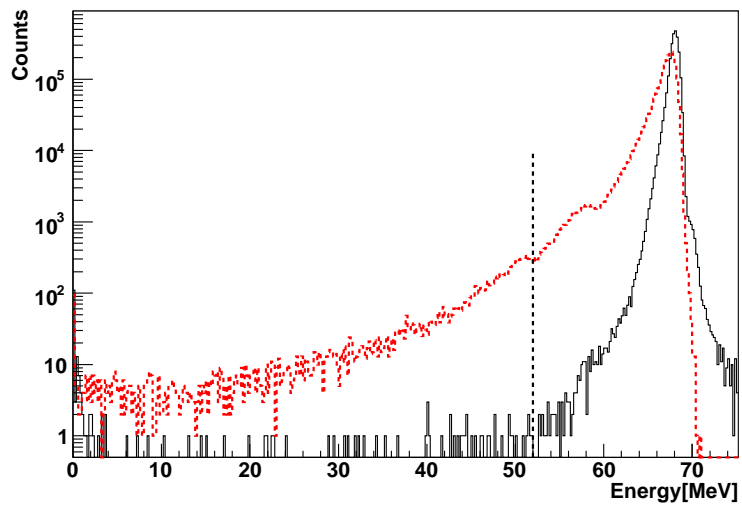


Figure 5.23:  $E_e$  (black) and  $E_{\text{NaICsI}}$  (dashed red) spectra at 0 degrees by MC. Dashed vertical black line indicates  $E_{\text{cut}}$  at 52 MeV.

### 5.3. COMBINATION OF TWO LIMITS

---

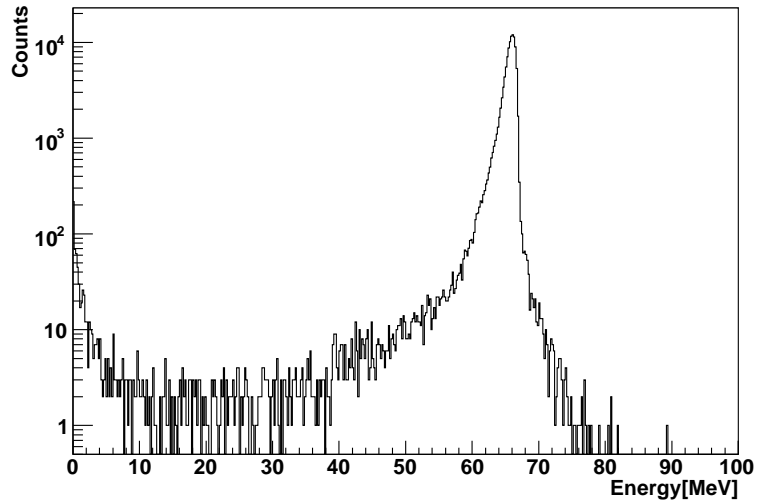


Figure 5.24:  $E_{\pi e \nu}$  spectrum for  $\pi^+ \rightarrow e^+ \nu_e$  decay produced by MC.

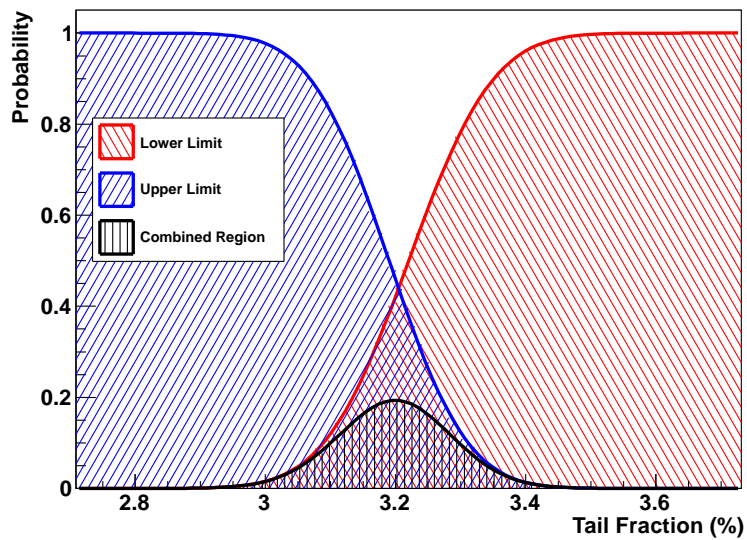


Figure 5.25: Combination of the lower (red) and upper (blue) limits. The black histogram represents the combined region of the two values.

## Chapter 6

# Systematic Correction –Acceptance Correction–

The positron acceptance for  $\pi^+ \rightarrow e^+ \nu_e$  and  $\pi^+ \rightarrow \mu^+ \rightarrow e^+$  events may be different due to the difference in their energy distributions. The correction arose from this difference is called “acceptance correction” and will be discussed in this chapter. The acceptance correction relied on MC calculations including multiple Coulomb scattering, Bhabha scattering, positron annihilation-in-flight, uncertainty of geometry, and trigger losses.

The beam momentum and its bite were different between 2010 and 2011. Additionally, the detector geometry was slightly different between 2010 and 2011 (§3.2.2). Thus, the acceptance correction for each data set was simulated with different beam information and detector geometry. MC studies for 2010 and 2011 data sets were performed. The statistical uncertainty of the acceptance correction on 2011 data set was at 0.03%.

### 6.1 Monte Carlo Calculation

The Monte Carlo calculation program was built on the Geant4 library package. The version of Geant4 package used was Geant4 9.6 patch-03 released in Mar 2014 [76]. The physics list simulation engine of Geant4 used for the studies was “QGSP\_BERT”. The simulated physics processes in this engine included electromagnetic (multiple scattering, Bremsstrahlung,  $e^+e^-$  annihilation and so on) and hadronic (elastic, inelastic of  $\pi^+$ ,  $\gamma$ - and  $e^+$ -nuclear and so on). See Refs. [77, 78] for more details of the registered physics processes in this engine. These processes were not modified from Geant4 package. The cut-off thresholds for electromagnetic processes were respectively set to 1 mm and 0.1 mm for  $\gamma$  and  $e^\pm$ .

The geometry of all detectors has been input into the MC. Dead materials which were not read out around the detectors (e.g. light guides and wrapping materials for the plastic scintillators, the steel support for the CsI crystals)

## 6.2. THE PION STOPPING POSITION

---

were also included.

The same cuts used in the data analysis were used for MC studies. The ratio of the acceptance,  $A=(\pi^+\rightarrow\mu^+\rightarrow e^+)/(\pi^+\rightarrow e^+\nu_e)$ , was obtained for the acceptance cut (§4.4.4) of the range 20–100 mm.

The systematic uncertainties were also estimated by MC simulation. The possible systematic effects are listed below.

- The pion stopping position.
- Detector geometry.
- Trigger threshold.

### 6.2 The Pion Stopping Position

An uncertainty of the pion stop position could lead to a different path length for decay positron. Therefore, the influence of different pion stopping positions along the beam axis was studied.

The track entering B3 was obtained by S1·2, and the track exiting B3 was obtained by S3 and WC3. The stopping position could be obtained from the point where two tracks took the closest distance. Figure 6.1 shows the reconstructed beam pion stopping positions along the beam axis for the standard physics data and MC for 2011 data set. The width of this distribution was about  $\sigma\simeq 2.1$  mm, which mainly came from the resolution of the track reconstruction. According to MC study, “real” beam pions stopping distribution had a width of  $\sigma\simeq 0.7$  mm (Figure 6.2).

The reconstructed distributions in Figure 6.1 for data and MC were consistent each other. The potential difference of the reconstructed distributions was a level of 0.06 mm in the mean value and 0.02 mm in the width.

The effects of stopping position was conservatively estimated by changing the stopping position up to  $\pm 0.2$  mm from the standard position in MC. Figure 6.3 shows the MC estimated effects of the pion stopping position. The ratio  $A$  at the normal position with 60 mm acceptance cut was  $0.9987\pm 0.0003(\text{stat})$  for 2011 data set. The effect of the difference in the mean stopping position was estimated to be  $\Delta A < 0.0001$ .

The cases of 10% wider and narrower stopping distribution were also simulated. Figure 6.4 shows the effects of this study. The effect of different width for stopping distribution was estimated to be  $\Delta A < 0.0001$ .

### 6.3 Detector Geometry

The position uncertainty of S3 and WC3 might contribute to the reconstruction of the decay positrons. The different detector thickness also changes the path length of the decay positrons. Table 6.1 lists the position uncertainty

### 6.3. DETECTOR GEOMETRY

---

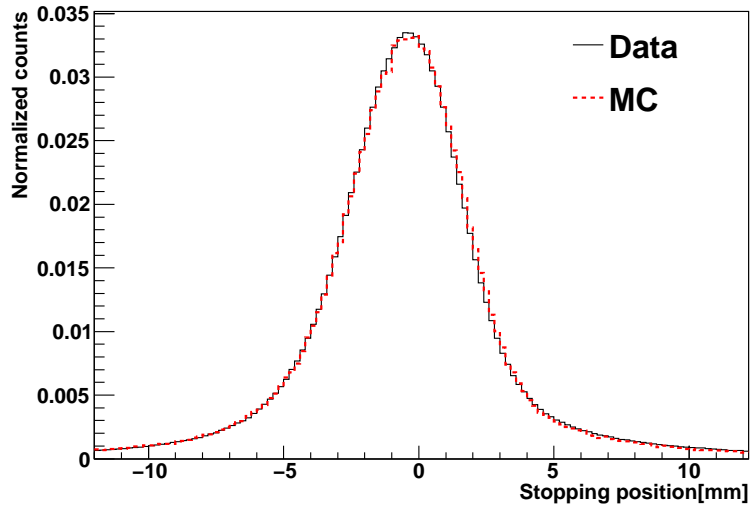


Figure 6.1: Reconstructed pion stopping position with data (black) and MC (dashed red) for 2011 data set.

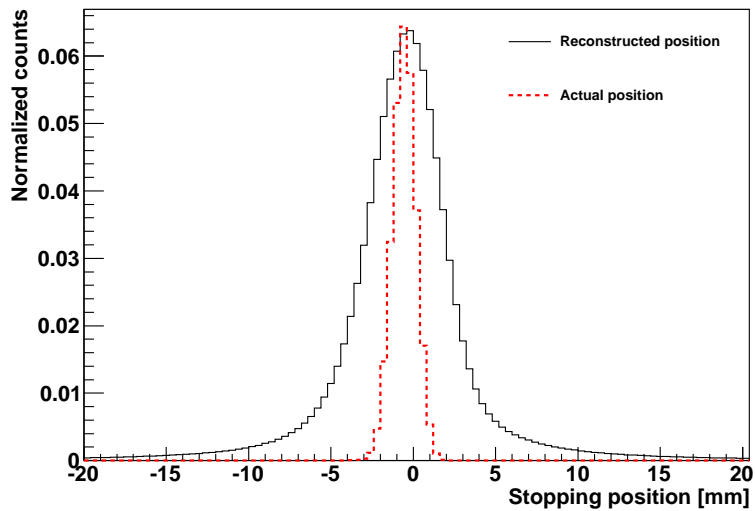


Figure 6.2: Comparison of the reconstructed (black) and actual (red) pion stopping distributions by MC (2011 data set).

### 6.3. DETECTOR GEOMETRY

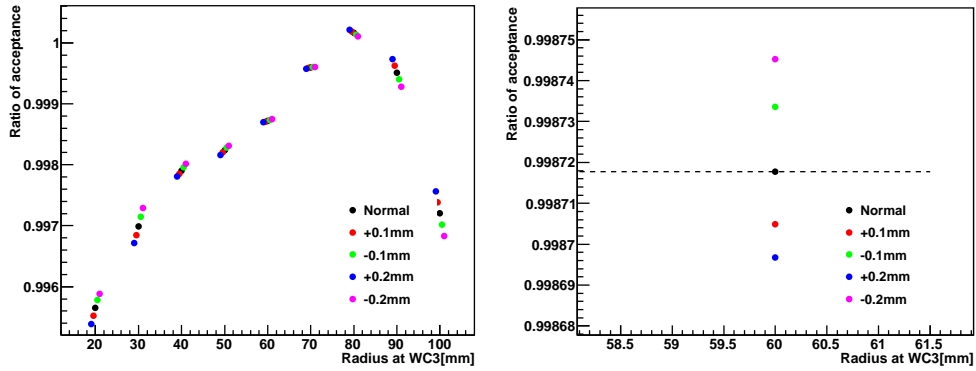


Figure 6.3: Result of the variation due to the different pion stopping position along the beam axis at each radius cut point (left) and zoom-in at 60 mm (right) (2011 data set).

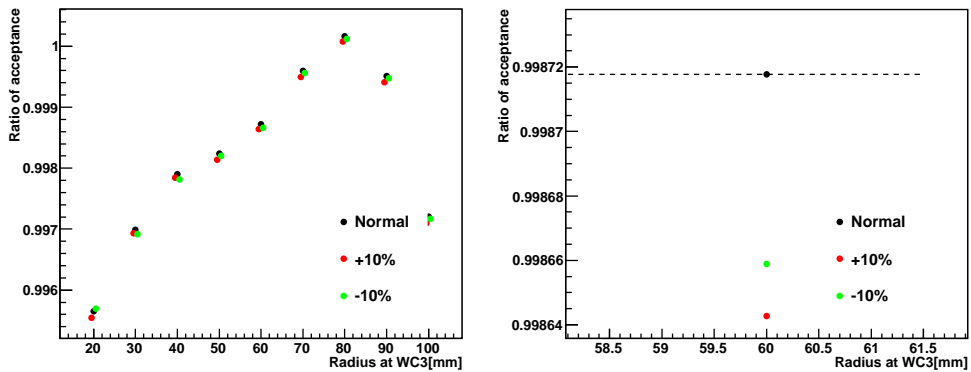


Figure 6.4: Result of the variation due to the different width of stopping distribution at each radius cut point (left) and zoom-in at 60 mm (right) (2011 data set).

## 6.4. TRIGGER THRESHOLD

---

Table 6.1: Uncertainties in the detector geometry measurement [3].

Detector	Measurement uncertainty [mm]
Z position of S3	0.100
Z position of WC3	2.000
Thickness of B3	0.025
Thickness of T1	0.090
Thickness of S3	0.005
X/Y position of S3	0.005
X/Y position of WC3	0.200

of each detector [3]. The geometry uncertainty of T2 does not influence the positron acceptance since T2 was located downstream of S3 and WC3.

The size of positron acceptance uncertainties were estimated by displacing the position of S3 and WC3. The different thickness of B3, T1, and S3 were also simulated. The result showed that those effects of detector geometry were extremely small,  $\Delta A < 0.00002$ .

## 6.4 Trigger Threshold

As described in §3.2 and 3.3, the coincidence of T1 and T2 was used for the trigger. In the data, on-line thresholds in T1 and T2 were set around 100 keV. Since the energy loss in matter depends on the energy of the decay positron, so if the thresholds were adjusted to wrong energy, the different on-line trigger inefficiency between  $\pi^+ \rightarrow e^+ \nu_e$  and  $\pi^+ \rightarrow \mu^+ \rightarrow e^+$  events might occur. The MC study was performed with increasing the energy thresholds of T1 and T2 up to 200 keV. Figure 6.5 shows the effects of threshold energy. The effect of the different energy threshold was estimated to be  $\Delta A = 0.0002$ .

## 6.5 Summary of Acceptance Correction

The acceptance correction with systematic uncertainties for 2010 data set was estimated with the same procedure discussed above. The multiplicative correction values (namely  $A$ ) with uncertainties for 2010 and 2011 data sets were respectively estimated to be

$$A_{2010} = 0.9991 \pm 0.0003(\text{syst}) \text{ (for 2010 data set [4])} \quad (6.1)$$

$$A_{2011} = 0.9987 \pm 0.0003(\text{stat}) \pm 0.0002(\text{syst}) \text{ (for 2011 data set)}. \quad (6.2)$$

The magnitude of systematic uncertainty in each data set was almost the same. Since the simulations for 2010 data were performed with 10 times more number of events than 2011 data set, the statistical error on 2010 data set was less than 0.0001, which was neglected in Eq. (6.1) .

## 6.5. SUMMARY OF ACCEPTANCE CORRECTION

---

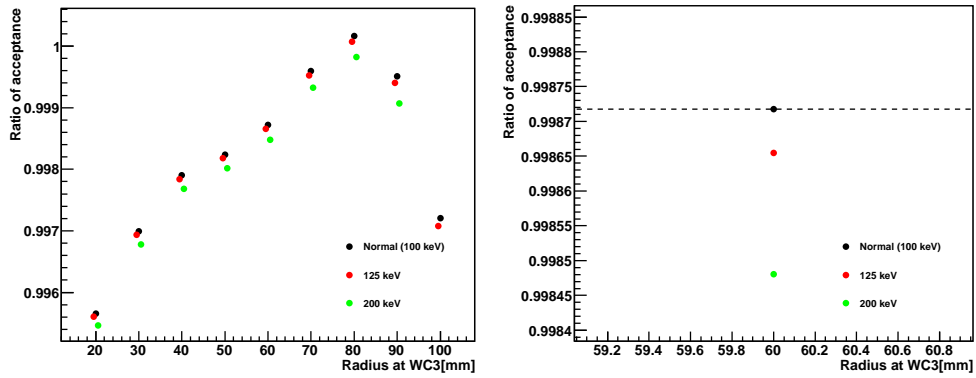


Figure 6.5: Result of the variation due to the different energy threshold of T1 and T2 at each radius cut point (left) and zoom-in at 60 mm (right) (2011 data set).

# Chapter 7

## Result

### 7.1 Measured Ratio of the Branching Ratios

Table 7.1 shows the result of the fit uncertainties and corrections in 2010 and 2011 data sets. The result for the measured ratio  $R_{\text{exp}}^\pi$  for 2010 data set was completed and published [4], and at present, the result of 2011 data set remains blinded. All systematic studies of 2011 data set were completed and improved compared to the result of 2010 data set.

If the central value of  $R_{\text{exp}}^\pi$  for 2011 data set is assumed to be the SM predicted value, and the common systematic uncertainties on 2010 and 2011 data sets are assumed to be the values of 2011 analysis, the uncertainty of the combined  $R_{\text{exp}}^\pi$  is

$$\Delta R_{\text{exp}}^\pi = [\pm 0.0014(\text{stat}) \pm 0.0013(\text{syst})] \times 10^{-4}. \quad (7.1)$$

### 7.2 Systematic Checks

Checking the stability of  $R_{\text{exp}}^\pi$  against major analysis parameters is very important to search for unknown systematics. The success of the check provides the validity of the corrections and background estimates. The study of the stability for 2010 was already completed and any systematic dependence was not found [4]. Figure 7.1 and 7.2 show the results of  $E_{\text{cut}}$  and the acceptance cut studies for 2011 data set. The time fit, tail correction, and acceptance correction were reanalyzed using each cut condition. There was no systematic dependence on the stability tests and confirmed validity of the analysis on 2011 data set.

## 7.2. SYSTEMATIC CHECKS

Table 7.1: Summary of the ratio of the pion branching ratios before corrections  $R_{\text{raw}}^\pi$ , the multiplicative corrections, and the result after applying the corrections with their uncertainties in 2010 [4] and 2011.  $R_{\text{raw}}^\pi$  for 2011 data set is still blinded, so it is represented by asterisks.

	2010			2011		
	Values	Uncertainties		Values	Uncertainties	
		Stat	Syst		Stat	Syst
$R_{\text{raw}}^\pi (\times 10^{-4})$	1.1972	0.0022	0.0006	1.****	0.0017	0.0006
Corrections						
Low-energy tail	1.0316		0.0012	1.0330		0.0009
Acceptance	0.9991		0.0003	0.9987	0.0003	0.0002
$t_0$ energy dependence	1.0004		0.0005	1.0006		0.0003
$R_{\text{exp}}^\pi (\times 10^{-4})$	1.2344	0.0023	0.0019	1.****	0.0018	0.0013

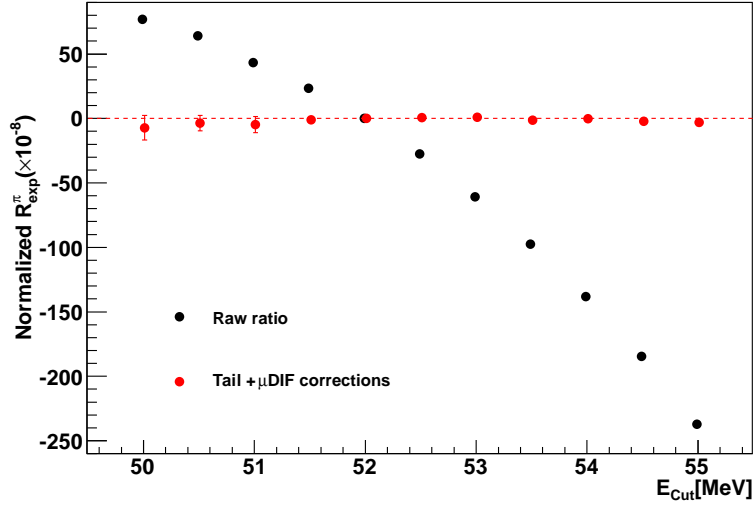


Figure 7.1:  $E_{\text{cut}}$  dependence for 2011 data set before (black) and after (red) corrections.  $R_{\text{exp}}^\pi$  were normalized to the value at 52 MeV.

## 7.2. SYSTEMATIC CHECKS

---

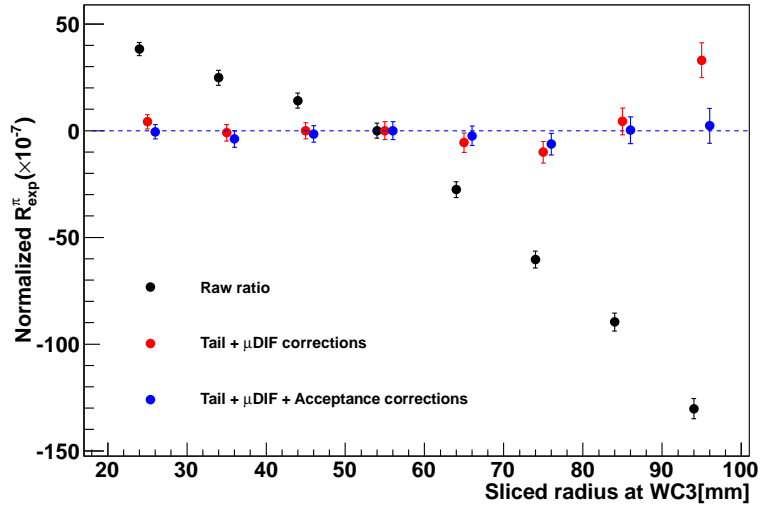


Figure 7.2: Dependence of the radius cut at WC3 (§4.4.4) for 2011 data set before (black) correction and after tail plus  $\mu$ DIF corrections (red) and all corrections (blue). In order to exclude the statistical correlation, 10 mm sliced cut was applied. For example, the cut value at 55 mm represents the radius cut with a range of 50 to 60 mm. The value of  $R_{\text{exp}}^{\pi}$  at each radius cut were normalized to the value at 55 mm.

# Chapter 8

## Discussion

### 8.1 Limits on Theoretical Models

$\pi^+ \rightarrow e^+ \nu_e$  events analyzed in this thesis were about  $10^6$  decays, which corresponded to about 7 times larger statistics than the previous TRIUMF experiment. Thus, the statistical uncertainty was reduced by a factor 2.5.

Compared to the previous TRIUMF experiment, the systematic uncertainty on  $R_{\text{raw}}^\pi$  was improved by a factor of 4. Since we carefully estimated the background components using data and pulse shapes of the calorimeters, and a better time fit could be obtained due to better time measurement devices.

The dominant systematic source came from the correction of low-energy  $\pi^+ \rightarrow e^+ \nu_e$  tail. The  $\pi$ DIF events in the  $\pi^+ \rightarrow \mu^+ \rightarrow e^+$  suppressed spectrum were reduced due to the additional trackers S1–3 and pulse shape analysis by better waveform digitizers. The larger statistics also reduced the uncertainty of the lower limit. Since the measurements using positron beam were performed, we could obtain the value of the upper limit. Consequently, the uncertainty on the tail correction was improved by a factor 2.8.

The acceptance correction depends on the size of the detector acceptance. The uncertainty on the acceptance correction was improved due mainly to the larger acceptance of the PIENU detector.

The  $t_0$  energy dependence highly depends on the statistics. Since the additional muon data were taken in 2011, we could achieve precision of a 0.03% level.

#### 8.1.1 Limit on Lepton Universality

The limit on the universality test of 2010 data set is  $g_\mu/g_e = 1.0004 \pm 0.0012$  [4]. Using the combined result of 2010 and 2011 data sets, the uncertainty of  $g_\mu/g_e$  will be improved to 0.0009. This is more than factor 1.5 better than the uncertainty comes from  $\tau$  decay process shown in Table 1.5.

### 8.1.2 Sensitivity to Pseudoscalar Interaction

According to Eq. 1.20, the result of  $R_{\text{exp}}^\pi$  for 2010 data set gave sensitivity to new pseudoscalar up to mass scale  $\Lambda$  of 500 TeV/ $c^2$  [4]. Using the combined result, a 0.15% of  $R_{\text{exp}}^\pi$  allows potential access to  $\Lambda$  up to 820 TeV/ $c^2$ .

### 8.1.3 Limits on Massive Neutrino

As described in §1.3.3, the  $\pi^+ \rightarrow e^+ \nu_e$  measurement is much sensitive to the massive neutrino search. An initial analysis on massive neutrino with extra peak search was performed by K. Yamada [2] using data set taken in the summer 2009. The analysis was subsequently refined and published in Physical Review D [54]. Compared to the previous experiment [53], the upper limits on the neutrino mixing parameter  $|U_{ei}|^2$  was improved by a factor of up to 4 in the mass range of 68 to 129 MeV/ $c^2$ . The upper limit on the massive neutrino in the mass range below 55 MeV/ $c^2$  was analyzed by the  $R^\pi$  measurement, which was first published in Physical Review Letters [4].

At present, the analysis of the extra peak search using another data set is not completed. Thus, in this section, the only the latest result of the upper limit to the massive neutrino search by the  $R^\pi$  measurement is discussed.

### Brief Introduction of the Theory

Since pion decay is a two-body decay, the neutrino mass can be obtained from the equation:

$$m_\nu = \sqrt{m_\pi^2 + m_e^2 - 2m_\pi^2 E_e}, \quad (8.1)$$

where  $m_\nu$  is the neutrino mass,  $E_e$  and  $m_e$  are respectively the positron energy and mass, and  $m_\pi$  is the pion mass. If neutrinos have finite masses, the  $R^\pi$  is affected due to the change in the phase space, and an extra peak at low-energy could be detected. Some models predict the mixing of massive sterile neutrinos with ordinary neutrinos. The example of a sterile neutrino model is the Neutrino Minimal Standard Model that adds to the SM three massive gauge-singlet fermions (sterile neutrinos) [79]. The weak eigenstates  $\nu_{\chi_k}$  of such neutrinos are related to the mass eigenstates  $\nu_i$  by the neutrino mixing parameter  $U_{li}$ :

$$\nu_l = \sum_{i=1}^{3+k} U_{li} \nu_i, \quad (8.2)$$

where  $l = e, \mu, \tau, \chi_1, \dots, \chi_k$ .

For the kinematics,  $\pi^+ \rightarrow e^+ \nu_e$  decay is sensitive to the mass range of neutrino 0–130 MeV/ $c^2$ . The ratio of the decay to massive and normal neutrinos  $R_{ei} = \Gamma(\pi \rightarrow e \nu_i) / \Gamma(\pi \rightarrow e \nu_e)$  is related to the mixing parameter

with kinematic factor  $\rho_e$  by following equations:

$$R_{ei} = \frac{\Gamma(\pi \rightarrow e\nu_i)}{\Gamma(\pi \rightarrow e\nu_e)} = |U_{ei}|^2 \rho_e, \quad (8.3)$$

$$\rho_e = \frac{(\delta_e + \delta_i - (\delta_e - \delta_i)^2) \sqrt{1 + \delta_e^2 + \delta_i^2 - 2(\delta_e + \delta_i + \delta_e \delta_i)}}{\delta_e (1 - \delta_i)^2}, \quad (8.4)$$

$$\delta_e = \frac{m_e^2}{m_\pi^2}, \quad \delta_i = \frac{m_{\nu_i}^2}{m_\pi^2}, \quad (8.5)$$

where  $m_{\nu_i}$  is the mass of a massive neutrino.

### Limit from $R^\pi$ Measurement

The measured ratio we obtained from 2010 data set was [4]

$$R_{\text{exp}}^\pi = [1.2344 \pm 0.0023(\text{stat}) \pm 0.0019(\text{syst})] \times 10^{-4}. \quad (8.6)$$

In order to estimate the 90% C.L. upper limit on the neutrino mixing parameter  $U_{ei}$  between the weak electron-neutrino eigenstate and a hypothetical mass eigenstate  $\nu_i$ , the Feldman's and Cousins' method [80] was used. We obtained the limit in mass range of  $< 55 \text{ MeV}/c^2$  using the equation

$$|U_{ei}|^2 = \frac{r - 1}{\rho_e - 1} < \frac{0.0033}{\rho_e - 1}, \quad (8.7)$$

where  $r$  is the upper limit of the probability for the ratio  $R_{\text{exp}}^\pi/R_{\text{SM}}^\pi$  at 90% C.L.,

$$r = \frac{R_{\text{exp}}^\pi}{R_{\text{SM}}^\pi} \leq 1.0033. \quad (8.8)$$

Figure 8.1 shows the results of the upper limit to the massive neutrino in the PIENU experiment and previous work in 1992 [53]. The upper limit for the combined results was calculated with the assumption that the central value of  $R_{\text{exp}}^\pi$  for 2011 data set is the SM predicted value. The result of the combined  $R_{\text{exp}}^\pi$  will improve the upper limit of the massive neutrino by a factor of 2.

## 8.2 Foreseen Improvements

### 8.2.1 Lepton Universality Test

#### Statistical Uncertainty

The statistics used in this thesis corresponds to about 25% of full data set. Therefore, the statistical uncertainty will be improved by at least a factor of 2.

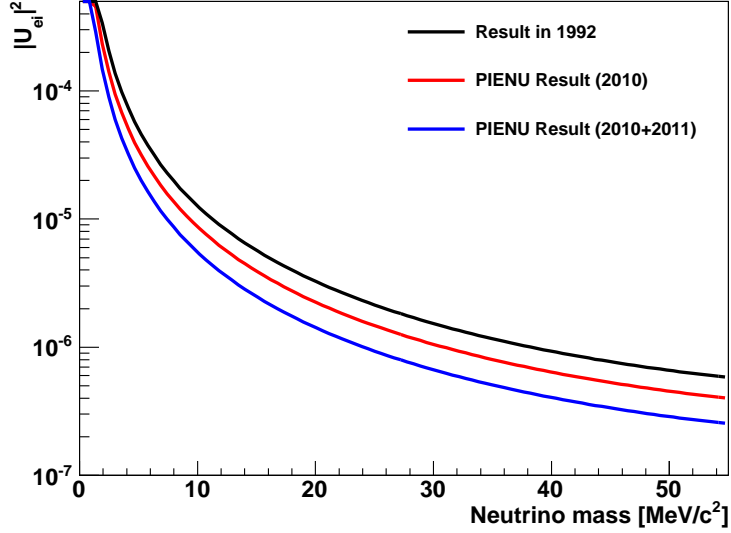


Figure 8.1: Upper limits to the mixing parameter  $U_{ei}$  in the mass range of  $< 55 \text{ MeV}/c^2$ . Compared to the previous work (black), the PIENU result in 2010 (red) improved by a factor of 1.5, and the combined PIENU result will improve by a factor of 2.

At present, the acceptance cut at WC3 with 60 mm was used to reduce the amount of  $\pi^+ \rightarrow e^+ \nu_e$  tail (§4.4.4). However, we confirmed that  $R_{\text{exp}}^\pi$  did not depend on the size of the acceptance cut (§7.2), and the systematic uncertainties on the tail and acceptance corrections at 70 mm were almost the same magnitude with those at 60 mm. If 70 mm instead of 60 mm is chosen for the acceptance cut, the statistics will increase by about 20%.

Additionally, the full range of the Pre-region was used for the pre pileup cut. Since we also checked that the choice for the range of the pre pileup cut did not affect  $R_{\text{raw}}^\pi$  (§4.5.4). If pre pileup cut is not used, the statistics will increase by about 10%.

### Systematic Uncertainty

The main systematic uncertainty came from the tail correction. The lower limit of the tail correction depends on the statistics of  $\pi^+ \rightarrow e^+ \nu_e$  events. Thus, the uncertainty on the lower limit will be improved by a factor of 2.

The difference of  $\pi^+ \rightarrow e^+ \nu_e$  energy spectrum between data and MC was due to the photo-nuclear effect in the NaI. Currently, we are tuning the code of Geant4 package about neutron's cross-section and photo-nuclear process to adjust the bumps of photo-nuclear effect. If the energy dependence on the cross-sections of  $\gamma$ -neutron reaction is well understood, a tuned MC can

reproduce the photo-nuclear effect. If a tuned MC is in good agreement with the special positron data set used for the upper limit estimate, we could use the MC shape for the tail estimation and it will improve the uncertainty on the tail correction.

Additionally, another special positron data were taken to estimate the contamination of the low-energy beam positron. The special data taking was performed with different tuned magnets and the width of the slits. The work of MC using G4 beamline package [81] is ongoing. If the effect of the contamination with low-energy positron is precisely estimated, the upper limit of the tail could be used as an actual tail fraction.

### 8.2.2 Sensitivity to Pseudoscalar Interaction

If the statistical and systematic uncertainties on  $R_{\text{exp}}^\pi$  is respectively improved and  $R_{\text{exp}}^\pi$  is obtained with 0.1% precision, the sensitivity to the mass scale of pseudoscalar  $\Lambda$  will be up to 1000 TeV/ $c^2$ .

If we obtain non-standard value of  $R_{\text{exp}}^\pi$ , new interactions or hypothetical particles can be included in physics. Alternatively if the result of the  $R_{\text{exp}}^\pi$  measurement is consistent with the SM, we can set tighter constraints on new physics. For example, as shown in Figure 1.7, the current limit on R-Parity violation SUSY will be constrained to the region shown by dashed red curve.

### 8.2.3 Massive Neutrino Analysis

Since the full statistics is about four times than the data set used in this analysis, the upper limit of the massive neutrino could be improved by at least factor of 2.

The extra peak search can be performed using  $\pi^+ \rightarrow \mu^+ \rightarrow e^+$  suppressed spectrum fitted to a function sum of the  $\pi^+ \rightarrow e^+ \nu_e$ ,  $\pi$ DIF- $\mu$ DAR,  $\mu$ DIF, and extra peak energy spectra. This method is similar to that described in chapter 5. Therefore, the extra peak search will quickly be completed because the tail analysis of 2010 and 2011 data set was completed. The remaining things are only optimization of the suppression cut for the neutrino search and to perform the suppressed spectrum fit. Extra peak search also highly depends on the amount of  $\pi^+ \rightarrow e^+ \nu_e$  events. Thus, we could expect at least a factor of 3 improvement over the current limit on  $|U_{ei}|^2$ .

## Chapter 9

# Conclusion

The PIENU experiment was performed at TRIUMF in Canada to measure the ratio of the pion branching ratios  $R^\pi = \Gamma[\pi^+ \rightarrow e^+ \nu_e(\gamma)] / \Gamma[\pi^+ \rightarrow \mu^+ \nu_\mu(\gamma)]$  with less than 0.1% of precision. The data taking was done by 2012, and we collected about  $6 \times 10^6$   $\pi^+ \rightarrow e^+ \nu_e$  events, which corresponds to about 30 times statistics than the previous experiment at TRIUMF. I analyzed the data set taken in Run-IV (2010) and -V (2011).

First of all, the time spectra analysis was performed. I estimated all the background shapes, and the number of events for each component, and included in the fitting functions. I also evaluated the statistical and systematic uncertainties of the raw ratio  $R_{\text{raw}}^\pi$ . The systematic uncertainty of  $R_{\text{raw}}^\pi$  was improved by a factor of 4. The  $\mu$ DIF correction was estimated using MC, and special muon data sets taken in 2010 and 2011 were analyzed to estimate the energy dependence of  $t_0$ . The effect of the uncertainty on  $\mu$ DIF correction was small enough to be negligible. Compared to the previous TRIUMF experiment, the uncertainty of the energy dependence of  $t_0$  was improved by a factor of 3.

Second, the low-energy  $\pi^+ \rightarrow e^+ \nu_e$  tail correction, which is the most dominant systematic uncertainty, was estimated. Tail correction was evaluated using two methods, suppressing dominant  $\pi^+ \rightarrow \mu^+ \rightarrow e^+$  events to obtain the lower limit, and using mono-energetic positron beam for the upper limit. I analyzed the lower limit of the low-energy  $\pi^+ \rightarrow e^+ \nu_e$  tail. Compared to the previous experiment, the uncertainty of the combined correction value of two limits was improved by factor of 2.8.

Third, the acceptance correction was estimated using MC. I simulated all the possible bias for the difference of the relative acceptance between  $\pi^+ \rightarrow e^+ \nu_e$  and  $\pi^+ \rightarrow \mu^+ \rightarrow e^+$  events. Compared to the previous experiment, the uncertainty of the acceptance correction was improved by a factor of 3.

Finally, I concluded all the uncertainties, and the result of the analysis for Run-IV was  $R_{\text{exp}}^\pi = [1.2344 \pm 0.0023(\text{stat}) \pm 0.0019(\text{syst})] \times 10^{-4}$ . The Run-V data set is still blinded, but the analysis of all the uncertainties was

---

completed. Combined result of two data sets was  $\Delta R_{\text{exp}}^\pi = [\pm 0.0014(\text{stat}) \pm 0.0013(\text{syst})] \times 10^{-4}$ . The combined uncertainty of  $R_{\text{exp}}^\pi$  will be 0.15%, which could improve the test of electron-muon universality compared to the previous TRIUMF experiment by factor of 2.6.

Using the full statistics, the uncertainty of  $R_{\text{exp}}^\pi$  will be improved by at least a factor of 2. This precision will allow access to the sensitivity to the mass scale of pseudoscalar interaction up to 1000 TeV/ $c^2$ .

# Bibliography

- [1] A. Aguilar-Arevalo *et al.*, Nucl. Instrum. Methods. A791, 38, 2015. <http://dx.doi.org/10.1016/j.nima.2015.04.004>
- [2] K. Yamada. “Search for massive neutrinos in  $\pi^+ \rightarrow e^+ \nu_e$  decay”, Ph.D Thesis, Osaka University, 2010.
- [3] C. Malbrunot. “Study of  $\pi^+ \rightarrow e^+ \nu_e$  decay”, Ph.D Thesis, University of British Columbia. 2012.
- [4] A. Aguilar-Arevalo *et al.*, Phys. Rev. Lett. 115, 071801, 2015 <http://dx.doi.org/10.1103/PhysRevLett.115.071801>
- [5] A. Palladino. “Investigating Lepton Universality via a Measurement of the Positronic Pion Decay Branching Ratio”. Ph.D Thesis, University of Virginia, 2012.
- [6] F. Abe, *et al.*, Phys. Rev. Lett. 74, 2626. 1995. <http://dx.doi.org/10.1103/PhysRevLett.74.2626>
- [7] S. Abachi, *et al.*, Phys. Rev. Lett. 74, 2422. 1995. <http://dx.doi.org/10.1103/PhysRevLett.74.2422>
- [8] K. Kodama, *et al.*, Phys. Lett. B. 504. 3. 2001. [http://dx.doi.org/10.1016/S0370-2693\(01\)00307-0](http://dx.doi.org/10.1016/S0370-2693(01)00307-0)
- [9] F. Englert and R. Brout. Phys. Rev. Lett. 13, 321. 1964 <http://dx.doi.org/10.1103/PhysRevLett.13.321>
- [10] Peter W. Higgs. Phys. Rev. Lett. 13, 508. 1964 <http://dx.doi.org/10.1103/PhysRevLett.13.508>
- [11] G. Aad, *et al.*, Phys. Lett. B. 716. 1. 2012. <http://dx.doi.org/10.1016/j.physletb.2012.08.020>
- [12] S. Chatrchyan, *et al.*, Phys. Lett. B. 716. 1. 2012. <http://dx.doi.org/10.1016/j.physletb.2012.08.021>
- [13] Web page. <http://home.cern/about/updates/2013/03/question-spin-new-boson>

## BIBLIOGRAPHY

---

- [14] H. Yukawa. On the Interaction of Elementary Particles. I. Proc. Physico-Math. Soc. Japan, 17:48—57, 1935.
- [15] C. M. G. Lattes, H. Muirhead, G. P. S. Occhialini, C. F. Powell. Processes involving charged mesons. *Nature*, 159:694-697 (1933).
- [16] K. A. Olive *et al.*, (Particle Data Group), *Chin. Phys.* C38 090001 (2014) and 2015 update. <http://pdg.lbl.gov/>
- [17] H. L. Anderson and C. Lattes. Search for the electronic decay of the positive pion. *Il Nuovo Cimento* (1955-1965), 6:1356-1381, 1957.
- [18] T. Fazzini *et al.* Phys. Rev. Lett.,1. 247, 1958. <http://dx.doi.org/10.1103/PhysRevLett.1.247>
- [19] H. L. Anderson *et al.* Phys. Rev., 119. 2050, 1960. <http://dx.doi.org/10.1103/PhysRev.119.2050>
- [20] E. Di Capua, R. Garland, L. Pondrom, and A. Strelzo. Phys. Rev., 133. B1333. 1964. <http://dx.doi.org/10.1103/PhysRev.133.B1333>
- [21] D. A. Bryman, *et al.*, Phys. Rev. D, 33(5):1211. 1986. <http://dx.doi.org/10.1103/PhysRevD.33.1211>
- [22] D. I. Britton, *et al.*, Phys. Rev. Lett. 68, 3000. 1992. <http://dx.doi.org/10.1103/PhysRevLett.68.3000>
- [23] D. I. Britton, *et al.*, Phys. Rev. D, 49(1):28. 1994. <http://dx.doi.org/10.1103/PhysRevD.49.28>
- [24] G. Czapek *et al.*, Phys. Rev. Lett., 70(1):17. 1993. <http://dx.doi.org/10.1103/PhysRevLett.70.17>
- [25] S. M. Berman, Phys. Rev. Lett. 1 468 1958. <http://dx.doi.org/10.1103/PhysRevLett.1.468>
- [26] T. Kinoshita, Phys. Rev. Lett. 2, 477 1959. <http://dx.doi.org/10.1103/PhysRevLett.2.477>
- [27] T. Goldman and W. J. Wilson, Phys. Rev. D 14 2428 1976. <http://dx.doi.org/10.1103/PhysRevD.14.2428>
- [28] W. J. Marciano and A. Sirlin, Phys. Rev. Lett. 36, 1425 1976. <http://dx.doi.org/10.1103/PhysRevLett.36.1425>
- [29] T. Goldman and W. J. Wilson, Phys. Rev. D 15 709 1977. <http://dx.doi.org/10.1103/PhysRevD.15.709>

## BIBLIOGRAPHY

---

- [30] D. Bryman, *et al.*, Ann. Rev. Nucl. Part. Sci. 61, 331 2011. <http://www.annualreviews.org/doi/abs/10.1146/annurev-nucl-102010-130431>
- [31] V. Cirigliano and I. Rosell, JHEP 0710, 005 (2007). <http://iopscience.iop.org/article/10.1088/1126-6708/2007/10/005/meta;jsessionid=671027DAAA8783993D2C53268EE5B5DE.c2.iopscience.cld.iop.org>
- [32] R. Aaij *et al.*, Phys. Rev. Lett. 113, 151601. 2014. <http://dx.doi.org/10.1103/PhysRevLett.113.151601>
- [33] A. Pich. Nucl. Phys. Proc. Suppl., 181. 300. 2008. <http://dx.doi.org/10.1016/j.nuclphysbps.2008.09.054>
- [34] A. Lusiani. *et al.*, PoS, ICHEP2010:251, 2010. [http://pos.sissa.it/archive/conferences/120/251/ICHEP%202010\\_251.pdf](http://pos.sissa.it/archive/conferences/120/251/ICHEP%202010_251.pdf)
- [35] C. Lazzeroni *et al.*, Phys. Lett. B., 698 2 105, 2011. <http://dx.doi.org/10.1016/j.physletb.2011.02.064>
- [36] W. Loinaz *et al.*, Phys Rev D70 113004 2004. <http://dx.doi.org/10.1103/PhysRevD.70.113004>
- [37] K. Nakamura *et al.*, J. Phys. G 37:075021 2010. <http://iopscience.iop.org/article/10.1088/0954-3899/37/7A/075021/meta>
- [38] S. Davidson, D. Bailey, and B. Z. Campbell., Phys. C 61 613-644 1994. And B.Campbell and A. Ismail. arXiv:0810.4918 [hep-ph] 2008.
- [39] O. Shanker. Nuclear Physics B, 204(3):375-386. 1982 [http://dx.doi.org/10.1016/0550-3213\(82\)90196-1](http://dx.doi.org/10.1016/0550-3213(82)90196-1)
- [40] B. A. Campbell and D. W. Maybury. Nucl. Phys. B 709. 419. 2005. <http://dx.doi.org/10.1016/j.nuclphysb.2004.12.015>
- [41] R. Barbier *et al.*, Phys.Rept.420:1-202,2005. <http://dx.doi.org/10.1016/j.physrep.2005.08.006>
- [42] M. J. Ramsey-Musolf *et al.*, Phys. Rev. D76, 095017,2007. <http://dx.doi.org/10.1103/PhysRevD.76.095017>
- [43] M. J. Ramsey-Musolf, Phys. Rev. D 62, 056009 2000. <http://dx.doi.org/10.1103/PhysRevD.62.056009>
- [44] D. V. Barger *et al.*, Phys. Lett. B 480, 149 2000. [http://dx.doi.org/10.1016/S0370-2693\(00\)00401-9](http://dx.doi.org/10.1016/S0370-2693(00)00401-9)
- [45] Qweak Collaboration: R. Carlini, J.M. Finn, S. Kowalski, and S. Page, spokespersons, JLab Experiment E-02-020.

## BIBLIOGRAPHY

---

- [46] D. Androic *et al*, Phys. Rev. Lett. 111, 141803. 2013. <http://dx.doi.org/10.1103/PhysRevLett.111.141803>
- [47] J. Schechter and J.W.F. Valle, Phys. Rev. D 22, 2227 1980. <http://dx.doi.org/10.1103/PhysRevD.22.2227>
- [48] J. Ellis *et al.*, Nucl. Phys. B 182 529, 1981.
- [49] O. Shanker, TRIUMF prepring TRI-PP-81-71.
- [50] Y. Ashie *et al.*, Phys. Rev. Lett., 93. 101801. 2004. <http://dx.doi.org/10.1103/PhysRevLett.93.101801>
- [51] B. Aharmim *et al.*, Phys. Rev. C, 72. 055502. 2005. <http://dx.doi.org/10.1103/PhysRevC.72.055502>
- [52] K. Eguchi *et al.*, Phys. Rev. Lett., 90:021802, 2003. <http://dx.doi.org/10.1103/PhysRevLett.90.021802>
- [53] D. I. Britton *et al.*, Phys.Rev.D 46:R885, 1992 <http://dx.doi.org/10.1103/PhysRevD.46.R885>
- [54] M. Aoki *et al.*, Phys.Rev.D 84:052002, 2011. <http://dx.doi.org/10.1103/PhysRevD.84.052002>
- [55] PEN Experiment web page. <http://pen.phys.virginia.edu/>
- [56] S. Ito *et al.* J.Phys.Conf.Ser. 631. 2015 <http://iopscience.iop.org/article/10.1088/1742-6596/631/1/012044/meta;jsessionid=62CF0077A958BB51C43D1A5712A8584A.c4.iopscience.cld.iop.org>
- [57] Geant4 web page. <https://geant4.web.cern.ch/geant4/>
- [58] A. Aguilar-Arevalo *et al.*, Nucl. Instrum. Methods. A609, 102, 2009. <http://dx.doi.org/10.1016/j.nima.2009.08.053>
- [59] G. Blanpied, *et al.*, Phys. Rev. Lett. 79.4337. 1997. <http://dx.doi.org/10.1103/PhysRevLett.79.4337>
- [60] I. H. Chiang, *et al.*, IEEE Transactionson Nuclear Science NS-42 (1995) 394. [http://ieeexplore.ieee.org/xpl/login.jsp?tp=&arnumber=467813&url=http%3A%2F%2Fieeexplore.ieee.org%2Fxppls%2Fabs\\_all.jsp%3Farnumber%3D467813](http://ieeexplore.ieee.org/xpl/login.jsp?tp=&arnumber=467813&url=http%3A%2F%2Fieeexplore.ieee.org%2Fxppls%2Fabs_all.jsp%3Farnumber%3D467813)
- [61] M. Kobayashi, *et al.*, Nucl. Instrum. Methods. A337, 355, 1994. [http://dx.doi.org/10.1016/0168-9002\(94\)91103-7](http://dx.doi.org/10.1016/0168-9002(94)91103-7)
- [62] A. Aguilar-Arevalo *et al.*, Nucl. Instrum. Methods. A621, 188, 2010. <http://dx.doi.org/10.1016/j.nima.2010.05.037>

## BIBLIOGRAPHY

---

- [63] Y. Igarashi, *et al.*, IEEE Transactions on Nuclear Science NS-52 (2005) 2866
- [64] K. Yamada, *et al.*, IEEE Transactions on Nuclear Science NS-54 (2006) 1222
- [65] N. Ito, "Improvements of COPPER 500-MHz Flash ADC for PIENU Experiment", Master Thesis, Osaka University, 2010.
- [66] J. P. Martin and P. A. Amaudruz, IEEE Transactions on Nuclear Science NS-53 (2006) 715
- [67] KOPIO web page. <http://www.hep.lancs.ac.uk/~athans/resinterests/KOPIO.html>
- [68] Y. Arai *et al.* Development and a SEU test of a TDC LSI for the ATLAS muon detector, in: KEK-PREPRINT-2001-123, 2001, p85.
- [69] J. P. Martin *et al.*, IEEE Transactions on Nuclear Science, NS-55 (2008) 84
- [70] S. Ritt and P. A. Amaudruz. The midas data acquisition system. Web page. [https://midas.triumf.ca/MidasWiki/index.php/Main\\_Page](https://midas.triumf.ca/MidasWiki/index.php/Main_Page)
- [71] NADS. Cry simulation package for cosmics, May 2010. Web page: <http://nuclear.llnl.gov/simulation/>
- [72] V. Tishchenko *et al.*, (MuLan Collaboration), Phys. Rev. D 87, 052003. 2013. <http://dx.doi.org/10.1103/PhysRevD.87.052003>
- [73] A. A. Poblaguev. Phys. Rev. D 68, 054020. 2003. <http://dx.doi.org/10.1103/PhysRevD.68.054020>
- [74] Yu. M. Bystritsky *et al.*, Phys. Rev. D 69, 114004. 2004. <http://dx.doi.org/10.1103/PhysRevD.69.114004>
- [75] M. Bychkov *et al.*, Phys. Rev. Lett. 103, 051802. 2009. <http://dx.doi.org/10.1103/PhysRevLett.103.051802>
- [76] Web page: [http://geant4.cern.ch/support/source\\_archive.shtml](http://geant4.cern.ch/support/source_archive.shtml)
- [77] Web page: [https://geant4.web.cern.ch/geant4/support/proc\\_mod\\_catalog/physics\\_lists/referencePL.shtml](https://geant4.web.cern.ch/geant4/support/proc_mod_catalog/physics_lists/referencePL.shtml)
- [78] Web page: [https://geant4.web.cern.ch/geant4/support/proc\\_mod\\_catalog/processes/](https://geant4.web.cern.ch/geant4/support/proc_mod_catalog/processes/)
- [79] T. Asaka *et al.*, JHEP, 1104, 11, 2011. [http://dx.doi.org/10.1007/JHEP04\(2011\)011](http://dx.doi.org/10.1007/JHEP04(2011)011)

## BIBLIOGRAPHY

---

- [80] G. J. Feldman and R. D. Cousins, Phys. Rev. D 57, 3873, 1998. <http://dx.doi.org/10.1103/PhysRevD.57.3873>
- [81] G4beamline web page. <http://www.muonsinternal.com/muons3/G4beamline>